

2017

## Derivatized Cyclodextrins and Their Modified Synthetic Architectures for Sensing and Catalysis

Sauradip Chaudhuri  
University of Rhode Island, sauradip\_c@yahoo.com

Follow this and additional works at: [https://digitalcommons.uri.edu/oa\\_diss](https://digitalcommons.uri.edu/oa_diss)

Terms of Use

All rights reserved under copyright.

---

### Recommended Citation

Chaudhuri, Sauradip, "Derivatized Cyclodextrins and Their Modified Synthetic Architectures for Sensing and Catalysis" (2017). *Open Access Dissertations*. Paper 649.  
[https://digitalcommons.uri.edu/oa\\_diss/649](https://digitalcommons.uri.edu/oa_diss/649)

This Dissertation is brought to you by the University of Rhode Island. It has been accepted for inclusion in Open Access Dissertations by an authorized administrator of DigitalCommons@URI. For more information, please contact [digitalcommons-group@uri.edu](mailto:digitalcommons-group@uri.edu). For permission to reuse copyrighted content, contact the author directly.

DERIVATIZED CYCLODEXTRINS AND THEIR  
MODIFIED SYNTHETIC ARCHITECTURES FOR  
SENSING AND CATALYSIS

BY

SAURADIP CHAUDHURI

A DISSERTATION SUBMITTED IN PARTIAL FULFILLMENT OF THE  
REQUIREMENTS FOR THE DEGREE OF  
DOCTOR OF PHILOSOPHY  
IN  
CHEMISTRY

UNIVERSITY OF RHODE ISLAND

2017

DOCTOR OF PHILOSOPHY DISSERTATION  
OF  
SAURADIP CHAUDHURI

APPROVED:

Dissertation Committee:

Major Professor      Mindy Levine

Brenton DeBoef

Arijit Bose

Nasser H. Zawia

DEAN OF THE GRADUATE SCHOOL

UNIVERSITY OF RHODE ISLAND

2017

## ABSTRACT

The overall theme of my graduate research is to understand forces involved in supramolecular, hydrophobically-driven interactions, primarily in cyclodextrin systems and to use those interactions in applications ranging from fluorescence-based sensing to supramolecular catalysis. This research has included a highly interdisciplinary research project exploring the effects of cation- $\pi$  interactions on surfactant/lipid bilayer vesicles for delivery applications. Cyclodextrins, which are commercially available, torus-shaped cyclic oligoamyloses, have been selected as the supramolecular hosts in these studies because of their well-defined hydrophobic interior cavity. The hydrophilic exterior, in turn imparts substantial aqueous solubility. Moreover, the primary and secondary hydroxyl groups of the cyclodextrin provide a myriad of synthetic handles for further modification and chemical derivatization.

Cyclodextrin-based catalytic systems have been envisioned for mild, environmentally friendly transformations in high-impact organic reactions. The basis of this research stems from the ability of cyclodextrins to form hydrophobic complexes with small molecules, thereby lowering the entropic barrier for the formation of a transition state in selected organic reactions. Moreover, the hydrophobic complexes of cyclodextrin with small molecules have also been shown to be more reactive from the perspective of many organic transformations.

The first manuscript “Cyclodextrin-promoted Diels Alder reactions of a polycyclic aromatic hydrocarbon under mild reaction conditions” describes Diels Alder reactions of a model polycyclic aromatic hydrocarbon (PAH), 9-anthracenemethanol with *N*-substituted maleimides under mild reaction conditions (aqueous solvent, 40°C) in the

presence of commercially available cyclodextrins. In this system, hydrophobic complexation of the *N*-substituent in turn modifies the electronics of the alkene double bond, resulting in its enhanced reactivity. We found that cyclodextrin complexation of the *N*-substituent on the maleimide (driven by hydrophobic interactions) was the key factor in determining the rate of the reaction and the overall conversion to product. Optimal results were found using *N*-cyclohexylmaleimide with a methyl- $\beta$ -cyclodextrin host, with 94% conversion obtained in 24 hours. A proposed model of the complexation with methyl- $\beta$ -cyclodextrin has been proposed, with cyclodextrin encapsulation perturbing the electronics of the dienophile double bond and enhancing its reactivity. Results of these experiments were published in *Tetrahedron Letters* in 2015, and this publication has already been cited multiple times.

The second manuscript “An Environmentally Friendly Procedure for the Aqueous Oxidation of Benzyl Alcohols to Aldehydes with Dibromodimethylhydantoin (DBDMH) and Cyclodextrin - Scope and Mechanistic Insights” discusses the cyclodextrin-promoted oxidation of benzyl alcohols to benzaldehydes using an inexpensive, commercially available reagent, 1,3-dibromo-5,5-dimethylhydantoin (DBDMH). This newly developed reaction has two notable advantages compared to previously reported benzylic oxidation reactions: (a) more environmentally friendly (*i.e.* “greener”) methodology through the use of an aqueous solvent system and mild reaction conditions; and (b) high specificity for benzyl alcohol substrates with limited side reactivity, including over-oxidation and aromatic bromination, observed. This reaction proceeds with moderate to good yields for a broad scope of benzyl alcohol substrates, with the cyclodextrin additive accomplishing two main objectives: (a) enhancement of

the desired reactivity as a result of the activation of the benzylic protons via interactions with the cyclodextrin rim; and (b) limitation of the undesired aromatic bromination side products as a result of steric shielding of the aromatic ring in the hydrophobic cyclodextrin pocket. Catalyst reusability up to three consecutive runs has been observed without substantial loss of product yield and selectivity, which further enhances the atom economy of this method. Results of these experiments were published in *Synthetic Communications* in 2016.

Non-covalent energy transfer has been used as a highly sensitive investigative tool in a wide variety of supramolecular systems. Owing to its exquisite sensitivity and dependence on a host of factors, this strategy has also been employed to study dynamic conformations of biomolecules such as nucleic acids and peptides. Our group has developed highly efficient energy transfer systems using  $\gamma$ -cyclodextrin as a supramolecular host for promoting non-covalent energy transfer from small molecule aromatic toxicants to high quantum yield fluorophores. Although  $\gamma$ -cyclodextrin has a cavity size that is well-known to be able to accommodate two small molecule guests simultaneously, limitations of  $\gamma$ -cyclodextrin include its limited specificity and ill-defined host: guest stoichiometry, as a result of its larger cavity size. There is neither control of the orientation of the guest molecule inside the cavity, nor selective binding of a single analyte in the presence of other competitive guest molecules, which often leads to sub-optimal detection sensitivity and anomalous false positive signals. In the third manuscript “Array based detection of isomeric and analogous analytes employing synthetically modified fluorophore attached  $\beta$ -cyclodextrin derivatives.” the scope of the cyclodextrin host has been expanded beyond that of  $\gamma$ -cyclodextrin, which permits

us to tailor and tune the hydrophobic domain of the hosts optimally to the size of specific guest molecules. This expansion in turn offers improvements in selectivity and sensitivity for the detection for a given analyte. The chapter highlights the synthesis of a series of fluorophore-appended  $\beta$ -cyclodextrins with specific degree of functionalization and high levels of regioselectivity. These are powerful architectures in our group's ongoing attempts at developing highly selective sensors for the efficient detection of persistent organic pollutants (POPs) at concentrations close to their environmental concentrations and literature-reported limits of concerns. By covalently linking a fluorophore directly to the cyclodextrin host, we obtained higher levels of system control in the cyclodextrin-promoted binding leading to unique fluorophore responses in the detection of several isomeric and analogous toxicants, including DDT pesticide analogues and polychlorinated biphenyl (PCBs) congeners. Advantages of using  $\beta$ -cyclodextrin include the smaller cavity size, which directly enables greater selectivity in binding as well as more efficient host-guest interactions, the lower cost of  $\beta$ -cyclodextrin compared to the  $\gamma$ -cyclodextrin isomer, and more straightforward methods for synthetically modifying the cyclodextrin host structure. We have demonstrated the ability of three architecturally distinct combinations of perbenzylated- $\beta$ -cyclodextrin/fluorophore sensor molecules to distinguish three isomeric and two analogous classes of analytes with 100% accuracy using linear discriminant analysis (LDA) of the fluorescence response signals. Each analyte-sensor binding event results in the modulation of the associated fluorophore, generating a unique chemical signature for each isomer across all the three sensors in an array based sensing strategy. Results of this work have recently been accepted for publication in *New Journal of Chemistry*.

Additionally, the synthesis of a series of cyclodextrin-incorporated higher order architectures has also been described in the fourth manuscript “Synthetic  $\beta$ -cyclodextrin dimers for squaraine binding: Effect of host architecture on photophysical properties, aggregate formation and chemical reactivity.” These architectures have been designed to exhibit higher binding affinity towards larger hydrophobic analytes like stilbene, tamoxifen and biphenyls based on hydrophobic binding of the guest from two or more distinct ends of the molecule. Two cyclodextrins were tethered by aromatic/alkyl amide linkages, and binding properties of these novel receptors were investigated for high quantum yield fluorophores (squaraine dyes in this case). A comparison of the binding constants of the different hosts was drawn to reveal the contribution from a flexible aromatic linker in the binding of hydrophobic guests. Investigation of the supramolecular interactions of hosts with a series of *N*-alkyl-*N*-methylanilino squaraines of progressively increasing alkyl chain length has produced a few notable results, including: (A) the ability of the dimers to suppress the squaraine H- and J-aggregate formations in solution very effectively (a phenomenon reported by Chen et. al. previously with  $\beta$ -cyclodextrin); (B) the ability of the dimers to protect the squaraine core from aqueous hydrolysis, thereby prolonging its half-life (a phenomenon previously reported by Smith and co-workers for squaraine pseudo-rotaxanes with synthetic tetralactam macrocycles) and finally (C) a particular dimer being able to act as an enzyme mimic for the aqueous hydrolysis of a squaraine dye with high selectivity and turn-over numbers (TON). The results of this work are being prepared for submission to the journal *Chemical Science*.



To develop sensitive and selective sensors, efforts have even been extended to synthetic macrocycles for the efficient binding of PAHs and other analytes. The fifth manuscript “A highly versatile fluorenone-based macrocycle for the sensitive detection of polycyclic aromatic hydrocarbons and fluoride anions” entails the synthesis and application of a fluorenone integrated triazolophane for the efficient binding of PAHs and fluoride anions. UV-vis and  $^1\text{H-NMR}$  spectroscopy results showed that the macrocycle has high sensitivity for selected PAHs and binds fluoride anions in a 1:2 stoichiometry. The bilateral symmetry of the macrocycle creates two binding pockets for the relatively small fluoride anion. This conclusion is well supported by the binding curve fitting of  $^1\text{H-NMR}$  titrations and Job’s plot analysis of the chemical shift of the triazole proton. A high association constant value of  $10^4 \text{ M}^{-2}$  is observed for the binding of fluoride anion in DMSO. Results of these experiments have been published in a co-first author publication in *RSC Advances* in 2016.

The final chapter of the thesis describes the application of basic supramolecular science in an industrial setting. In cosmetic industries, hydrated surfactant vesicles are used to deliver encapsulated perfume ingredients and counter skin dryness. However, addition of small concentrations of perfume-raw-materials (PRMs) has a drastic effect on vesicular suspensions, perturbing their microstructures and altering their rheological properties. In the sixth manuscript entitled, - “Impact of Nearly Water-Insoluble Additives on the Properties of Vesicular Suspensions” two model perfume-raw-material (PRM) compounds, linalyl acetate (LA) and eugenol, have been identified to have very different impacts on a multilamellar vesicular suspension made of diethylester dimethylammonium chloride (DEEDMAC) surfactant. While the former has negligible

effect, the latter triggers a change from multilamellar to unilamellar vesicles, resulting in a sharp rise in the suspension viscosity. Employing time-resolved cryogenic transmission electron microscopy, microstructural changes related to viscosity variations were observed. In addition,  $^1\text{H-NMR}$  spectroscopy was used to examine the interactions between the additives and DEEDMAC, revealing the underlying mechanisms behind the structural transformations. To provide additional insights, changes induced upon addition of non-allyl substituted structural analogs of eugenol with increasing aromaticity, cyclohexanol, phenol, catechol and guaiacol, to DEEDMAC suspensions were investigated. These molecules are therefore characterized as 'intermediate' between LA and eugenol, in terms of transitioning from the non-aromatic character of LA to the highly aromatic character of eugenol. By examining NMR results from all the additives, strong interaction of the  $\pi$  electrons in aromatic rings with the cationic DEEDMAC head groups was determined to play a significant role in vesicular exfoliation phenomena. Such interactions are strong in eugenol but not present in LA. Results of these experiments were published in a co-first author publication in *Industrial & Engineering Chemistry Research* in 2016.

## ACKNOWLEDGEMENTS

I acknowledge many people, who were key in the successful completion of the graduate school phase of my career. Firstly, I am grateful to my parents for allowing me to chase my dreams. Their trust and support mean a lot to me.

I would like to express my deepest gratitude and sincere thanks to my advisor Dr. Mindy Levine, for allowing me to be a part of her group for a long six years. I thoroughly enjoyed the intellectual freedom granted to me, which I feel has a lot in shaping my career as an independent researcher. Moreover, the numerous opportunities of attending various conferences and be a part of discussions amongst the peers is something I owe a lot to her. Also, my heartfelt thanks to her for speaking highly about me to employers and fellow scientists, recommending me as a valuable addition to their groups.

My sincere thanks to Dr. Brenton DeBoef and Dr. Matt Kiesewetter for putting up with my unrestrained inquisitiveness to know every possible detail of organic chemistry – be it C-H activation mechanisms or insightful discussions about host-guest chemistry. I apologize for knocking on the office doors everytime with all my doubts and questions. My sincere thanks to Dr. Arijit Bose for allowing me to work on one of his projects. It was a pleasure learning new techniques and addressing challenges pertaining to industrial fields of research.

I would like to thank all my wonderful past and present group members and fellow graduate students: Dr. Nicole Serio, Dr. Bhasker Radaram, Dr. Ingrid-Suzy Tamgho, William Talbert, Dana DiScenza, Teresa Mako, Daniel Jones, Benjamin Smith, Reid Yocum, Benjamin Cromwell, Missy Smith. They have been an immense source of inspiration and help in every aspect of research, from constructive criticism in group

meetings to helping me out with hands-on experiments. Special thanks to graduate students beyond my own research group: Dr. Amitesh Saha (former graduate student), Nuwan Bandara, Ashvin Fernando and Partha Datta, for sharing knowledge and ideas in various fields of research.

Finally, I am fortunate to have mentored a number of talented undergraduate students throughout my graduate career – Molly Verderame, Tyler Phelan, Gordon Rix, Hossam Zaki, Chitapom Chanthalyima and Rebecca Thurber. Their hard work and intellectual contributions to each successful project are highly appreciated.

## PREFACE

The dissertation of my research has been presented in manuscript format according to guidelines of the graduate school of the University of Rhode Island. The complete dissertation is divided into six manuscripts. The first manuscript (Chapter 1) was published in *Tetrahedron Letters* in 2015 with authors S. Chaudhuri, T. Phelan, and M. Levine. The second manuscript (Chapter 2) was published in *Synthetic Communications* in 2016, with authors S. Chaudhuri, H. Zaki, and M. Levine. The third manuscript (Chapter 3) has been accepted for publication in *New Journal of Chemistry* in 2017 with authors S. Chaudhuri, D. J. DiScenza, B. Smith, R. Yocum and M. Levine. The fourth manuscript (Chapter 4) will be submitted to *Chemical Science* with authors S. Chaudhuri, M. Verderame, Y. M. N. D. Y. Bandara, A. I. Fernando, T. Mako and M. Levine. The fifth manuscript (Chapter 5) was published in *RSC Advances* in 2017 with authors I. -S. Tamgho, S. Chaudhuri, M. Verderame, D. J. DiScenza and M. Levine. The sixth manuscript (Chapter 6) was published in *Industrial and Engineering Chemistry Research* in 2017 with authors A. Saha, S. Chaudhuri, M. Godfrin, M. Mamak, B. Reeder, T. Hodgdon, P. Saveyn, A. Tripathi and A. Bose.

## TABLE OF CONTENTS

<b>ABSTRACT</b> .....	ii
<b>ACKNOWLEDGEMENTS</b> .....	ix
<b>PREFACE</b> .....	xi
<b>TABLE OF CONTENTS</b> .....	xii
<b>LIST OF TABLES</b> .....	xiii
<b>LIST OF FIGURES</b> .....	xvii
<b>LIST OF SPECTRA</b> .....	xxxii
<b>CHAPTER 1</b> .....	1
<i>Supporting Information</i> .....	16
<b>CHAPTER 2</b> .....	22
<i>Supporting Information</i> .....	37
<b>CHAPTER 3</b> .....	51
<i>Supporting Information</i> .....	72
<b>CHAPTER 4</b> .....	109
<i>Supporting Information</i> .....	137
<b>CHAPTER 5</b> .....	216
<i>Supporting Information</i> .....	231
<b>CHAPTER 6</b> .....	266
<i>Supporting Information</i> .....	287

## LIST OF TABLES

TABLE	PAGE
<b>Chapter 1</b>	
Table 1. Changes in the alkene proton chemical shifts in 5 mM cyclodextrin solutions.....	6
Table S1. Percentage conversions of reactions at different stoichiometric ratio of methyl- $\beta$ -cyclodextrin, dienophile and the diene ([CD]: [2]: [1]).....	18
Table S2. Changes in the $^1\text{H-NMR}$ chemical shifts of the cyclodextrin protons upon binding of compound <b>1</b> in binary complexes.....	18
Table S3. Changes in the $^1\text{H-NMR}$ chemical shifts of the anomeric cyclodextrin proton upon binding of compounds <b>2a-2d</b> in binary complexes.....	19
Table S4. $^1\text{H-NMR}$ shifts of alkene protons of compounds <b>2a-2d</b> in ternary complexes.....	19
Table S5. Changes in the $^1\text{H-NMR}$ chemical shifts of the anomeric cyclodextrin proton upon the formation of ternary complexes.....	19
Table S6. Average percentage conversion data for Diels Alder reaction of 9-anthracenemethanol with compound <b>2a</b> .....	19
Table S7. Average percentage conversion data for Diels Alder reaction of 9-anthracenemethanol with compound <b>2b</b> .....	20
Table S8. Average percentage conversion data for Diels Alder reaction of 9-anthracenemethanol with compound <b>2c</b> .....	20
Table S9. Average percentage conversion data for Diels Alder reaction of 9-anthracenemethanol with compound <b>2d</b> .....	20
<b>Chapter 2</b>	
Table 1. Percent conversions of alcohol substrates <b>1</b> to aldehydes <b>2</b> .....	26
Table 2. Percent formation of compound <b>4</b> in the presence of cyclodextrins and substrate <b>1a</b> .....	30
Table 3. Percent conversions to aldehydes with different <i>N</i> -halo reagents and equivalents.....	32

Table S1. Percent conversions of alcohol substrates <b>1a</b> and <i>d2-1a</i> to aldehyde <b>2a</b> .....	39
TABLE DEMONSTRATING CATALYST REUSABILITY .....	40
TABLE ILLUSTRATING THE %N-Br BOND DISSOCIATION OF REAGENT <b>3</b> IN THE PRESENCE OF CYCLODEXTRIN ONE EQUIVALENT OF <b>1a</b> AT STANDARD REACTION CONDITIONS (CALCULATED BASED ON THE NMR PEAK INTEGRALS OF <b>3</b> AND <b>4</b> ).....	50

### Chapter 3

Table 1. Association constants of analyte <b>5</b> in per-benzylated $\beta$ -cyclodextrin, <b>S2</b> , and <b>S3</b> .....	61
Table 2. Fluorescence modulation of supramolecular sensors in the presence of aromatic alcohol analyte <b>5-8</b> .....	61
Table 3. Fluorescence modulation of sensors <b>S1-S3</b> in the presence of analytes <b>9-26</b> ...	63
Table 4. Calculated limits of detection and comparisons to known levels of concern....	67
FLUORESCENCE MODULATION SUMMARY TABLES.....	82
LIMIT OF DETECTION SUMMARY TABLE.....	83
SUMMARY TABLES FOR ARRAYS.....	84
Table S1. Benesi-Hildebrand equations for titrations of hosts ( <b>1-3</b> ) with analyte <b>5</b> ...	108

### Chapter 4

Table 1. Calculated association constant values for $\beta$ -cyclodextrin dimer hosts ( <b>1-3</b> ) for squaraines ( <b>4-11</b> ). .....	126
Table 2. Calculated stabilization energy values of $\beta$ -cyclodextrin dimer hosts ( <b>1-3</b> ) with squaraine dye guest <b>6</b> , <b>10</b> (with <b>3</b> ) & <b>11</b> (with <b>3</b> ). .....	130
Table S1. Concentrations of squaraine dye ( <b>4-11</b> ) guests added for fluorescence titration experiments.....	141
Table S2. Two sets of dimer host and squaraine guest mixtures (overall concentration of host + guest was constant) compared for Job's plot analysis.....	142
Table S3. Synthetic yields of <i>N</i> -substituted, <i>N</i> -methyl aniline precursors.....	158
Table S4. Synthetic yields and UV-vis absorption details of <i>N</i> -substituted, <i>N</i> -methylanilino squaraine guests ( <b>4-11</b> ).....	159



Table S5. Summary table of ratio of H-aggregate ( <b>I/II</b> ) and J-aggregate ( <b>III/II</b> ) to monomeric bands for various concentrations of squaraine <b>4</b> for control; compound <b>1</b> (8 $\mu$ M); compound <b>2</b> (8 $\mu$ M); compound <b>3</b> (8 $\mu$ M).....	163
Table S6. Summary table of ratio of H-aggregate ( <b>I/II</b> ) and J-aggregate ( <b>III/II</b> ) to monomeric bands for various concentrations of squaraine <b>5</b> for control; compound <b>1</b> (8 $\mu$ M); compound <b>2</b> (8 $\mu$ M); compound <b>3</b> (8 $\mu$ M).....	165
Table S7. Summary table of ratio of H-aggregate ( <b>I/II</b> ) and J-aggregate ( <b>III/II</b> ) to monomeric bands for various concentrations of squaraine <b>6</b> for control; compound <b>1</b> (8 $\mu$ M); compound <b>2</b> (8 $\mu$ M); compound <b>3</b> (8 $\mu$ M).....	166
Table S8. Summary table of ratio of H-aggregate ( <b>I/II</b> ) and J-aggregate ( <b>III/II</b> ) to monomeric bands for various concentrations of squaraine <b>7</b> for control; compound <b>1</b> (8 $\mu$ M); compound <b>2</b> (8 $\mu$ M); compound <b>3</b> (8 $\mu$ M).....	168
Table S9. Summary table of ratio of H-aggregate ( <b>I/II</b> ) and J-aggregate ( <b>III/II</b> ) to monomeric bands for various concentrations of squaraine <b>8</b> for control; compound <b>1</b> (8 $\mu$ M); compound <b>2</b> (8 $\mu$ M); compound <b>3</b> (8 $\mu$ M).....	169
Table S10. Summary table of ratio of H-aggregate ( <b>I/II</b> ) and J-aggregate ( <b>III/II</b> ) to monomeric bands for various concentrations of squaraine <b>9</b> for control; compound <b>1</b> (8 $\mu$ M); compound <b>2</b> (8 $\mu$ M); compound <b>3</b> (8 $\mu$ M).....	171
Table S11. Summary table of ratio of H-aggregate ( <b>I/II</b> ) and J-aggregate ( <b>III/II</b> ) to monomeric bands for various concentrations of squaraine <b>10</b> for control; compound <b>1</b> (8 $\mu$ M); compound <b>2</b> (8 $\mu$ M); compound <b>3</b> (8 $\mu$ M).....	172
Table S12. Summary table of ratio of H-aggregate ( <b>I/II</b> ) and J-aggregate ( <b>III/II</b> ) to monomeric bands for various concentrations of squaraine <b>11</b> for control; compound <b>1</b> (8 $\mu$ M); compound <b>2</b> (8 $\mu$ M); compound <b>3</b> (8 $\mu$ M).....	174
Table S13. Summary table of intercept (c), decay constant (k), and T (hydrolytic protection parameter, T = c/k) for hydrolytic decay of squaraines ( <b>4-11</b> ) under control, compound <b>1</b> , compound <b>2</b> and compound <b>3</b> . The values are calculated from the linear plots of hydrolytic decay as per Equation S3.....	184
Table S14. Tabulated data of Job's plot for 1:2 host-guest binding dimer <b>1</b> and squaraine <b>4</b> ( $\gamma_{\max}$ is approximately 0.67 indicating 1:2 association).....	194
Table S15. Tabulated data of Job's plot for 1:2 host-guest binding dimer <b>2</b> and squaraine <b>4</b> ( $\gamma_{\max}$ is approximately 0.34 indicating 1:2 association).....	195
Table S16. Tabulated data of Job's plot for 1:2 host-guest binding dimer <b>3</b> and squaraine <b>4</b> ( $\gamma_{\max}$ is approximately 0.34 indicating 1:2 association).....	195

Table S17. Tabulated data of Job's plot for 1:2 host-guest binding dimer **3** and squaraine **5** ( $\gamma_{\max}$  is approximately 0.67 indicating 1:2 association).....196

Table S18. Tabulated data of Job's plot for 1:1 host-guest binding dimer **3** and squaraine **9** ( $\gamma_{\max}$  is approximately 0.5 indicating 1:1 association).....197

## **Chapter 5**

Table 1. Decrease in fluorescence of analytes **4-7** in the presence of the compound **1**.....221

Table 2. Limit of detection for analytes **4-7** and comparisons to literature-reported values.....223

Table 3. Illustration of the changes in the  $^1\text{H-NMR}$  chemical signal of macrocycle **1** with binding of fluoride anions.....225

Table 4. Illustration of the changes in the  $^1\text{H-NMR}$  chemical signal of triazole proton with the binding of 10 equivalents of anions.....226

SUMMARY TABLE FOR  $^1\text{H-NMR}$  EXPERIMENTS.....238

SUMMARY TABLES FOR LIMIT OF DETECTION EXPERIMENTS.....240

SUMMARY TABLES FOR JOB'S PLOT ANALYSIS.....240

## LIST OF FIGURES

FIGURE	PAGE
<b>Chapter 1</b>	
Figure 1. <sup>1</sup> H-NMR peaks of protons (marked in red) integrated from the starting material <b>1</b> and product <b>3</b> .....	4
Figure 2. Percent conversion of compounds <b>1</b> and <b>2</b> to product <b>3</b> in various cyclodextrins for (A) compound <b>2a</b> ; (B) compound <b>2b</b> ; (C) compound <b>2c</b> ; (D) compound <b>2d</b> .....	5
Figure 3. Graphical representation of the average conversion after 24 hours for various <i>N</i> -substituted maleimides in the presence of cyclodextrins.....	8
Figure 4. Schematic illustration of how cyclodextrin complexation activates the dienophile through a combination of hydrophobic binding and electronic perturbation of the $\pi$ -bond.....	8
Figure 5. (A) Illustration of the chemical shifts of alkene protons of <b>2a</b> in binary cyclodextrin complexes (5 mM cyclodextrin); (B) Illustration of the increasing intensity of aromatic protons for compound <b>1</b> in the presence of increasing concentrations of methyl- $\beta$ -cyclodextrin.....	10
Figure 6. (A) Comparison of the <sup>1</sup> H-NMR shifts of the alkene protons in a three component mixture and in the <b>2a</b> :methyl- $\beta$ -cyclodextrin binary complex; (B) Comparison of the <sup>1</sup> H-NMR shifts of the protons of compound <b>1</b> in a three component mixture and in the <b>1</b> :methyl- $\beta$ -cyclodextrin binary complex.....	11
Figure 7. The hypothesized supramolecular assembly involving HOMO and LUMO interactions between an uncomplexed <b>1</b> and cyclodextrin-complexed <b>2</b> .....	12
Figure S1. <sup>1</sup> H-NMR peaks of protons (marked in red) integrated for the starting material, 9-anthracenemethanol ( <b>1</b> ) and calibrated for the product ( <b>3</b> ).....	17
Figure S2. General molecular structure of (A) $\alpha$ -cyclodextrin (R = H, n = 6); (B) $\beta$ -cyclodextrin (R = H, n = 7); (C) methyl- $\beta$ -cyclodextrin (R = H/CH <sub>3</sub> , n = 7); (D) $\gamma$ -cyclodextrin (R = H, n = 8).....	20
Figure S3. <sup>1</sup> H-NMR chemical shifts of H1 protons of (A) $\alpha$ -cyclodextrin; (B) $\beta$ -cyclodextrin; (C) methyl- $\beta$ -cyclodextrin; (D) $\gamma$ -cyclodextrin in presence of <i>N</i> -substituted maleimides [(i) control, without guest; (ii) compound <b>2d</b> ; (iii) compound <b>2c</b> ; (iv) compound <b>2b</b> ; and (v) compound <b>2a</b> ].....	21

Figure S4. <sup>1</sup>H NMR chemical shifts of *N*-substituent protons of compounds (A) **2a**; (B) **2b**; and (C) **2c** (only methyl protons are shown, the methylene protons merge with the cyclodextrin peaks) in the presence of cyclodextrins.....21

## Chapter 2

Figure 1. Benzyl alcohol substrates.....26

Figure 2. Illustration of the complexation of benzyl alcohols in cyclodextrin.....29

Figure 3. <sup>1</sup>H-NMR peaks of protons (marked in red) integrated for the starting material **1** and product **2**.....34

## Chapter 3

Figure 1. Schematic illustration of this work compared to previously published work.....54

Figure 2. Structures of sensors **S1-S3**.....58

Figure 3. Structures of small molecule analytes **5-26**.....58

Figure 4. Fluorescence emission spectra of supramolecular hosts **S1-S3** (1 μM) (inset shows the fluorescence of **S2** and **S3** in more detail) in 80:20 water-DMSO solution.....60

Figure 5. Fluorescence emission of (A) sensor **S1**; (B) sensor **S2**; and (C) sensor **S3** in the presence of analyte **8**.....62

Figure 6. Linear discriminant analysis showing 100% differentiation between analytes **5-8** based on their interactions with supramolecular hosts **S1-S3**.....62

Figure 7. (A) Fluorescence response of host **S1** in the presence of analytes **9-12**; (B) Linear discriminant analysis of the fluorescence responses, leading to 100% differentiation of the analyte signals. ....64

Figure 8. (A) Fluorescence response of host **S2** in the presence of analytes **13-16**; (B) Linear discriminant analysis of the fluorescence responses, leading to 100% differentiation of the analyte signals. ....65

Figure 9. (A) Fluorescence response of host **S3** in the presence of analytes **17-21**; (B) Linear discriminant analysis of the fluorescence responses, leading to 100% differentiation of the analyte signals.....65

Figure 10. (A) Fluorescence response of host **S2** in the presence of analytes **22-26**; (B) Linear discriminant analysis of the fluorescence responses, leading to 100% differentiation of the analyte signals. ....66

Figure 11. Linear discriminant analysis results of binary mixtures of analytes **5-8**. ....68

SUMMARY FIGURES.....88

SUMMARY FIGURES FOR HPLC ANALYSIS OF COMPOUNDS **S2** AND **S3**....88

SUMMARY FIGURES FOR FLUORESCENCE MODULATION.....89

SUMMARY FIGURES FOR LIMIT OF DETECTION EXPERIMENTS.....95

SUMMARY FIGURES FOR ARRAY GENERATION EXPERIMENTS.....100

## Chapter 4

Figure 1. Structures of new cyclodextrin dimers hosts **1-3**. ....113

Figure 2. Structures of *N*-substituted *N*-methylanilino squaraine dye guests **4-11**. ....113

Figure 3. Energy minimized semi-empirical PM3-level calculations of hosts **1-3**. ....116

Figure 4. Illustration of Donor-Acceptor-Donor (D-A-D) structure of squaraine dye **10**, resulting in the formation of intense H-aggregate (red) and J-aggregate (green) bands in aqueous solution. The aggregate forms are in equilibrium with monomeric squaraine, giving rise to additional blue shifted (**I**) and red shifted (**III**) UV-vis absorption bands. ....118

Figure 5. Spectral deconvolution process for investigation of H- & J- aggregate formation with increasing concentration of squaraine **6**. (A) UV-vis spectra of squaraine **6** ( $[6] = 1.3, 2.6, 3.9, 5.2, 6.5, 7.8, 9.1, 10.4, 11.7, 13.0 \mu\text{M}$ ); (B) Representative deconvoluted spectra of squaraine **6** ( $[6] = 7.8 \mu\text{M}$ , H-aggregate (**I**), Monomeric state (**II**), J-aggregate (**III**)); (C) Plot of H- aggregate (blue, ratio **I/II**) & J- aggregate (red, ratio **III/II**) against concentration for squaraine **6**; (D) Chemical structure of squaraine dye **6**. ....119

Figure 6. Plots of ratio of H-aggregate (**I/II**, grey) and J-aggregate (**III/II**, red) to monomeric bands against concentrations of Squaraine **6** for (A) control; (B) **1** ( $8\mu\text{M}$ ); (C) **2** ( $8\mu\text{M}$ ); (D) **3** ( $8\mu\text{M}$ ). ....120

Figure 7. Bar graph showing the H & J-aggregate formations for various squaraines in presence of: (A) no cyclodextrin (control); (B) **1** ( $8 \mu\text{M}$ ); (C) **2** ( $8\mu\text{M}$ ); and (D) **3** ( $8$

$\mu\text{M}$ ). Downward arrows indicate the significant reduction of aggregate formation for squaraines **6** & **10**. .....120

Figure 8. (A) Plot of  $A/A_0$  vs time for first order exponential hydrolytic decay of squaraine **6** measured at every half an hour over **5** hours. (B) Linear plot for first order exponential hydrolytic decay of squaraine **6** for (i) control; (ii) **1**; (iii) **2**; (iv) **3** (slope of the plot is a measure of the exponential decay constant  $k$ ; intercept  $c$  of the plot is a measure of the aggregate concentration  $C$ ).....122

Figure 9. Bar graph plot of the ratio of hydrolytic protection ( $T_{\text{dimer}}/T_{\text{control}}$ ) of squaraines in presence of the dimers (**1-3**) ( $T$ , defined as the hydrolytic protection parameter is given as the ratio of the Y-intercept to the slope of the linear plot;  $T = -\text{Log}(1-C)/k$ ) (downward arrows indicate the larger extent of hydrolytic decay for the squaraine **6**; calculated  $T$  values are measured from the Y-intercept and slope  $k$  of the best fitting linear plot of average  $A/A_0$  values of four trials; errors are calculated from standard deviations of  $c$  and  $k$  from the linear plot; error bars are within 10% of the calculated  $T$  values).....123

Figure 10. Schematic representation of the host-guest association in dimer host **1**, showing the H-bonding interactions of the two amide linkers to the oxoanion of the squaraine core.....124

Figure 11. Plot of  $\log K$  (association constants) versus  $N$ -substituted  $N$ -methylanilino squaraines (**4-11**) for  $\beta$ -cyclodextrin dimer hosts (**1-3**). Values for squaraine **4** (for all hosts) and squaraine **5** (for host **3**) are for 1:2 host-guest complexes (Error bars included for at least three trials).....128

Figure 12. Energy minimized (semi-empirical PM3) computational models for (A) squaraine-dimer combination (**3** + **6**); (B) squaraine-dimer combination (**3** + **10**), illustrating the different location of the anthracene core w.r.t the electrophilic squaraine core in both the cases.....129

Figure 13. Possible modes of squaraine core - linker interactions resulting in a significantly large (case **I**) and minimum (case **II**) difference in the measured oxoanion-amide distances ( $d_2 - d_1$ ).....131

Figure 14. Illustration of the disruption of aggregates of squaraine **6** in the presence of host **3**, resulting in markedly reduced insoluble aggregate and unique coloration of the complexed dye in aqueous solution (Solution of **6** (1.0 mg) + **3** (1.0 mg, 0.2 eq.) compared against **6** (1.0 mg) in 10 vol. % THF in aqueous solution).....132

Figure S1. UV-vis absorption spectra of **1** (8  $\mu\text{M}$ ) in aqueous phosphate-buffered saline (PBS) solution.....160

Figure S2. Fluorescence emission spectra of **1** (0.5  $\mu\text{M}$ ) in aqueous phosphate-buffered saline (PBS) solution ( $\lambda_{\text{excitation}} = 260 \text{ nm}$ ).....160

Figure S3. Integrated fluorescence emission vs concentration curve for compound <b>1</b> in aqueous phosphate-buffered saline (PBS) solution ( $\lambda_{\text{excitation}} = 260$ nm). The poor linear fit indicates to higher-order aggregate formations.....	160
Figure S4. UV-vis absorption spectra of <b>2</b> (8 $\mu\text{M}$ ) in aqueous phosphate-buffered saline (PBS) solution.....	161
Figure S5. Fluorescence emission spectra of <b>2</b> (0.5 $\mu\text{M}$ ) in aqueous phosphate-buffered saline (PBS) solution ( $\lambda_{\text{excitation}} = 275$ nm).....	161
Figure S6. Integrated fluorescence emission vs concentration curve for compound <b>2</b> in aqueous phosphate-buffered saline (PBS) solution ( $\lambda_{\text{excitation}} = 275$ nm).....	161
Figure S7. UV-vis absorption spectra of <b>3</b> (8 $\mu\text{M}$ ) in aqueous phosphate-buffered saline (PBS) solution .....	162
Figure S8. Fluorescence emission spectra of <b>3</b> (0.5 $\mu\text{M}$ ) in aqueous phosphate-buffered saline (PBS) solution ( $\lambda_{\text{excitation}} = 360$ nm).....	162
Figure S9. Integrated fluorescence emission vs concentration curve for compound <b>3</b> in aqueous phosphate-buffered saline (PBS) solution ( $\lambda_{\text{excitation}} = 360$ nm).....	162
Figure S10. UV-vis absorption spectra of squaraine <b>4</b> for (A) control; (B) compound <b>1</b> (8 $\mu\text{M}$ ); (C) compound <b>2</b> (8 $\mu\text{M}$ ); and (D) compound <b>3</b> (8 $\mu\text{M}$ ) (squaraine <b>4</b> concentrations increase in the order as follows: 1.5 $\mu\text{M}$ ; 2.9 $\mu\text{M}$ ; 4.4 $\mu\text{M}$ ; 5.9 $\mu\text{M}$ ; 7.4 $\mu\text{M}$ ; 8.9 $\mu\text{M}$ ; 10.4 $\mu\text{M}$ ; 11.9 $\mu\text{M}$ ; 13.3 $\mu\text{M}$ ; 14.8 $\mu\text{M}$ ).....	163
Figure S11. Plots of ratio of H-aggregate ( <b>I/II</b> , blue) and J-aggregate ( <b>III/II</b> , red) to monomeric bands against concentration of squaraine <b>4</b> for (A) control; (B) compound <b>1</b> (8 $\mu\text{M}$ ); (C) compound <b>2</b> (8 $\mu\text{M}$ ); and (D) compound <b>3</b> (8 $\mu\text{M}$ ).....	164
Figure S12. UV-vis absorption spectra of squaraine <b>5</b> for (A) control; (B) compound <b>1</b> (8 $\mu\text{M}$ ); (C) compound <b>2</b> (8 $\mu\text{M}$ ); and (D) compound <b>3</b> (8 $\mu\text{M}$ ). (squaraine <b>5</b> concentrations increase in the order as follows: 1.4 $\mu\text{M}$ ; 2.8 $\mu\text{M}$ ; 4.2 $\mu\text{M}$ ; 5.5 $\mu\text{M}$ ; 6.9 $\mu\text{M}$ ; 8.3 $\mu\text{M}$ ; 9.7 $\mu\text{M}$ ; 11.1 $\mu\text{M}$ ; 12.5 $\mu\text{M}$ ; 13.9 $\mu\text{M}$ ).....	164
Figure S13. Plots of ratio of H-aggregate ( <b>I/II</b> , blue) and J-aggregate ( <b>III/II</b> , red) to monomeric bands against concentration of squaraine <b>5</b> for (A) control; (B) <b>1</b> (8 $\mu\text{M}$ ); (C) <b>2</b> (8 $\mu\text{M}$ ); and (D) <b>3</b> (8 $\mu\text{M}$ ).....	165
Figure S14. UV-vis absorption spectra of squaraine <b>6</b> for (A) control; (B) <b>1</b> (8 $\mu\text{M}$ ); (C) <b>2</b> (8 $\mu\text{M}$ ); and (D) <b>3</b> (8 $\mu\text{M}$ ) (squaraine <b>6</b> concentrations increase in the order as follows: 1.3 $\mu\text{M}$ ; 2.6 $\mu\text{M}$ ; 3.9 $\mu\text{M}$ ; 5.2 $\mu\text{M}$ ; 6.5 $\mu\text{M}$ ; 7.8 $\mu\text{M}$ ; 9.1 $\mu\text{M}$ ; 10.4 $\mu\text{M}$ ; 11.7 $\mu\text{M}$ ; 13.0 $\mu\text{M}$ ).....	166

Figure S15. Plots of ratio of H-aggregate (**I/II**, blue) and J-aggregate (**III/II**, red) to monomeric bands against concentration of squaraine **6** for (A) control; (B) **1** (8 $\mu$ M); (C) **2** (8 $\mu$ M); and (D) **3** (8 $\mu$ M).....167

Figure S16. UV-vis absorption spectra of squaraine **7** for (A) control; (B) compound **1** (8 $\mu$ M); (C) compound **2** (8 $\mu$ M); and (D) compound **3** (8 $\mu$ M) (squaraine **7** concentrations increase in the order as follows: 1.2 $\mu$ M; 2.4 $\mu$ M; 3.7 $\mu$ M; 4.9 $\mu$ M; 6.1 $\mu$ M; 7.4 $\mu$ M; 8.6 $\mu$ M; 9.8 $\mu$ M; 11.0 $\mu$ M; 12.2 $\mu$ M). .....167

Figure S17. Plots of ratio of H-aggregate (**I/II**, blue) and J-aggregate (**III/II**, red) to monomeric bands against concentration of squaraine **7** for (A) control; (B) compound **1** (8 $\mu$ M); (C) compound **2** (8 $\mu$ M); and (D) compound **3** (8 $\mu$ M).....168

Figure S18. UV-vis absorption spectra of squaraine **8** for (A) control; (B) compound **1** (8 $\mu$ M); (C) compound **2** (8 $\mu$ M); and (D) compound **3** (8 $\mu$ M) (squaraine **8** concentrations increase in the order as follows: 1.2 $\mu$ M; 2.3 $\mu$ M; 3.5 $\mu$ M; 4.6 $\mu$ M; 5.8 $\mu$ M; 6.9 $\mu$ M; 8.1 $\mu$ M; 9.3 $\mu$ M; 10.4 $\mu$ M; 11.6 $\mu$ M).....169

Figure S19. Plots of ratio of H-aggregate (**I/II**, blue) and J-aggregate (**III/II**, red) to monomeric bands against concentration of squaraine **8** for (A) control; (B) compound **1** (8 $\mu$ M); (C) compound **2** (8 $\mu$ M); and (D) compound **3** (8 $\mu$ M).....170

Figure S20. UV-vis absorption spectra of squaraine **9** for (A) control; (B) compound **1** (8 $\mu$ M); (C) compound **2** (8 $\mu$ M); and (D) compound **3** (8 $\mu$ M) (squaraine **9** concentrations increase in the order as follows: 1.1 $\mu$ M; 2.2 $\mu$ M; 3.3 $\mu$ M; 4.4 $\mu$ M; 5.5 $\mu$ M; 6.6 $\mu$ M; 7.7 $\mu$ M; 8.8 $\mu$ M; 9.9 $\mu$ M; 11.0 $\mu$ M).....170

Figure S21. Plots of ratio of H-aggregate (**I/II**, blue) and J-aggregate (**III/II**, red) to monomeric bands against concentration of squaraine **9** for (A) control; (B) compound **1** (8 $\mu$ M); (C) compound **2** (8 $\mu$ M); and (D) compound **3** (8 $\mu$ M).....171

Figure S22. UV-vis absorption spectra of squaraine **10** for (A) control; (B) **1** (8 $\mu$ M); (C) **2** (8 $\mu$ M); and (D) **3** (8 $\mu$ M) (squaraine **10** concentrations increase in the order as follows: 1.2 $\mu$ M; 2.5 $\mu$ M; 3.7 $\mu$ M; 4.9 $\mu$ M; 6.2 $\mu$ M; 7.4 $\mu$ M; 8.6 $\mu$ M; 9.9 $\mu$ M; 11.1 $\mu$ M; 12.4 $\mu$ M)....172

Figure S23. Plots of ratio of H-aggregate (**I/II**, blue) and J-aggregate (**III/II**, red) to monomeric bands against concentration of squaraine **10** for (A) control; (B) compound **1** (8 $\mu$ M); (C) compound **2** (8 $\mu$ M); and (D) compound **3** (8 $\mu$ M).....173

Figure S24. UV-vis absorption spectra of squaraine **11** for (A) control; (B) **1** (8 $\mu$ M); (C) **2** (8 $\mu$ M); and (D) **3** (8 $\mu$ M). (squaraine **11** concentrations increase in the order as follows: 1.0 $\mu$ M; 2.0 $\mu$ M; 3.1 $\mu$ M; 4.1 $\mu$ M; 5.1 $\mu$ M; 6.2 $\mu$ M; 7.2 $\mu$ M; 8.2 $\mu$ M; 9.2 $\mu$ M; 10.3 $\mu$ M).....173

Figure S25. Plots of ratio of H-aggregate (**I/II**, blue) and J-aggregate (**III/II**, red) to monomeric bands against concentration of squaraine **11** for (A) control; (B) **1** (8 $\mu$ M); (C) **2** (8 $\mu$ M); and (D) **3** (8 $\mu$ M).....174



Figure S26. Photographs illustrating the hydrolysis of Squaraine <b>6</b> (24 $\mu\text{M}$ ) after (A) 0 hrs; (B) 3 hrs.....	176
Figure S27. UV-vis absorption spectra of squaraine <b>4</b> (24 $\mu\text{M}$ ) for (A) control; (B) <b>1</b> (24 $\mu\text{M}$ ); (C) <b>2</b> (24 $\mu\text{M}$ ); (D) <b>3</b> (24 $\mu\text{M}$ ). (Each spectrum is recorded at 30 minutes over a period of 5 hours). ....	176
Figure S28. Linear plot for first order exponential hydrolytic decay of squaraine <b>4</b> (24 $\mu\text{M}$ ) for (A) control; (B) <b>1</b> (24 $\mu\text{M}$ ); (C) <b>2</b> (24 $\mu\text{M}$ ); (D) <b>3</b> (24 $\mu\text{M}$ ) (slope of the plot is a measure of the exponential decay constant $k$ ; intercept of the plot is a measure of the aggregated concentration $C$ ).....	177
Figure S29. UV-vis absorption spectra of squaraine <b>5</b> (24 $\mu\text{M}$ ) for (A) control; (B) <b>1</b> (24 $\mu\text{M}$ ); (C) <b>2</b> (24 $\mu\text{M}$ ); (D) <b>3</b> (24 $\mu\text{M}$ ). (Each spectrum is recorded at 30 minutes over a period of 5 hours). ....	177
Figure S30. Linear plot for first order exponential hydrolytic decay of squaraine <b>5</b> (24 $\mu\text{M}$ ) for (A) control; (B) <b>1</b> (24 $\mu\text{M}$ ); (C) <b>2</b> (24 $\mu\text{M}$ ); (D) <b>3</b> (24 $\mu\text{M}$ ) (slope of the plot is a measure of the exponential decay constant $k$ ; intercept of the plot is a measure of the aggregated concentration $C$ ).....	178
Figure S31. UV-vis absorption spectra of squaraine <b>6</b> (24 $\mu\text{M}$ ) for (A) control; (B) <b>1</b> (24 $\mu\text{M}$ ); (C) <b>2</b> (24 $\mu\text{M}$ ); (D) <b>3</b> (24 $\mu\text{M}$ ). (Each spectrum is recorded at 30 minutes over a period of 5 hours). ....	178
Figure S32. Linear plot for first order exponential hydrolytic decay of squaraine <b>6</b> (24 $\mu\text{M}$ ) for (A) control; (B) <b>1</b> (24 $\mu\text{M}$ ); (C) <b>2</b> (24 $\mu\text{M}$ ); (D) <b>3</b> (24 $\mu\text{M}$ ) (slope of the plot is a measure of the exponential decay constant $k$ ; intercept of the plot is a measure of the aggregated concentration $C$ ).....	179
Figure S33. UV-vis absorption spectra of squaraine <b>7</b> (24 $\mu\text{M}$ ) for (A) control; (B) compound <b>1</b> (24 $\mu\text{M}$ ); (C) compound <b>2</b> (24 $\mu\text{M}$ ); (D) compound <b>3</b> (24 $\mu\text{M}$ ). (Each spectrum is recorded at 30 minutes over a period of 5 hours). ....	179
Figure S34. Linear plot for first order exponential hydrolytic decay of squaraine <b>7</b> (24 $\mu\text{M}$ ) for (A) control; (B) compound <b>1</b> (24 $\mu\text{M}$ ); (C) compound <b>2</b> (24 $\mu\text{M}$ ); (D) compound <b>3</b> (24 $\mu\text{M}$ ) (slope of the plot is a measure of the exponential decay constant $k$ ; intercept of the plot is a measure of the aggregated concentration $C$ ).....	180
Figure S35. UV-vis absorption spectra of squaraine <b>8</b> (24 $\mu\text{M}$ ) for (A) control; (B) compound <b>1</b> (24 $\mu\text{M}$ ); (C) compound <b>2</b> (24 $\mu\text{M}$ ); (D) compound <b>3</b> (24 $\mu\text{M}$ ). (Each spectrum is recorded at 30 minutes over a period of 5 hours).....	180
Figure S36. Linear plot for first order exponential hydrolytic decay of squaraine <b>8</b> (24 $\mu\text{M}$ ) for (A) control; (B) <b>1</b> (24 $\mu\text{M}$ ); (C) <b>2</b> (24 $\mu\text{M}$ ); (D) <b>3</b> (24 $\mu\text{M}$ ) (slope of the plot is	

a measure of the exponential decay constant $k$ ; intercept of the plot is a measure of the aggregated concentration $C$ ).....	181
Figure S37. UV-vis absorption spectra of squaraine <b>9</b> (24 $\mu\text{M}$ ) for (A) control; (B) <b>1</b> (24 $\mu\text{M}$ ); (C) <b>2</b> (24 $\mu\text{M}$ ); (D) <b>3</b> (24 $\mu\text{M}$ ). (Each spectrum is recorded at 30 minutes over a period of 5 hours).....	181
Figure S38. Linear plot for first order exponential hydrolytic decay of squaraine <b>9</b> (24 $\mu\text{M}$ ) for (A) control; (B) <b>1</b> (24 $\mu\text{M}$ ); (C) <b>2</b> (24 $\mu\text{M}$ ); (D) <b>3</b> (24 $\mu\text{M}$ ) (slope of the plot is a measure of the exponential decay constant $k$ ; intercept of the plot is a measure of the aggregated concentration $C$ ).....	182
Figure S39. UV-vis absorption spectra of squaraine <b>10</b> (24 $\mu\text{M}$ ) for (A) control; (B) <b>1</b> (24 $\mu\text{M}$ ); (C) <b>2</b> (24 $\mu\text{M}$ ); (D) <b>3</b> (24 $\mu\text{M}$ ). (Each spectrum is recorded at 30 minutes over a period of 5 hours). ....	182
Figure S40. Linear plot for first order exponential hydrolytic decay of squaraine <b>10</b> (24 $\mu\text{M}$ ) for (A) control; (B) <b>1</b> (24 $\mu\text{M}$ ); (C) <b>2</b> (24 $\mu\text{M}$ ); (D) <b>3</b> (24 $\mu\text{M}$ ) (slope of the plot is a measure of the exponential decay constant $k$ ; intercept of the plot is a measure of the aggregated concentration $C$ ).....	183
Figure S41. UV-vis absorption spectra of Squaraine <b>11</b> (24 $\mu\text{M}$ ) for (A) control; (B) <b>1</b> (24 $\mu\text{M}$ ); (C) <b>2</b> (24 $\mu\text{M}$ ); and (D) <b>3</b> (24 $\mu\text{M}$ ). (Each spectrum is recorded at 30 minutes over a period of 5 hours).....	183
Figure S42. Linear plot for first order exponential hydrolytic decay of squaraine <b>11</b> (24 $\mu\text{M}$ ) for (A) control; (B) <b>1</b> (24 $\mu\text{M}$ ); (C) <b>2</b> (24 $\mu\text{M}$ ) (slope of the plot is a measure of the exponential decay constant $k$ ; intercept of the plot is a measure of the aggregated concentration $C$ ).....	184
Figure S43. Linear plot for zero order behavior of hydrolytic decay of squaraine <b>11</b> (24 $\mu\text{M}$ ) with dimer host <b>3</b> (24 $\mu\text{M}$ ) (rate of decay $k = 0.05 \text{ h}^{-1}$ ).....	185
Figure S44. 1:2 host-guest binding isotherm for <b>1</b> and squaraine <b>4</b> ( $K_1 = 2.8 (0.3) \times 10^3 \text{ M}^{-1}$ ; $K_2 = 2.7 (0.4) \times 10^{11} \text{ M}^{-1}$ ; Equation S5 was used for calculation).....	186
Figure S45. 1:1 host-guest binding isotherm for <b>1</b> and squaraine <b>5</b> ( $K_1 = 2.7 (0.5) \times 10^6 \text{ M}^{-1}$ ; Equation S4 was used for calculation).....	186
Figure S46. 1:1 host-guest binding isotherm for <b>1</b> and squaraine <b>6</b> ( $K_1 = 3.5 (0.5) \times 10^6 \text{ M}^{-1}$ ; Equation S4 was used for calculation).....	186
Figure S47. 1:1 host-guest binding isotherm for <b>1</b> and squaraine <b>7</b> ( $K_1 = 1.5 (0.7) \times 10^6 \text{ M}^{-1}$ ; Equation S4 was used for calculation).....	187

Figure S48. 1:1 host-guest binding isotherm for <b>1</b> and squaraine <b>8</b> ( $K_1 = 4.5 (0.8) \times 10^6 \text{ M}^{-1}$ ; Equation S4 was used for calculation).....	187
Figure S49. 1:1 host-guest binding isotherm for <b>1</b> and squaraine <b>9</b> ( $K_1 = 6.6 (0.8) \times 10^6 \text{ M}^{-1}$ ; Equation S4 was used for calculation).....	187
Figure S50. 1:1 host-guest binding isotherm for <b>1</b> and squaraine <b>10</b> ( $K_1 = 1.7 (0.4) \times 10^5 \text{ M}^{-1}$ ; Equation S4 was used for calculation).....	188
Figure S51. 1:1 host-guest binding isotherm for <b>1</b> and squaraine <b>11</b> ( $K_1 = 1.2 (0.2) \times 10^7 \text{ M}^{-1}$ ; Equation S4 was used for calculation).....	188
Figure S52. 1:2 host-guest binding isotherm for <b>2</b> and squaraine <b>4</b> ( $K_1 = 1.6 (0.4) \times 10^4 \text{ M}^{-1}$ ; $K_2 = 5.4 (0.8) \times 10^9 \text{ M}^{-1}$ ; Equation S5 was used for calculation).....	188
Figure S53. 1:1 host-guest binding isotherm for <b>2</b> and squaraine <b>5</b> ( $K_1 = 2.6 (0.4) \times 10^6 \text{ M}^{-1}$ ; Equation S4 was used for calculation).....	189
Figure S54. 1:1 host-guest binding isotherm for <b>2</b> and squaraine <b>6</b> ( $K_1 = 3.5 (1.2) \times 10^5 \text{ M}^{-1}$ ; Equation S4 was used for calculation).....	189
Figure S55. 1:1 host-guest binding isotherm for <b>2</b> and squaraine <b>7</b> ( $K_1 = 2.1 (0.8) \times 10^5 \text{ M}^{-1}$ ; Equation S4 was used for calculation).....	189
Figure S56. 1:1 host-guest binding isotherm for <b>2</b> and squaraine <b>8</b> ( $K_1 = 3.1 (0.1) \times 10^5 \text{ M}^{-1}$ ; Equation S4 was used for calculation).....	190
Figure S57. 1:1 host-guest binding isotherm for <b>2</b> and squaraine <b>9</b> ( $K_1 = 2.4 (0.7) \times 10^5 \text{ M}^{-1}$ ; Equation S4 was used for calculation).....	190
Figure S58. 1:1 host-guest binding isotherm for <b>2</b> and squaraine <b>10</b> ( $K_1 = 4.2 (1.0) \times 10^5 \text{ M}^{-1}$ ; Equation S4 was used for calculation).....	190
Figure S59. 1:1 host-guest binding isotherm for <b>2</b> and squaraine <b>11</b> ( $K_1 = 1.0 (0.1) \times 10^6 \text{ M}^{-1}$ ; Equation S4 was used for calculation).....	191
Figure S60. 1:2 host-guest binding isotherm for <b>3</b> and squaraine <b>4</b> ( $K_1 = 3.3 (0.4) \times 10^3 \text{ M}^{-1}$ ; $K_2 = 7.1 (0.9) \times 10^9 \text{ M}^{-1}$ ; Equation S5 was used for calculation).....	191
Figure S61. 1:2 host-guest binding isotherm for <b>3</b> and squaraine <b>5</b> ( $K_1 = 3.6 (0.6) \times 10^3 \text{ M}^{-1}$ ; $K_2 = 1.2 (0.2) \times 10^{10} \text{ M}^{-1}$ ; Equation S5 was used for calculation).....	191
Figure S62. 1:1 host-guest binding isotherm for <b>3</b> and squaraine <b>6</b> ( $K_1 = 2.3 (0.1) \times 10^8 \text{ M}^{-1}$ ; Equation S4 was used for calculation).....	192

Figure S63. 1:1 host-guest binding isotherm for <b>3</b> and squaraine <b>7</b> ( $K_1 = 4.1 (0.5) \times 10^6 \text{ M}^{-1}$ ; Equation S4 was used for calculation).....	192
Figure S64. 1:1 host-guest binding isotherm for <b>3</b> and squaraine <b>8</b> ( $K_1 = 3.2 (0.4) \times 10^7 \text{ M}^{-1}$ ; Equation S4 was used for calculation).....	192
Figure S65. 1:1 host-guest binding isotherm for <b>3</b> and squaraine <b>9</b> ( $K_1 = 8.1 (0.5) \times 10^5 \text{ M}^{-1}$ ; Equation S4 was used for calculation).....	193
Figure S66. 1:1 host-guest binding isotherm for <b>3</b> and squaraine <b>10</b> ( $K_1 = 2.4 (0.6) \times 10^6 \text{ M}^{-1}$ ; Equation S4 was used for calculation).....	193
Figure S67. 1:1 host-guest binding isotherm for <b>3</b> and squaraine <b>11</b> ( $K_1 = 3.0 (0.2) \times 10^6 \text{ M}^{-1}$ ; Equation S4 was used for calculation).....	193
Figure S68. Job's plot for 1:2 host-guest binding dimer <b>1</b> and squaraine <b>4</b> ( $\gamma_{\text{max}}$ is approximately 0.67 indicating 1:2 association).....	194
Figure S69. Job's plot for 1:2 host-guest binding dimer <b>2</b> and squaraine <b>4</b> ( $\gamma_{\text{max}}$ is approximately 0.34 indicating 1:2 association). ....	194
Figure S70. Job's plot for 1:2 host-guest binding dimer <b>3</b> and squaraine <b>4</b> ( $\gamma_{\text{max}}$ is approximately 0.34 indicating 1:2 association).....	195
Figure S71. Job's plot for 1:2 host-guest binding dimer <b>3</b> and squaraine <b>5</b> ( $\gamma_{\text{max}}$ is approximately 0.67 indicating 1:2 association).....	196
Figure S72. Job's plot for 1:1 host-guest binding dimer <b>3</b> and squaraine <b>9</b> ( $\gamma_{\text{max}}$ is approximately 0.5 indicating 1:1 association).....	197
Figure S73. Energy minimized (semi-empirical PM3) computational models for squaraine-dimer combination ( <b>1</b> + <b>6</b> ), (A) transverse view; (B) cross-sectional view.....	198
Figure S74. Energy minimized (semi-empirical PM3) computational models for squaraine-dimer combination ( <b>1</b> + <b>6</b> ) (Guest <b>6</b> is in depicted in space-filling model while host <b>1</b> is depicted in stick model generated via Molecular Operating Environment (MOE) <sup>3</sup> ).....	198
Figure S75. Energy minimized (semi-empirical PM3) computational models for squaraine-dimer combination ( <b>2</b> + <b>6</b> ), (A) transverse view; (B) cross-sectional view.....	199
Figure S76. Energy minimized (semi-empirical PM3) computational models for squaraine-dimer combination ( <b>2</b> + <b>6</b> ) (Guest squaraine <b>6</b> is in depicted in space-filling	

model while host dimer **2** is depicted in stick model generated via Molecular Operating Environment (MOE)<sup>3</sup>.....199

Figure S77. Energy minimized (semi-empirical PM3) computational models for squaraine-dimer combination (**3** + **6**), (A) transverse view; (B) cross-sectional view.....200

Figure S78. Energy minimized (semi-empirical PM3) computational models for squaraine-dimer combination (**3** + **6**) (Guest squaraine **6** is in depicted in space-filling model while host dimer **3** is depicted in stick model generated via Molecular Operating Environment (MOE)<sup>3</sup>).....200

Figure S79. Energy minimized (semi-empirical PM3) computational models for squaraine-dimer combination (**3** + **10**), (A) transverse view; (B) cross-sectional view.....201

Figure S80. Energy minimized (semi-empirical PM3) computational models for squaraine-dimer combination (**3** + **10**) (Guest squaraine **10** is in depicted in space-filling model while host dimer **3** is depicted in stick model generated via Molecular Operating Environment (MOE)<sup>3</sup>).....201

Figure S81. Energy minimized (semi-empirical PM3) computational models for squaraine-dimer combination (**3** + **11**), (A) transverse view; (B) cross-sectional view.....202

Figure S82. Energy minimized (semi-empirical PM3) computational models for squaraine-dimer combination (**3** + **11**) (Guest squaraine **11** is in depicted in space-filling model while host dimer **3** is depicted in stick model generated via Molecular Operating Environment (MOE)<sup>3</sup>).....202

Figure S83. TLC plates after elution with methanol:chloroform (1:9) as the mobile phase (A) under ambient light; and (B) under a UV lamp light (short wavelength, 254 nm).....203

## Chapter 5

Figure 1. Synthesis of macrocycle **1** *via* the reaction of precursors **2** and **3**.....219

Figure 2. (A) Energy minimized structure of compound **1**; (B) Electron density mapping of compound **1**, with the blue regions corresponding to the electron-deficient segments and the red regions corresponding to the electron-rich segments.....220

Figure 3. Structures of polycyclic aromatic hydrocarbons **4-7** with electron density mapping of each compound highlighting their electron rich aromatic natures.....220

Figure 4. Structures of photophysically active components <b>8</b> and <b>9</b> (structurally tethered in <b>1</b> ).....	222
Figure 5. Fluorescence emission changes of analytes <b>5-7</b> in the presence of macrocycle <b>1</b> (A-C) and component moieties <b>8</b> and <b>9</b> (D-F). (A and D) analyte <b>5</b> ; (B and E) analyte <b>6</b> ; and (C and F) analyte <b>7</b> . The black line represents the fluorescence emission from the analyte alone, and the red line represents the fluorescence emission from the analyte in the presence of the other compounds.....	222
Figure 6. Illustration of changes in the UV-visible absorption spectrum of macrocycle <b>1</b> with the addition of up to 10 equivalents of fluoride anion.....	224
Figure 7. Illustration of the changes in the <sup>1</sup> H-NMR chemical shifts of macrocycle <b>1</b> with the titration of fluoride anions.....	225
Figure 8. Proposed geometry of how macrocycle <b>1</b> binds two fluoride anions.....	226
SUMMARY FIGURES FOR COMPUTATIONAL EXPERIMENTS.....	240
SUMMARY FIGURES FOR ABSORBANCE EXPERIMENTS.....	243
SUMMARY FIGURES FOR FLUORESCENCE EXPERIMENTS.....	247
SUMMARY FIGURES FOR LIMIT OF DETECTION EXPERIMENTS.....	250
SUMMARY FIGURES FOR NMR TITRATION EXPERIMENTS.....	254
SUMMARY FIGURE FOR JOB'S PLOT ANALYSIS.....	257

## Chapter 6

Figure 1. Suspension rheometric data. After mixing, the samples were aged to the reported times and then characterized. <b>(a)</b> Steady shear viscosity versus shear rate for DEEDMAC suspensions, as well as LA and eugenol added to DEEDMAC suspensions. Given the error bars which correspond to the spread in the data from 3 runs, the increase in viscosity of the LA + DEEDMAC suspension compared to DEEDMAC by itself is small. The increase in viscosity for the eugenol + DEEDMAC suspension is about an order of magnitude higher. The error bars for the eugenol + DEEDMAC suspension are within the size of the plotting symbols <b>(b)</b> Viscosity, measured at a shear rate of 0.1 sec <sup>-1</sup> , versus time. Addition of 2 wt% LA to the DEEDMAC vesicle suspension results in a small increase of the viscosity. Addition of 2 wt% eugenol results in a 100-200-fold increase in viscosity.....	273
Figure 2. Cryo-TEM image of <b>(a)</b> multilamellar vesicles in a DEEDMAC vesicle suspension, indicated by white arrows. BD indicates beam damage. <b>(b)</b> DEEDMAC suspension diluted 1:1 by volume with 1200 ppm CaCl <sub>2</sub> . The structures remain the same as in <b>(a)</b> because of the isotonic dilution. <b>(c)</b> DEEDMAC suspension after 1:1 dilution by volume with deionized water, showing unilamellar vesicles. ....	275

Figure 3. Cryo-TEM images showing no changes after of addition of 2wt% LA to a DEEDMAC vesicle suspension **(a)** 10 secs after mixing and **(b)** 24 hrs after mixing. BD indicates beam damage. White arrows indicate vesicles. Multilamellar vesicles remain as the predominant structure after addition of LA.....276

Figure 4. Cryo-TEM images of a DEEDMAC vesicle suspension with 2wt% eugenol **(a)** 10 secs after mixing, showing multiple lamellae; **(b)** 6 hrs after mixing, showing undulations, marked by arrows and **(c)** 12 hrs after mixing, showing exfoliation and breakup of bilayers marked by yellow arrows, and free bilayer fragments indicated by green arrows. **(d)** 24 hrs after mixing, showing unilamellar vesicles, tubules and bilayer fragments **(e)** morphologies from (d) after tilting the TEM stage by 20°. Vesicle projections do not change shape, but their distance from each other can change. Bilayer fragments are not always visible in 4(d) but become visible as lines in 4(e). The distance between tubule edges does not change upon tilting. Scale bars = 100 nm. BD indicates beam damage.....277

Figure 5. <sup>1</sup>H-NMR spectra showing the impact of adding a DEEDMAC vesicle suspension (DVD) to 2wt% and 4wt% eugenol dissolved in a 1200 ppm CaCl<sub>2</sub> solution in D<sub>2</sub>O 24 hrs after mixing. The broadening of several proton peaks from eugenol, marked by the arrows, indicates that the eugenol interacts with the DEEDMAC.....279

Figure 6. Time evolution of <sup>1</sup>H-NMR spectra after the addition of a 2wt% DEEDMAC vesicle suspension (DVD) to a 2wt% eugenol dissolved in a 1200ppm CaCl<sub>2</sub> solution in D<sub>2</sub>O. The peak intensity corresponding to methyl protons from the DEEDMAC head group, marked by the arrows, increases up to 24 hrs after mixing.....280

Figure 7. <sup>1</sup>H-NMR spectra showing the impact of adding 2 wt % DEEDMAC vesicle suspension (DVD) to LA, showing no peak broadening. The intensity of the peaks also remains stable over time.....281

Figure 8. <sup>1</sup>H-NMR spectra showing the impact of adding 2 wt % DEEDMAC vesicle suspension (DVD) to various additives. While <sup>1</sup>H-NMR peaks of cyclohexanol and LA exhibit no change, the aromatic proton peaks of phenol, catechol, guaiacol and eugenol show strong broadening due to cation-  $\pi$  electrons interaction with the cationic DEEDMAC head group. The thickness of the dashed lines is meant to indicate the strength of the interactions.....282

Figure S1 (A) Cryo-TEM image showing effect of addition of 2wt% cyclohexanol to a DEEDMAC vesicle suspension after 24 hrs. Multilamellar vesicles (white arrows). Scale bar = 100nm.....287

Figure S1 (B) <sup>1</sup>H-NMR spectra of addition of 2wt% DEEDMAC suspension to cyclohexanol after 24 hrs showing no peak broadening.....287

Figure S2 (A) Cryo-TEM image showing effect of addition of 2wt% phenol to a DEEDMAC vesicle suspension after 24 hrs. Undulated vesicles (white arrows) and bilayer fragments (white box) Scale bar = 100nm.....	288
Figure S2 (B) <sup>1</sup> H-NMR spectra of addition of 2wt% DEEDMAC suspension to phenol after 24 hrs showing modest peak broadening.....	288
Figure S3 (A) Cryo-TEM image showing effect of addition of 2wt% catechol to a DEEDMAC vesicle suspension after 24 hrs. Tubules (yellow boxes) and bilayer fragments (white box). Scale bar = 100nm. ....	289
Figure S3 (B) <sup>1</sup> H-NMR spectra of addition of 2wt% DEEDMAC suspension to catechol after 24 hrs showing strong peak broadening. ....	289
Figure S4 (A) Cryo-TEM image showing effect of addition of 2wt% guaiacol to a DEEDMAC vesicle suspension after 24 hrs. Unilamellar vesicles (green box) and bilayer fragments (white boxes). Scale bar = 100nm. ....	290
Figure S4 (B) <sup>1</sup> H-NMR spectra of addition of 2wt% DEEDMAC suspension to guaiacol after 24 hrs showing strong peak broadening. ....	290



## LIST OF SPECTRA

SPECTRA	PAGE
<b>Chapter 2</b>	
<sup>1</sup> H-NMR SPECTRA FOR REACTION ANALYSIS.....	40
Benzyl alcohol <b>1a</b> .....	40
4-methyl benzyl alcohol <b>1b</b> .....	41
3-methyl benzyl alcohol <b>1c</b> .....	41
4-chloro benzyl alcohol <b>1d</b> .....	42
4-trifluoromethyl benzyl alcohol <b>1e</b> .....	42
3-bromo benzyl alcohol <b>1f</b> .....	43
4-bromo benzyl alcohol <b>1g</b> .....	43
4-nitro benzyl alcohol <b>1h</b> .....	44
2-nitro benzyl alcohol <b>1i</b> .....	44
4-iodo benzyl alcohol <b>1j</b> .....	45
2-chloro-5-methylhydroxy pyridine <b>1k</b> .....	45
2-chloro benzyl alcohol <b>1l</b> .....	46
4-methoxy benzyl alcohol <b>1m</b> .....	46
<sup>1</sup> H-NMR SPECTRA DEMONSTRATING CATALYST REUSABILITY.....	47
<sup>1</sup> H-NMR SPECTRA DEMONSTRATING REACTIVITY OF REAGENT <b>3</b> IN THE PRESENCE OF CYCLODEXTRIN.....	48
<sup>1</sup> H-NMR SPECTRA DEMONSTRATING THE REACTIVITY OF REAGENT <b>3</b> IN THE PRESENCE OF CYCLODEXTRIN AND ONE EQUIVALENT OF <b>1a</b> .....	49
<b>Chapter 3</b>	
NMR SPECTRA OF ALL NEW COMPOUNDS.....	103

Compound <b>2</b>	
<sup>1</sup> H-NMR.....	103
<sup>13</sup> C-NMR.....	103
COSY NMR.....	104
Compound <b>3</b>	
<sup>1</sup> H-NMR.....	104
<sup>13</sup> C-NMR.....	105
COSY NMR.....	105
<b>Chapter 4</b>	
NMR SPECTRA OF β-CD DIMER HOSTS AND SQUARAIN GUESTS.....	203
<sup>1</sup> H-NMR spectrum of compound <b>1</b> recorded in DMSO- <i>d</i> <sub>6</sub> (400 MHz) at room temperature.....	203
<sup>13</sup> C-NMR spectrum of compound <b>1</b> recorded in D <sub>2</sub> O (400 MHz) at room temperature.....	204
<sup>1</sup> H-NMR spectrum of compound <b>2</b> recorded in DMSO- <i>d</i> <sub>6</sub> (400 MHz) at room temperature.....	204
<sup>13</sup> C-NMR spectrum of compound <b>2</b> recorded in DMSO- <i>d</i> <sub>6</sub> (400 MHz) at room temperature.....	205
ROESY spectrum of compound <b>2</b> recorded in DMSO- <i>d</i> <sub>6</sub> (400 MHz) at room temperature.....	205
<sup>1</sup> H-NMR spectrum of compound <b>3</b> recorded in DMSO- <i>d</i> <sub>6</sub> (400 MHz) at room temperature.....	206
<sup>13</sup> C-NMR spectrum of compound <b>3</b> recorded in DMSO- <i>d</i> <sub>6</sub> (400 MHz) at room temperature.....	206
ROESY spectrum of compound <b>3</b> recorded in DMSO- <i>d</i> <sub>6</sub> (400 MHz) at room temperature.....	207
Comparison of <sup>1</sup> H-NMR spectrum of compound <b>1, 2 &amp; 3</b> recorded in DMSO- <i>d</i> <sub>6</sub> (400 MHz) at room temperature.....	207

Comparison of <sup>1</sup> H-NMR spectrum of compound <b>S10</b> & <b>S16</b> recorded in DMSO- <i>d</i> <sub>6</sub> (400 MHz) at room temperature.....	208
<sup>1</sup> H-NMR spectrum of compound <b>4</b> recorded in CDCl <sub>3</sub> (400 MHz) at room temperature.....	208
<sup>1</sup> H-NMR spectrum of compound <b>5</b> recorded in CDCl <sub>3</sub> (400 MHz) at room temperature.....	209
<sup>1</sup> H-NMR spectrum of compound <b>6</b> recorded in CDCl <sub>3</sub> (400 MHz) at room temperature.....	209
<sup>1</sup> H-NMR spectrum of compound <b>7</b> recorded in CDCl <sub>3</sub> (400 MHz) at room temperature.....	210
<sup>1</sup> H-NMR spectrum of compound <b>8</b> recorded in CDCl <sub>3</sub> (400 MHz) at room temperature.....	210
<sup>1</sup> H-NMR spectrum of compound <b>9</b> recorded in CDCl <sub>3</sub> (400 MHz) at room temperature.....	211
<sup>1</sup> H-NMR spectrum of compound <b>10</b> recorded in CDCl <sub>3</sub> (400 MHz) at room temperature.....	211
<sup>1</sup> H-NMR spectrum of compound <b>11</b> recorded in CDCl <sub>3</sub> (400 MHz) at room temperature.....	212
<b>MASS SPECTRA OF β-CD DIMER HOSTS AND SQUARAIN GUESTS</b>	
Mass spectrometry data of compound <b>1</b> recorded in Waters Q-TOF Micro Mass Spectrometer.....	212
Mass spectrometry data of compound <b>2</b> recorded in Bruker Omflex MALDI-TOF.....	213
Mass spectrometry data of compound <b>3</b> recorded in Waters Q-TOF Micro Mass Spectrometer.....	213
Mass spectrometry data of compound <b>4</b> recorded in Thermo Scientific LTQ Orbitrap XL™ mass spectrometer.....	214
Mass spectrometry data of compound <b>6</b> recorded in Thermo Scientific LTQ Orbitrap XL™ mass spectrometer.....	214
Mass spectrometry data of compound <b>10</b> recorded in Thermo Scientific LTQ Orbitrap XL™ mass spectrometer.....	215

## Chapter 5

COPIES OF ALL SPECTRA.....	258
<sup>1</sup> H-NMR spectrum of compound <b>1</b> in DMSO- <i>d</i> <sub>6</sub> .....	258
<sup>13</sup> C-NMR of <b>1</b> in DMSO- <i>d</i> <sub>6</sub> .....	259
COSY NMR spectrum of compound <b>1</b> .....	260
Zoomed-in close-up on the COSY NMR.....	261
<sup>1</sup> H-NMR of <b>2</b> in DMSO- <i>d</i> <sub>6</sub> .....	262
<sup>13</sup> C-NMR of <b>2</b> in CDCl <sub>3</sub> .....	263
<sup>1</sup> H-NMR of <b>3</b> in DMSO- <i>d</i> <sub>6</sub> .....	264
High resolution mass spectrometry of compound <b>1</b> .....	265
High resolution mass spectrometry of compound <b>2</b> .....	265

## CHAPTER 1

Published in *Tetrahedron Letters* **2015**, 56(13), 1619-1623

Cyclodextrin-promoted Diels-Alder reactions of a polycyclic aromatic hydrocarbon  
under mild reaction conditions

Sauradip Chaudhuri, Tyler Phelan, Mindy Levine

Department of Chemistry, University of Rhode Island, Kingston, RI, USA

Corresponding Author:

Mindy Levine, Ph.D.

Department of Chemistry

University of Rhode Island

Kingston, Rhode Island, 02881, USA

[mlevine@chm.uri.edu](mailto:mlevine@chm.uri.edu)

## Manuscript 1

### **Cyclodextrin-promoted Diels-Alder reactions of a polycyclic aromatic hydrocarbon under mild reaction conditions**

#### ABSTRACT

Reported herein is the effect of cyclodextrins on the rates of aqueous Diels-Alder reactions of 9- anthracenemethanol with a variety of *N*-substituted maleimides. These reactions occurred under mild reaction conditions (aqueous solvent, 40 °C), and were most efficient for the reaction of *N*-cyclohexylmaleimide with a methyl- $\beta$ -cyclodextrin additive (94% conversion in 24 hours). These results can be explained on the basis of a model wherein the cyclodextrins bind the hydrophobic substituents on the maleimides and activate the dienophile via electronic modulation of the maleimide double bond. The results reported herein represent a new mechanism for cyclodextrin-promoted Diels-Alder reactions, and have significant potential applications in the development of other cyclodextrin-promoted organic transformations. Moreover, the ability to deplanarize polycyclic aromatic hydrocarbons (PAHs) under mild conditions, as demonstrated herein, has significant applications for PAH detoxification.

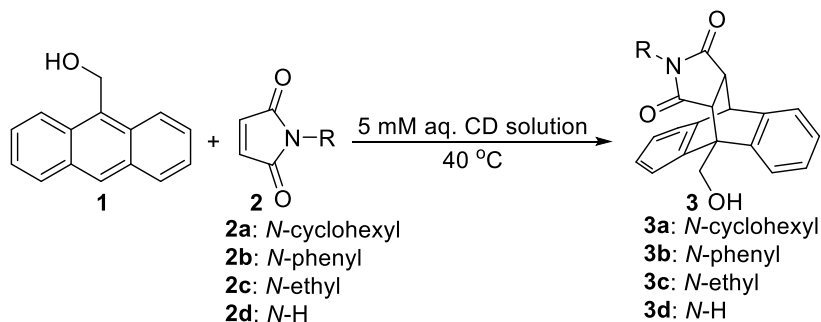
#### MANUSCRIPT TEXT

Cyclodextrins are torus shaped cyclic oligoamyloses, with the size of the interior cavity determined by the number of repeating amylose units. The ability of cyclodextrins to form host-guest complexes with hydrophobic guests occurs as a result of their hydrophobic interiors, whereas their relatively hydrophilic exteriors enable them to be used in mostly aqueous environments.<sup>1</sup> Once host-guest complexes form, the guests can

undergo cyclodextrin-mediated catalysis;<sup>2</sup> such catalysis has been reported for sigmatropic rearrangements,<sup>3</sup> for Diels-Alder reactions,<sup>4</sup> and for a variety of other organic transformations.<sup>5</sup> Cyclodextrins have also been used for a number of applications based on their ability to form host-guest complexes, including the solubilization of pharmaceutically active compounds,<sup>6</sup> the extraction of polycyclic aromatic hydrocarbons (PAHs) from contaminated sediments,<sup>7</sup> soil,<sup>8</sup> and water,<sup>9</sup> and the promotion of proximity-induced energy transfer.<sup>10</sup> Previous research in our group has focused on the development of cyclodextrin-based systems for the detection of a wide variety of aromatic toxicants in multiple complex environments via cyclodextrin-promoted energy transfer from the toxicants to high quantum yield fluorophores.<sup>11</sup> We have also reported the ability of cyclodextrins to extract aromatic toxicants, in particular PAHs, from complex oils, including motor oil, vegetable oil, and vacuum pump oil, as well as oil collected directly from an oil spill site.<sup>12</sup> This dual function system of extraction followed by detection has significant applications in oil spill remediation efforts.

Much of the toxicity of PAHs is related to their highly planar structures, which enable the PAHs to intercalate in DNA and form covalent, carcinogenic adducts.<sup>13</sup> Converting the PAHs to non-planar products using chemical transformations disrupts this facile intercalation and limits their ability to form carcinogenic adducts. Reported herein is the ability of cyclodextrins to promote such transformations for one PAH, 9-anthracenemethanol (compound 1), via its Diels-Alder reactions with *N*-substituted maleimides. Mechanistic investigations demonstrate that the rate enhancements achieved in the presence of cyclodextrin rely on cyclodextrin-induced activation of the

maleimide double bond via binding of the hydrophobic substituents to promote the reaction and achieve substantial rate accelerations.



**Equation 1.** Cyclodextrin-catalyzed aqueous Diels Alder reactions of 9-anthracenemethanol **1** with *N*-substituted maleimides **2**.

The conversion of compound **1** to its corresponding Diels-Alder adduct **3** was calculated after various time intervals under standard reaction conditions (5 mM aqueous cyclodextrin, 40 °C) (Equation 1). The percent conversion of each reaction was calculated based on the following equation:

$$\% \text{ Conversion} = \left[ \frac{\text{Integration of the product peak}}{\text{Integration of the product peak} + \text{Integration of the starting material peak}/3} \right] \times 100\%$$

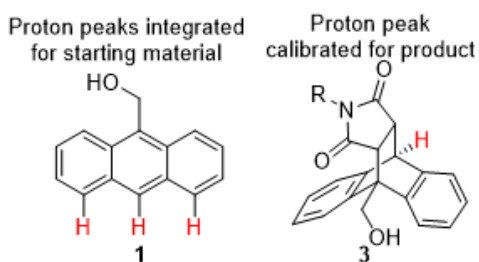


**Figure 1.** <sup>1</sup>H-NMR peaks of protons (marked in red) integrated from the starting material **1** and product **3**.

The starting material <sup>1</sup>H-NMR peak used in this equation corresponds to 3 aromatic protons of the 9-anthracenemethanol and the product peak used for this equation corresponds to 1 proton at the bridgehead of the Diels-Alder adduct **3** (Figure 1). The



integration of the NMR peaks were the relative areas under the curve measured against a calibrated internal standard corresponding to the residual  $\text{CHCl}_3$  peak at 7.26 ppm.

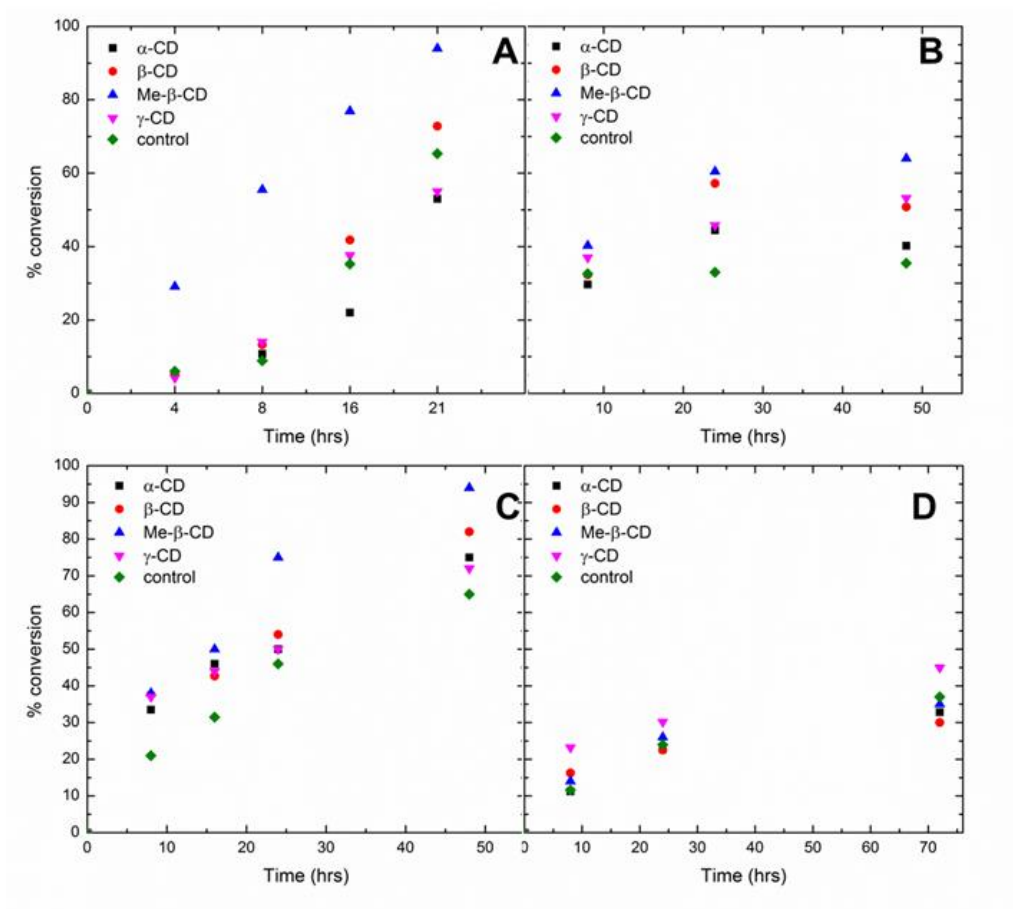


**Figure 2.** Percent conversion of compounds **1** and **2** to product **3** in various cyclodextrins for (A) compound **2a**; (B) compound **2b**; (C) compound **2c**; (D) compound **2d**.

Methyl-  $\beta$ -cyclodextrin yielded the highest percent conversion to product for any of the various reactions studied (94% for the conversion of **2a** to **3a** after 24 hours, compared to 65% for the cyclodextrin-free reaction under analogous conditions) (Figure 2). The beneficial effect of methyl-  $\beta$ -cyclodextrin (as well as all of the cyclodextrin derivatives) diminished for the less bulky maleimides. For example, the conversion of **2d** to **3d** in the presence of methyl-  $\beta$ -cyclodextrin was 26% after 24 hours, compared to 24%

conversion in the cyclodextrin-free solution under analogous conditions. The dependence of the cyclodextrin efficacy on the structure of the maleimide dienophile indicates that binding of the hydrophobic *N*-substituent in the cyclodextrin cavity is necessary for achieving optimal rate accelerations.

**Table 1.** Changes in the alkene proton chemical shifts in 5 mM cyclodextrin solutions. ( $\Delta$  ppm is defined as  $\delta(\text{CD solution}) - \delta(\text{control})$ )

Compound	$\Delta$ ppm $\alpha$ -CD	$\Delta$ ppm $\beta$ -CD	$\Delta$ ppm Me- $\beta$ -CD	$\Delta$ ppm $\gamma$ -CD
<b>2a</b>	0.018	0.047	0.078	0.033
<b>2b</b>	0.014	0.014	0.029	0.001
<b>2c</b>	0.004	0.016	0.013	0.003
<b>2d</b>	0.005	0.004	0.001	0.000

The dependence of the rate enhancements on the structures of the dienophiles (and in particular on the size and hydrophobicity of the nitrogen substituent) was further probed by  $^1\text{H-NMR}$  spectroscopy of the maleimide-cyclodextrin binary complexes. These studies revealed that all of the substituted maleimides (compounds **2a–2c**) demonstrated significant changes in the  $^1\text{H-NMR}$  shifts of the maleimide alkene protons (Table 1), indicating strong binding to the cyclodextrin hosts (approximately  $300 \text{ M}^{-1}$  for compound **2a**, and  $8 \text{ M}^{-1}$  for compound **2c**).<sup>14</sup> The changes in the chemical shifts of the protons were directly proportional to the hydrophobicity of the nitrogen substituent, with the largest changes and the strongest binding observed for *N*-cyclohexylmaleimide (compound **2a**). Virtually no shift in the alkene protons was observed for maleimide **2d**, which lacks a hydrophobic *N*-substituent.

Analysis of the conversion efficiencies with different dienophiles reveals that the dienophiles that bound most strongly in the methyl- $\beta$ -cyclodextrin cavity (as indicated

by greatest changes in the  $^1\text{H-NMR}$  chemical shifts) were also the most reactive (Figure 3). This binding strength in turn depends largely on the hydrophobicity of the *N*-substituent of the maleimide, with compound **2a** demonstrating the greatest binding affinities and fastest reaction rate.

The proposed mechanism by which the cyclodextrin derivatives promote the Diels-Alder reaction of compounds **1** and **2** likely involves the binding of hydrophobic *N*-substituted maleimides **2** in the hydrophobic cyclodextrin cavity, with additional stabilization provided by hydrogen bonding between the cyclodextrin hydroxyl groups and the carbonyl groups of the maleimide (Figure 4).

This additional binding withdraws electron density from the  $\pi$ -bond, activating the alkene for the resultant cycloaddition reaction. This effect was maximal for the binding of **2a** in methyl- $\beta$ -cyclodextrin, due to the highly hydrophobic nature of the cyclohexyl substituent<sup>15</sup> and the optimal size match between the cyclohexyl and the methyl- $\beta$ -cyclodextrin cavity.<sup>16</sup> A similar phenomenon has been reported by Ritter and co-workers, wherein cyclodextrin binding of *N*-substituted maleimides led to enhanced reactivity in free radical polymerization reactions.<sup>17</sup> However, the mechanism by which such binding led to activation of the alkene bond in the *N*-substituted maleimides was not explicitly discussed.

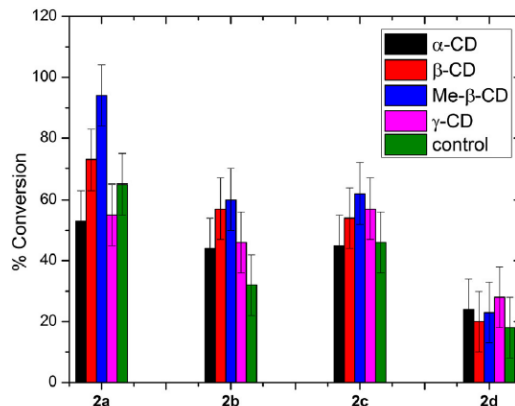


**Figure 3.** Graphical representation of the average conversion after 24 hours for various *N*-substituted maleimides in the presence of cyclodextrins.

Interestingly, methyl- $\beta$ -cyclodextrin was significantly more efficient than  $\beta$ -cyclodextrin at promoting this Diels-Alder reaction, despite the fact that methyl- $\beta$ -cyclodextrin and  $\beta$ -cyclodextrin have similar cavity dimensions. This trend is likely a result of the fact that methyl- $\beta$ -cyclodextrin is both more flexible and has a more non-polar cavity than  $\beta$ -cyclodextrin, a fact that has been reported in the literature but has been rarely exploited in organic reactions.<sup>18</sup>

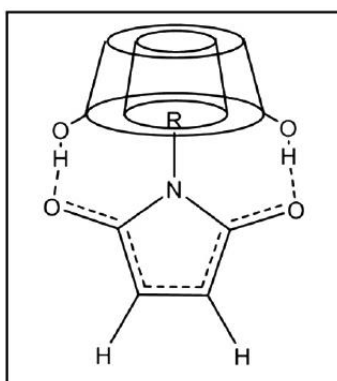


**Figure 4.** Schematic illustration of how cyclodextrin complexation activates the dienophile through a combination of hydrophobic binding and electronic perturbation of the  $\pi$ -bond.

A closer look at the reaction conversions (Figure 3) reveals that as the *N*-substituent decreases in bulk, the conversions obtained with  $\gamma$ -cyclodextrin approach those

observed with methyl- $\beta$ -cyclodextrin. For example, the difference between the conversions achieved with methyl- $\beta$ -cyclodextrin compared to  $\gamma$ -cyclodextrin was 39% for substrate **2a**; this difference drops to 25% for substrate **2c** and to 4% in favor of  $\gamma$ -cyclodextrin for substrate **2d**. The less bulky substrates can form ternary complexes in  $\gamma$ -cyclodextrin, with both the diene and dienophile binding simultaneously in the cavity interior.  $\gamma$ -Cyclodextrin is known to form ternary complexes,<sup>19</sup> and such ternary complexes have already been used in  $\gamma$ -cyclodextrin mediated dimerization reactions.<sup>20</sup> This ternary complexation binding mode is distinct from the binding mode proposed in Figure 4, which is expected to be the dominant mechanism for methyl- $\beta$ -cyclodextrin binding of bulky *N*-substituents.

Interestingly, <sup>1</sup>H-NMR investigations of the binary complexes indicate that the binding of alkene **2a** in cyclodextrin leads to shifts in the alkene protons, with the magnitude of the shift greatest for binding in methyl- $\beta$ -cyclodextrin (Figure 5A). Binding of compound **1** in methyl- $\beta$ -cyclodextrin led to increasing intensity in the signals of the aromatic protons as a result of the increased solubilization conferred through complex formation (Figure 5B).

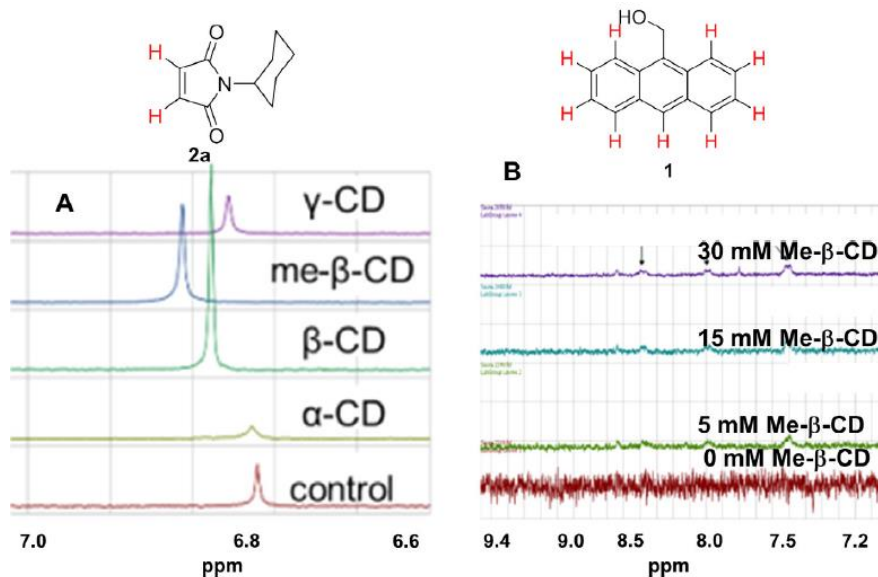


**Figure 5.** (A) Illustration of the chemical shifts of alkene protons of **2a** in binary cyclodextrin complexes (5 mM cyclodextrin); (B) Illustration of the increasing intensity of aromatic protons for compound **1** in the presence of increasing concentrations of methyl- $\beta$ -cyclodextrin.

$^1\text{H-NMR}$  analysis of the three-component mixture (diene **1**, dienophile **2a**, and cyclodextrin host) indicated that binding of the diene led to a slight upfield shift in the  $^1\text{H-NMR}$  spectrum of the dienophile compared to its binding in binary complexes (1:1 ratio of maleimide **2a** and diene **1**). The aromatic protons of compound **1** shifted downfield in the three-component mixture (compared to their chemical shifts in a binary cyclodextrin:**1** complex) (Figure 6). The  $^1\text{H-NMR}$  peak shifts for the three component complexes can be explained based on the orbital interaction between the HOMO of diene **1** and the LUMO of dienophile **2a**.<sup>21</sup> As the  $\pi$ -electron cloud of the electron rich diene redistributes along the electron deficient dienophile, the alkene protons get shielded whereas the aromatic protons get deshielded. Moreover, the magnitude of these chemical shifts depends on the concentration of the methyl- $\beta$ -cyclodextrin, with a 30

mM cyclodextrin solution leading to more pronounced chemical shifts compared to a 5 mM cyclodextrin solution.

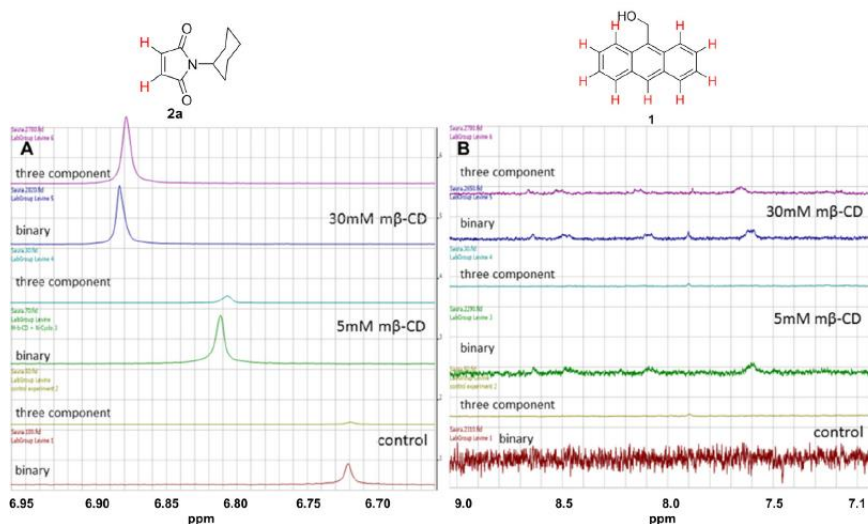


**Figure 6.** (A) Comparison of the <sup>1</sup>H-NMR shifts of the alkene protons in a three component mixture and in the **2a**:methyl-β-cyclodextrin binary complex; (B) Comparison of the <sup>1</sup>H-NMR shifts of the protons of compound **1** in a three component mixture and in the **1**:methyl-β-cyclodextrin binary complex.

As a whole, the data reported herein suggests a supramolecular assembly of the type shown in Figure 7, wherein a hydrophobically bound dienophile is linked by hydrogen bonding to the diene. The hydroxyl group in the diene **1** is believed to contribute to the solubility of the diene in the aqueous medium (an important criterion for the reaction, since unsubstituted anthracene failed to react under similar conditions).

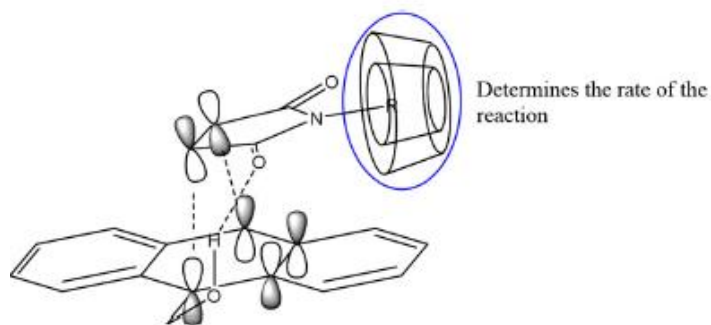
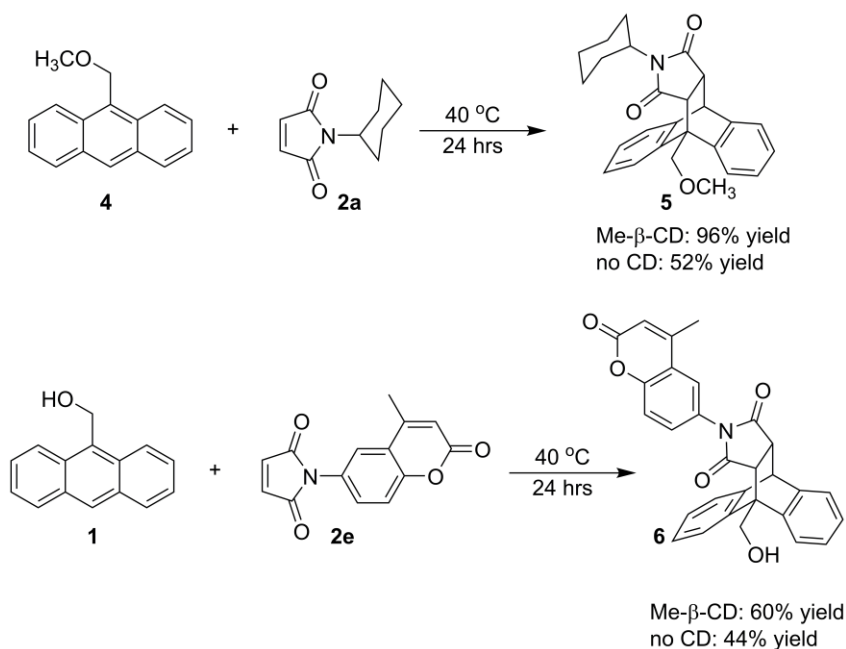


**Figure 7.** The hypothesized supramolecular assembly involving HOMO and LUMO interactions between an uncomplexed **1** and cyclodextrin-complexed **2**.

Preliminary efforts to expand the scope of this cyclodextrin-mediated Diels-Alder reaction have demonstrated that other anthracene dienes and other maleimide dienophiles also participate in this reaction efficiently, including compounds **4** and **2e** (Scheme 1). Compound **2e** is of particular interest, as both the maleimide **2e** and the product **6** are photophysically active, which provides a facile tool for tracking in complex environments. Moreover, the methyl- $\beta$ -cyclodextrin promoted reaction of compounds **1** and **2a** (Equation 1) proceeded in up to 60% yield when run in unpurified seawater (compared to 15% for the cyclodextrin-free reaction), which indicates the ability to run these Diels-Alder reactions in real world environments for environmental detoxification applications.





**Scheme 1.** Diels-Alder reactions of other dienes and dienophiles under analogous conditions.

In summary, these experiments demonstrate the ability of methyl- $\beta$ -cyclodextrin to catalyze the conversion of a PAH to non-planar hydrophobic adducts under mild reaction conditions. This rate enhancement is primarily due to the superior hydrophobic binding of methyl- $\beta$ -cyclodextrin to hydrophobic substituents on the *N*-substituted maleimides, which in turn enhances the alkene reactivity. The resulting adducts **3** are both less planar and more hydrophobic than the starting PAH, which will help to mitigate toxicity by reducing the degree of PAH intercalation in the DNA as well as the mobility of the PAH adduct in highly polar biological environments. Current efforts are focused on expanding the scope of this Diels-Alder reaction to include other hydrophobically-substituted dienophiles and other aromatic dienes, as well as investigations of other cyclodextrin-promoted organic transformations. Results of these and other investigations will be reported in due course.

## ACKNOWLEDGEMENTS

This research was funded by a grant from the Gulf of Mexico Research Initiative (GOMRI) and by a grant from the National Cancer Institute (1R21CA185435-01).

## NOTES AND REFERENCES

1. (a) Breslow, R. *Acc. Chem. Res.* **1991**, *24*, 317–324. (b) Harada, A. *Acta Polym.* **1998**, *49*, 3-17. (c) Takajashi, K.; Hattori, K. *J. Inclusion Phenom. Molec. Recognition Chem.* **1994**, *17*, 1-24.
2. Marchetti, L.; Levine, M. *ACS Catal.* **2011**, *1*, 1090–1118.
3. Harano, K.; Kiyonaga, H.; Hisano, T. *Tetrahedron Lett.* **1991**, *32*, 7557–7558.
4. (a) Breslow, R.; Maitra, U.; Rideout, D. *Tetrahedron Lett.* **1983**, *24*, 1901–1904. (b) Gonzalez, A.; Holt, S. L. *J. Org. Chem.* **1982**, *47*, 3186–3188. (c) Schneider, H. J.; Sangwan, N. K. *J. Chem. Soc., Chem. Commun.* **1986**, 1787–1789. (d) Sternbach, D. D.; Rossana, D. M. *J. Am. Chem. Soc.* **1982**, *104*, 5853–5854.
5. (a) Hapiot, F.; Bricout, H.; Tilloy, S.; Monflier, E. *Eur. J. Inorg. Chem.* **2012**, *2012*, 1571–1578. (b) Hromadova, M.; Sokolova, R. *Curr. Org. Chem.* **2011**, *15*, 2950–2956.
6. Agrawal, R.; Gupta, V. *Int. J. Pharma. Frontier Res.* **2012**, *2*, 95–112.
7. Gao, H.; Ma, J.; Xu, L.; Jia, L. *Environ. Sci. Pollution Res.* **2014**, *21*, 8620–8630.
8. Petitgirard, A.; Djehiche, M.; Persello, J.; Fievet, P.; Fatin-Rouge, N. *Chemosphere.* **2009**, *75*, 714–718.
9. Gao, H.; Miles, M. S.; Meyer, B. M.; Wong, R. L.; Overton, E. B. *J. Environ. Monitoring.* **2012**, *14*, 2164-2169.
10. (a) Sforazzini, G.; Kahnt, A.; Wykes, M.; Sprafke, J. K.; Brovelli, S.; Montarnal, D.; Meinardi, F.; Ciaciali, F.; Beljonne, D.; Albinsson, B.; Anderson, H. L. *J. Phys. Chem. C.* **2014**, *118*, 4553–4566. (b) Klotz, E. J. F.; Claridge, T. D. W.; Anderson, H. L. *J. Am. Chem. Soc.* **2006**, *128*, 15374–15375.
11. (a) Mako, T.; Marks, P.; Cook, N.; Levine, M. *Supramol. Chem.* **2012**, *24*, 743–747. (b) Serio, N.; Miller, K.; Levine, M. *Chem. Commun.* **2013**, *49*, 4821–4823. (c) Serio, N.; Chanthalyma, C.; Prignano, L.; Levine, M. *Supramol. Chem.* **2014**, *26*,

- 714–721. (d) Serio, N.; Prignano, L.; Peters, S.; Levine, M. *Polycyclic Aromatic Compounds*. **2014**, *34*, 561–572.
12. (a) Serio, N.; Chanthalya, C.; Peters, S.; Levine, D.; Levine, M. *J. Inclusion Phenom. Macrocyclic Chem.* **2014** Ahead of Print; (b) Serio, N.; Chanthalya, C.; Prignano, L.; Levine, M. *ACS Appl. Mater. Interfaces*. **2013**, *5*, 11951–11957.
13. Tang, Y.; Liu, Z.; Ding, S.; Lin, C. H.; Cai, Y.; Rodriguez, F. A.; Sayer, J. M.; Jerina, D. M.; Amin, S.; Broyde, S.; Geacintov, N. E. *Biochem.* **2012**, *51*, 9751–9762.
14. Efforts to measure the binding affinity of compound **2b** were unsuccessful to date.
15. Sahin-Toth, M.; Gunawan, P.; Lawrence, M. C.; Toyokuni, T.; Kaback, H. R. *Biochem.* **2002**; *41*, 13039–13045.
16. Chau, N. T. T.; Handjani, S.; Guegan, J-P.; Guerrero, M.; Monflier, E.; Philippot, K.; Denicourt-Nowicki, A.; Roucoux, A. *ChemCatChem*. **2013**, *5*, 1497–1503.
17. (a) Bernhardt, S.; Gloeckner, P.; Theis, A.; Ritter, H. *Macromolecules*. **2001**, *34*, 1647–1649. (b) Bernhardt, S.; Glockner, P.; Ritter, H. *Polym. Bull.* **2001**, *46*, 153–157. (c) Born, M.; Koch, Th.; Ritter, H.; *Acta Polym.* **1994**, *45*, 68–72. (d) Born, M.; Ritter, H. *Angew. Chem. Int. Ed.* **1995**, *34*, 309–311.
18. (a) Zoppi, A.; Delrivo, A.; Aiassa, V.; Longhi, M. R. *AAPS PharmSciTech.* **2013**, *14*, 727–735. (b) Yang, C.; Castelvetro, V.; Scarlone, D.; Bianchi, S.; Zhang, Y. *J. Polym. Sci. A Polym. Chem.* **2011**, *49*, 4518–4530.
19. (a) Hamai, S. *Bull. Chem. Soc. Japan.* **2007**, *80*, 1527–1533. (b) Hamai, S. *J. Inclusion Phenom. Macrocyclic Chem.* **2010**, *67*, 471–481.
20. (a) Tamaki, T.; Kokubu, T.; Ichimura, K. *Tetrahedron.* **1987**, *43*, 1485–1494. (b) Tamaki, T.; Kawanishi, Y.; Seki, T.; Sakuragi, M. *J. Photochem. Photobiol. A Chem.* **1992**, *65*, 313–320.
21. (a) Jensen, K. L.; Dickmeiss, G.; Jiang, H.; Albrecht, L.; Jorgensen, K. A. *Acc. Chem. Res.* **2012**, *45*, 248–264. (b) Li, J-L.; Liu, T-Y.; Chen, Y-C. *Acc. Chem. Res.* **2012**, *45*, 1491–1500.

*Supporting Information*

**Cyclodextrin-promoted Diels Alder reactions of a polycyclic aromatic hydrocarbon under mild reaction conditions**

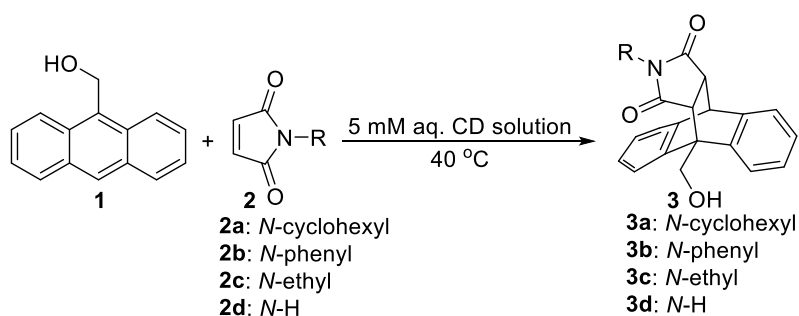
**MATERIALS AND METHODS**

<sup>1</sup>H-NMR spectra (300 MHz) were recorded on a Bruker-Advance 300 MHz NMR spectrometer using tetramethylsilane (TMS) as an internal standard. All reagents were obtained from Sigma Aldrich and used as received. Four different cyclodextrin solutions were screened:  $\alpha$ -cyclodextrin,  $\beta$ -cyclodextrin, methyl- $\beta$ -cyclodextrin and  $\gamma$ -cyclodextrin (5.0 mM aqueous solutions in distilled water). Distilled water without cyclodextrin was used as a control. Cyclodextrin complexations were studied by comparing the chemical shifts of the protons of the complexed species against the free species. Percentage conversions were calculated from the <sup>1</sup>H-NMR spectra of the crude products (extracted in chloroform), based on the stoichiometric analysis of the reactions.

**GENERAL EXPERIMENTAL PROCEDURES**

To a clean and dry vial, *N*-substituted maleimide (15.0  $\mu$ mol, 1.0 equivalent) and 9-anthracenemethanol (3.1 mg, 15.0  $\mu$ mol, 1.0 equivalent) were added, followed by a 5.0 mM aqueous cyclodextrin solution (1.0 mL, 5.0  $\mu$ mol, 0.33 equivalents). The mixture was sonicated to make sure all the reagents were well suspended. The mixture was heated at 40 °C for the desired period of time with occasional shaking to maintain the homogeneity of the solution. The solution was then extracted with 8.0 mL of chloroform and 2.0 mL of distilled water. The top aqueous layer was carefully syringed out. The

organic layer was treated with a small amount of anhydrous Na<sub>2</sub>SO<sub>4</sub> and decanted into a separate clean vial. The organic layer was subsequently dried on the rotary evaporator and further dried under a high-vacuum line. <sup>1</sup>H-NMR of the sample was recorded in CDCl<sub>3</sub> using a Bruker 300 MHz instrument.



**Equation 1.** Cyclodextrin-catalyzed aqueous Diels-Alder reactions of 9-anthracenemethanol (**1**) with *N*-substituted maleimides (**2**)

<sup>1</sup>H-NMR Analysis: The percentage conversion of each reaction with respect to the starting material (9-anthracenemethanol) was calculated based on the following equation:

$$\% \text{ Conversion} = \left[ \frac{\text{Integration of the product peak}}{\text{Integration of the product peak} + \text{Integration of the starting material peak} / 3} \right] \times 100\%$$

The starting material <sup>1</sup>H-NMR peak used in this equation corresponds to 3 aromatic protons of the 9-anthracenemethanol and the product peak used for this equation corresponds to 1 proton at the bridgehead of the Diels-Alder adduct **3** (Figure S1).

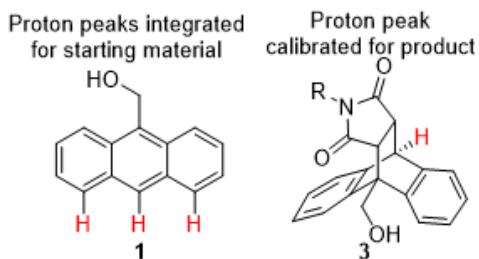


**Figure S1.** <sup>1</sup>H-NMR peaks of protons (marked in red) integrated for the starting material, 9-anthracenemethanol (**1**) and calibrated for the product (**3**).

## RATE STUDIES

Two separate *N*-substituted maleimides were investigated for rate studies: *N*-cyclohexyl maleimide (**2a**) and maleimide (**2d**). These two dienophiles were purposely chosen to study the rate of the reaction based on the mechanistic pathway involving methyl- $\beta$ -cyclodextrin complexation (maximum for **2a**; absent for **2d**). Percentage conversions of reactions were studied for different stoichiometric ratio of methyl- $\beta$ -cyclodextrin, dienophile and the diene ([CD]: [**2**]: [**1**]).

**Table S1.** Percentage conversions of reactions at different stoichiometric ratio of methyl- $\beta$ -cyclodextrin, dienophile and the diene ([CD]: [**2**]: [**1**]).

Time (hrs)	% Conversion				
<b>N-cyclohexylmaleimide (2a)</b>					
	[CD]:[2a]:[1] = 1:3:3 (5, 15, 15) mM	[CD]:[2a]:[1] = 2:3:3 (10, 15, 15) mM	[CD]:[2a]:[1] = 2:1:1 (30, 15, 15) mM	[CD]:[2a]:[1] = 1:6:3 (5, 30, 15) mM	[CD]:[2a]:[1] = 1:3:6 (5, 15, 30) mM
4	29.1	11.6	14.2	42.8	6.8
8	55.5	14.6	22.1	60.0	8.3
16	76.9	58.4	32.2	75.0	9.8
<b>Maleimide (2d)</b>					
	[CD]:[2d]:[1] = 1:3:3 (5, 15, 15) mM	[CD]:[2d]:[1] = 2:3:3 (10, 15, 15) mM	[CD]:[2d]:[1] = 2:1:1 (30, 15, 15) mM	[CD]:[2d]:[1] = 1:6:3 (5, 30, 15) mM	[CD]:[2d]:[1] = 1:3:6 (5, 15, 30) mM
8	14.0	19.7	21.1	27.2	10.8
24	26.0	22.8	27.0	35.3	14.6
72	35.0	47.6	55.5	52.6	13.7

## SUPPLEMENTARY TABLES

**Table S2.** Changes in the  $^1\text{H-NMR}$  chemical shifts of the cyclodextrin protons upon binding of compound **1** in binary complexes

Cyclodextrin	$\Delta$ ppm anomeric proton
$\alpha$ -cyclodextrin	-0.010
$\beta$ -cyclodextrin	-0.003
Me- $\beta$ -cyclodextrin	-0.010
$\gamma$ -cyclodextrin	-0.002

**Table S3.** Changes in the <sup>1</sup>H-NMR chemical shifts of the anomeric cyclodextrin proton upon binding of compounds **2a-2d** in binary complexes<sup>a</sup>

Compound	α-CD	β-CD	Me-β-CD	γ-CD
<b>2a</b>	-0.010	-0.012	-0.050	-0.005
<b>2b</b>	-0.002	-0.030	-0.065	-0.010
<b>2c</b>	-0.013	-0.008	-0.025	-0.003
<b>2d</b>	-0.005	-0.001	-0.010	-0.001

<sup>a</sup>The negative changes in the chemical shift signifies an upfield movement of the peaks on complexation.

**Table S4.** <sup>1</sup>H-NMR shifts of alkene protons of compounds **2a-2d** in ternary complexes<sup>a</sup>

Compound	α-CD	β-CD	Me-β-CD	γ-CD
<b>2a</b>	0.012	-0.007	-0.005	-0.010
<b>2b</b>	-0.009	0.007	0.008	0.002
<b>2c</b>	0.006	0.002	0.001	-0.001
<b>2d</b>	0.001	0.002	0.006	0.004

<sup>a</sup>The shifts are calculated as the change between the NMR signal in binary complexes and the NMR signal in the ternary complex mixtures.

**Table S5.** Changes in the <sup>1</sup>H-NMR chemical shifts of the anomeric cyclodextrin proton upon the formation of ternary complexes<sup>a</sup>

Compound	α-CD	β-CD	Me-β-CD	γ-CD
<b>2a</b>	0.008	-0.002	-0.002	0.002
<b>2b</b>	-0.006	0.008	0.007	0.006
<b>2c</b>	0.006	0.002	0.000	0.000
<b>2d</b>	0.002	0.001	0.005	0.003

<sup>a</sup>The shifts are calculated as the change between the NMR signal in binary complexes and the NMR signal in the ternary complex mixtures.

**Table S6.** Average percentage conversion data for Diels Alder reaction of 9-anthracenemethanol with compound **2a**.

Time (hrs)	α-CD	β-CD	Me-β-CD	γ-CD	no CD
4	6	5	29	4	6
8	11	13	56	14	9
16	22	42	77	38	35
24	53	73	94	55	65

**Table S7.** Average percentage conversion data for Diels Alder reaction of 9-anthracenemethanol with compound **2b**.

Time (hrs)	$\alpha$ -CD	$\beta$ -CD	Me- $\beta$ -CD	$\gamma$ -CD	no CD
8	30	32	40	37	33
24	44	57	61	46	33
48	40	51	64	53	35

**Table S8.** Average percentage conversion data for Diels Alder reaction of 9-anthracenemethanol with compound **2c**.

Time (hrs)	$\alpha$ -CD	$\beta$ -CD	Me- $\beta$ -CD	$\gamma$ -CD	no CD
8	34	38	38	37	21
16	46	43	50	44	32
24	50	54	75	50	46
48	75	82	94	72	65

**Table S9.** Average percentage conversion data for Diels Alder reaction of 9-anthracenemethanol with compound **2d**.

Time (hrs)	$\alpha$ -CD	$\beta$ -CD	Me- $\beta$ -CD	$\gamma$ -CD	no CD
8	11	16	14	23	12
24	23	23	26	30	24
72	33	30	35	45	37

#### SUPPLEMENTARY FIGURES

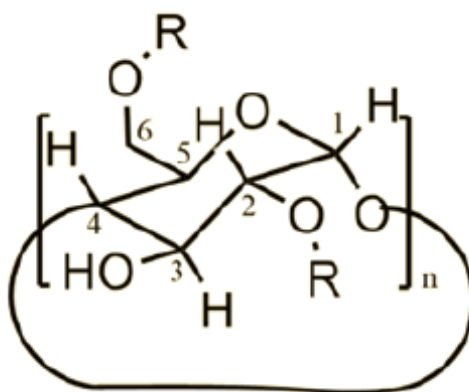


**Figure S2.** General molecular structure of (A)  $\alpha$ -cyclodextrin (R = H, n = 6); (B)  $\beta$ -cyclodextrin (R = H, n = 7); (C) methyl- $\beta$ -cyclodextrin (R = H/CH<sub>3</sub>, n = 7); (D)  $\gamma$ -cyclodextrin (R = H, n = 8)



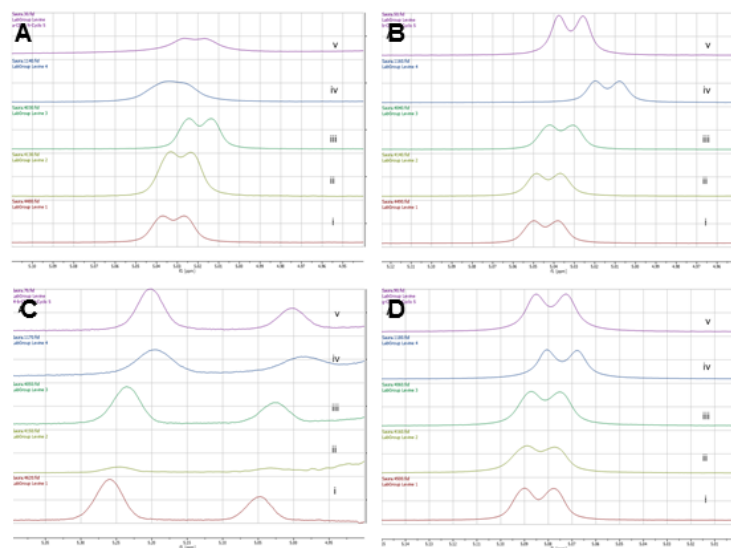


**Figure S3.**  $^1\text{H}$ -NMR chemical shifts of H1 protons of (A)  $\alpha$ -cyclodextrin; (B)  $\beta$ -cyclodextrin; (C) methyl- $\beta$ -cyclodextrin; (D)  $\gamma$ -cyclodextrin in presence of  $N$ -substituted maleimides [(i) control, without guest; (ii) compound **2d**; (iii) compound **2c**; (iv) compound **2b**; and (v) compound **2a**].

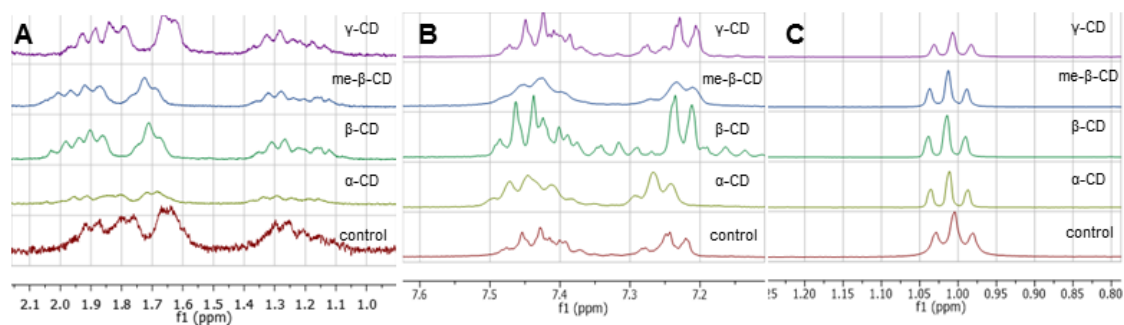


**Figure S4.**  $^1\text{H}$  NMR chemical shifts of  $N$ -substituent protons of compounds (A) **2a**; (B) **2b**; and (C) **2c** (only methyl protons are shown, the methylene protons merge with the cyclodextrin peaks) in the presence of cyclodextrins.

## CHAPTER 2

Published in *Synthetic Communications* **2016**, 46(7), 636-644

An Environmentally Friendly Procedure for the Aqueous Oxidation of Benzyl  
Alcohols to Aldehydes with Dibromodimethylhydantoin (DBDMH) and Cyclodextrin  
- Scope and Mechanistic Insights

Sauradip Chaudhuri, Hossam Zaki, Mindy Levine

Department of Chemistry, University of Rhode Island, Kingston, RI, USA

Corresponding Author:

Mindy Levine, Ph.D.

Department of Chemistry

University of Rhode Island

Kingston, Rhode Island, 02881, USA

[mlevine@chm.uri.edu](mailto:mlevine@chm.uri.edu)

## Manuscript 2

# **An Environmentally Friendly Procedure for the Aqueous Oxidation of Benzyl Alcohols to Aldehydes with Dibromodimethylhydantoin (DBDMH) and Cyclodextrin - Scope and Mechanistic Insights**

### ABSTRACT

Reported herein is an environmentally friendly procedure for the oxidation of benzyl alcohols to aldehydes using an inexpensive, commercially available reagent, 1,3-dibromo-5,5-dimethylhydantoin (DBDMH) and a variety of cyclodextrin additives under fully aqueous solvent conditions. This reaction proceeds with moderate to good yields for a broad scope of benzyl alcohol substrates, with the cyclodextrin acting to enhance the desired reactivity and limit undesired aromatic bromination side products. The reported experiments provide substantial mechanistic insight that will drive further reaction optimization and broad-reaching applications.

### INTRODUCTION

Cyclodextrins are well-studied supramolecular hosts<sup>1-4</sup> that have been used for a variety of high impact applications,<sup>5,6</sup> including the catalysis of organic reactions,<sup>7</sup> the environmental remediation of anthropogenic disasters,<sup>8</sup> and the solubilization of active pharmaceutical agents and food additives.<sup>9,10</sup> Cyclodextrin-promoted reactions usually occur under aqueous solvent conditions,<sup>11</sup> which has significant benefit in limiting the use of organic solvents and minimizing the generation of hazardous waste.<sup>12</sup>

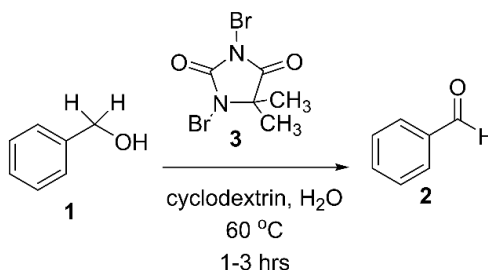
One example of an organic transformation with significant impact in synthetic research is the oxidation of primary alcohols to aldehydes, and some examples of cyclodextrin

promoted oxidation have been reported.<sup>13</sup> Other cyclodextrin-promoted oxidation reactions have been reported in the literature, and include the use of *N*-bromosuccinimide,<sup>14</sup> sodium hypochlorite,<sup>15,16</sup> hydrogen peroxide,<sup>17,18</sup> and oiodoxybenzoic acid<sup>19</sup> as reagents in combination with cyclodextrin. These reactions have some additional drawbacks, including the potential toxicity of the reagents<sup>20</sup> as well as the use of a compound that is a significant explosion hazard.<sup>21</sup>

Reagents with polarized *N*-halogen bonds such as 1,3-dibromo-5,5-dimethylhydantoin (DBDMH, compound **3**, Equation 1) have been shown to effect oxidation reactions on a variety of substrates,<sup>22,23</sup> and have significant operational advantages including commercial availability,<sup>24</sup> air- and moisture-stability,<sup>25</sup> and general high reactivity.<sup>26</sup> Initial reports of DBDMH-promoted oxidation of benzyl alcohols only demonstrated efficacy in the conversion of secondary alcohols to ketones<sup>27</sup> likely because of the higher sensitivity of primary alcohols to over-oxidation and other side reactions, or require the use of organic solvents such as methanol and dichloromethane.<sup>28</sup>

The use of cyclodextrin in combination with DBDMH for accomplishing the oxidation of primary alcohols to aldehydes has not been reported to date, despite the fact that this combination is expected to demonstrate numerous operational advantages including all advantages of using cyclodextrin (aqueous solvent system, mild reaction conditions) and DBDMH (air- and moisture-insensitivity, commercial availability, limited human toxicity) to accomplish a synthetically useful transformation. Reported herein is the cyclodextrin-promoted DBDMH oxidation of a variety of benzyl alcohols **1** to benzaldehydes **2** (Equation 1), which proceeds under fully aqueous conditions, with limited generation of byproducts, and in moderate to high reaction yields. Detailed

mechanistic investigations provide substantial insight that will guide further reaction development and applications.



**Equation 1.** Oxidation reaction of primary benzyl alcohols to benzaldehydes

## DISCUSSION

A variety of benzyl alcohol substrates **1** (Figure 1) were converted into their respective aldehydes **2**, using mild heating in aqueous media to achieve moderate to high conversions. The amount of cyclodextrin varied from 0.33 equivalents relative to the benzyl alcohol up to 1.5 equivalents, with the amount used independently optimized for each substrate. Table 1 summarizes the results of these experiments, and includes results obtained using the highest performing cyclodextrin host and the optimal amount of cyclodextrin, which depended strongly on the substrate structure. For example, the reaction with the smallest substrate **1a** was accelerated most strongly with the smallest cyclodextrin host  $\alpha$ -cyclodextrin. As the size of the *para* substituent on the benzyl alcohol increased, the optimal cyclodextrin host size increased as well, with substrate **1d** (*p*-chloro) optimally catalyzed by  $\beta$ -cyclodextrin, substrate **1g** (*p*-bromo) by methyl- $\beta$ -cyclodextrin, and substrate **1j** (*p*-iodo) by  $\gamma$ -cyclodextrin. Moving the same substituent from the *para* position to the *ortho* or *meta* position required a slightly larger cyclodextrin host to accommodate this geometry and achieve optimal reactivity (compare for example **1b** vs. **1c**; **1f** vs. **1g**; **1h** vs. **1i**).

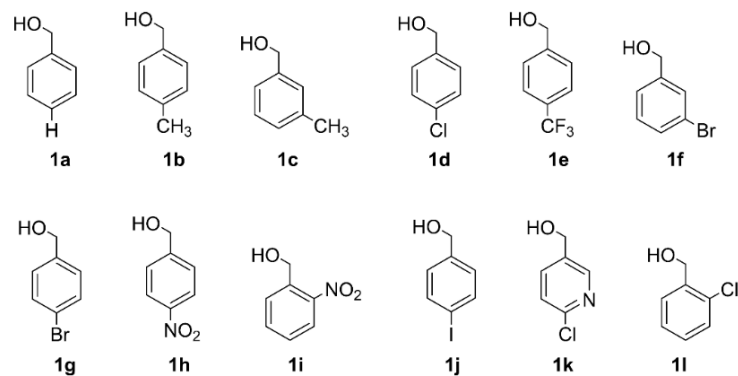


**Figure 1.** Benzyl alcohol substrates

**Table 1.** Percent conversions of alcohol substrates **1** to aldehydes **2**

Substrate	Time (hrs)	CDs (eq.)	Conversions with CD (%) <sup>a</sup>	Conversions without CD (%) <sup>a</sup>
<b>1a</b>	1	$\alpha$ -CD (0.33)	50	3
<b>1b</b>	3	$\beta$ -CD (0.5)	60	40 <sup>b</sup> (59)
<b>1c</b>	3	m $\beta$ -CD (1.5)	33 <sup>b</sup> (18)	11 <sup>b</sup> (85)
<b>1d</b>	3	$\beta$ -CD (0.33)	88	1
<b>1e</b>	3	$\beta$ -CD (0.5)	55	8
<b>1f</b>	1	$\gamma$ -CD (0.33)	25	15
<b>1g</b>	3	m $\beta$ -CD(0.33)	100	23
<b>1h</b>	1	$\alpha$ -CD (0.33)	80 <sup>c</sup>	16
<b>1i</b>	3	$\beta$ -CD (0.33)	33	4
<b>1j</b>	0.25	$\gamma$ -CD (0.33)	34	9
<b>1k</b>	3	$\alpha$ -CD (0.33)	40	6
<b>1l</b>	3	$\alpha$ -CD (0.33)	100	8

<sup>a</sup> Percent conversions were calculated based on the <sup>1</sup>H-NMR analysis of the reaction mixture.

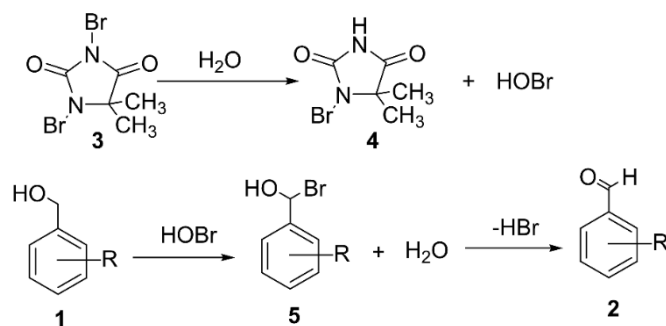
<sup>b</sup> Percentage in parentheses indicates the amount of aromatic brominated side product formed.

<sup>c</sup> the reaction was run at elevated temperature (80 °C). No product formation was observed at 60 °C.

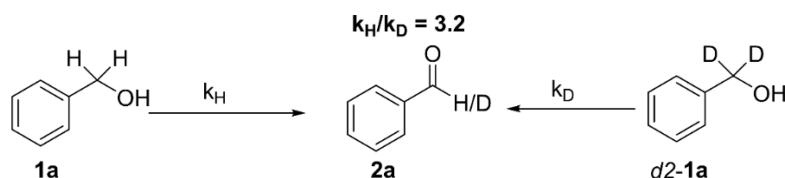
In general, electron-deficient and electron-neutral substrates displayed markedly higher conversions compared to the electron-rich substrates (see for example **1d** and **1g** compared to **1b**), which is a consequence both of their higher reactivity as well as the lower amounts of side products resulting from bromination of the aromatic ring. These

reaction conditions were not effective in oxidizing aliphatic primary alcohols to aldehydes, which confirms the importance of aromatic ring-cyclodextrin interactions in the reaction mechanism, nor did other *N*-halogenated reagents such as 1,3-dichloro-5,5-dimethylhydantoin (DCDMH) or 1,3-diiodo-5,5-dimethylhydantoin (DIDMH) effect the desired transformation. In all cases, the conversions obtained in the absence of cyclodextrin were markedly lower than those obtained in the presence of cyclodextrin, highlighting the crucial role for this supramolecular scaffold in promoting the desired reactivity.

A plausible reaction mechanism is shown in Scheme 1, and involves the formation of a key intermediate **5** from alcohol **1** and HOBr as the rate-determining step, followed by fast elimination of HBr to form the desired product. This mechanism also highlights the possibility of obtaining acyl bromides **6** from the same reaction, via the transfer of two bromine atoms to form intermediate **5'** followed by elimination of HBr to give product **6**. The mechanistic hypothesis is supported by (a) the negative free energy of formation of the intermediate **5**, calculated based on DFT calculations;<sup>29</sup> and (b) a strong primary kinetic isotope effect (KIE) of 3.2 on replacing benzyl alcohol **1a** with deuterated benzyl alcohol *d*2-**1a** (Equation 2), which implicates the involvement of C-H bond cleavage in the rate determining step, likely to be the conversion of starting material **1** to intermediate **5**.



**Scheme 1.** Plausible mechanism for the synthesis of aldehyde **2** from alcohols **1**



**Equation 2.** Illustration of the primary kinetic isotope effect observed

The general trend observed is that the conversions of electron deficient substrates is lower than benzyl alcohol and electron rich substrates (**1h** or **1i** < **1a** < **1b**). This supports the plausible formation of intermediate **5** via activation of the benzylic protons. On the contrary, an alternate mechanism leading to the formation of a hypobromite followed by HBr elimination would have favored electron deficient substrates as they make the benzylic protons more acidic. Furthermore, the KIE experiments done by replacing the benzylic protons with deuterium concur with the fact that benzylic deprotonation is involved in the rate determining step of the reaction.

The roles of cyclodextrin in the proposed mechanism shown in Scheme 1 are two-fold: (1) Acceleration of the C-H bond cleavage in the rate-determining first step; and (2) shielding of the aromatic ring from undesired aromatic bromination. Both of these roles are enabled through binding of the aromatic guests in the cyclodextrin cavity in a geometry such as that shown in Figure 2. This complexation activates the benzylic protons



through interactions between the cyclodextrin rim and the benzyl position, leading to markedly faster C-H bond cleavage, and protects the aromatic core of the substrate from electrophilic aromatic bromination through hydrophobic interactions between the aromatic ring and the cyclodextrin cavity.<sup>30</sup>

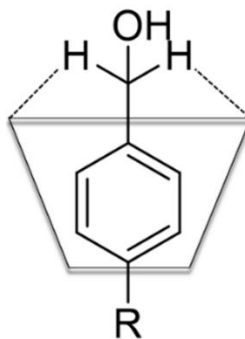


**Figure 2.** Illustration of the complexation of benzyl alcohols in cyclodextrin.

In addition to interactions between the cyclodextrin host and alcohol substrates **1**, cyclodextrin can also interact directly with compound **3**. Literature precedent indicates that cyclodextrins interact with hydantoins, and such interaction is used for efficient chromatographic separation of hydantoin enantiomers.<sup>31,32</sup> In this system, <sup>1</sup>H-NMR analysis of DBDMH-cyclodextrin mixtures indicates that complexation of DBDMH in cyclodextrin leads to marked decreases in the rate of N-Br bond dissociation (Table 2). The addition of substrate **1a** to the reaction mixture markedly increases the formation of compound **4** in the presence  $\alpha$ -cyclodextrin,  $\beta$ -cyclodextrin, and methyl- $\beta$ -cyclodextrin.  $\gamma$ -Cyclodextrin showed no real change in the amount of compound **4** formed in the presence and absence of substrate **1a**, and in the absence of any cyclodextrin the addition of compound **1a** led to a decrease in the formation of compound **4**. These results can be explained by a weak, hydrophobically-driven interaction between **1a** and **3**, which has some stabilizing effect in the absence of

cyclodextrin. Introduction of the cyclodextrin hosts results in the selective binding of the substrate **1a**, in turn rendering compound **3** more reactive.

**Table 2.** Percent formation of compound **4** in the presence of cyclodextrins and substrate **1a**<sup>a</sup>

CDs (eq.)	% of <b>4</b> (with <b>3</b> )	% of <b>4</b> (with <b>3</b> and <b>1a</b> )	$\Delta\%$ of <b>4</b> (due to <b>1a</b> ) <sup>b</sup>
$\alpha$ -CD (0.33)	50	80	30
$\beta$ -CD (0.33)	67	88	21
m $\beta$ -CD (0.33)	68	91	23
$\gamma$ -CD (0.33)	11	10	-1
No CDs	100	78	22

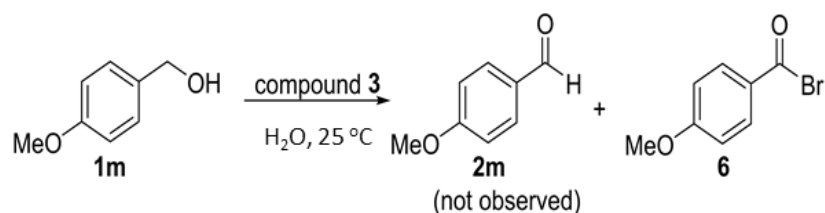
<sup>a</sup> Percent conversion was calculated based on the NMR analysis of the reaction.

<sup>b</sup>  $\Delta\%$  of **4** calculated as the change in % conversion on the introduction of 1.0 equivalent of substrate **1a**

Aliphatic alcohols cyclohexanol and 4-methylcyclohexylmethanol (4-MCHM)<sup>33</sup> were investigated as substrates, and no reaction was observed. The fact that these aliphatic alcohols were not competent substrates under these reaction conditions provides further evidence for the crucial role of the aromatic ring in ensuring favorable host-guest complexation, and argues against literature reports that the role of cyclodextrin in organic reactions is merely as a phase-transfer catalyst.<sup>34,35</sup> Moreover, the fact that aliphatic alcohols are inert to oxidation allows for the recycling and re-use of the aliphatic alcohol rich cyclodextrin host without concerns about interfering reactivity (*vide infra*).

Investigation of the effect of electron density of the aromatic ring on its reactivity reveals a strong effect on the substrate reactivity, with strongly electron donating substrates such as *p*-methoxy benzyl alcohol **1m** yielded none of the desired aldehyde **2m**, with complete conversion to the acid bromide **6** observed at 25 °C (Equation 3) (see ESI for spectral characterization of compound **6**). This is likely because the highly

electron-rich aromatic ring facilitates the formation of the dibromo intermediate **5'** (Scheme 1). Other somewhat less electron rich substrates, such as **1b**, proceeded to give the product in high yields in the presence of the cyclodextrin host, whereas in the absence of the host aromatic bromination products were observed (Table 1). Electron-deficient substrates such as **1h** and **1i** were inert in the absence of the cyclodextrin, but underwent efficient reaction in the presence of the cyclodextrin. In summary, electron deficient substrates required activation by the cyclodextrin (catalytic activation), whereas electron rich substrates need protection from side reactions (chemoselective influence).



**Equation 3.** Alternate reaction pathway for highly electron rich substrates.

Moreover, decreasing the amount of *N*-halo reagent led to drastic decreases in the conversion of compound **1m** to acid bromide **6**, in comparison to the less drastic decreases observed for the conversion of **1a** to **2a** and **1h** to **2h** (Table 3). This result supports the mechanism proposed in Scheme 1, wherein acid bromide **6** is formed via dibromo intermediate **5'** and requires multiple equivalents of the *N*-halo reagent for the reaction to proceed.

**Table 3.** Percent conversions to aldehydes with different *N*-halo reagents and equivalents<sup>a</sup>

Substrate	1.0 eq. <b>3</b>	0.5 eq. <b>3</b>	$\Delta\%$ conversion <sup>b</sup>
<b>1a</b>	63	48	15
<b>1h</b>	80	67	13
<b>1m<sup>c</sup></b>	100	58	42

<sup>a</sup> Percent conversion was calculated based on the NMR analysis of the reaction.

<sup>b</sup>  $\Delta\%$  Conversion calculated as the change in % conversion on going from 1.0 equivalent of reagent **3** to 0.5 equivalents of reagent **3**

<sup>c</sup> Percent conversion to acid bromide, calculated based on the <sup>1</sup>H-NMR analysis of the reaction mixture.

The methodology reported here is markedly more efficient in achieving the oxidation of primary alcohols to aldehydes using cyclodextrin-based aqueous systems compared to literature-reported results. Substantially higher conversions are reported within a three-hour reaction time frame, in comparison to previously-reported reaction times of eight hours or more. A variety of commercially available cyclodextrins screened for this purpose reveals their ability to outperform conventionally used  $\beta$ -cyclodextrin (the only cyclodextrin employed in previous works), and provides substantial mechanistic insight in the factors responsible for efficient cyclodextrin-promoted binding and cyclodextrin promoted reaction acceleration.

In summary, a novel aqueous oxidation procedure for the conversion of primary benzyl alcohols to benzaldehydes is demonstrated, using DBDMH as an environmentally friendly oxidant and cyclodextrins as supramolecular additives that promote the highly efficient reaction and limit the formation of undesired side products. Importantly, the cyclodextrin hosts are unaltered throughout the course of the reaction, and can be recovered and reused (conversion of **1a** to **2a**: first run: 75%; second run: 74%; third run: 62%). This was accomplished simply by extracting the aldehyde products into an organic solvent and then re-using the cyclodextrin-containing aqueous layer. The results

indicate that the aliphatic hydroxyl groups of the cyclodextrin are relatively stable to oxidation under these reaction conditions, in accord with our previously reported results on inert aliphatic alcohol substrates. This procedure has significant potential in environmentally friendly reaction optimization and complex product synthesis. Efforts in these areas are currently underway in our laboratory, and results of these and other investigations will be reported in due course.

## EXPERIMENTAL

<sup>1</sup>H-NMR spectra were recorded using a Bruker 300 MHz instrument, with the singlet peak of HDO at 4.79 ppm as reference. All reagents, substrates, and solvents were obtained from Sigma Aldrich. Four different cyclodextrin solutions were screened:  $\alpha$ -cyclodextrin,  $\beta$ -cyclodextrin, methyl  $\beta$ -cyclodextrin and  $\gamma$ -cyclodextrin dissolved in deuterated water (D<sub>2</sub>O). A cyclodextrin-free D<sub>2</sub>O solution was used as the control.

To a clean and dry small vial, a solution of substrate **1** (15.0  $\mu$ mol, 1.0 equivalent) was made using an aqueous cyclodextrin solution (1.0 mL) of the specified concentration in D<sub>2</sub>O. DBDMH, **3** (4.3 mg, 15.0  $\mu$ mol, 1.0 equivalent) was added to the reaction mixture and sonicated to make sure that the reagents were well suspended. The reaction mixture was heated at 60 °C with occasional shaking to maintain the homogeneity of the solution. After the desired period of time, the <sup>1</sup>H-NMR spectrum of the reaction mixture was recorded to determine the percent conversion. The percent conversion of each reaction was calculated based on the following equation:

$$\% \text{ Conversion} = \left[ \frac{\text{Integration of the product peak}}{\left( \frac{\text{Integration of the product peak}}{2} + \text{Integration of the starting material peak} \right)} \right] \times 100\%$$

The starting material  $^1\text{H-NMR}$  peak used in this equation corresponds to 2 benzyl protons of compound **1** and the product peak used for this equation corresponds to the 1 aldehyde proton of the product **2** (Figure 3). The integrations of the NMR peaks were the relative areas under the curve measured against a calibrated standard corresponding to the anomeric protons of the cyclodextrin hosts.

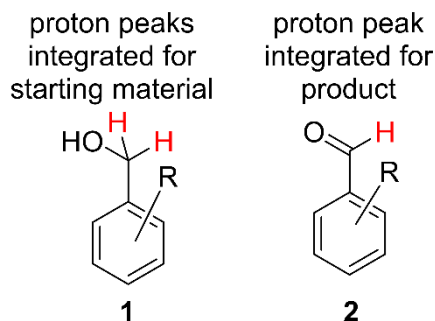


**Figure 3.**  $^1\text{H-NMR}$  peaks of protons (marked in red) integrated for the starting material **1** and product **2**.

#### ACKNOWLEDGEMENTS

Funding is acknowledged from the University of Rhode Island start-up funds and from the Gulf of Mexico Research Initiative.

#### NOTES AND REFERENCES

1. D'Souza, V. T.; Lipkowitz, K. B. *Chem. Rev.* **1998**, *98*, 1741-1742.
2. Chen, G.; Jiang, M. *Chem. Soc. Rev.* **2011**, *40*, 2254-2266.
3. Schneider, H.-J.; Hacket, F.; Ruediger, V.; Ikeda, H. *Chem. Rev.* **1998**, *98*, 1755-1785.
4. Szejtli, J. *Chem. Rev.* **1998**, *98*, 1743-1753.
5. Harada, A.; Takashima, Y.; Nakahata, M. *Acc. Chem. Res.* **2014**, *47*, 2128-2140.
6. Ghale, G.; Nau, W. M. *Acc. Chem. Res.* **2014**, *47*, 2150-2159.

7. Chaudhuri, S.; Phelan, T.; Levine, M. *Tetrahedron Lett.* **2015**, *56*, 1619-1623.
8. Serio, N.; Chanthalya, C.; Prignano, L.; Levine, M. *ACS Appl. Mater. Interfaces* **2013**, *5*, 11951-11957.
9. Akasha, A. A.; Elwahedi, M. A.; Eldeeb, A. M. *PharmaTutor Magazine* **2014**, *2*, 40-46.
10. Laokuldilok, N.; Thakeow, P.; Kopermsub, P.; Utama-ang, N. *Food Chem.* **2016**, *194*, 695-704.
11. Breslow, R. *Acc. Chem. Res.* **1995**, *28*, 146-153.
12. Kumar, A.; Dutt Shukla, R. *Green Chem.* **2015**, *17*, 848-851.
13. Zhu, J.; Wang, P.-c.; Lu, M. *J. Brazilian Chem. Soc.* **2013**, *24*, 171-176.
14. Krishnaveni, N. S.; Surendra, K.; Rao, K. R. *Adv. Synth. Catal.* **2004**, *346*, 346-350.
15. Surendra, K.; Krishnaveni, N. S.; Rao, K. R. *Canadian J. Chem.* **2004**, *82*, 1230-1233.
16. Chen, H.; Ji, H. *Chinese J. Chem. Engineering* **2011**, *19*, 972-977.
17. Marinescu, L. G.; Bols, M. *Angew. Chem. Int. Ed.* **2006**, *45*, 4590-4593.
18. Marinescu, L. G.; Doyagueez, E. G.; Petrillo, M.; Fernandez-Mayoralas, A.; Bols, M. *Eur. J. Org. Chem.* **2010**, 157-167.
19. Surendra, K.; Krishnaveni, N. S.; Reddy, M. A.; Nageswar, Y. V. D.; Rao, K. R. *J. Org. Chem.* **2003**, *68*, 2058-2059.
20. Verma, A.; Vanguri, V. K.; Golla, V.; Rhyee, S.; Trainor, M.; Abramov, K. *J. Medical Toxicol.* **2013**, *9*, 71-74.
21. Oxley, J. C.; Brady, J.; Wilson, S. A.; Smith, J. L. *J. Chem. Health Safety* **2012**, *19*, 27-33.
22. Azarifar, D.; Zolfigol, M. A.; Maleki, B. *Bull. Korean Chem. Soc.* **2004**, *25*, 23-24.
23. Alam, A.; Takaguchi, Y.; Tsuboi, S. *Synth. Commun.* **2005**, *35*, 1329-1333.
24. Suzuki, N.; Takahashi, A.; Mashiko, S.; Mizumoto, I.; Inaba, H. *Agricultural Biol. Chem.* **1990**, *54*, 459-462.
25. Hernandez-Torres, G.; Tan, B.; Barbas, C. F. *Org. Lett.* **2012**, *14*, 1858-1861.

26. Radaram, B.; Levine, M. *Tetrahedron Lett.* **2014**, *55*, 4905-4908.
27. Liu, R.; Dong, C.; Liang, X.; Wang, X.; Hu, X. *J. Org. Chem.* **2005**, *70*, 729-731.
28. Li, Z.; Zhu, W.; Bao, J.; Zou, X. *Synth. Commun.* **2014**, *44*, 1155-1164.
29. Fan, J.-C.; Shang, Z.-C.; Liang, J.; Liu, X.-H.; Liu, Y. *J. Phys. Org. Chem.* **2008**, *21*, 945-953.
30. Schneider, H.-J. *Acc. Chem. Res.* **2015**, *48*, 1815-1822.
31. Cabordery, A. C.; Toussaint, M.; Bonte, J. P.; Melnyk, P.; Vaccher, C.; Foulon, C. *J. Chromatography A* **2010**, *1217*, 3871-3875.
32. Maguire, J. H. *J. Chromatography* **1987**, *387*, 453-458.
33. Sain, A. E.; Dietrich, A. M.; Smiley, E.; Gallagher, D. L. *Sci. Total Environ.* **2015**, *538*, 298-305.
34. Yang, Z.-J.; Jiang, H.-G.; Zhou, X.-T.; Fang, Y.-X.; Ji, H.-B. *Supramol Chem.* **2012**, *24*, 379-384.
35. Yang, Z.; Zeng, H.; Zhou, X.; Ji, H. *Tetrahedron* **2012**, *68*, 5912-5919.



*Supporting Information*

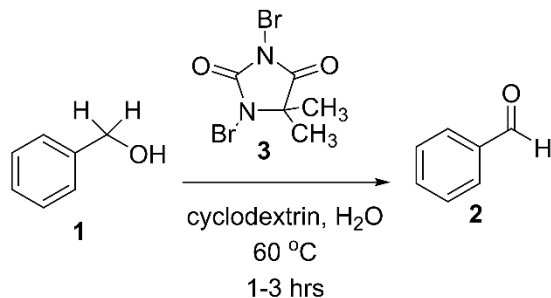
**An Environmentally Friendly Procedure for the Aqueous Oxidation of Benzyl Alcohols to Aldehydes with Dibromodimethylhydantoin (DBDMH) and Cyclodextrin - Scope and Mechanistic Insights**

**MATERIALS AND METHODS**

Proton NMR spectra were recorded using a Bruker 300 MHz instrument, with the singlet peak of HDO at 4.79 ppm as reference. All reagents, substrates, and solvents were obtained from Sigma Aldrich and used as received. Four different cyclodextrin solutions were screened:  $\alpha$ -cyclodextrin,  $\beta$ -cyclodextrin, methyl  $\beta$ -cyclodextrin and  $\gamma$ -cyclodextrin dissolved in deuterated water (D<sub>2</sub>O). A cyclodextrin-free D<sub>2</sub>O solution was used as the control. The same procedure was adopted for all the cyclodextrins and the control.

**STANDARD REACTION CONDITIONS**

To a clean and dry small vial, a solution of substrate **1** (15.0  $\mu$ mol, 1.0 equivalent) was made using an aqueous cyclodextrin solution (1.0 mL) in D<sub>2</sub>O. DBDMH **3** (4.3 mg, 15.0  $\mu$ mol, 1.0 equivalent) was added to the reaction mixture and sonicated to make sure that the reagents were well suspended. The reaction mixture was heated at 60 °C with occasional shaking to maintain the homogeneity of the solution. After the desired period of time, the <sup>1</sup>H-NMR spectrum of the reaction mixture was recorded to determine the percent conversion.



### NMR ANALYSIS

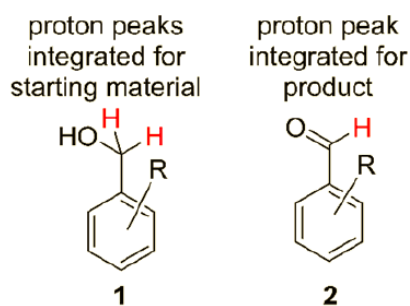


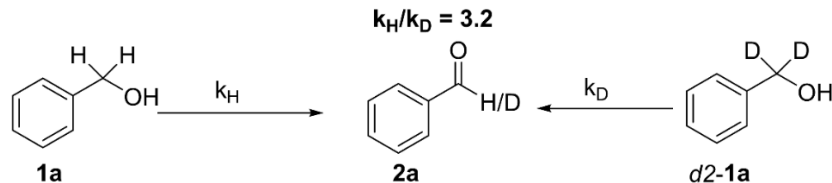
**Figure 3.** <sup>1</sup>H-NMR peaks of protons (marked in red) integrated for the starting material **1** and product **2**.

The percent conversion of each reaction was calculated based on the following equation:

$$\% \text{ Conversion} = \left[ \frac{\text{Integration of the product peak}}{(\text{Integration of the product peak}) + (\text{Integration of the starting material peak})/2} \right] \times 100\%$$

The starting material NMR peak used in this equation corresponds to 2 benzylic protons of compound **1** and the product peak used for this equation corresponds to the 1 aldehyde proton of the product **2** (Figure 1). The integrations of the NMR peaks were the relative areas under the curve measured against a calibrated standard corresponding to the anomeric protons of the cyclodextrin hosts.

## KINETIC ISOTOPE EFFECT EXPERIMENTS



Two separate solutions of substrate **1a** and *d2-1a* (15.0  $\mu\text{mol}$ , 1.0 equivalent) were made using 5 mM aqueous  $\alpha$ -cyclodextrin solution (1.0 mL, 5.0  $\mu\text{mol}$ , 0.33 equivalents) in  $\text{D}_2\text{O}$ . DBDMH **3** (4.3 mg, 15.0  $\mu\text{mol}$ , 1.0 equivalent) was added to the reaction mixtures and sonicated to make sure that the reagents were well suspended. The reaction mixtures were heated at 60°C with occasional shaking to maintain the homogeneity of the solutions for 1 hour.  $^1\text{H-NMR}$  spectra of the reaction mixtures were recorded to determine the percent conversions.

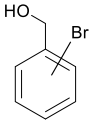
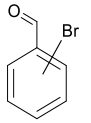
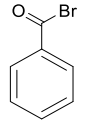
**Table S1.** Percent conversions of alcohol substrates **1a** and *d2-1a* to aldehyde **2a**<sup>a</sup>

Substrate	Equivalents of substrate	Equivalents of compound <b>3</b>	% Conversion <sup>b</sup>	$k_H/k_D$
<b>1a</b>	15 $\mu\text{mol}$	15 $\mu\text{mol}$	26	<b>3.2</b>
<i>d2-1a</i>	15 $\mu\text{mol}$	15 $\mu\text{mol}$	8	

<sup>a</sup> Percent conversion was calculated based on the NMR analysis of the reaction.

<sup>b</sup> The reaction was run with  $\alpha$ -cyclodextrin (0.33 equivalents) for 0.5 hours at 60°C.

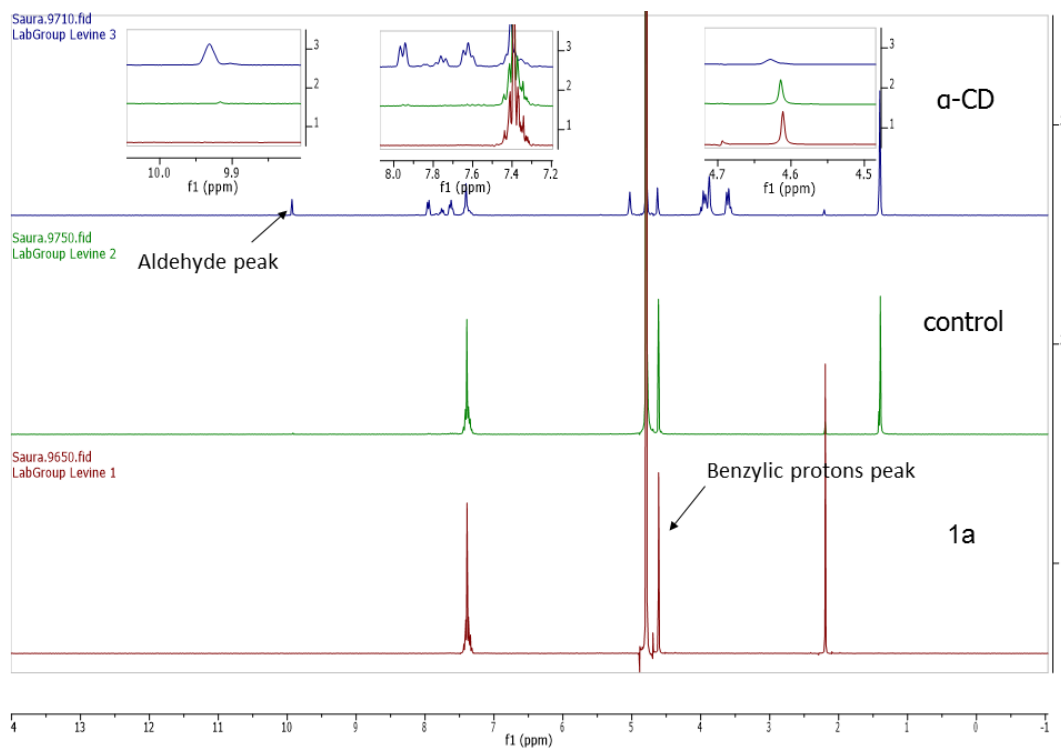
TABLE DEMONSTRATING CATALYST REUSABILITY

Number of Re-runs of Catalyst	Starting Material <b>1a</b> (%) <sup>a</sup>	Br-benzyl alcohol (%) <sup>a</sup>	Br-Aldehyde (%) <sup>a</sup>	Acid bromide (%) <sup>a</sup>	Product <b>2a</b> (%) <sup>a</sup>
1 <sup>st</sup>	15				75
2 <sup>nd</sup>	-	-	-	26	74
3 <sup>rd</sup>	-	-	22	16	62

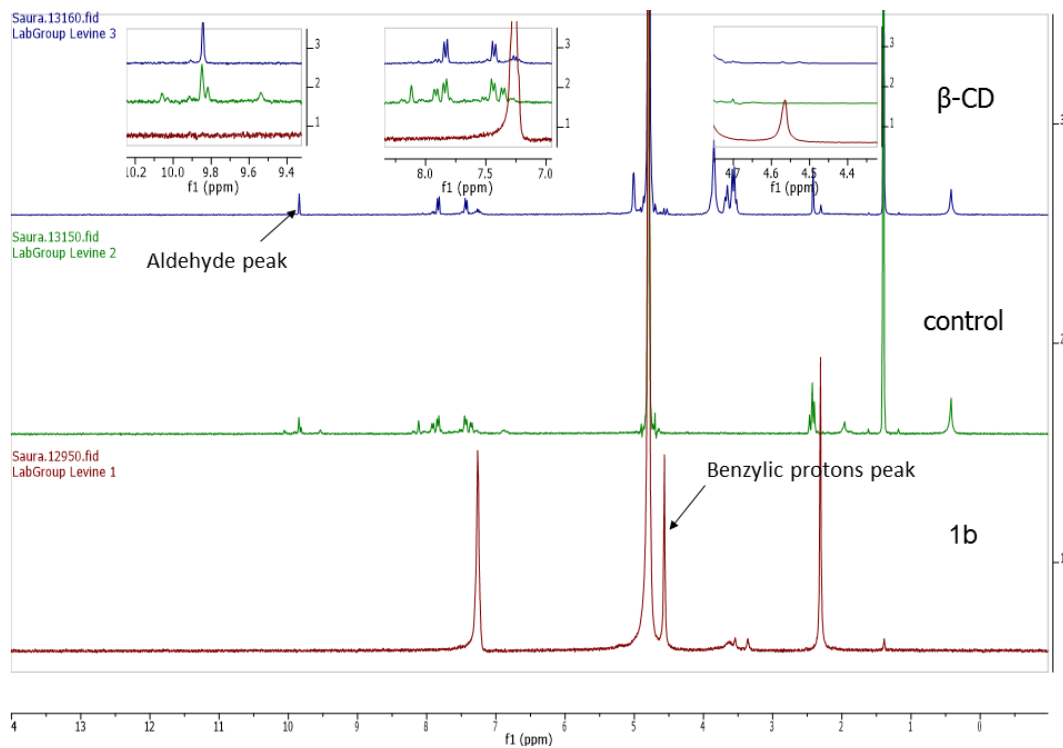
<sup>a</sup> Percent conversions were calculated based on the <sup>1</sup>H-NMR analysis of the reaction mixture.

### <sup>1</sup>H-NMR SPECTRA FOR REACTION ANALYSIS

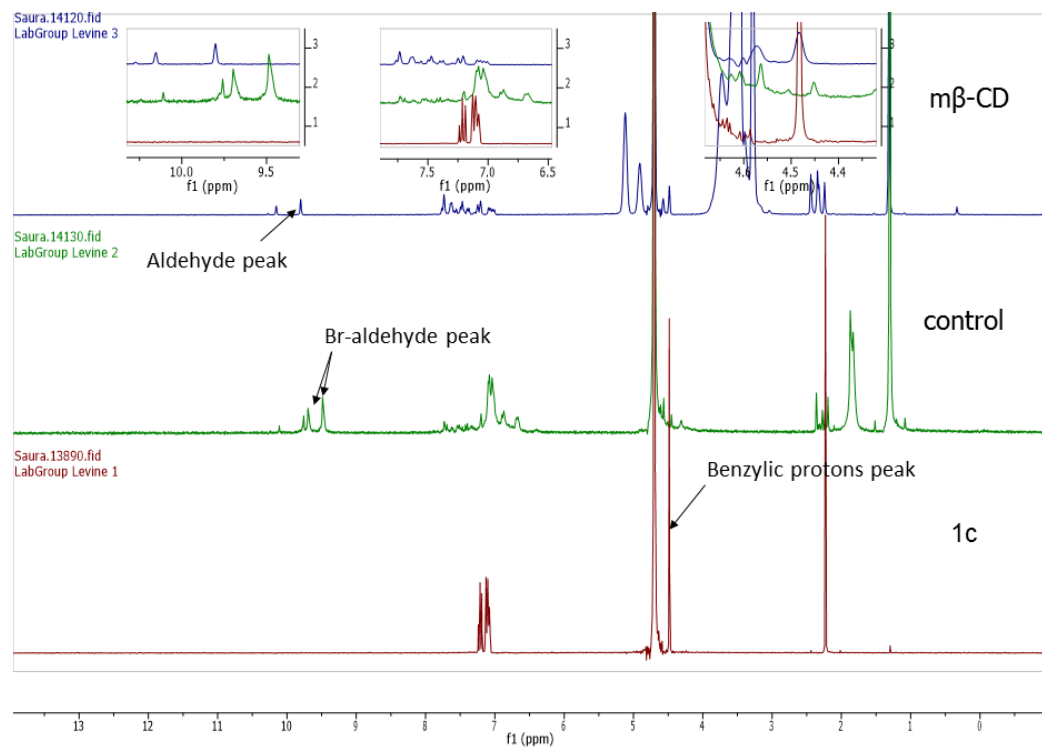
#### Benzyl alcohol **1a**



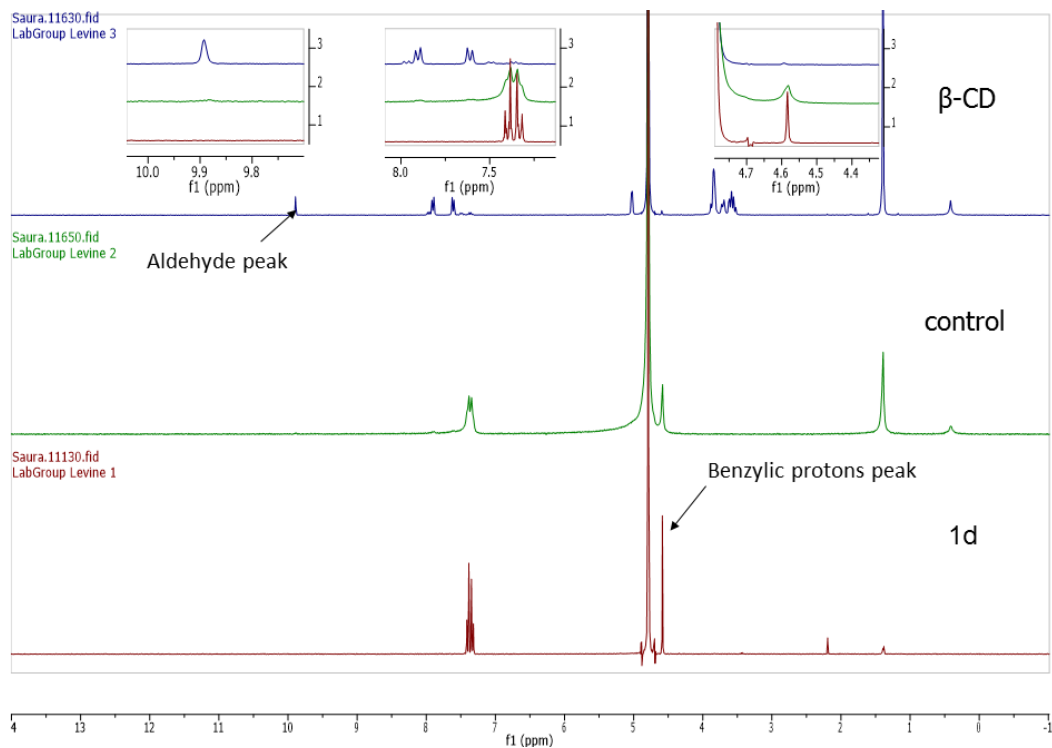
### 4-methyl benzyl alcohol **1b**



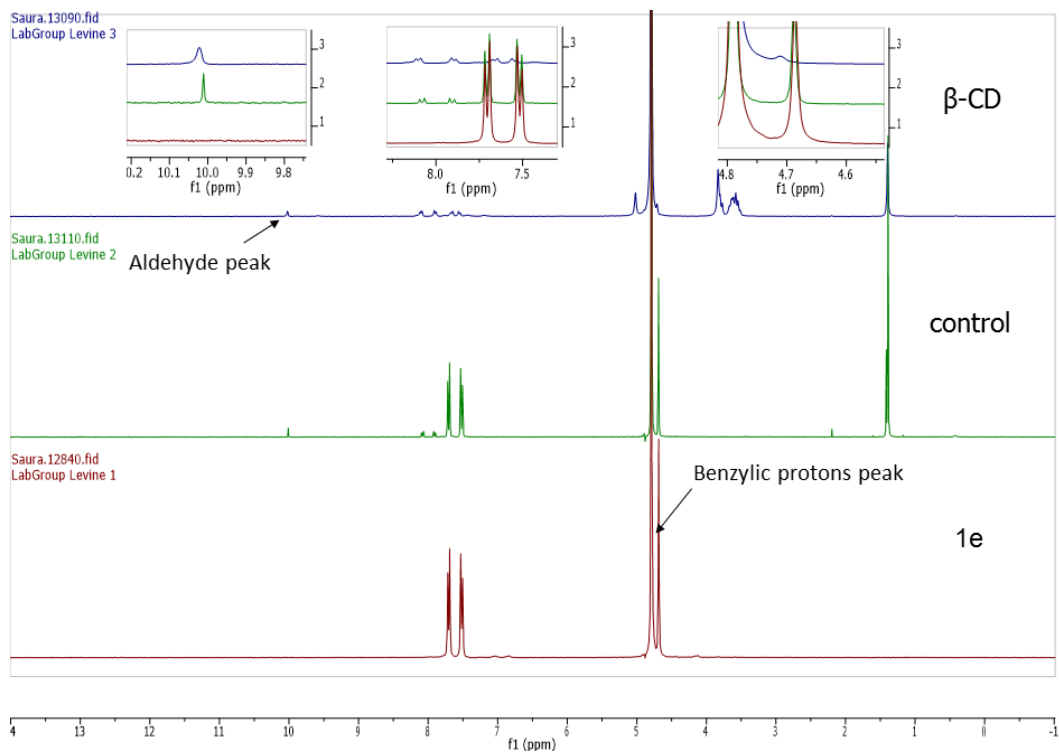
### 3-methyl benzyl alcohol **1c**



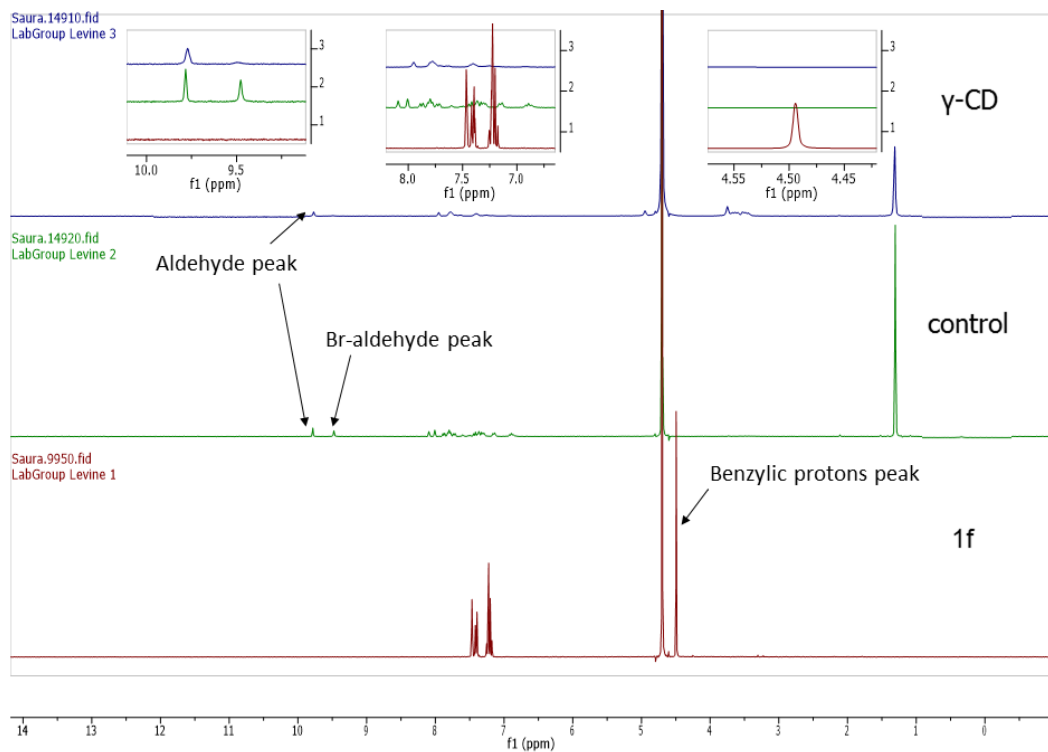
### 4-chloro benzyl alcohol **1d**



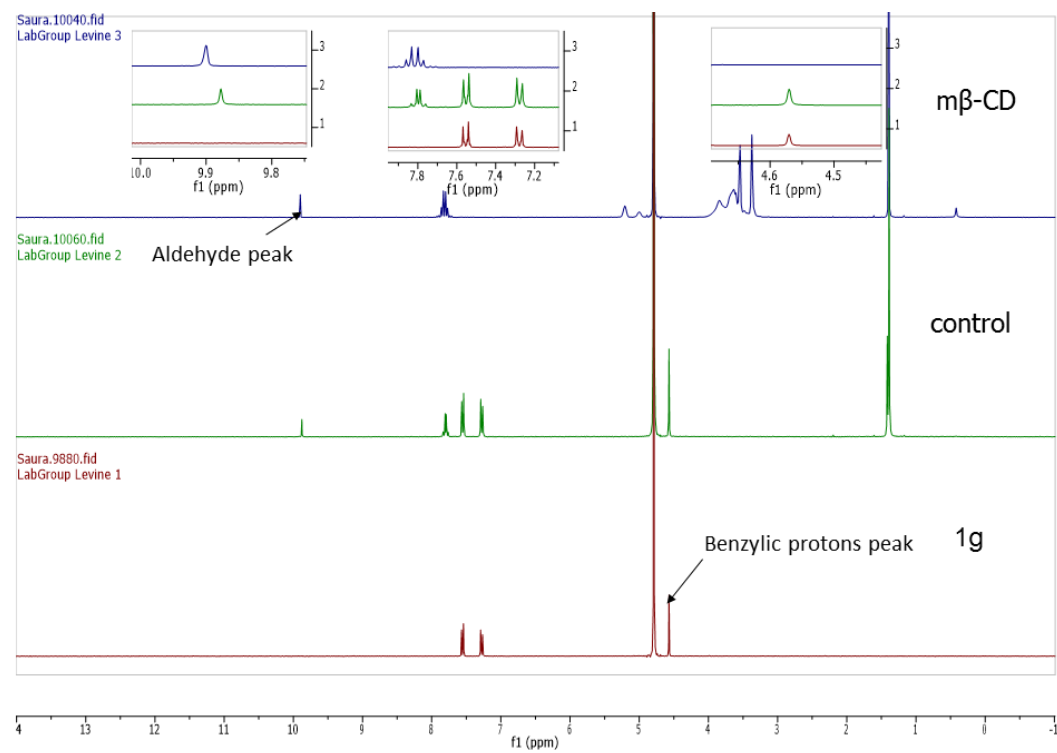
### 4-trifluoromethyl benzyl alcohol **1e**



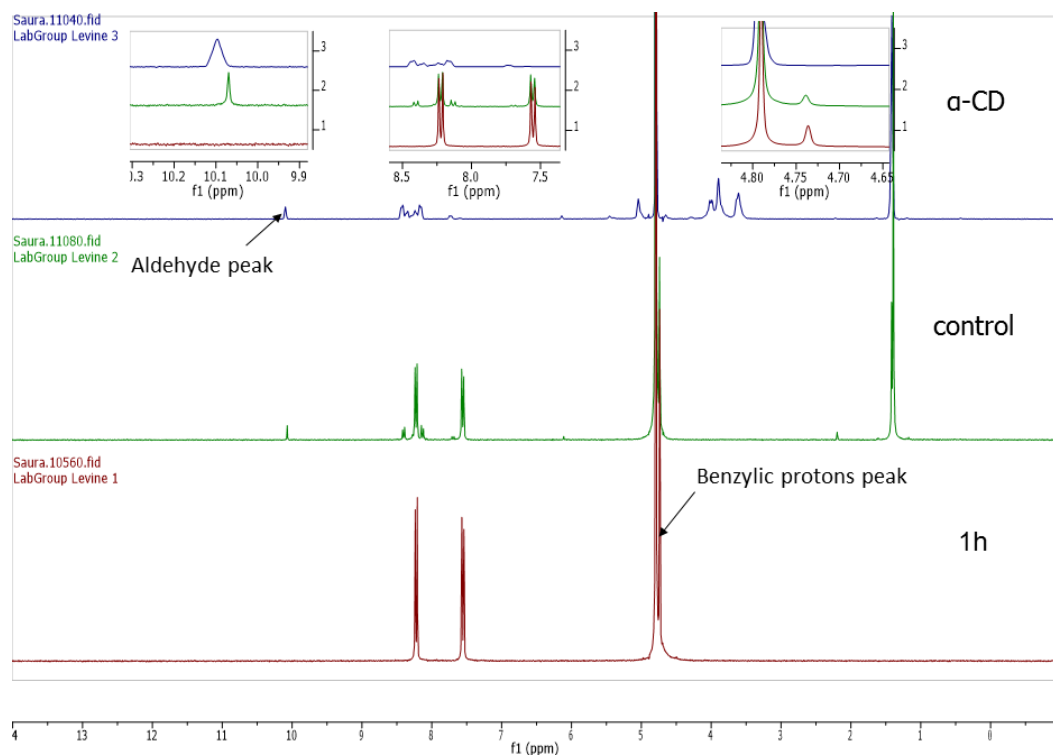
### 3-bromo benzyl alcohol **1f**



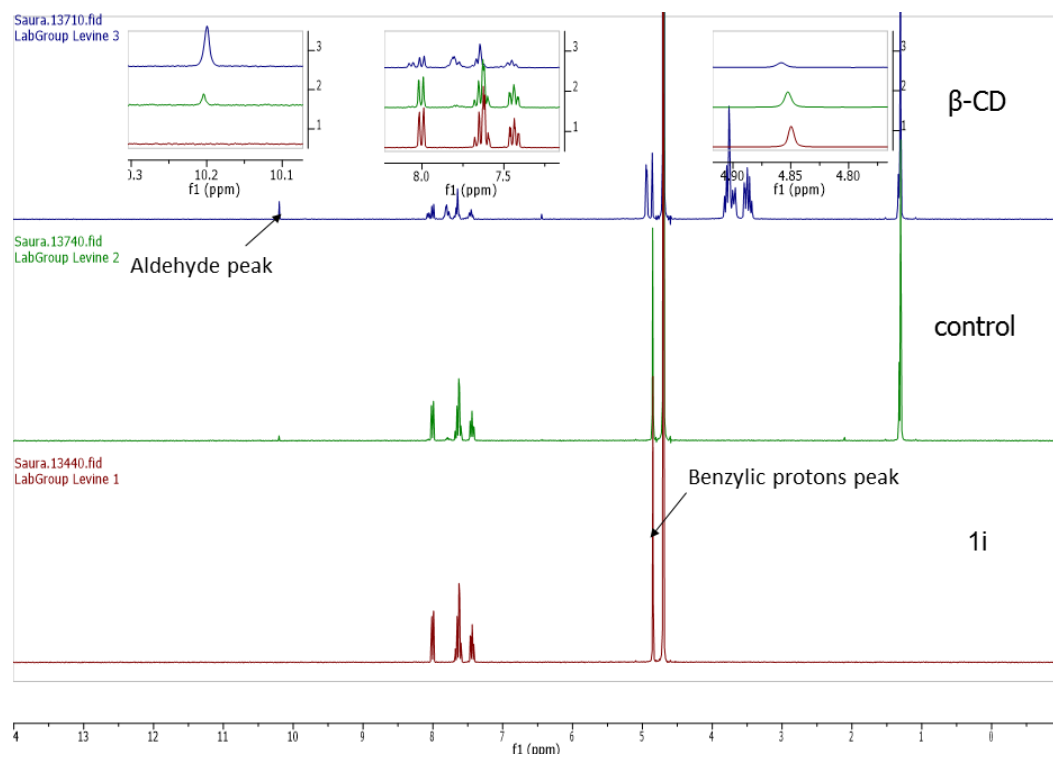
### 4-bromo benzyl alcohol **1g**



## 4-nitro benzyl alcohol **1h**

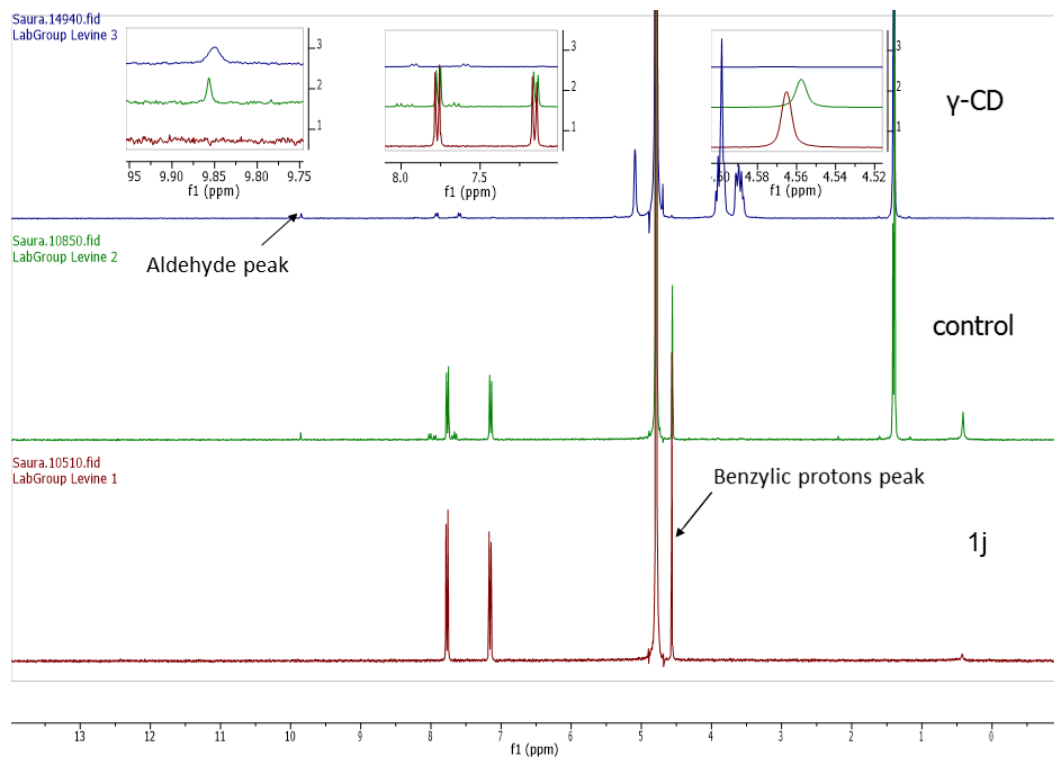


## 2-nitro benzyl alcohol **1i**

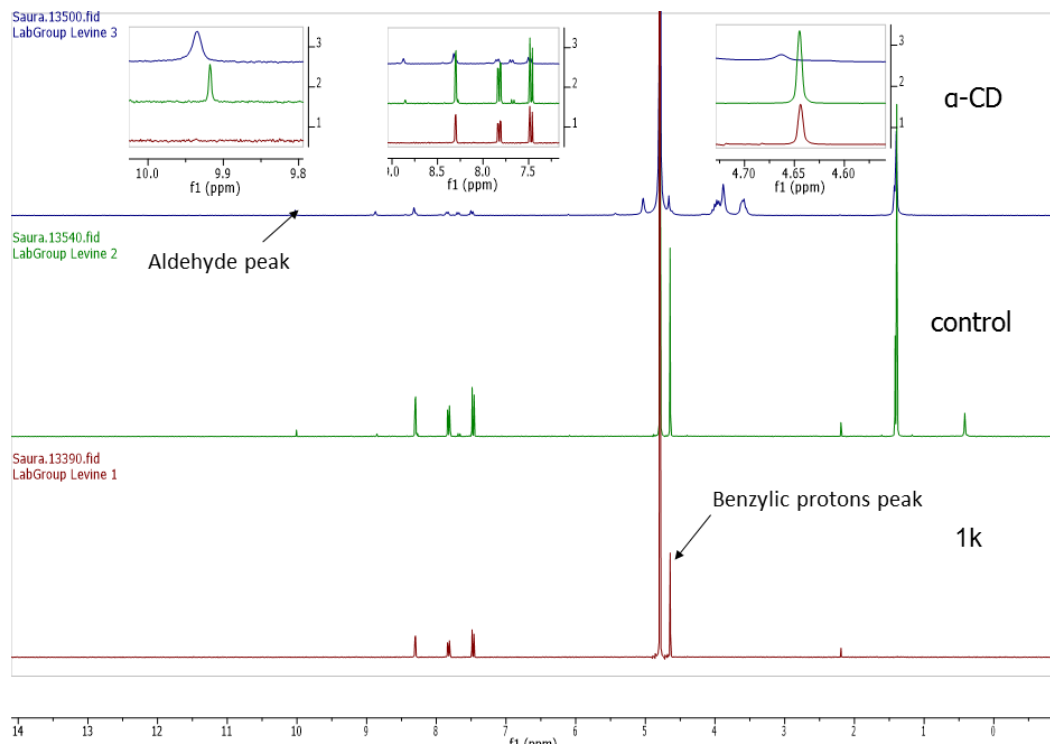




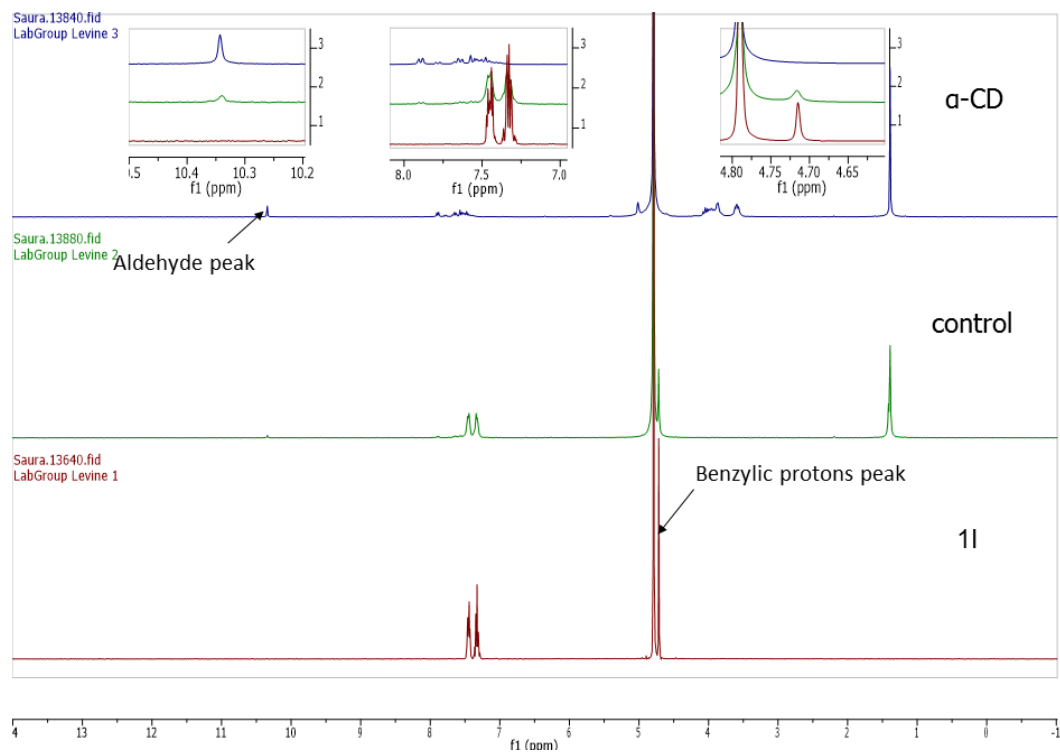
## 4-iodo benzyl alcohol **1j**



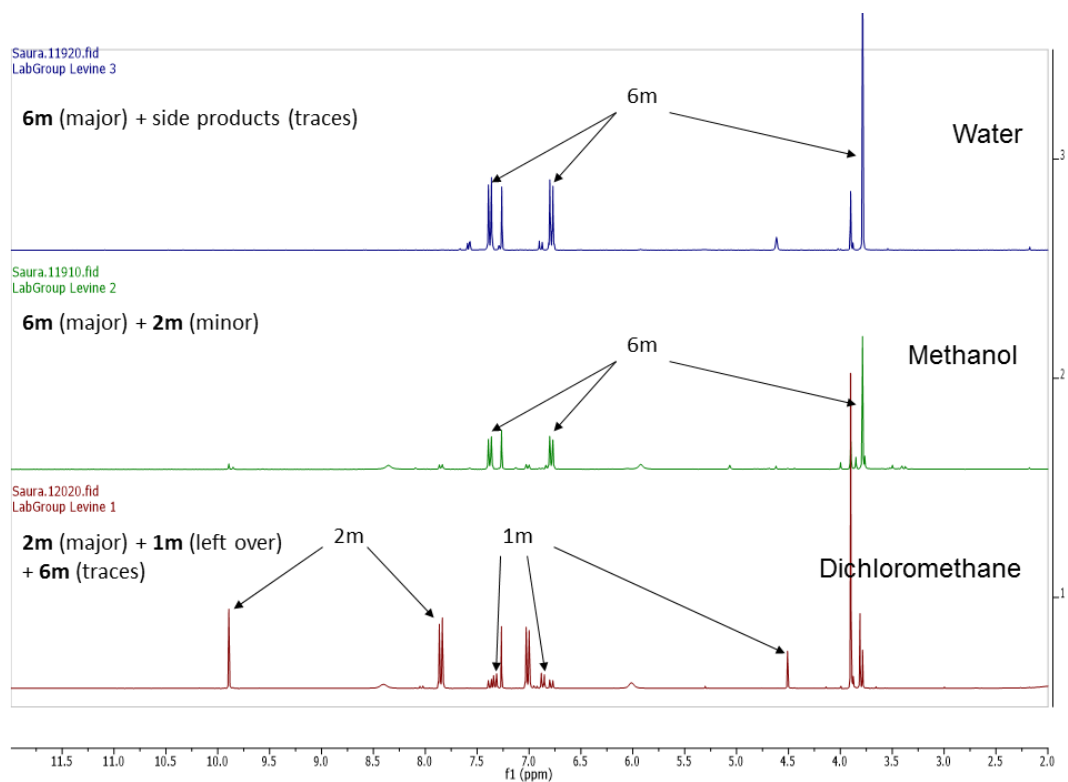
## 2-chloro-5-methylhydroxy pyridine **1k**



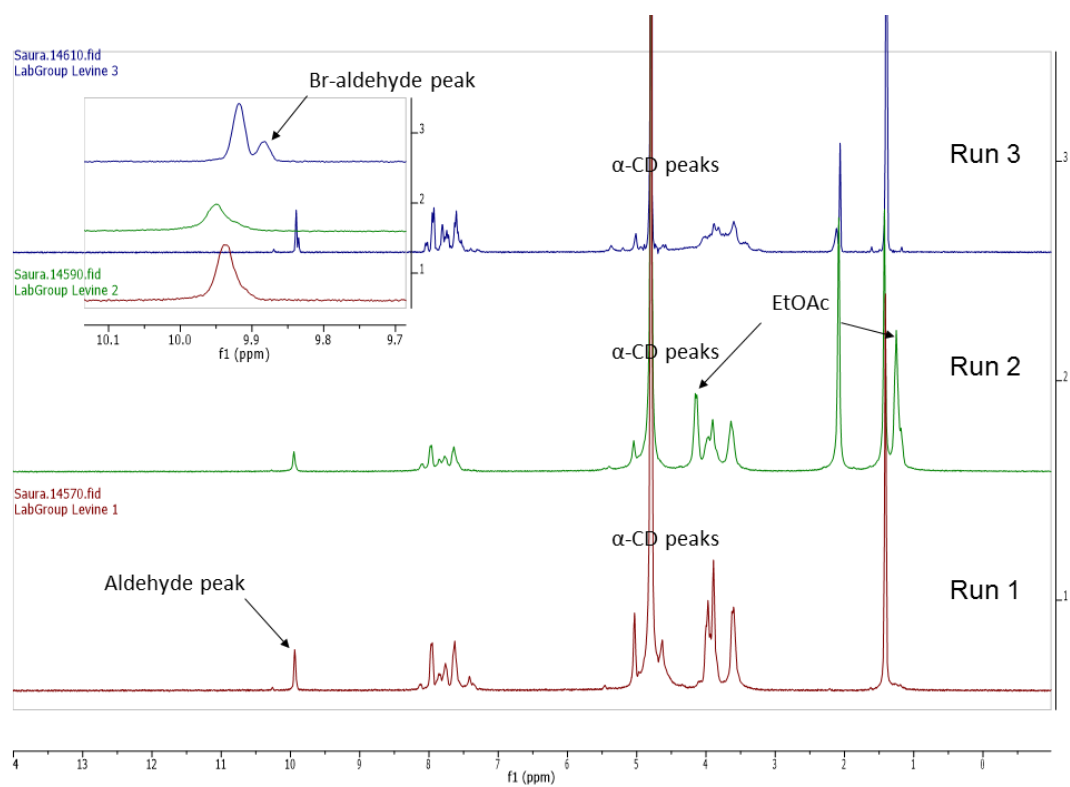
## 2-chloro benzyl alcohol **1l**



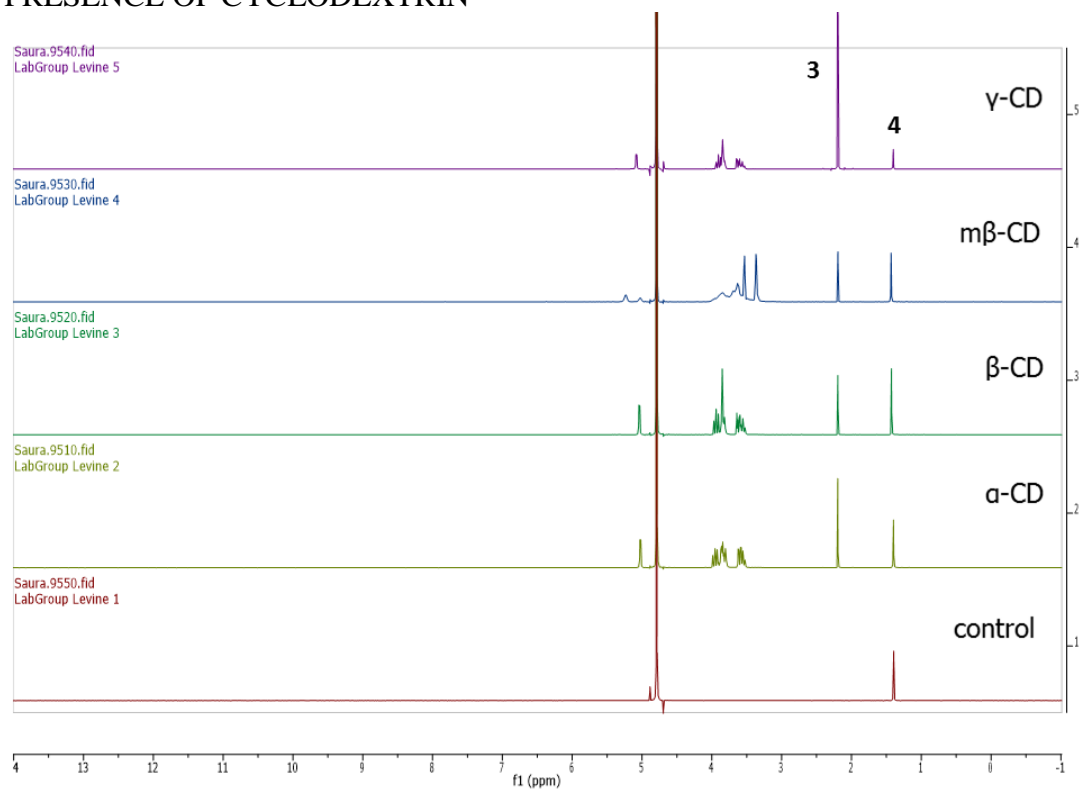
## 4-methoxy benzyl alcohol **1m**



# $^1\text{H-NMR}$ SPECTRA DEMONSTRATING CATALYST REUSABILITY



# <sup>1</sup>H-NMR SPECTRA DEMONSTRATING REACTIVITY OF REAGENT 3 IN THE PRESENCE OF CYCLODEXTRIN



**<sup>1</sup>H-NMR SPECTRA DEMONSTRATING THE REACTIVITY OF REAGENT 3 IN THE PRESENCE OF CYCLODEXTRIN AND ONE EQUIVALENT OF 1a**

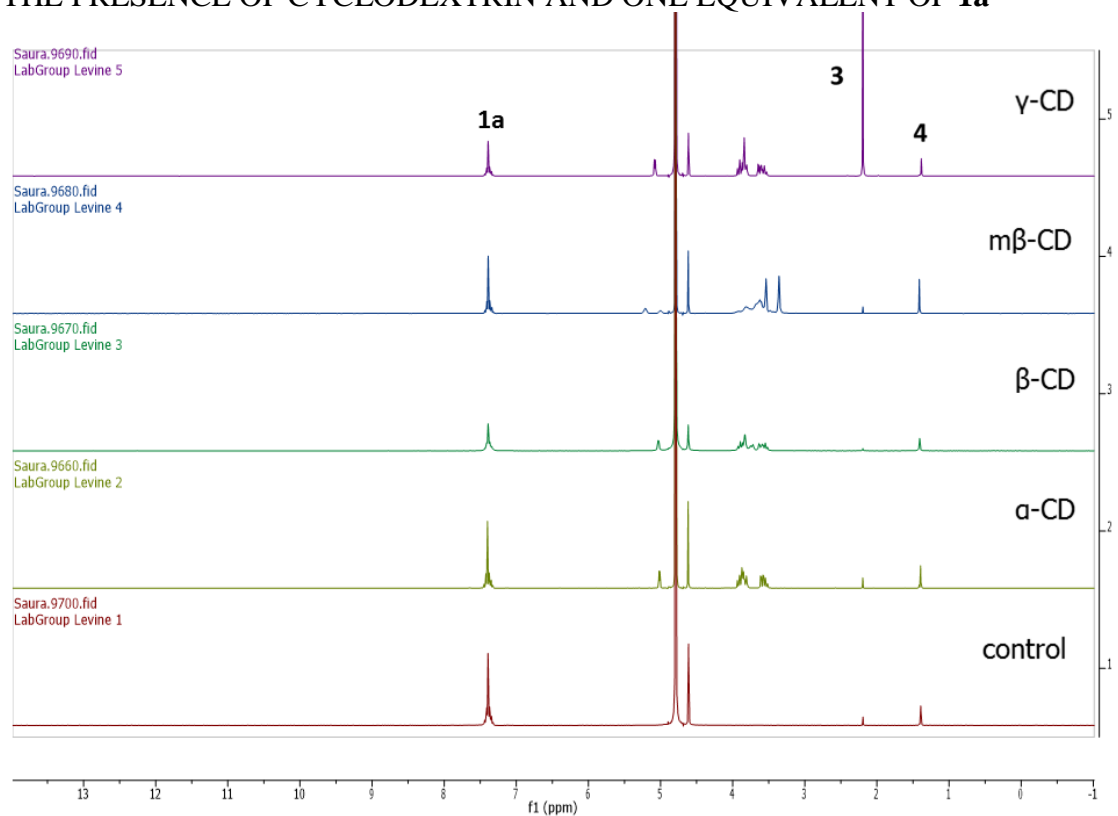


TABLE ILLUSTRATING THE %N-Br BOND DISSOCIATION OF REAGENT **3** IN THE PRESENCE OF CYCLODEXTRIN AND ONE EQUIVALENT OF **1a** AT STANDARD REACTION CONDITIONS (CALCULATED BASED ON THE NMR PEAK INTEGRALS OF **3** AND **4**)

CDs (0.33 eq.)	<b>3</b> (rt, 0 mins)	<b>3</b> + <b>1a</b> (60°C, 0.5 hrs)
$\alpha$ -CD	50	58
$\beta$ -CD	66	66
m $\beta$ -CD	68	69
$\gamma$ -CD	11	14
control	100	100

### CHAPTER 3

Accepted for publication in *New Journal of Chemistry*

Array based detection of isomeric and analogous analytes employing synthetically  
modified fluorophore attached  $\beta$ -cyclodextrin derivatives

Sauradip Chaudhuri, Dana J. DiScenza, Benjamin Smith, Reid Yocum, Mindy Levine

Department of Chemistry, University of Rhode Island, Kingston, RI, USA

Corresponding Author:

Mindy Levine, Ph.D.

Department of Chemistry

University of Rhode Island

Kingston, Rhode Island, 02881, USA

[mlevine@chm.uri.edu](mailto:mlevine@chm.uri.edu)

## Manuscript 3

### **Array based detection of isomeric and analogous analytes employing synthetically modified fluorophore attached $\beta$ -cyclodextrin derivatives**

#### ABSTRACT

Reported herein is a sensitive and selective array-based sensing strategy based on differential interactions with three supramolecular cyclodextrin-fluorophore sensors. Each interaction results in a distinct fluorescence modulation response, and linear discriminant analyses of these responses results in 100% successful classification of three classes of isomeric analytes and two classes of analogous analytes. Calculated limits of detection for this system are at or near literature-reported levels of concern.

#### INTRODUCTION

The selective detection and accurate quantification of structurally similar analytes is a major challenge for scientists, as structurally similar analytes often have widely disparate toxicities.<sup>1</sup> The most common strategy is to use mass spectrometry methods, such as liquid chromatography-mass spectrometry (LC-MS)<sup>2</sup> or gas chromatography-mass spectrometry (GC-MS).<sup>3</sup> However, there are significant drawbacks associated with this approach, including the costs and time necessary to conduct such analyses,<sup>4</sup> which limits the ability to conduct high throughput assays.<sup>5</sup>

An alternate strategy is to use array-based sensing systems, which have recently gained in popularity.<sup>6</sup> This approach relies on the development of a chemical signature for each analyte based on analyte-specific interactions with a sensor series. Array-based sensing



systems can be combined with supramolecular sensors, which rely on differential non-covalent interactions of analytes with supramolecular hosts, including cyclodextrins,<sup>7</sup> fluorescent polymers,<sup>8</sup> molecularly imprinted polymers,<sup>9</sup> and metal-organic frameworks (MOFs).<sup>10</sup>

Although supramolecular array-based systems overcome many challenges associated with mass-spectrometry based detection methods, the analyte scope explored in most of these reports have been limited to aromatic small molecules.<sup>11</sup> In a real-world contaminated environment, the nature of the various pollutants is highly complex,<sup>12</sup> and includes mixtures of aromatic and non-aromatic compounds.<sup>13</sup> This kind of situation requires the development of a sensing system which is rapid, simple, and efficient in classifying a broad range of persistent organic pollutants (POPs).<sup>14</sup>

Our group has previously reported the use of  $\beta$ -cyclodextrin and  $\gamma$ -cyclodextrin in array-based detection systems for the sensing of a wide variety of environmental toxicants and POPs.<sup>15</sup> The sensing strategy is based on cyclodextrin promoted analyte-to-fluorophore energy transfer as well as cyclodextrin-promoted, analyte-induced fluorescence modulation. In the fluorescence modulation systems, the fluorophore was added to the cyclodextrin solution prior to analyte addition, which can result in fluorophore-cyclodextrin binding that reduces the cyclodextrin's ability to bind the target analyte. As such, introduction of the analyte to the fluorophore-cyclodextrin solution requires the analyte-cyclodextrin association constants to be higher than those of the fluorophore-cyclodextrin (Figure 1A), or it requires the formation of higher order association complexes between the analyte, cyclodextrin and fluorophore (Figure 1B). Such higher order association complexation is probable only for  $\gamma$ -cyclodextrin.<sup>16</sup>

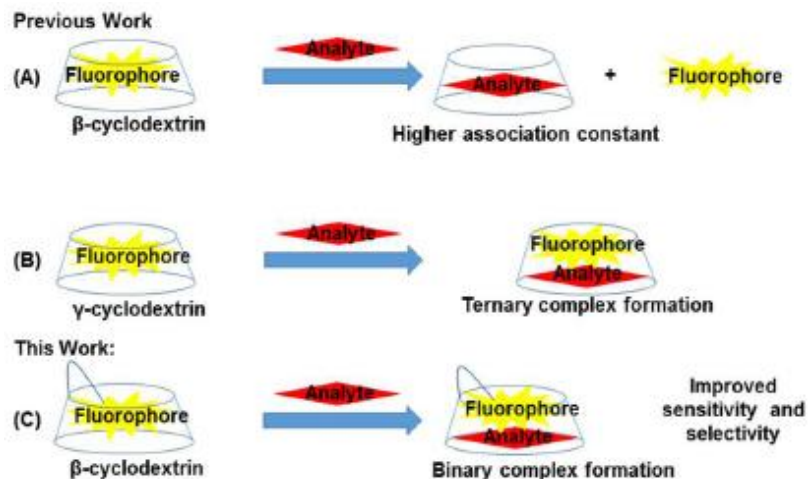


**Figure 1.** Schematic illustration of this work compared to previously published work.

Herein, we report the development of an array-based detection system using fluorophore-functionalized perbenzylated  $\beta$ -cyclodextrin sensors, which enables binary complex formation between the functionalized cyclodextrin and the target analyte (Figure 1C). Each sensor is selective, meaning the array is able to distinguish three classes of isomeric analytes and two classes of structurally similar analytes, with 100% classification accuracy. High sensitivity is demonstrated as well, with limits of detection approaching or surpassing literature-reported levels of concern. Finally, preliminary efforts at using this system for the accurate identification of binary analyte mixtures are also reported.

## EXPERIMENTAL SECTION

### *Materials and Methods*

All the reagents were obtained from Sigma Aldrich or Fisher Scientific and used without further purification, unless otherwise noted.  $\beta$ -cyclodextrin was dried in the oven prior to use. Reagent grade solvents (99.9% purity) were used for the synthetic reactions.

### *Fluorescence Modulation Experiments*

Fluorescence emission spectra were obtained using a Shimadzu RF-5301PC spectrophotofluorimeter with 3 nm excitation and 3 nm emission slit widths. 0.5 mL of **S1**, **S2**, or **S3** solutions (5  $\mu$ M in DMSO) and 2 mL of deionized water were combined in a quartz cuvette. The solution was excited at 320 nm, and the fluorescence emission spectra were recorded.

The fluorescence emission spectra were integrated vs. wavenumber on the X-axis, and the fluorescence modulation was measured as the ratio of the integrated emission of the fluorophore in the presence of the analyte to integrated emission of the fluorophore in the absence of the analyte (Equation 1):

$$\text{Fluorescence Modulation} = Fl_{\text{analyte}} / Fl_{\text{blank}} \quad (\text{Equation 1})$$

Where  $Fl_{\text{analyte}}$  is the integrated fluorescence emission of the fluorophore in the presence of 10  $\mu$ L of analyte (1 mg/mL in THF), and  $Fl_{\text{blank}}$  is the integrated fluorescence emission of the fluorophore in the absence of the analyte.

### *Array Generation Experiments*

Array analysis was performed using SYSTAT 13 statistical computing software with the following settings:

- (a) Classical Discriminant Analysis
- (b) Grouping Variable: Analytes
- (c) Predictors: **S1**, **S2**, and **S3**
- (d) Long-Range Statistics: Mahal

### *Limit of Detection Experiments*

The limit of detection (LOD) is defined as the lowest concentration of analyte at which a signal can be detected. To determine this value, the following steps were performed for each cyclodextrin-analyte combination. In a quartz cuvette, 0.5 mL of **S1**, **S2**, or **S3** solutions (5  $\mu\text{M}$  in DMSO) and 2 mL of deionized water were combined. The solution was excited at 320 nm, and the fluorescence emission spectra were recorded starting at 330 nm. Six repeat measurements were taken.

Next, 2  $\mu\text{L}$  of analyte (1 mg/mL in THF) was added, and again the solution was excited at the fluorophore's excitation wavelength, and the fluorescence emission spectra were recorded. Six repeat measurements were taken. This step was repeated for 4  $\mu\text{L}$ , 6  $\mu\text{L}$ , 8  $\mu\text{L}$ , 10  $\mu\text{L}$ , 12  $\mu\text{L}$ , 14  $\mu\text{L}$ , 16  $\mu\text{L}$ , 18  $\mu\text{L}$ , and 20  $\mu\text{L}$  of analyte.

All of the fluorescence emission spectra were integrated vs. wavenumber on the X-axis, and calibration curves were generated. The curves plotted the analyte concentration in  $\mu\text{M}$  on the X-axis, and the fluorescence modulation ratio on the Y-axis. The curve was fitted to a straight line and the equation of the line was determined.

The limit of detection is defined according to Equation 2:

$$\text{LOD} = 3(\text{SD}_{\text{blank}})/m \quad (\text{Equation 2})$$

Where  $\text{SD}_{\text{blank}}$  is the standard deviation of the blank sample and  $m$  is the slope of the calibration curve.

## RESULTS AND DISCUSSION

We employed a series of three cyclodextrin-based supramolecular sensors (Figure 2) for the detection of a broad variety of small molecule analytes (Figure 3). In these sensors, the perbenzylated  $\beta$ -cyclodextrin cavity acts as the receptor domain, and the attached fluorophore units act as the transducers, which are responsible for fluorescence-based responses to changes in their environment in the presence of the target analyte. The covalent attachment strategy used in sensors **S2** and **S3**, with one and two degrees of functionalization on the primary rim, respectively, ensures the close proximity of the fluorophore units to the cyclodextrin receptor cavity, thereby facilitating productive fluorophore-analyte interactions. In contrast, sensor **S1** is a non-covalent combination of the perbenzylated  $\beta$ -cyclodextrin and fluorophore **4** (1:1 molar ratio), and is included to enable a direct determination of the benefits of covalent attachment in sensor design. The synthesis of supramolecular hosts **S2** and **S3** is shown in Scheme 1. Perbenzylated  $\beta$ -cyclodextrin was obtained from the reaction of  $\beta$ -cyclodextrin with excess benzyl chloride.<sup>17</sup> Regioselective debenzylation of the primary rim was affected by treating the perbenzylated  $\beta$ -cyclodextrin with DIBAL-H.<sup>18</sup> This was followed by esterification<sup>19</sup> with the acid derivative of fluorophore **4**, yielding mono- and di-functionalized sensors **S2** and **S3**. Compounds **S2** and **S3** were fully characterized by <sup>1</sup>H-NMR, <sup>13</sup>C-NMR, MALDI-TOF mass spectrometry, UV-visible and fluorescence spectroscopy.

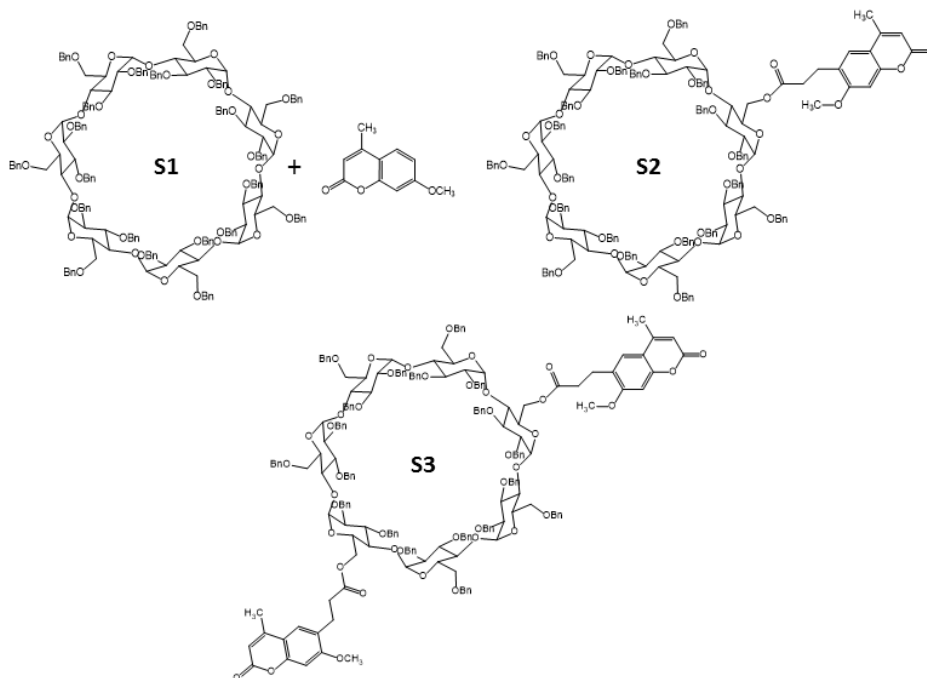


**Figure 2.** Structures of sensors **S1-S3**.

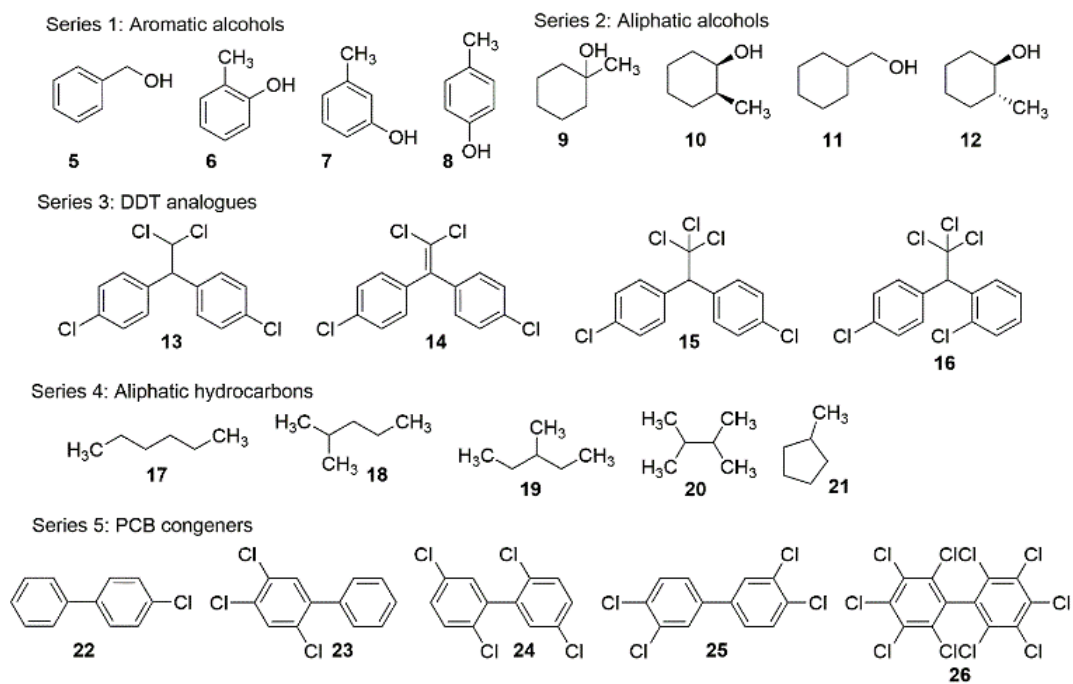
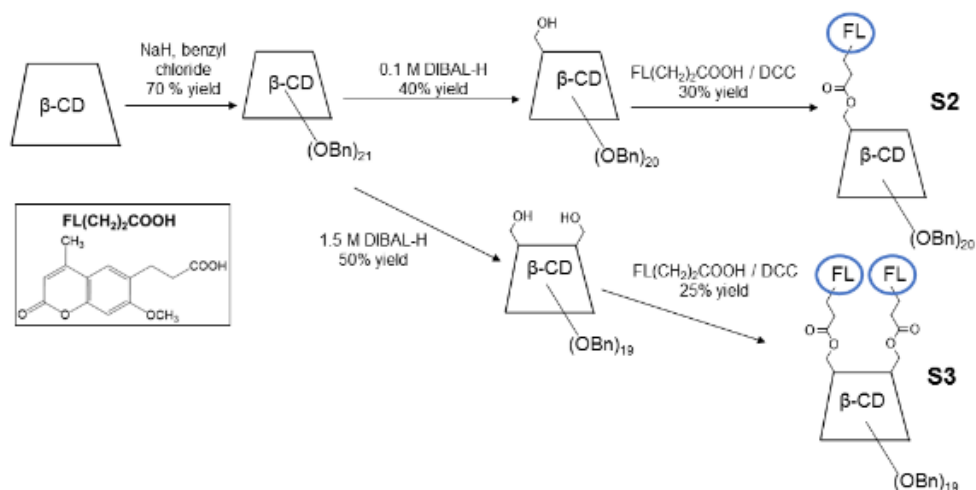


**Figure 3.** Structures of small molecule analytes **5-26**.



**Scheme 1.** Synthesis of supramolecular hosts **S2** and **S3**.

The sensitivity of the fluorescence emission responses of sensors **S1-S3** to solvent composition was investigated, with the goal of ensuring full dissolution of the sensor while enabling strong binding of analytes in the cyclodextrin (optimal in aqueous environments). These competing considerations led us to choose an 80:20 water-DMSO mixture as the optimal sensing solvent. Of note, covalent attachment of the fluorophores in **S2** and **S3** led to a reduction of the fluorescence emission compared to the free fluorophore in **S1** (Figure 4). This decrease is in agreement with literature precedence in analogous systems, and occurs as a result of increased non-radiative decay pathways that are available through covalent attachment to a highly flexible macromolecule. This decrease is offset by the markedly improved fluorescence modulation results in the presence of various analytes.<sup>20</sup>

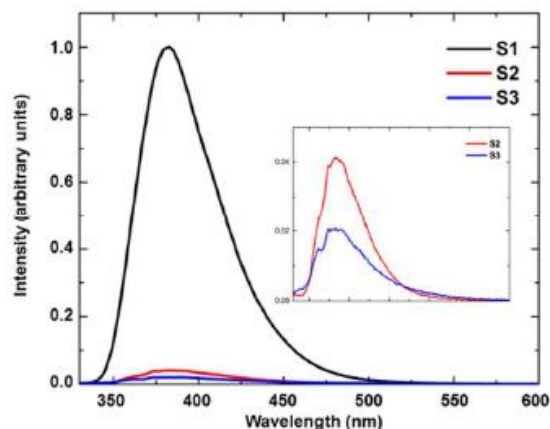


**Figure 4.** Fluorescence emission spectra of supramolecular hosts **S1-S3** (1  $\mu\text{M}$ ) (inset shows the fluorescence of **S2** and **S3** in more detail) in 80:20 water-DMSO solution. ( $\lambda_{\text{excitation}} = 320 \text{ nm}$ ; 3 nm excitation slit width; 3 nm emission slit width).

The choice of perbenzylated  $\beta$ -cyclodextrin as a receptor is due to the strong binding of organic guest molecules in the extended hydrophobic cavity. A comparison of association constants of analyte **5** revealed a 1000-fold increase in the binding constant with perbenzylated  $\beta$ -cyclodextrin compared to  $\beta$ -cyclodextrin, with further increases in the fluorophore-functionalized cyclodextrins **S2** and **S3** (Table 1). These binding constants are orders of magnitude higher than the highest literature-reported binding constants for analyte **5** in  $\beta$ -cyclodextrin ( $K_a = 50\text{-}215 \text{ M}^{-1}$ ).<sup>21</sup> Higher association constants for analyte-sensor binding are known to lead to improved sensor performance,<sup>22</sup> a phenomenon that is also borne out in this system (*vide infra*). Similarly, in this case, strong binding of analytes **5-8** in hosts **S1-S3** induced marked changes in the resulting fluorescence emission due to proximity-induced interactions between the analyte and the fluorophore. These changes were quantified according to Equation 1.



**Table 1.** Association constants of analyte **5** in per-benzylated  $\beta$ -cyclodextrin, **S2**, and **S3**<sup>a</sup>

Host	Association Constant (M <sup>-1</sup> )
Perbenzylated $\beta$ -cyclodextrin	3.6 (0.1) x 10 <sup>4</sup> M <sup>-1</sup>
<b>S2</b>	4.8 (0.5) x 10 <sup>4</sup> M <sup>-1</sup>
<b>S3</b>	24.9 (0.5) x 10 <sup>4</sup> M <sup>-1</sup>

<sup>a</sup>Association constants calculated using <sup>1</sup>H-NMR titrations in 80:20 water-DMSO mixture. Values in parentheses indicate the error in the association constant values.

The sensor **S1** shows a fluorescence modulation value close to 1.00 for all the tested analytes, indicating minimal to no effect on the fluorescence emission of the fluorophore with the introduction of the analyte. In contrast to this, fluorescence modulation values measured for sensors **S2** and **S3** are significantly different from that of **S1**, and display widespread variability between different classes of analytes as well as within each analyte class (Table 2). These results clearly demonstrate the effect of the sensor architecture, and in particular the effects of covalent fluorophore attachment and the number of fluorophore units. The covalent attachment ensures close proximity between the cyclodextrin-bound analyte and the fluorophore moiety(ies), causing various degree of fluorescence modulation to occur. An example of analyte-induced fluorescence modulation for analyte **8** is shown in Figure 5.

**Table 2.** Fluorescence modulation of supramolecular sensors in the presence of aromatic alcohol analyte **5-8**<sup>a</sup>

Analyte	<b>S1</b>	<b>S2</b>	<b>S3</b>
<b>5</b>	1.00 ± 0.00	1.04 ± 0.01	0.98 ± 0.01
<b>6</b>	1.01 ± 0.00	0.82 ± 0.01	0.88 ± 0.01
<b>7</b>	0.99 ± 0.00	0.90 ± 0.00	1.05 ± 0.02
<b>8</b>	1.01 ± 0.01	0.87 ± 0.01	0.75 ± 0.01

<sup>a</sup>Results were calculated using Equation 1. All results represent an average of at least three trials.

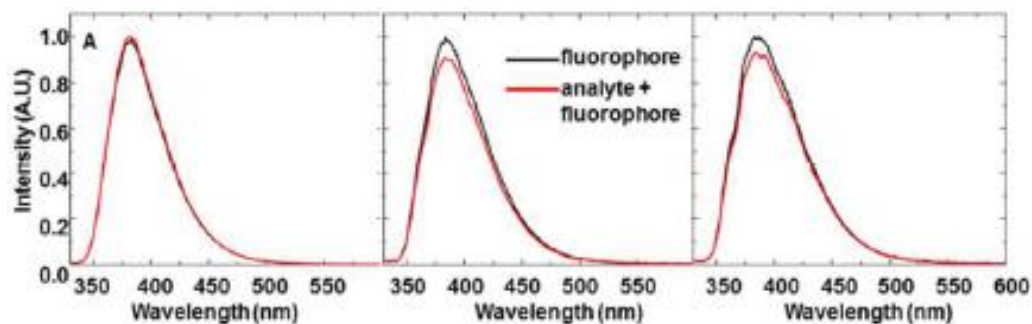


**Figure 5.** Fluorescence emission of (A) sensor **S1**; (B) sensor **S2**; and (C) sensor **S3** in the presence of analyte **8** ( $\lambda_{\text{excitation}} = 320$  nm; 3 nm excitation slit width; 3 nm emission slit width).

The fluorescence signals of sensors **S1-S3** in the presence of analytes **5-8** were subjected to linear discriminant analysis, and enabled 100% selectivity between the different aromatic alcohol isomers (Figure 6). This selectivity is particularly noteworthy as such isomers are challenging to separate using other analytical techniques.<sup>23</sup> The binding of other structural isomers and analogues in supramolecular hosts **S1-S3** also led to analyte-specific changes in the fluorescence emission (Table 3), with selected results highlighted in Figures 7-10.

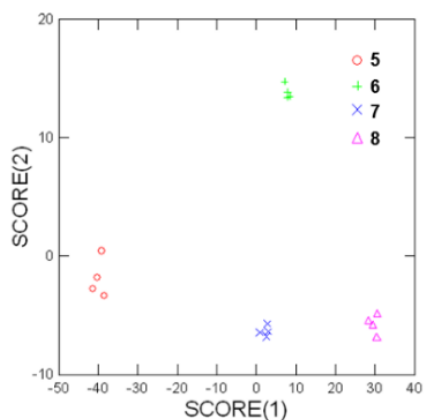


**Figure 6.** Linear discriminant analysis showing 100% differentiation between analytes **5-8** based on their interactions with supramolecular hosts **S1-S3**.

Analytes **9-12** represent a class of aliphatic alcohols consisting of cyclohexylmethanol (**11**) and its isomers. These compounds are widely used as alkene precursors,<sup>24</sup> and a

structurally similar analogue was part of a recent chemical spill.<sup>25</sup> While all the analytes are structural isomers, analytes **10** and **12** are also stereoisomers. Distinct fluorescence modulation values are noted for sensor **S3** in combination with stereoisomers **10** and **12**, highlighting the power of the cyclodextrin-based sensor in differentiating even small structural changes. Overall, the use of sensors **S1-S3** in combination with these analytes enabled 100% differentiation using linear discriminant analysis (Figure 7).

**Table 3.** Fluorescence modulation of sensors **S1-S3** in the presence of analytes **9-26**<sup>a</sup>

Analyte	S1	S2	S3
<b>9</b>	1.01 ± 0.00	0.89 ± 0.00	1.07 ± 0.05
<b>10</b>	1.01 ± 0.00	0.90 ± 0.00	0.97 ± 0.01
<b>11</b>	1.01 ± 0.00	0.99 ± 0.03	0.77 ± 0.06
<b>12</b>	0.99 ± 0.00	0.89 ± 0.00	1.14 ± 0.01
<b>13</b>	1.00 ± 0.00	0.93 ± 0.01	1.33 ± 0.03
<b>14</b>	1.01 ± 0.00	0.95 ± 0.01	1.07 ± 0.04
<b>15</b>	0.98 ± 0.01	1.17 ± 0.01	1.35 ± 0.05
<b>16</b>	0.99 ± 0.01	1.08 ± 0.01	1.04 ± 0.05
<b>17</b>	1.00 ± 0.00	1.01 ± 0.01	0.94 ± 0.02
<b>18</b>	1.05 ± 0.00	1.06 ± 0.00	0.93 ± 0.02
<b>19</b>	0.98 ± 0.00	1.09 ± 0.01	0.95 ± 0.02
<b>20</b>	1.00 ± 0.00	0.99 ± 0.01	1.01 ± 0.01
<b>21</b>	1.03 ± 0.01	1.03 ± 0.02	0.89 ± 0.01
<b>22</b>	1.03 ± 0.00	1.06 ± 0.06	0.85 ± 0.01
<b>23</b>	1.01 ± 0.01	1.02 ± 0.04	0.98 ± 0.03
<b>24</b>	1.01 ± 0.00	1.07 ± 0.04	0.89 ± 0.02
<b>25</b>	1.05 ± 0.00	0.56 ± 0.01	0.98 ± 0.01
<b>26</b>	1.00 ± 0.01	0.92 ± 0.03	1.14 ± 0.02

<sup>a</sup>Fluorescence modulation results were calculated using Equation 1. All results represent an average of at least three trials.

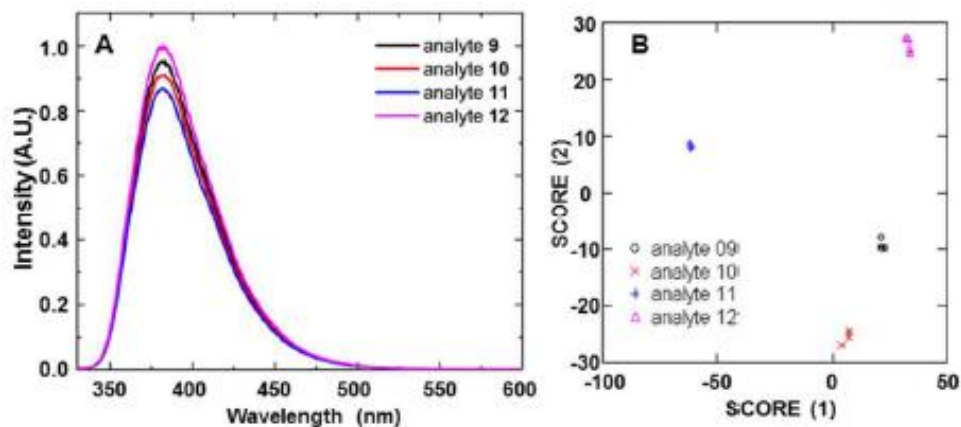


**Figure 7.** (A) Fluorescence response of host **S1** in the presence of analytes **9-12**; (B) Linear discriminant analysis of the fluorescence responses, leading to 100% differentiation of the analyte signals ( $\lambda_{\text{excitation}} = 320 \text{ nm}$ ; 3 nm excitation slit width; 3 nm emission slit width).

Analytes **13-16** represents aromatic pesticide *p,p*-DDT (compound **15**), its known metabolites DDE (compound **13**) and DDD (compound **14**),<sup>26</sup> and its co-occurring structural isomer *o,p*-DDT (compound **16**).<sup>27</sup> These compounds are suspected carcinogens<sup>28</sup> and toxicants,<sup>29</sup> and are important targets for detection. Despite the structural similarity between the analytes, 100% accurate classification was achieved (Figure 8). Interestingly, although sensor **S3** demonstrated nearly identical fluorescence modulation values in response to analytes **13** and **15**, sensor **S2** was able to clearly differentiate between those two analytes. These results illustrate that altering the degree of functionalization of the sensor can alter its response.

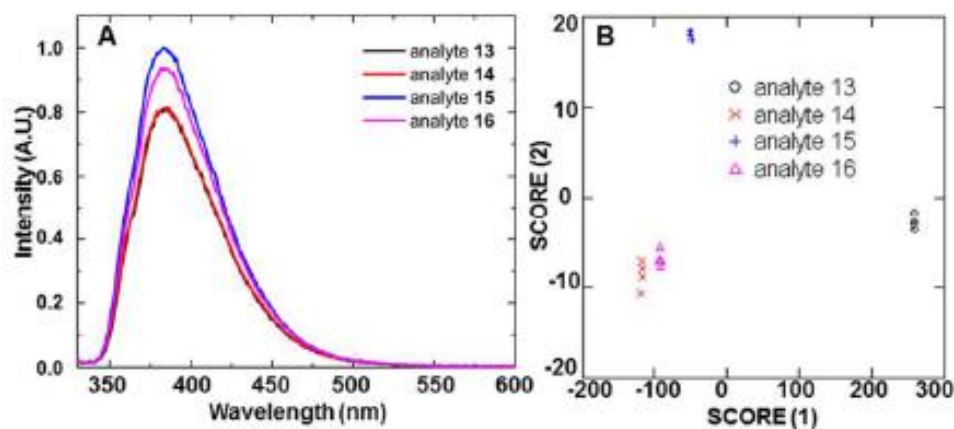


**Figure 8.** (A) Fluorescence response of host **S2** in the presence of analytes **13-16**; (B) Linear discriminant analysis of the fluorescence responses, leading to 100% differentiation of the analyte signals ( $\lambda_{\text{excitation}} = 320 \text{ nm}$ ; 3 nm excitation slit width; 3 nm emission slit width).

Analytes **17-21** represent aliphatic *n*-hexane (compound **17**), its commonly occurring structural isomers (compounds **18-20**, generated in 10-30% yield from industrial production of hexane)<sup>30</sup> and its cyclopentane analogue (compound **21**). The fact that hexanes co-occur as isomeric mixtures complicates a variety of applications that require accurate characterization.<sup>31</sup> Using this supramolecular sensing strategy, 100% accurate classification between these analytes is achieved (Figure 9).

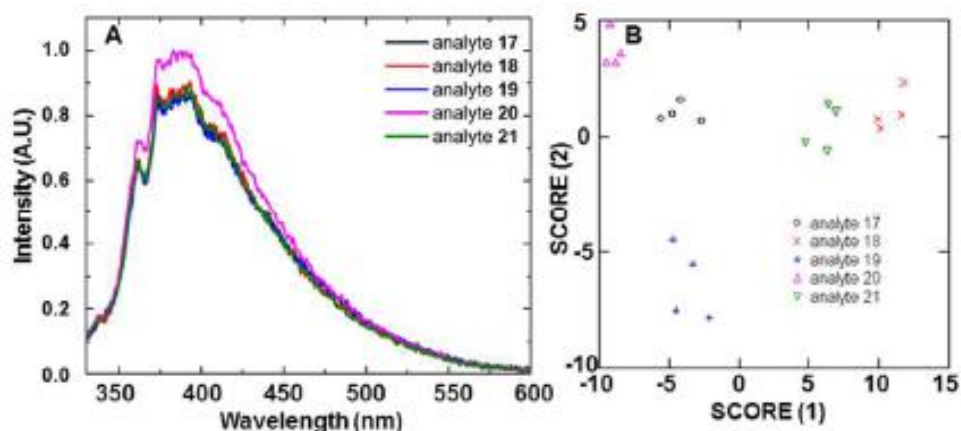


**Figure 9.** (A) Fluorescence response of host **S3** in the presence of analytes **17-21**; (B) Linear discriminant analysis of the fluorescence responses, leading to 100% differentiation of the analyte signals ( $\lambda_{\text{excitation}} = 320 \text{ nm}$ ; 3 nm excitation slit width; 3 nm emission slit width).

Analytes **22-26** represent polychlorinated biphenyls (PCBs), a class of POPs that cause neurotoxicity<sup>32</sup> and endocrine disruption.<sup>33</sup> As a result of these effects, the use of PCBs has been banned in many countries; however, their environmental persistence means that significant amounts of PCBs are still found in the environment.<sup>34</sup> 100% accurate classification has been achieved for these analytes (Figure 10), which is particularly crucial because these analytes have widely disparate toxicities.

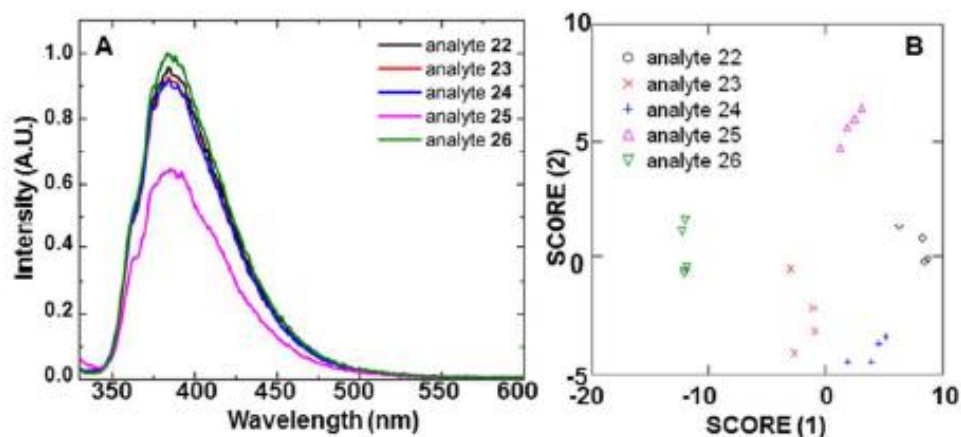


**Figure 10.** (A) Fluorescence response of host **S2** in the presence of analytes **22-26**; (B) Linear discriminant analysis of the fluorescence responses, leading to 100% differentiation of the analyte signals ( $\lambda_{\text{excitation}} = 320 \text{ nm}$ ; 3 nm excitation slit width; 3 nm emission slit width).

The ability of this detection method to generate well-separated signals was further investigated by generating an array with all analytes from all classes. In this case, the array exhibited well-separated clusters based on compound class, as well as excellent separation within each class. Overall, 100% accurate identification was obtained (see ESI for more details).

The limits of detection for each sensor **S1**, **S2** and **S3** for each class of analytes were calculated, to determine their ability to sense analytes at environmental levels of concern and at levels that induce toxicity. In every case, the calculated limits of detection were

at or below the literature reported limits of concern (Table 4), highlighting the sensitivity of this method.

**Table 4.** Calculated limits of detection and comparisons to known levels of concern.

Analytes	Sensors	LOD calculated ( $\mu\text{M}$ )	Limit of concern ( $\mu\text{M}$ )
<b>5</b>	<b>S2</b>	$7.1 \pm 0.9$	<i>a</i>
<b>6</b>	<b>S1</b>	$5.5 \pm 0.2$	$21.27^{35}$
<b>6</b>	<b>S3</b>	$7.3 \pm 0.5$	$21.27^{35}$
<b>11</b>	<b>S1</b>	$1.2 \pm 0.01$	<i>a</i>
<b>11</b>	<b>S2</b>	$1.4 \pm 0.1$	<i>a</i>
<b>15</b>	<b>S1</b>	$0.43 \pm 0.04$	$2.82^{36}$
<b>15</b>	<b>S2</b>	$0.48 \pm 0.05$	$2.82^{36}$
<b>15</b>	<b>S3</b>	$2.1 \pm 0.03$	$2.82^{36}$
<b>18</b>	<b>S1</b>	$2.1 \pm 0.2$	$5801.81^{37}$
<b>19</b>	<b>S2</b>	$21.1 \pm 1.4$	$5801.81^{38}$
<b>21</b>	<b>S3</b>	$8.4 \pm 0.6$	<i>a</i>
<b>22</b>	<b>S3</b>	$5.2 \pm 0.2$	$1.00^{38}$
<b>25</b>	<b>S1</b>	$0.30 \pm 0.01$	$1.71^{39}$
<b>26</b>	<b>S2</b>	$0.17 \pm 0.01$	$1.00^{38}$

<sup>a</sup>Limits of concern have not been established for these compounds

Practical applications of this system require the capability to identify analyte mixtures, because environmental contamination scenarios almost always involve such mixtures. To that end, preliminary work focused on identification of 1:1 binary mixtures of aromatic alcohol analytes **5-8**. Using the supramolecular sensors combined with linear discriminant analytical techniques, 83% accurate identification of the 1:1 binary mixtures was obtained (Figure 11). Interestingly, the mixture of analytes **5 + 7** is grouped near the mixtures of analytes **6 + 8** and **5 + 8**, which reduces the overall classification accuracy slightly. This kind of co-clustering of analyte groups has been observed previously, and can be attributed to similar sensor responses originating from competing interactions between each component of the mixture. Other than those

combinations, the mixtures demonstrated excellent signal separation and accurate identification. Current work in our group is focused on improving classification accuracy of analyte mixtures, expanding such techniques to multiple analyte classes, and moving from binary mixtures to ternary and even quaternary mixtures of analytes.

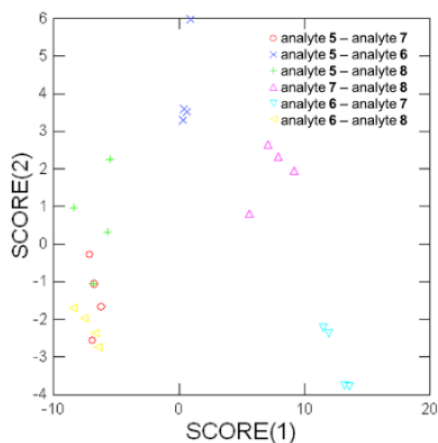


**Figure 11.** Linear discriminant analysis results of binary mixtures of analytes **5-8**.

## CONCLUSIONS

In conclusion, we have developed an efficient array-based detection strategy for isomeric and analogous analytes. The array employs three architecturally unique perbenzylated  $\beta$ -cyclodextrin-fluorophore sensors for identification of a particular isomer within a class of isomeric or structurally similar analytes. The binding of analytes to the cyclodextrin induces a distinct change in the fluorescence emission of the attached fluorophores, which is then statistically translated into array clusters of maximum separation via linear discriminant analysis. We demonstrate 100% successful classification of three isomeric (aromatic alcohols, aliphatic alcohols, aliphatic hexanes) and two analogous (DDT pesticides, PCB congeners) analyte classes. Sensitivity measurements highlight limits of detection at or near literature-reported levels of



concern. Preliminary attempts on binary mixtures demonstrated fairly selective levels of classification with 83% accuracy. This method in tandem with chromatographic analysis of complex isomeric mixtures would complement each other in determining the nature of each isomer. Current work in our laboratory is focused on expanding the classes of analytes detectable via this system, improving analyte mixture identification, and developing a practical cyclodextrin-based detection device. The results of these and other investigations will be reported in due course.

#### NOTES AND REFERENCES

1. Willett, K. L.; Ulrich, E. M.; Hites, R. A. *Environ. Sci. Technol.* **1998**, *32*, 2197-2207.
2. Rodriguez, I.; Fraga, M.; Alfonso, A.; Guillebault, D.; Medlin, L.; Baudart, J.; Jacob, P.; Helmi, K.; Meyer, T.; Breitenbach, U.; Holden, N. M.; Boots, B.; Spurio, R.; Cimarelli, L.; Mancini, L.; Marcheggiani, S.; Albay, M.; Akcaalan, R.; Koeker, L.; Botana, L. M. *Environ. Toxicol. Chem.* **2017**, *36*, 645-654.
3. Bergknut, M.; Kucera, A.; Frech, K.; Andersson, E.; Engwall, M.; Rannug, U.; Koci, V.; Andersson, P. L.; Haglund, P.; Tysklind, M. *Environ. Toxicol. Chem.* **2007**, *26*, 208-217.
4. Shafique, U.; Schulze, S.; Slawik, C.; Kunz, S.; Paschke, A.; Schueuermann, G. *Anal. Chim. Acta* **2017**, *949*, 8-22.
5. Rager, J. E.; Strynar, M. J.; Liang, S.; McMahan, R. L.; Richard, A. M.; Grulke, C. M.; Wambaugh, J. F.; Isaacs, K. K.; Judson, R.; Williams, A. J.; Sobus, J. R. *Environ. Int.* **2016**, *88*, 269-280.
6. (a) Miranda, O. R.; Creran, B.; Rotello, V. M. *Curr. Opinion Chem. Biol.* **2010**, *14*, 728-736. (b) Diehl, K. L.; Anslyn, E. V. *Chem. Soc. Rev.* **2013**, *42*, 8596-8611.
7. (a) Xu, X.; Liu, Z.; Zhang, X.; Duan, S.; Xu, S.; Zhou, C. *Electrochim. Acta* **2011**, *58*, 142-149. (b) Chen, X.; Cheng, X.; Gooding, J. J. *Anal. Chem.* **2012**, *84*, 8557-8563.
8. Hussain, S.; Malik, A. H.; Iyer, P. K. *J. Mater. Chem. B* **2016**, *4*, 4439-4446.
9. Prasad, B. B.; Pandey, I. *Sensors Actuators B: Chem.*, **2013**, *181*, 596-604.

10. Zhang, J.; Zhang, X.; Chen, J.; Deng, C.; Xu, N.; Shi, W.; Cheng, P. *Inorg. Chem. Commun.* **2016**, *69*, 1-3.
11. (a) Hatanaka, S.; Ono, T.; Hisaeda, Y. *Chem. Eur. J.* **2016**, *22*, 10346-10350. (b) Mukherjee, S.; Desai, A. V.; Inamdar, A. I.; Manna, B.; Ghosh, S. K. *Crystal Growth Design* **2015**, *15*, 3493-3497. (c) Gole, B.; Song, W.; Lackinger, M.; Mukherjee, P. S. *Chem. Eur. J.* **2014**, *20*, 13662-13680.
12. Cohen Hubal, E. A.; Richard, A.; Aylward, L.; Edwards, S.; Gallagher, J.; Goldsmith, M. -R.; Isukapalli, S.; Tornero-Velez, R.; Weber, E.; Kavlock, R. J. *Toxicol. Environ. Health* **2010**, *13*, 299-313.
13. Gensburg, L. J.; Pantea, C.; Kielb, C.; Fitzgerald, E.; Stark, A.; Kim, N. *Environ. Health Perspectives* **2009**, *117*, 1265-1271.
14. Megson, D.; Reiner, E. J.; Jobst, K. J.; Dorman, F. L.; Robson, M.; Focant, J. -F. *Anal. Chim. Acta* **2016**, *941*, 10-25.
15. (a) DiScenza, D. J.; Levine, M. *New J. Chem.* **2016**, *40*, 789-793. (b) Serio, N.; Moyano, D. F.; Rotello, V. M.; Levine, M. *Chem. Commun.* **2015**, *51*, 11615-11618. (c) Serio, N.; Miller, K.; Levine, M. *Chem. Commun.* **2013**, *49*, 4821-4823.
16. Higashi, K.; Ideura, S.; Waraya, H.; Limwikrant, W.; Moribe, K.; Yamamoto, K. *Chem. Pharmaceutical Bull.* **2010**, *58*, 769-772.
17. Bjerre, J.; Fenger, T. H.; Marinescu, L. G.; Bols, M. *Eur. J. Org. Chem.* **2007**, 704-710.
18. Lecourt, T.; Herault, A.; Pearce, J.; Sollogoub, M.; Sinaÿ, P. *Chem. Eur. J.* **2004**, *10*, 2960-2971.
19. Choi, B. S.; Choi, J.; Bak, S.; Koo, S. *Eur. J. Org. Chem.* **2015**, 514-524.
20. Huo, C.; Chambron, J. -C.; Meyer, M. *New J. Chem.* **2008**, *32*, 1536-1542.
21. Meindersma, G. W.; van Schoonhoven, T.; Kuzmanovic, B.; de Haan, A. B. *Chem. Engin. Processing* **2006**, *45*, 175-183.
22. Dsouza, R. N.; Pischel, U.; Nau, W. M. *Chem. Rev.* **2011**, *111*, 7941-7980.
23. Peng, J.; Zhang, Y.; Yang, X.; Qi, M. *J. Chromatography A* **2016**, *1466*, 148-154.
24. Cawley, J. J.; Lindner, P. E. *J. Chem. Educ.*, 1997, **74**, 102-104.
25. Whelton, A. J.; McMillan, L.; Connell, M.; Kelley, K. M.; Gill, J. P.; White, K. D.; Gupta, R.; Dey, R.; Novy, C. *Environ. Sci. Technol.* **2015**, *49*, 813-823.

26. Ricking, M.; Schwarzbauer, J. *Environ. Chem. Lett.* **2012**, *10*, 317-323.
27. Arrebola, J. P.; Cuellar, M.; Bonde, J. P.; Gonzalez-Alzaga, B.; Mercado, L. A. *Environ. Res.* **2016**, *151*, 469-477.
28. Soto, A. M.; Chung, K. L.; Sonnenschein, C. *Environ. Health Perspectives*, **1994**, *102*, 380-383.
29. Mansouri, A.; Cregut, M.; Abbes, C.; Durand, M. -J.; Landoulsi, A.; Thouand, G. *Appl. Biochem. Biotechnol.* **2017**, *181*, 309-339.
30. Myers, R. A. *Handbook of Petroleum Refining Process*, McGraw-Hill, New York, **2004**; Clavier, R. *Wiley Critical Content: Petroleum Technology*, Wiley-Interscience, Hoboken, New Jersey, **2007**.
31. Hayati, R.; Abghari, S. Z.; Sadighi, S.; Bayat, M. *Korean J. Chem. Engineering*, **2015**, *32*, 629-635.
32. Winneke, G. *J. Neurological Sci.* **2011**, *308*, 9-15.
33. Grzeskowiak, T.; Czarczynska-Goslinska, B.; Zgola-Grzeskowiak, A. *TrAC, Trends Anal. Chem.* **2016**, *75*, 209-226.
34. Shifrin, N. S.; Toole, A. P. *Environ. Engineering Sci.* **1998**, *15*, 247-257.
35. Center for Disease Control and Prevention. The National Institute for Occupational Safety and Health (NIOSH): Cresols (o, m, p isomers) <https://www.cdc.gov/niosh/idlh/cresol.html> (accessed Dec 20, 2016).
36. Center for Disease Control and Prevention. The National Institute for Occupational Safety and Health (NIOSH): DDT <https://www.cdc.gov/niosh/idlh/50293.html> (accessed Dec 20, 2016).
37. Center for Disease Control and Prevention. The National Institute for Occupational Safety and Health (NIOSH): 2-methylpentane. <https://www.cdc.gov/niosh/ipcsneng/neng1262.html> (accessed Dec 20, 2016).
38. Center for Disease Control and Prevention. The National Institute for Occupational Safety and Health (NIOSH): 3-methylpentane. <https://www.cdc.gov/niosh/ipcsneng/neng1263.html> (accessed Dec 20, 2016).
39. Center for Disease Control and Prevention. The National Institute for Occupational Safety and Health (NIOSH): Polychlorinated Biphenyls (PCB's). <https://www.cdc.gov/niosh/docs/86-111/default.html> (accessed Dec 20, 2016).

*Supporting Information*

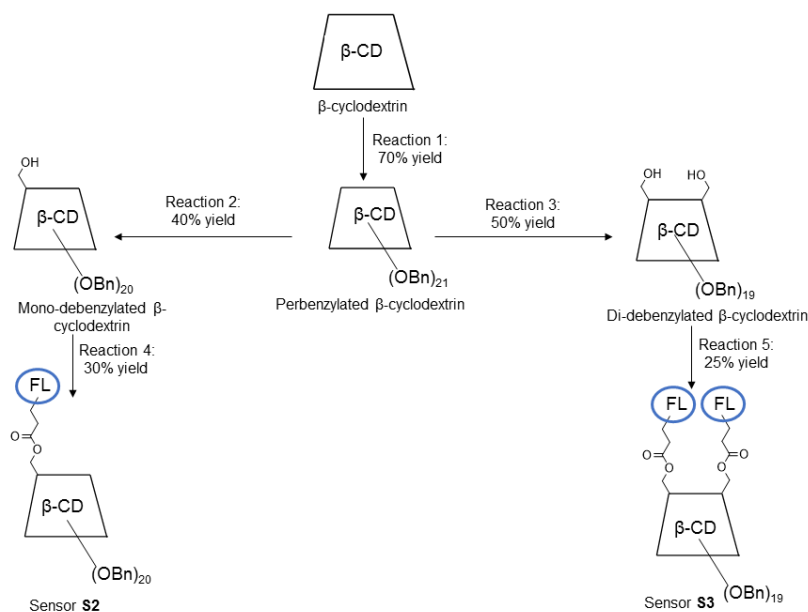
**Array-based detection of isomeric and analogous analytes employing synthetically modified fluorophore attached  $\beta$ -cyclodextrin derivatives**

**MATERIALS AND METHODS**

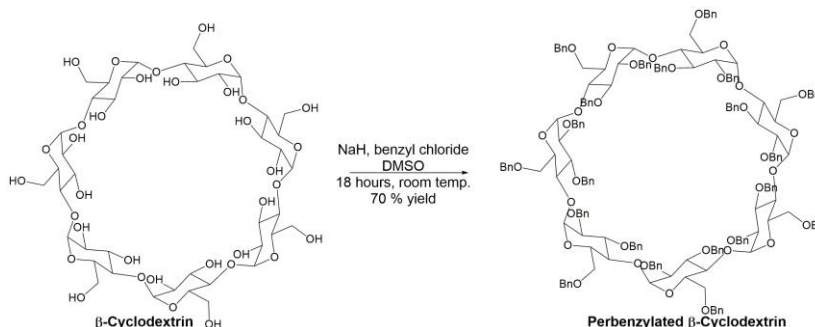
All of the reagents were obtained from Sigma Aldrich or Fisher Scientific and used without further purification, unless otherwise noted.  $\beta$ -cyclodextrin was dried in the oven prior to use. Reagent grade solvents (99.9% purity) were used for the synthetic reactions. Column chromatography was performed in a Yamazen AKROS-Automatic TLC Smart Flash Chromatography System.  $^1\text{H}$  and  $^{13}\text{C}$ -NMR spectra were recorded in a 400 MHz Bruker AVANCE and 500 MHz Varian NMR spectrometer, with assistance from Dr. Al Bach. Mass spectra were recorded in a Bruker Omnix MALDI-TOF instrument with 2,5-dihydroxybenzoic acid as a matrix at the Department of Chemistry Instrumentation Facility (DCIF) at the Massachusetts Institute of Technology (MIT), with samples run by Dr. Li Li. All of the fluorescence measurements were performed using a Shimadzu RF 5301 spectrophotometer. Both the excitation and emission slit widths were 3 nm. All of the fluorescence spectra were integrated vs. wavenumber on the X-axis using Origin Pro Version 9.1 software. All arrays were generated using SYSTAT Version 13.

## DETAILED SYNTHETIC PROCEDURES

### Overall Synthetic Scheme:



### Reaction 1: Synthesis of Perbenzylated $\beta$ -Cyclodextrin

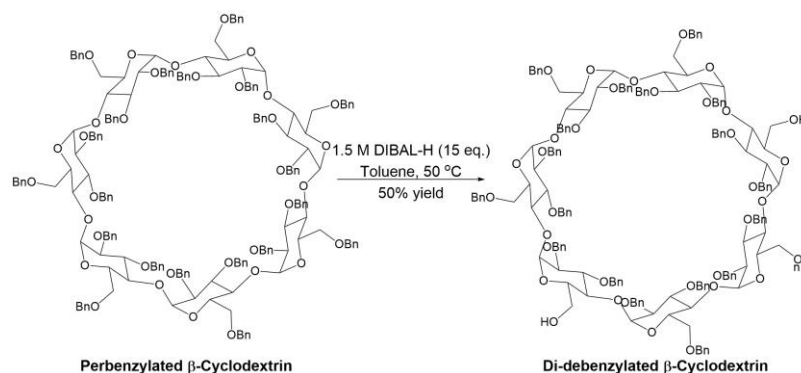


To a stirred solution of oven-dried  $\beta$ -cyclodextrin (2.00 g, 1.76 mmol, 1.0 eq.) in DMSO (100 mL) under nitrogen, sodium hydride (2.60 g, 65 mmol, 36 eq.) was added carefully. The solution was allowed to stir for one hour at room temperature, after which time benzyl chloride (18.5 mL, 65 mmol, 36 eq.) was added over the course of one hour. The reaction mixture was stirred for 18 hours at room temperature, followed by the addition of methanol (20 mL). The reaction mixture was then diluted with water (200 mL) and extracted with diethyl ether (3 x 200 mL). The combined organic layers were washed



addition of 10% aqueous HCl (15 mL) for 15 minutes. The crude product was extracted with ethyl acetate (100 mL), treated with anhydrous Na<sub>2</sub>SO<sub>4</sub> and dried under reduced pressure. Purification via column chromatography (1:3 ethyl acetate/hexane gradient elution) led to a white compound, mono-debenzylated β-cyclodextrin (250 mg, 40 % yield). <sup>1</sup>H-NMR (400 MHz, CDCl<sub>3</sub>): δ = 2.48 (br s, 1 H; OH), 3.34-4.07 (m, 42 H; 7x2-H, 7x3-H, 7x4-H, 7x5-H, 14x6-H), 4.27-4.51 (m, 24H; CH<sub>2</sub>Ph), 4.60-4.75 (m, 10H; CH<sub>2</sub>Ph), 4.88-5.01 (m, 6H; 6x1-H), 5.08-5.18 (m, 4 H; CH<sub>2</sub>Ph), 5.25 (dd, <sup>3</sup>J<sub>1,2</sub> = 12.0, 4.0 Hz, 2 H; CH<sub>2</sub>Ph), 5.36 (d, <sup>3</sup>J<sub>1,2</sub> = 4.0 Hz, 1 H; 1x1-H), 7.04-7.30 (m, 100 H; aromatic-H) ppm; <sup>13</sup>C-NMR (100 MHz, CDCl<sub>3</sub>): δ = 61.6, 68.8, 69.2, 69.3, 69.4, 71.4, 71.5, 71.6, 71.7, 71.7, 71.8, 71.9, 72.5, 72.6, 72.7, 72.7, 72.9, 73.0, 73.3, 73.4, 73.4, 74.8, 75.0, 75.1, 75.3, 75.8, 75.9, 75.9, 76.0, 77.4, 77.7, 78.1, 78.8, 79.0, 79.1, 79.5, 79.6, 79.9, 80.1, 80.9, 81.0, 81.0, 81.1, 98.0, 98.3, 98.4, 98.4, 98.6, 98.8, 98.9, 127.0-128.4, 137.9, 138.1, 138.2, 138.2, 138.2, 138.3, 138.3, 138.4, 138.5, 138.5, 139.0, 139.1, 139.3, 139.3, 139.4, 139.4 ppm; MS (MALDI-TOF): m/z = 2960.29 [M+Na]<sup>+</sup> (Calculated for C<sub>182</sub>H<sub>190</sub>O<sub>35</sub> + Na = 2960.43).

### Reaction 3: Synthesis of Di-debenzylated β-cyclodextrin:

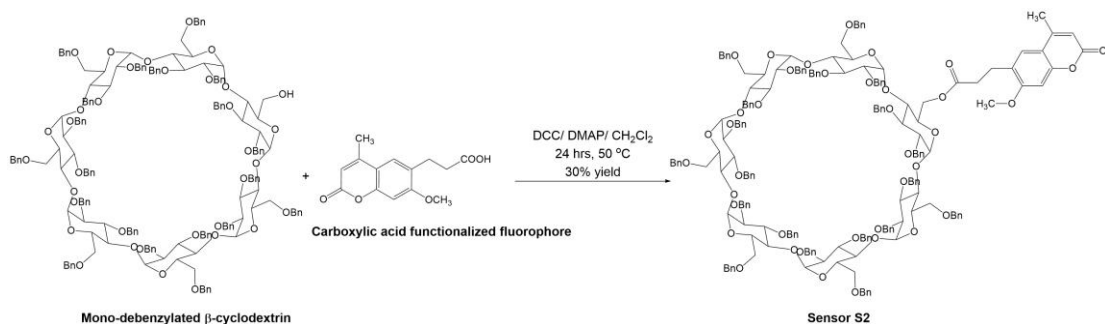


To a stirred solution of perbenzylated β-cyclodextrin (1.2 g, 0.4 mmol, 1.0 eq.) under nitrogen, DIBAL-H (4.0 mL, 6.0 mmol, 15 eq.) was added dropwise. The reaction

mixture was stirred for 6 hours at 50 °C until a complete disappearance of starting material was observed via TLC analysis. After an additional 15 minutes of stirring, the reaction mixture was cooled to 0 °C and hydrolyzed by vigorously stirring with 10 % aqueous HCl (15 mL) for 20 minutes. The crude product was extracted with ethyl acetate (100 mL), treated with anhydrous Na<sub>2</sub>SO<sub>4</sub> and dried under reduced pressure. Purification via column chromatography (1:3 ethyl acetate/hexanes) led to a white compound di-debenzylated β-cyclodextrin (566 mg, 50 % yield). <sup>1</sup>H-NMR (400 MHz, CDCl<sub>3</sub>): δ = 2.69 (br s, 1 H ; OH), 2.78 (br s, 1 H ; OH), 3.44-3.54 (m, 5 H ; 5x2-H), 3.60-4.15 (m, 37 H ; 2x2-H, 7x3-H, 7x4-H, 7x5-H, 14x6-H), 4.44-4.88 (m, 33 H ; CH<sub>2</sub>Ph), 4.89 (d, <sup>3</sup>J<sub>1,2</sub> = 3.3 Hz, 1 H ; 1-H), 4.98 (d, <sup>3</sup>J<sub>1,2</sub> = 3.7 Hz, 1H ; 1-H), 5.00 (d, <sup>3</sup>J<sub>1,2</sub> = 4.0 Hz, 1 H ; 1-H), 5.02 (d, <sup>3</sup>J<sub>1,2</sub> = 3.4 Hz, 1 H ; 1-H), 5.04 (d, <sup>3</sup>J<sub>1,2</sub> = 3.5 Hz, 1 H ; 1-H), 5.06 (d, <sup>2</sup>J = 12.3 Hz, 1 H ; CH<sub>2</sub>Ph), 5.21-5.25 (m, 3 H ; 3xCH<sub>2</sub>Ph), 5.30 (d, <sup>2</sup>J = 10.7 Hz, 1 H ; CH<sub>2</sub>Ph), 5.56 (d, <sup>3</sup>J<sub>1,2</sub> = 3.8 Hz, 1 H ; 1-H), 5.67 (d, <sup>3</sup>J<sub>1,2</sub> = 3.7 Hz, 1 H ; 1-H), 7.12-7.33 (m, 95H ; aromatic-H) ppm; <sup>13</sup>C-NMR (100 MHz, CDCl<sub>3</sub>): δ = 61.6, 69.5, 69.6, 71.2, 71.6, 72.0, 72.1, 72.9, 73.2, 73.25, 73.3, 73.9, 74.1, 76.1, 76.4, 77.6, 79.0, 79.7, 80.6, 80.9, 81.0, 81.6, 81.7, 97.6, 97.7, 98.2, 126.3-128.3, 137.7, 137.8, 137.9, 138.2, 138.6, 137.7, 139.2 ppm; MS (MALDI-TOF): m/z = 2870.1 [M+Na]<sup>+</sup> (Calculated for C<sub>175</sub>H<sub>184</sub>O<sub>35</sub> + Na = 2870.31).



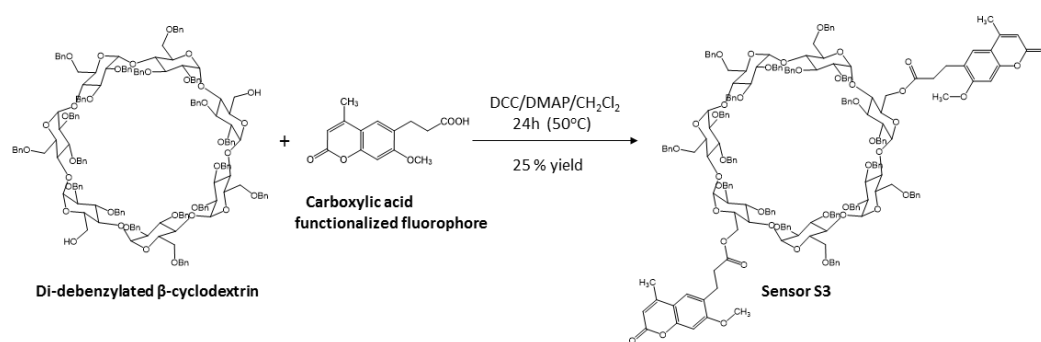
#### Reaction 4: Synthesis of sensor S2:



A mixture of mono-debenzylated  $\beta$ -cyclodextrin (100 mg, 0.034 mmol, 1.0 eq.), carboxylic acid functionalized fluorophore (10.5 mg, 0.04 mmol, 1.17 eq.), *N,N'*-dicyclohexylcarbodiimide (DCC) (8.3 mg, 0.04 mmol, 1.17 eq.) and 4-dimethylaminopyridine (DMAP) (0.5 mg, 0.004 mmol, 0.1 eq.) in dichloromethane (1 mL) was stirred at 50 °C for 24 hrs. The mixture was filtered, treated with 5% aqueous acetic acid (2 x 3 mL) and extracted with dichloromethane (2 x 4 mL). The combined organic layer was dried under anhydrous  $\text{Na}_2\text{SO}_4$  and subjected to solvent removal under reduced pressure. The crude product was purified via column chromatography (1:3 ethyl acetate/hexanes) to yield a white amorphous compound sensor **S2** (32 mg, 30% yield).  $^1\text{H-NMR}$  (500 MHz, acetone- $d_6$ ):  $\delta$  = 2.31 (s, 3 H;  $\text{ArCH}_3$ ), 2.62 (m, 2 H;  $\text{CH}_2\text{FL3}$ ), 2.93 (t,  $^3J_{1,2} = ^3J_{1,2'} = 10.0$  Hz, 2 H;  $\text{CH}_2\text{CHFL3}$ ), 3.43-3.50 (m, 7 H; 2-H), 3.62-3.74 (m, 7 H; 6-H), 3.84 (br t, 2 H; 6-H), 3.89 (s, 3 H;  $\text{OCH}_3$ ), 3.92-4.16 (m, 26 H; 3-H, 4-H, 5-H, 6-H), 4.40-4.62 (m, 26 H;  $\text{CH}_2\text{Ph}$ ), 4.75-4.78 (m, 7 H;  $\text{CH}_2\text{Ph}$ ), 5.09-5.13 (m, 7 H;  $\text{CH}_2\text{Ph}$ ), 5.16 (d,  $^3J_{1,2} = 3.5$  Hz, 1 H; 1-H), 5.27 (dd,  $^3J_{1,2} = 10, 3.5$  Hz, 2 H; 1-H), 5.30 (m, 3 H; 1-H), 5.33 (d,  $^3J_{1,2} = 3.5$  Hz, 1 H; 1-H), 6.02 (s, 1 H;  $\text{CH}=\text{CCH}_3$ ), 6.86 (s, 1 H;  $\text{ArH}$ ), 7.12-7.33 (m, 80 H;  $\text{PhH}$ ), 7.48 (s, 1 H;  $\text{ArH}$ ) ppm;  $^{13}\text{C-NMR}$  (125 MHz, acetone- $d_6$ ):  $\delta$  = 17.8, 25.3, 33.6, 55.7, 63.5, 69.5, 69.8, 71.7, 71.9, 72.4, 72.7, 73.0, 75.2, 78.3-79.4, 80.8-81.1, 97.8-98.0, 98.2, 98.7, 98.7, 111.5, 112.8, 124.5, 125.6,

126.8, 127.29-128.25, 138.6, 138.7-138.8, 139.5-139.6, 152.8, 154.3, 160.1, 160.6, 172.0 ppm; MS (MALDI-TOF):  $m/z = 3204.57 [M+Na]^+$  (Calculated for  $C_{196}H_{202}O_{39} + Na = 3204.67$ ).

### Reaction 5: Synthesis of sensor S3:



A mixture of di-debenzylated  $\beta$ -cyclodextrin (100 mg, 0.035 mmol, 1.0 eq.), carboxylic acid functionalized fluorophore (21.0 mg, 0.08 mmol, 2.34 eq.), *N, N'*-dicyclohexylcarbodiimide (16.5 mg, 0.08 mmol, 2.34 eq.) and 4-dimethylaminopyridine (1.1 mg, 0.008 mmol, 0.2 eq.) in dichloromethane (1 mL) was stirred at 50 °C for 24 hrs. The mixture was filtered, treated with 5% aqueous acetic acid (2 x 3 mL) and extracted with dichloromethane (2 x 4 mL). The combined organic layer was dried under anhydrous  $\text{Na}_2\text{SO}_4$  and subjected to solvent removal under reduced pressure. The crude product was purified via column chromatography (1:3 ethyl acetate: hexanes) to lead to a white amorphous compound sensor **S3** (30 mg, 25 % yield).  $^1\text{H-NMR}$  (500 MHz, acetone- $d_6$ ):  $\delta = 2.31$  (s, 6 H;  $\text{ArCH}_3$ ), 2.62 (m, 4 H;  $\text{CHFL}_3$ ), 2.93 (m, 4 H;  $\text{CHCHFL}_3$ ), 3.44-3.51 (m, 7 H; 2-H), 3.62-3.74 (m, 7 H; 6-H), 3.82-3.89 (multiplet overlapped, 4 H; 6-H), 3.89 (singlet overlapped, 6 H;  $\text{OCH}_3$ ), 3.94-4.16 (m, 24 H; 3-H, 4-H, 5-H, 6-H), 4.41-4.64 (m, 26H;  $\text{CH}_2\text{Ph}$ ), 4.74-4.78 (m, 6H;  $\text{CH}_2\text{Ph}$ ), 5.08-5.12 (m, 6H;  $\text{CH}_2\text{Ph}$ ), 5.22 (dd,  $^3J_{1,2} = 8.5, 3.5$  Hz, 2H; 1-H), 5.26 (m, 3 H; 1-H),

5.29 (m, 2 H; 1-H), 6.01 (s, 2 H; CH=CCH<sub>3</sub>), 6.86 (s, 2 H; ArH), 7.06-7.30 (m, 80 H; PhH), 7.46 (d, <sup>3</sup>J<sub>1,2</sub> = 6.5 Hz, 2H; ArH) ppm; <sup>13</sup>C-NMR (125 MHz, acetone-*d*<sub>6</sub>): δ = 17.8, 24.6, 25.2-25.4, 25.6, 25.8, 30.6, 32.1, 33.5, 34.1, 55.7, 63.5, 69.3-69.8, 71.6-73.1, 75.2, 78.3-79.4, 80.7-81.0, 97.9-98.7, 111.5, 112.7, 125.4-125.5, 126.8, 127.3-128.3, 138.6, 138.7-138.8, 139.4-139.6, 152.7, 154.3, 160.0, 160.6, 172.1 ppm; MS (MALDI-TOF): m/z = 3358.82 [M+Na]<sup>+</sup> (Calculated for C<sub>203</sub>H<sub>208</sub>O<sub>43</sub> + Na = 3358.40).

#### DETAILED PROCEDURES FOR FLUORESCENCE MODULATION EXPERIMENTS

Fluorescence emission spectra were obtained using a Shimadzu RF-5301PC spectrofluorimeter with 3 nm excitation and 3 nm emission slit widths. In a quartz cuvette, 0.5 mL of **S1**, **S2**, or **S3** solutions (5 μM in DMSO) and 2 mL of DI water were combined. Then, the solution was excited at 320 nm, and the fluorescence emission spectra were recorded. Repeat measurements were recorded for four separate trials.

The fluorescence emission spectra were integrated vs. wavenumber on the X-axis, and fluorescence modulation was measured by the ratio of integrated emission of the fluorophore in the presence of the analyte to integrated emission of the fluorophore in the absence of the analyte, as shown in Equation S1:

$$\text{Fluorescence Modulation} = Fl_{\text{analyte}} / Fl_{\text{blank}} \quad (\text{Equation S1})$$

Where  $Fl_{\text{analyte}}$  is the integrated fluorescence emission of the fluorophore in the presence of 10 μL of analyte (1 mg/mL in THF), and  $Fl_{\text{blank}}$  is the integrated fluorescence emission of the fluorophore in the absence of the analyte.

## DETAILED PROCEDURES FOR ARRAY GENERATION EXPERIMENTS

Array analysis was performed using SYSTAT 13 statistical computing software with the following settings:

- (a) Classical Discriminant Analysis
- (b) Grouping Variable: Analytes
- (c) Predictors: **S1**, **S2**, and **S3**
- (d) Long-Range Statistics: Mahal

## DETAILED PROCEDURES FOR LIMIT OF DETECTION EXPERIMENTS

The limit of detection (LOD) is defined as the lowest concentration of analyte at which a signal can be detected. To determine this value, the following steps were performed for each cyclodextrin-analyte combination. In a quartz cuvette, 0.5 mL of **S1**, **S2**, or **S3** solutions (5  $\mu\text{M}$  in DMSO) and 2 mL of deionized (DI) water were combined. Then, the solution was excited at 320 nm, and the fluorescence emission spectra were recorded starting at 330 nm. Six repeat measurements were taken.

Next, 2  $\mu\text{L}$  of analyte (1 mg/mL in THF) was added, and again the solution was excited at the fluorophore's excitation wavelength, and the fluorescence emission spectra were recorded. Six repeat measurements were taken. This step was repeated for 4  $\mu\text{L}$  of analyte, 6  $\mu\text{L}$  of analyte, 8  $\mu\text{L}$  of analyte, 10  $\mu\text{L}$  of analyte, 12  $\mu\text{L}$  of analyte, 14  $\mu\text{L}$  of analyte, 16  $\mu\text{L}$  of analyte, 18  $\mu\text{L}$  of analyte, 20  $\mu\text{L}$  of analyte.

All of the fluorescence emission spectra were integrated vs. wavenumber on the X-axis, and calibration curves were generated. The curves plotted the analyte concentration in  $\mu\text{M}$  on the X-axis, and the fluorescence modulation ratio on the Y-axis. The curve was fitted to a straight line and the equation of the line was determined.

The limit of detection is defined according to Equation S2:

$$\text{LOD} = 3(\text{SD}_{\text{blank}})/m \quad (\text{Equation S2})$$

Where  $\text{SD}_{\text{blank}}$  is the standard deviation of the blank sample and  $m$  is the slope of the calibration curve. In cases where the slope of the trendline was negative, the absolute value of the slope was used to calculate the LOD. In all cases, the LOD was calculated in  $\mu\text{M}$ .

#### DETAILED PROCEDURES FOR THE HPLC ANALYSIS OF **S2** AND **S3**

The HPLC analysis of the cyclodextrin-fluorophore covalent hosts was performed on a Waters Acquity<sup>®</sup> Arc<sup>™</sup> system using a Waters 2998 Photo Diode Array (PDA) detector and a Cortecs<sup>®</sup> C18 2.7 $\mu\text{m}$  4.6x50 mm column. The solvent system was an isocratic solution of 0.1% formic acid in acetonitrile, run at a rate of 1mL/minute for 5 minutes. All samples were prepared in the same solution of 0.1% formic acid in acetonitrile. The PDA detector was set to collect from 210-400 nm.

SUMMARY TABLES

FLUORESCENCE MODULATION SUMMARY TABLES

Analyte	S1	S2	S3
benzyl alcohol	1.00 ± 0.00	1.04 ± 0.01	0.98 ± 0.01
<i>o</i> -cresol	1.01 ± 0.00	0.82 ± 0.01	0.88 ± 0.01
<i>m</i> -cresol	0.99 ± 0.00	0.90 ± 0.00	1.05 ± 0.02
<i>p</i> -cresol	1.01 ± 0.01	0.87 ± 0.01	0.75 ± 0.01

Analyte	S1	S2	S3
1-methylcyclohexanol	1.01 ± 0.00	0.89 ± 0.00	1.07 ± 0.05
<i>cis</i> -2-methylcyclohexanol	1.01 ± 0.00	0.90 ± 0.00	0.97 ± 0.01
cyclohexylmethanol	1.01 ± 0.00	0.99 ± 0.03	0.77 ± 0.06
<i>trans</i> -2-methylcyclohexanol	0.99 ± 0.00	0.89 ± 0.00	1.14 ± 0.01

Analyte	S1	S2	S3
DDD	1.00 ± 0.00	0.93 ± 0.01	1.33 ± 0.03
DDE	1.01 ± 0.00	0.95 ± 0.01	1.07 ± 0.04
<i>o,p</i> -DDT	0.99 ± 0.01	1.08 ± 0.01	1.04 ± 0.05
<i>p,p</i> -DDT	0.98 ± 0.01	1.17 ± 0.01	1.35 ± 0.05

Analyte	S1	S2	S3
<i>n</i> -hexanes	1.00 ± 0.00	1.01 ± 0.01	0.94 ± 0.02
2-methylpentane	1.05 ± 0.00	1.06 ± 0.00	0.93 ± 0.02
3-methylpentane	0.98 ± 0.00	1.09 ± 0.01	0.95 ± 0.02
2,3-dimethylbutane	1.00 ± 0.00	0.99 ± 0.01	1.01 ± 0.01
1-methylcyclopentane	1.03 ± 0.01	1.03 ± 0.02	0.89 ± 0.01

Analyte	S1	S2	S3
PCB3	1.03 ± 0.00	1.06 ± 0.06	0.85 ± 0.01
PCB29	1.01 ± 0.01	1.02 ± 0.04	0.98 ± 0.03
PCB52	1.01 ± 0.00	1.07 ± 0.04	0.89 ± 0.02
PCB77	1.05 ± 0.00	0.56 ± 0.01	0.98 ± 0.01
PCB209	1.00 ± 0.01	0.92 ± 0.03	1.14 ± 0.02

LIMIT OF DETECTION SUMMARY TABLE

Analyte	Host	Equation	R <sup>2</sup>	LOD (μM)
<i>p,p</i> -DDT	S1	$y = 0.0094x + 1.0385$	0.939	0.39
<i>p,p</i> -DDT	S2	$y = 0.011x + 0.971$	0.9406	0.51
<i>p,p</i> -DDT	S3	$y = 0.0188x + 0.9592$	0.9547	2.20
<i>o</i> -Cresol	S1	$y = 0.0018x + 1.0195$	0.9748	4.97
Benzyl alcohol	S2	$y = 0.0032x + 0.932$	0.8521	8.34
<i>o</i> -Cresol	S3	$y = -0.0026x + 0.7242$	0.9893	11.79
Cyclohexylmethanol	S1	$y = 0.01x + 0.9866$	0.9708	1.17
Cyclohexylmethanol	S2	$y = -0.0031x + 0.9648$	0.9405	1.85
1-Methylcyclohexanol	S3	$y = 0.0012x + 0.942$	0.9236	26.30
2-Methylpentane	S1	$y = 0.0026x + 0.9776$	0.9555	2.20
3-Methylpentane	S2	$y = 0.0017x + 1.0775$	0.9864	15.74
1-Methylcyclopentane	S3	$y = 0.0038x + 0.7209$	0.9421	19.82
PCB 77	S1	$y = 0.0116x + 1.0153$	0.8832	0.29
PCB 209	S2	$y = -0.0077x + 0.8402$	0.9655	0.88
PCB 209	S3	$y = 0.0079x + 1.0621$	0.8686	4.59

## SUMMARY TABLES FOR ARRAYS

### All analytes

#### Jackknifed Classification Matrix

	1-methylcyclohexanol	1-methylcyclopentane	2,3-dimethylbutane	2-methylpentane	3-methylpentane	DDD	DDE
1-methylcyclohexanol	4	0	0	0	0	0	0
1-methylcyclopentane	0	4	0	0	0	0	0
2,3-dimethylbutane	0	0	4	0	0	0	0
2-methylpentane	0	0	0	4	0	0	0
3-methylpentane	0	0	0	0	4	0	0
DDD	0	0	0	0	0	4	0
DDE	0	0	0	0	0	0	4
benzyl alcohol	0	0	0	0	0	0	0
cis-2methylcyclohexanol	0	0	0	0	0	0	0
cyclohexylmethanol	0	0	0	0	0	0	0
m-cresol	0	0	0	0	0	0	0
n-hexanes	0	0	0	0	0	0	0
o-cresol	0	0	0	0	0	0	0
opDDT	0	0	0	0	0	0	0
p-cresol	0	0	0	0	0	0	0
pcb209	0	0	0	0	0	0	0
pcb29	0	0	0	0	0	0	0
pcb3	0	0	0	0	0	0	0
pcb52	0	0	0	0	0	0	0
pcb77	0	0	0	0	0	0	0
ppDDT	0	0	0	0	0	0	0
trans-2methylcyclohexano	0	0	0	0	0	0	0
Total	4	4	4	4	4	4	4

#### Jackknifed Classification Matrix (Contd.)

	benzyl alcohol	cis-2methylcyclohexanol	cyclohexylmethanol	m-cresol	n-hexanes	o-cresol	opDDT	p-cresol	pcb209
1-methylcyclohexanol	0	0	0	0	0	0	0	0	0
1-methylcyclopentane	0	0	0	0	0	0	0	0	0
2,3-dimethylbutane	0	0	0	0	0	0	0	0	0
2-methylpentane	0	0	0	0	0	0	0	0	0
3-methylpentane	0	0	0	0	0	0	0	0	0
DDD	0	0	0	0	0	0	0	0	0
DDE	0	0	0	0	0	0	0	0	0
benzyl alcohol	4	0	0	0	0	0	0	0	0
cis-2methylcyclohexanol	0	4	0	0	0	0	0	0	0
cyclohexylmethanol	0	0	4	0	0	0	0	0	0
m-cresol	0	0	0	4	0	0	0	0	0
n-hexanes	0	0	0	0	4	0	0	0	0
o-cresol	0	0	0	0	0	4	0	0	0
opDDT	0	0	0	0	0	0	4	0	0
p-cresol	0	0	0	0	0	0	0	4	0
pcb209	0	0	0	0	0	0	0	0	4
pcb29	0	0	0	0	0	0	0	0	0
pcb3	0	0	0	0	0	0	0	0	0
pcb52	0	0	0	0	0	0	0	0	0
pcb77	0	0	0	0	0	0	0	0	0
ppDDT	0	0	0	0	0	0	0	0	0
trans-2methylcyclohexano	0	0	0	0	0	0	0	0	0
Total	4	4	4	4	4	4	4	4	4



**Jackknifed Classification Matrix (Contd.)**

	pcb29	pcb3	pcb52	pcb77	ppDDT	trans-2methylcy- clohexano	%correct
1-methylcyclohexanol	0	0	0	0	0	0	100
1-methylcyclopentane	0	0	0	0	0	0	100
2,3-dimethylbutane	0	0	0	0	0	0	100
2-methylpentane	0	0	0	0	0	0	100
3-methylpentane	0	0	0	0	0	0	100
DDD	0	0	0	0	0	0	100
DDE	0	0	0	0	0	0	100
benzyl alcohol	0	0	0	0	0	0	100
cis-2methylcyclohexanol	0	0	0	0	0	0	100
cyclohexylmethanol	0	0	0	0	0	0	100
m-cresol	0	0	0	0	0	0	100
n-hexanes	0	0	0	0	0	0	100
o-cresol	0	0	0	0	0	0	100
opDDT	0	0	0	0	0	0	100
p-cresol	0	0	0	0	0	0	100
pcb209	0	0	0	0	0	0	100
pcb29	4	0	0	0	0	0	100
pcb3	0	4	0	0	0	0	100
pcb52	0	0	4	0	0	0	100
pcb77	0	0	0	4	0	0	100
ppDDT	0	0	0	0	4	0	100
trans-2methylcyclohexano	0	0	0	0	0	4	100
Total	4	4	4	4	4	4	100

**Cumulative Proportion of Total Dispersion**

0.908	0.994	1.000
-------	-------	-------

**Aromatics**

**Jackknifed Classification Matrix**

	benzyl alcohol	m-cresol	o-cresol	p-cresol	%correct
benzyl alcohol	4	0	0	0	100
m-cresol	0	4	0	0	100
o-cresol	0	0	4	0	100
p-cresol	0	0	0	4	100
Total	4	4	4	4	100

**Cumulative Proportion of Total Dispersion**

0.859	0.950	1.000
-------	-------	-------

## Pesticides

### Jackknifed Classification Matrix

	DDD	DDE	opDDT	ppDDT	%correct
DDD	4	0	0	0	100
DDE	0	4	0	0	100
opDDT	0	0	4	0	100
ppDDT	0	0	0	4	100
Total	4	4	4	4	100

### Cumulative Proportion of Total Dispersion

0.995	1.000	1.000
-------	-------	-------

## Alkanes

### Jackknifed Classification Matrix

	1-methylcyclopentane	2,3-dimethylbutane	2-methylpentane	3-methylpentane	n-hexanes	%correct
1-methylcyclopentane	4	0	0	0	0	100
2,3-dimethylbutane	0	4	0	0	0	100
2-methylpentane	0	0	4	0	0	100
3-methylpentane	0	0	0	4	0	100
n-hexanes	0	0	0	0	4	100
Total	4	4	4	4	4	100

### Cumulative Proportion of Total Dispersion

0.767	0.930	1.000
-------	-------	-------

## Aliphatic alcohols

### Jackknifed Classification Matrix

	1-methylcyclohexanol	cis-2methylcyclohexanol	cyclohexylmethanol	trans-2methylcyclohexanol	%correct
1-methylcyclohexanol	4	0	0	0	100
cis-2methylcyclohexanol	0	4	0	0	100
cyclohexylmethanol	0	0	4	0	100
trans-2methylcyclohexanol	0	0	0	4	100
Total	4	4	4	4	100

### Cumulative Proportion of Total Dispersion

0.775	0.990	1.000
-------	-------	-------

## PCBs

### Jackknifed Classification Matrix

	pcb209	pcb29	pcb3	pcb52	pcb77	%correct
pcb209	4	0	0	0	0	100
pcb29	0	4	0	0	0	100
pcb3	0	0	4	0	0	100
pcb52	0	0	0	4	0	100
pcb77	0	0	0	0	4	100
Total	4	4	4	4	4	100

Cumulative Proportion of Total Dispersion

0.806	0.996	1.000
-------	-------	-------

1:1 binary mixtures of analytes 5-8

Jackknifed Classification Matrix

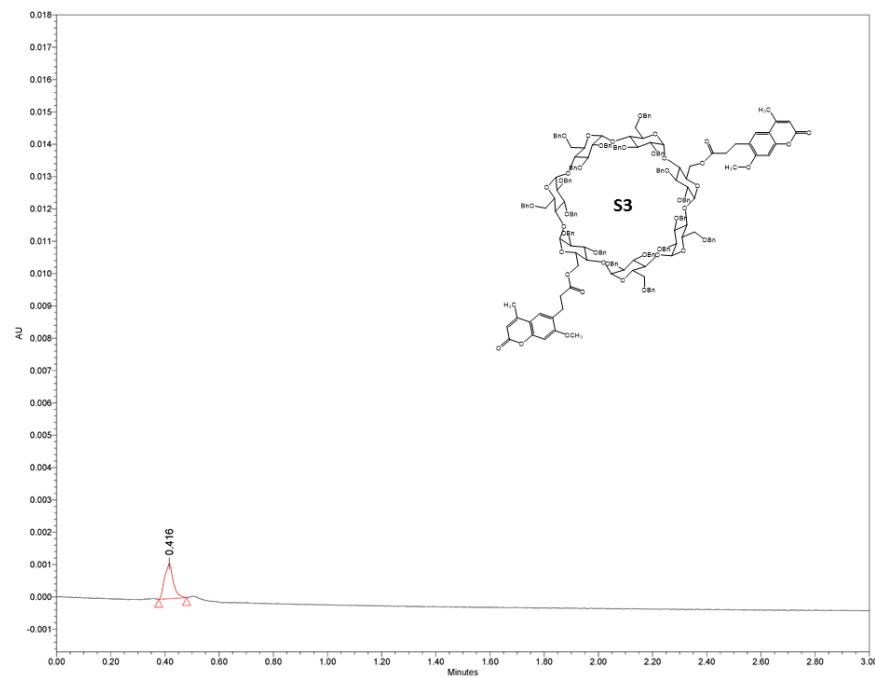
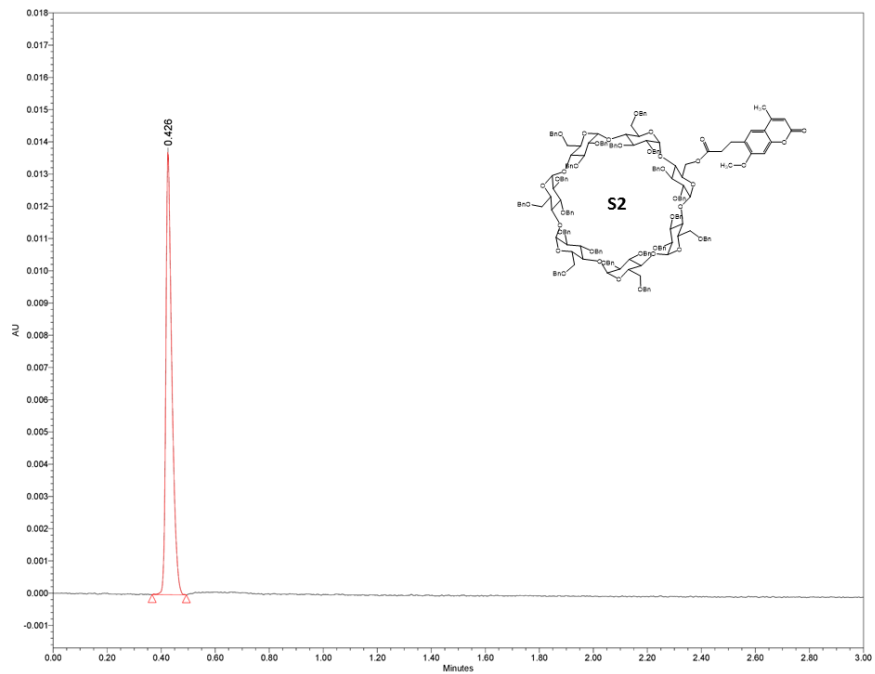
	BA-M	BA-O	BA-P	M-P	O-M	O-P	%correct
BA-M	2	0	0	0	0	2	50
BA-O	0	4	0	0	0	0	100
BA-P	1	0	3	0	0	0	75
M-P	0	0	0	4	0	0	100
O-M	0	0	0	0	4	0	100
O-P	1	0	0	0	0	3	75
Total	4	4	3	4	4	5	83

Cumulative Proportion of Total Dispersion

0.889	0.981	1.000
-------	-------	-------

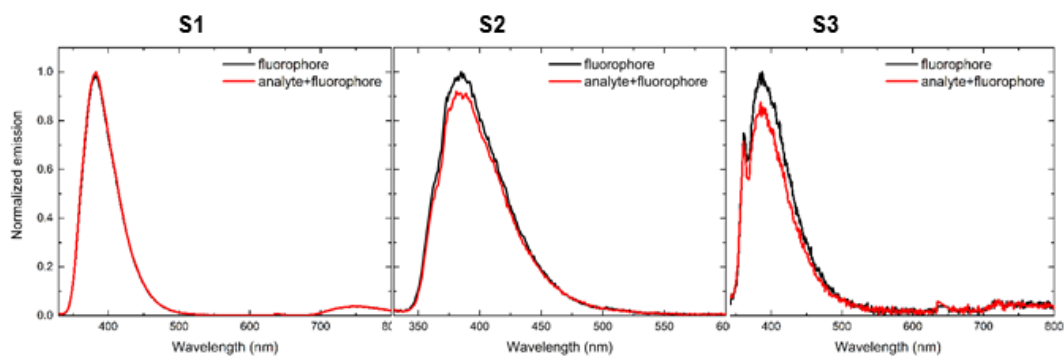
## SUMMARY FIGURES

### SUMMARY FIGURES FOR HPLC ANALYSIS OF COMPOUNDS S2 AND S3

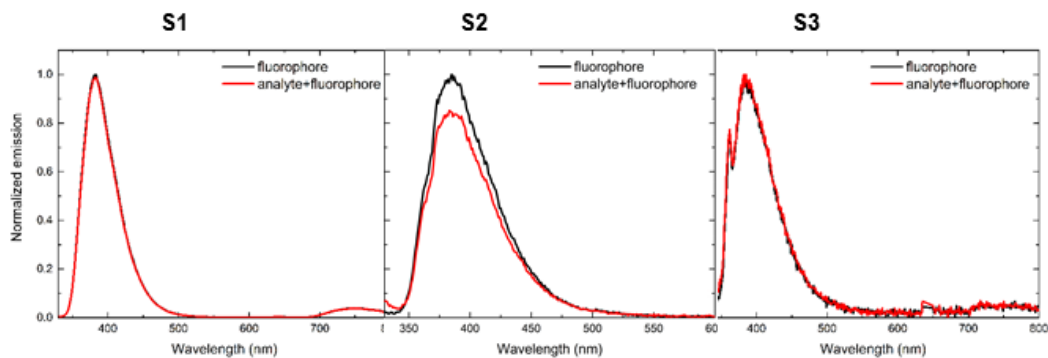


## SUMMARY FIGURES FOR FLUORESCENCE MODULATION

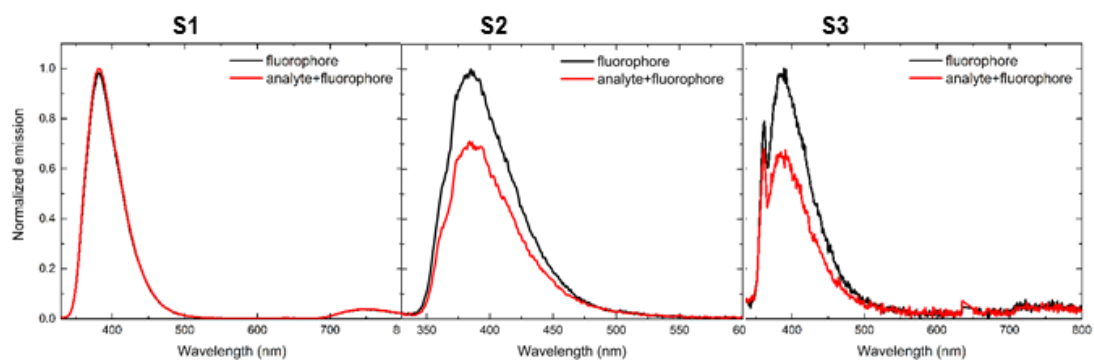
*o*-Cresol



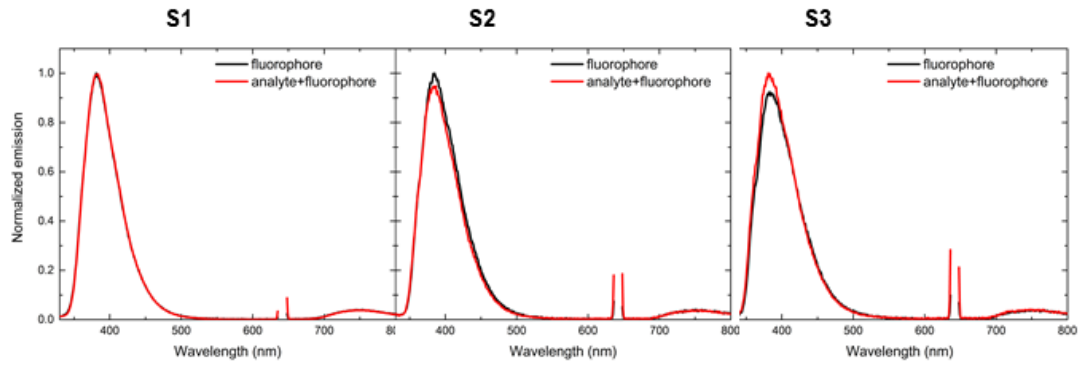
*m*-Cresol



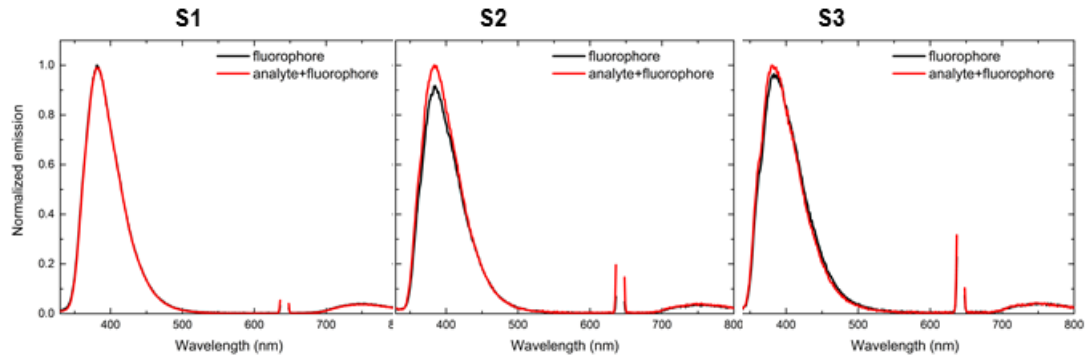
*p*-Cresol



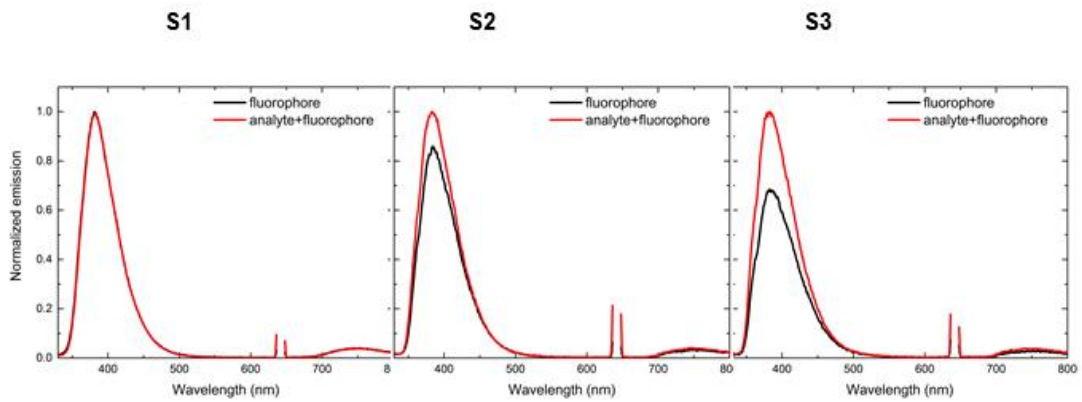
DDD



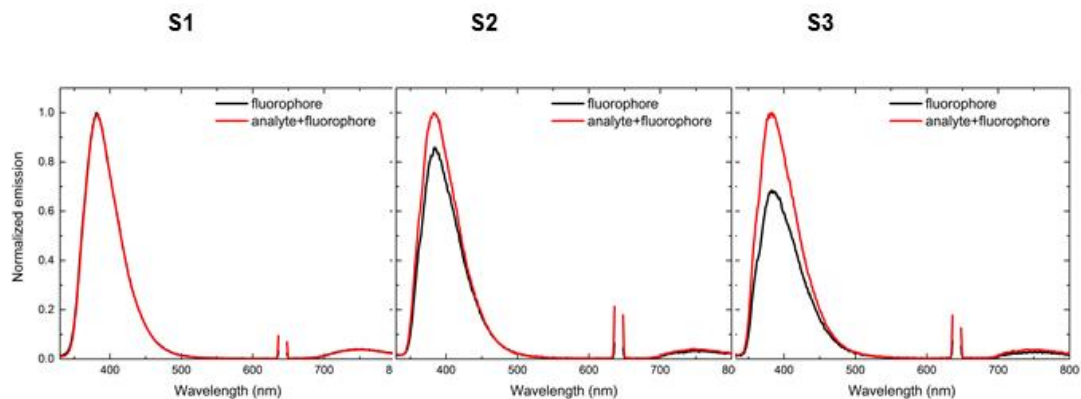
DDE



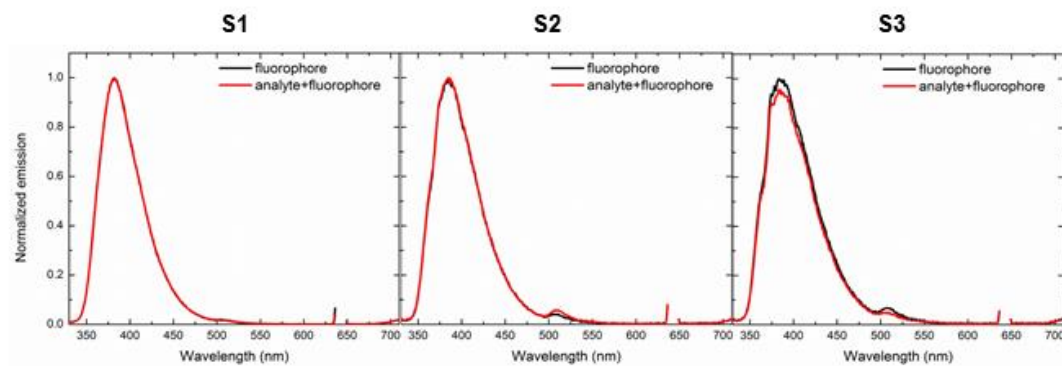
*o,p*-DDT



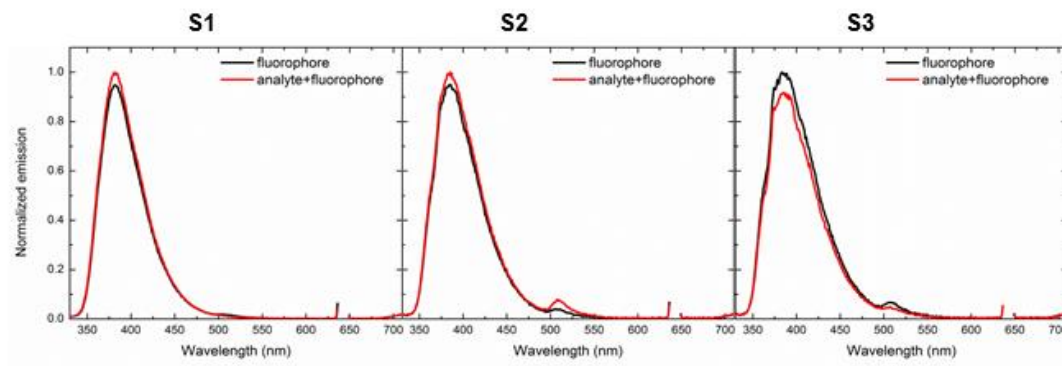
*p,p*-DDT



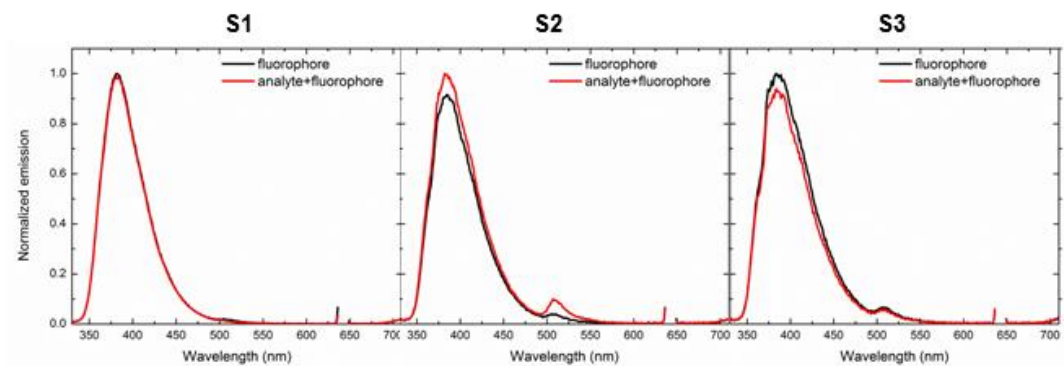
*n*-Hexanes



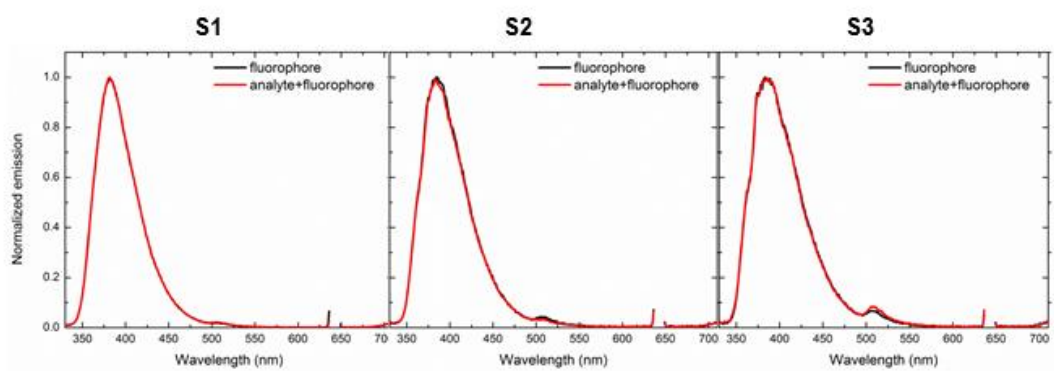
2-Methylpentane



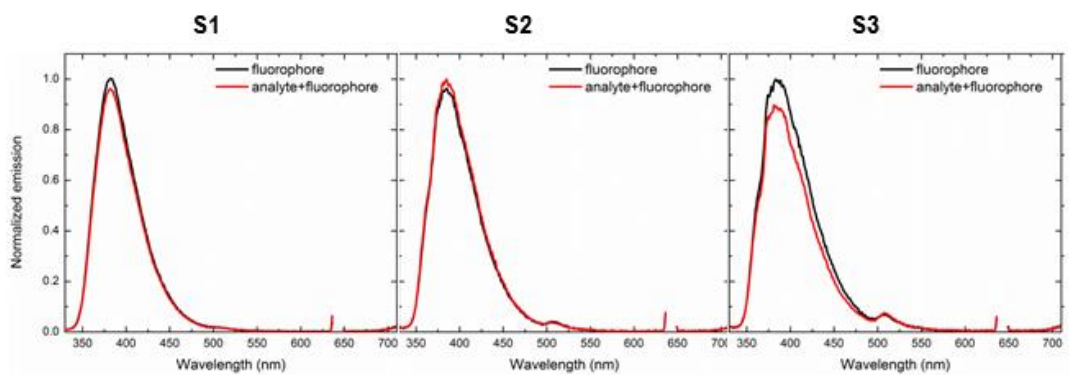
### 3-Methylpentane



### 2,3-Dimethylbutane

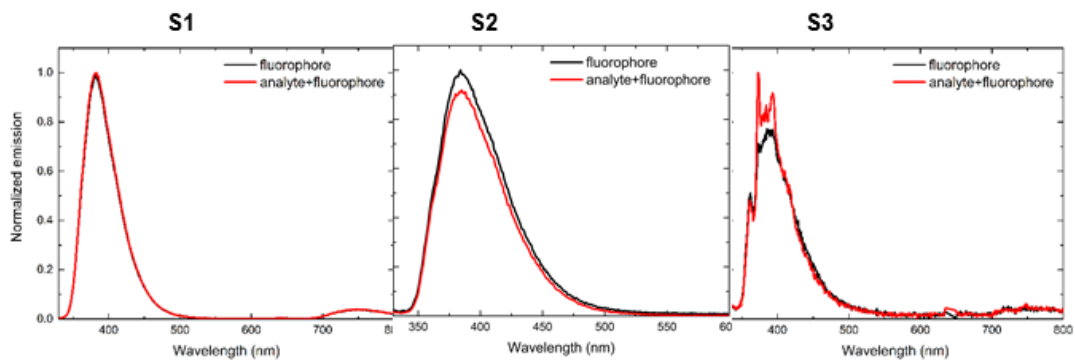


### 1-Methylcyclopentane

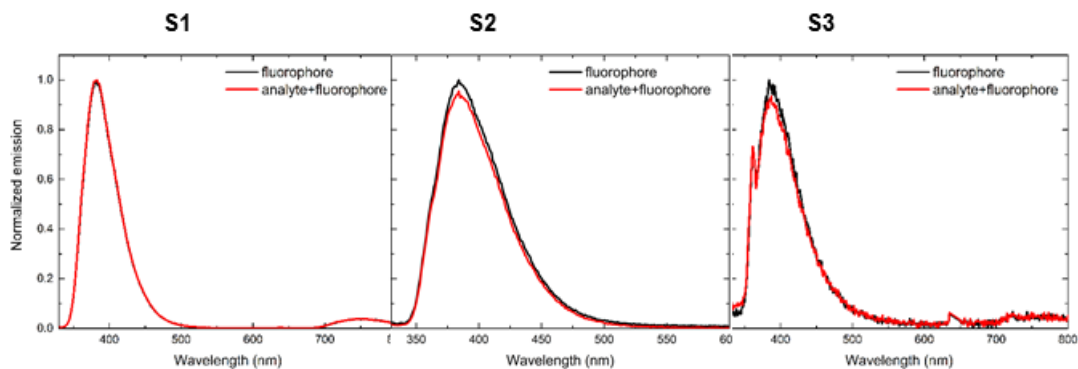




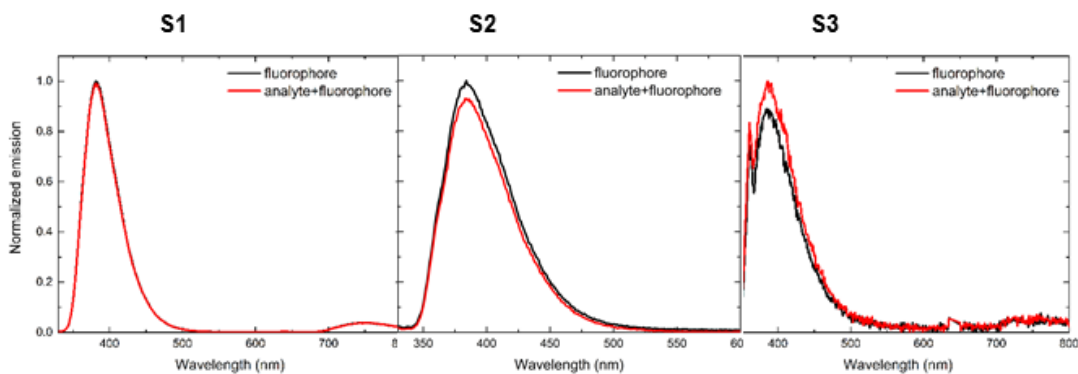
## 1-Methylcyclohexanol



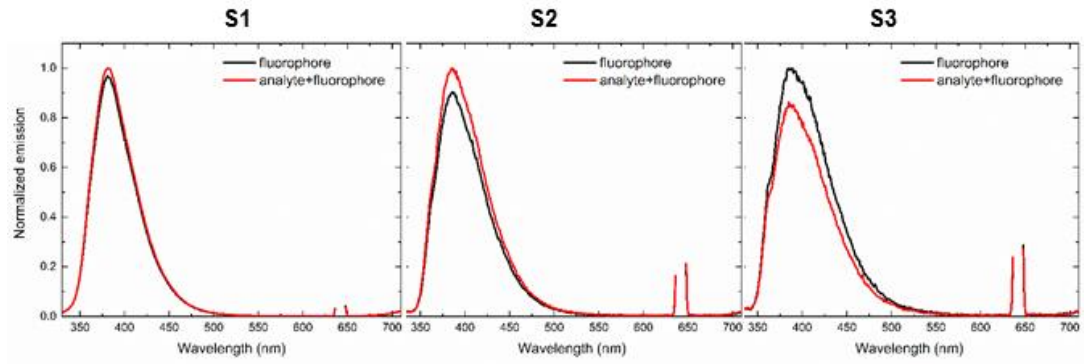
## *cis*-2-Methylcyclohexanol



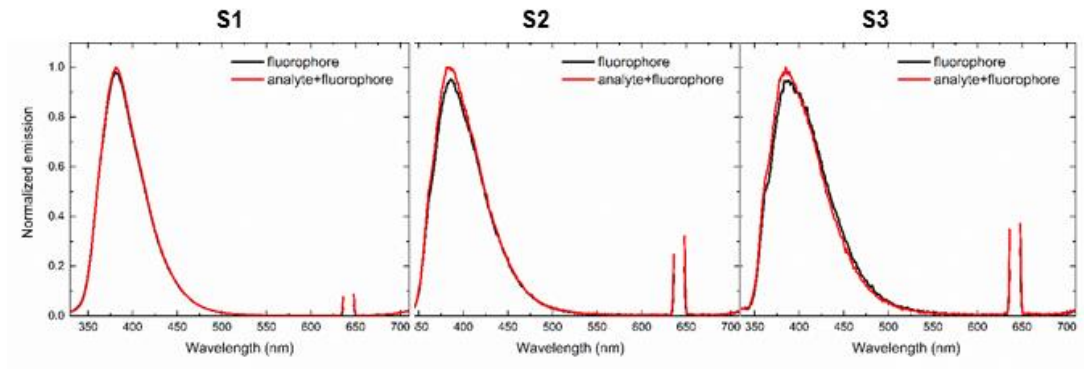
## *trans*-2-Methylcyclohexanol



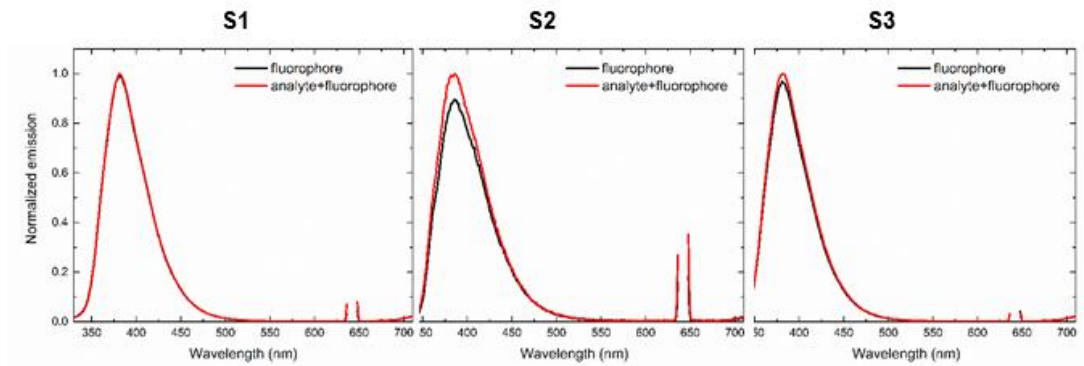
### PCB3



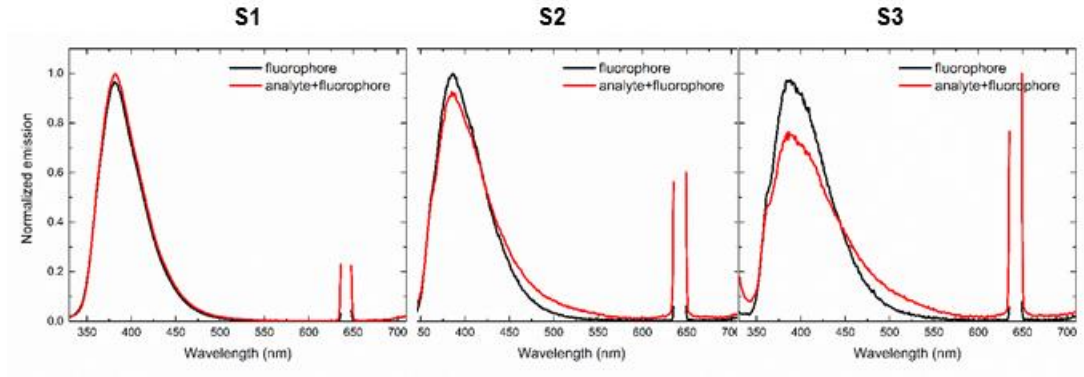
### PCB29



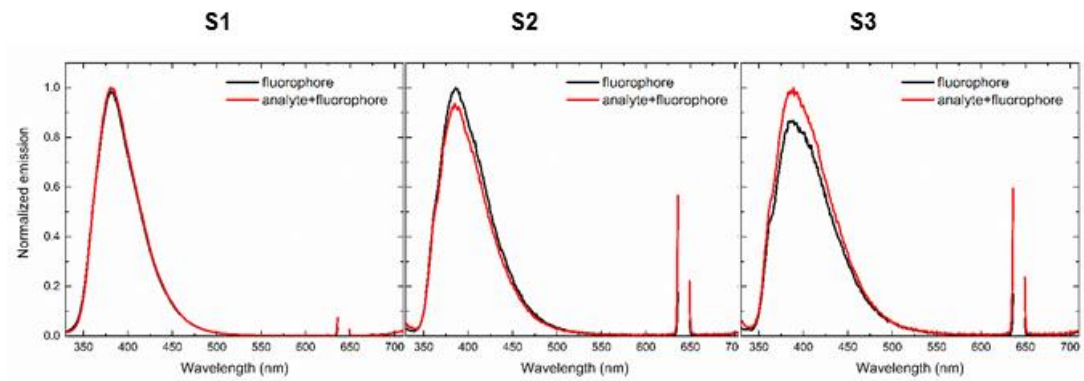
### PCB52



PCB77

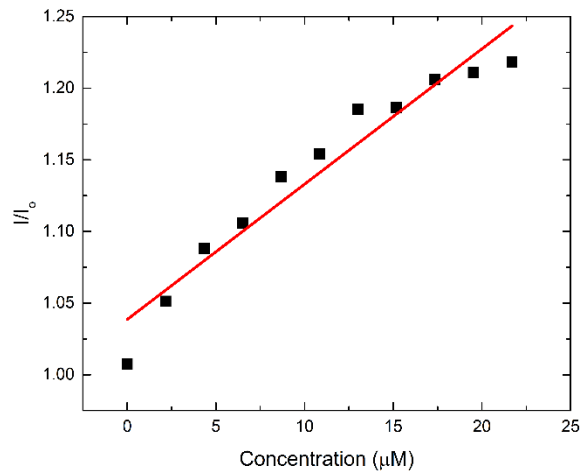


PCB209

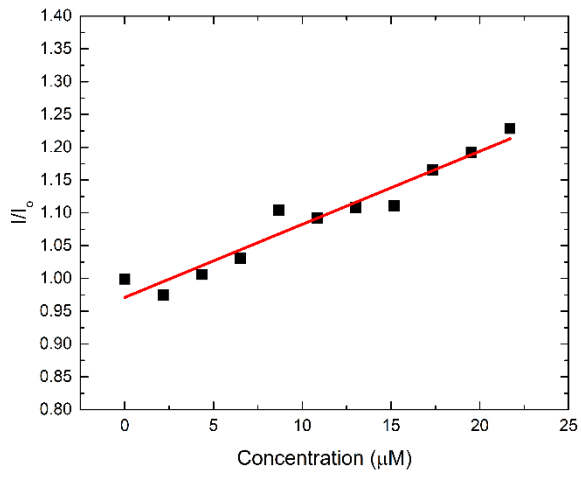


### SUMMARY FIGURES FOR LIMIT OF DETECTION EXPERIMENTS

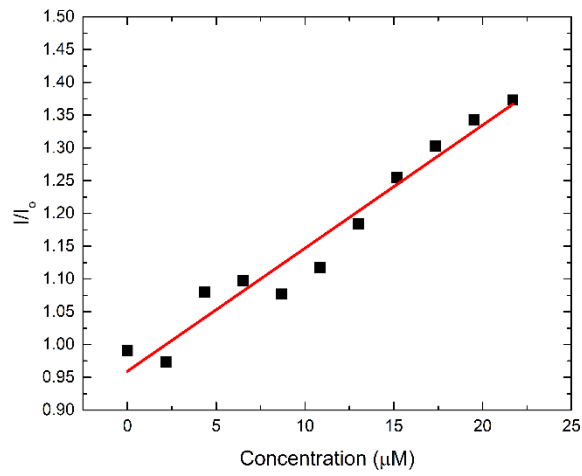
*p,p*-DDT – S1



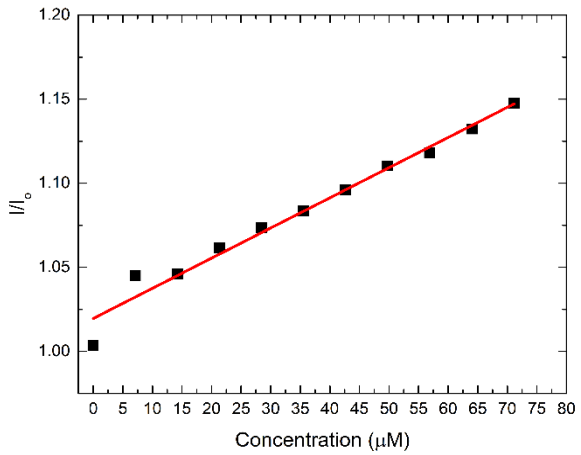
*p,p*-DDT – S2



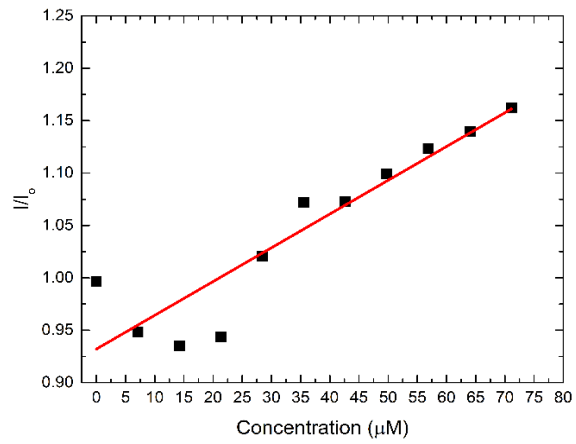
*p,p*-DDT – S3



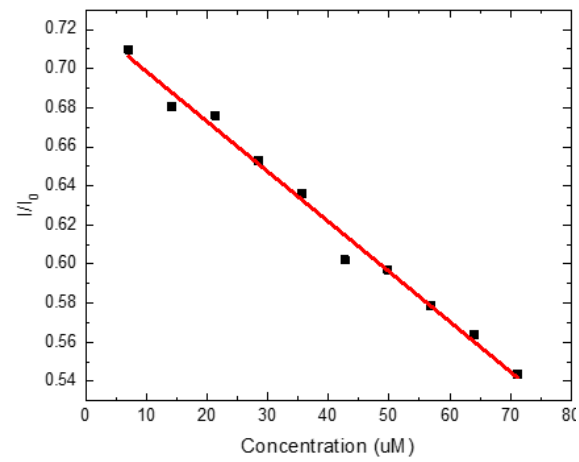
*o*-Cresol – S1



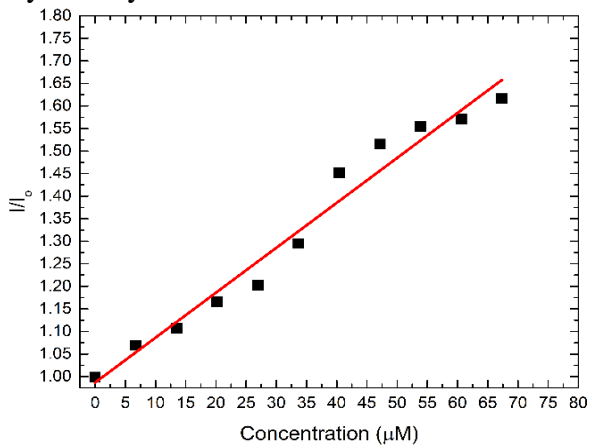
### Benzyl alcohol – S2



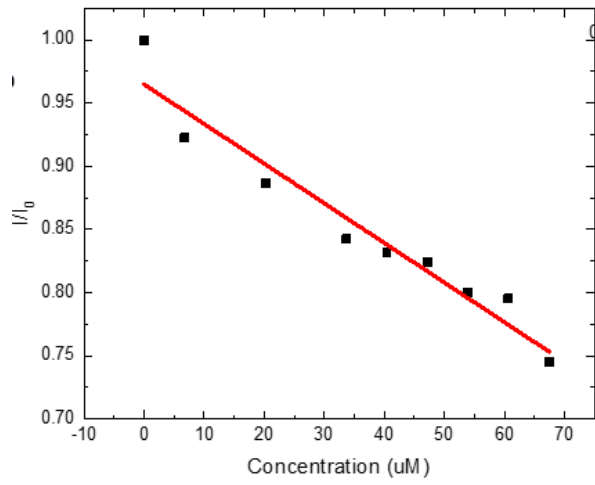
### *o*-Cresol – S3



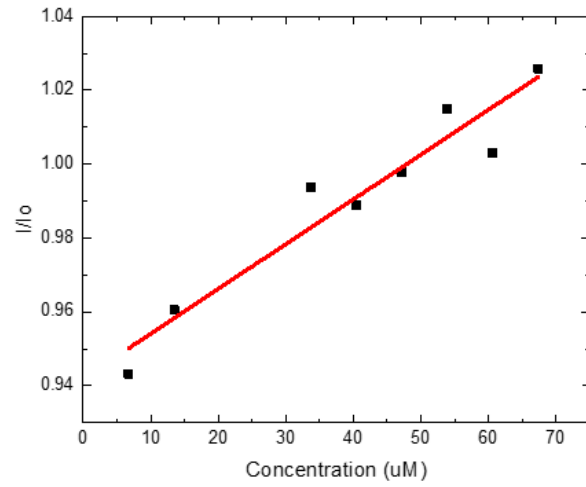
### Cyclohexylmethanol – S1



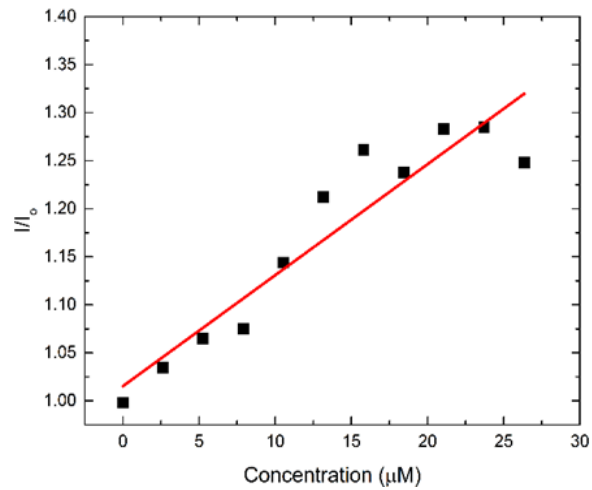
### Cyclohexylmethanol – S2



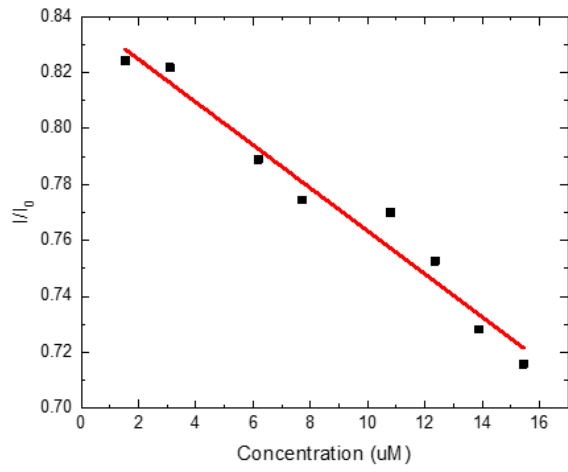
### 1-Methylcyclohexanol – S3



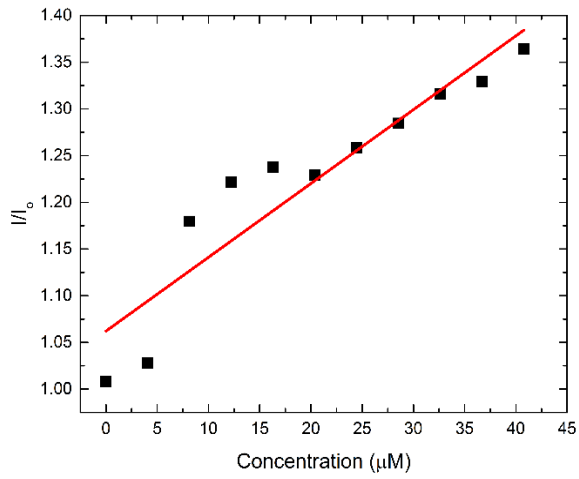
### PCB77 – S1



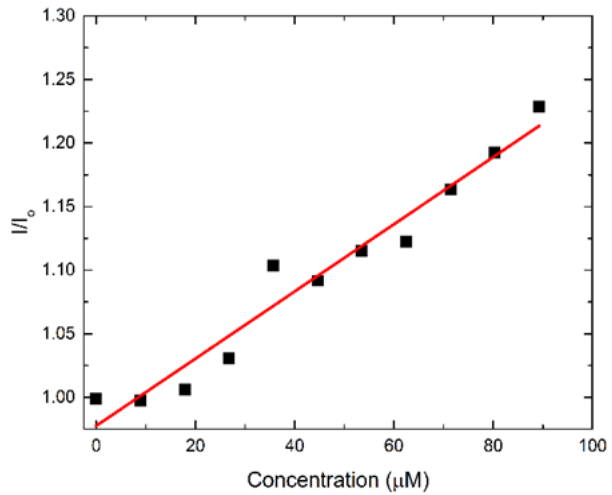
PCB209 – S2



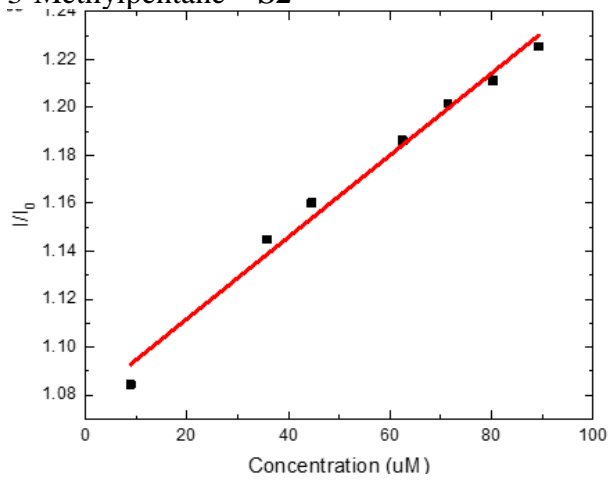
PCB209 – S3



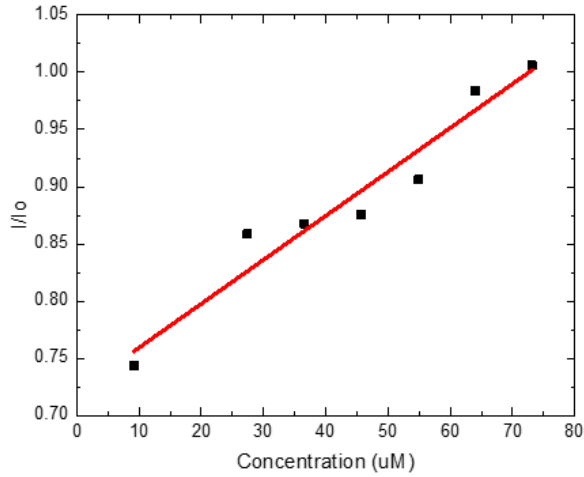
2-Methylpentane – S1



3-Methylpentane – S2

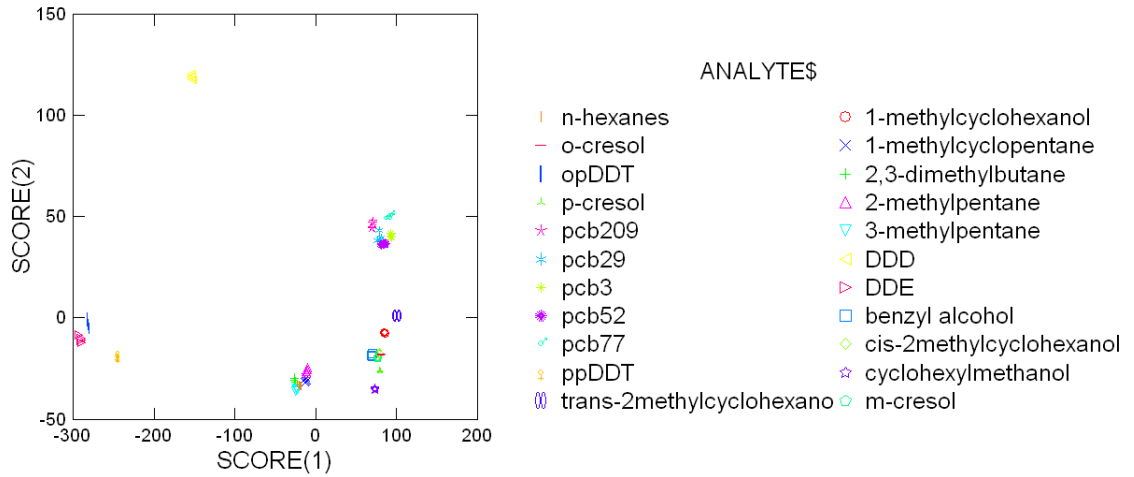


1-Methylcyclopentane – S3



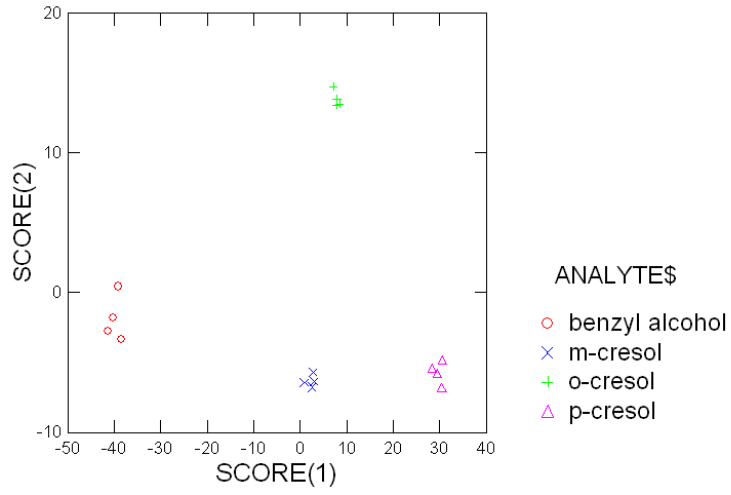
SUMMARY FIGURES FOR ARRAY GENERATION EXPERIMENTS

All Analytes

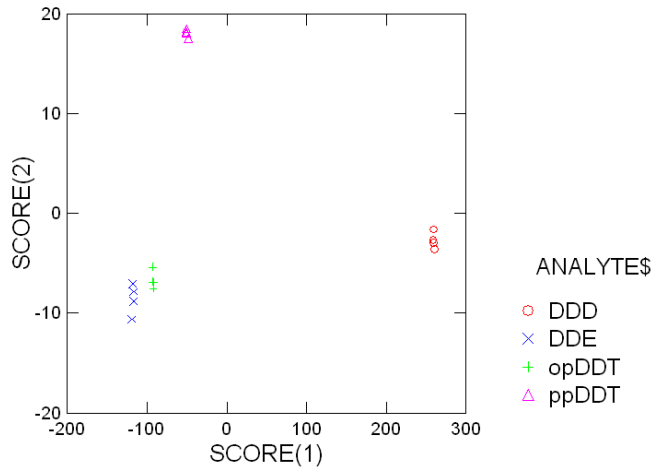




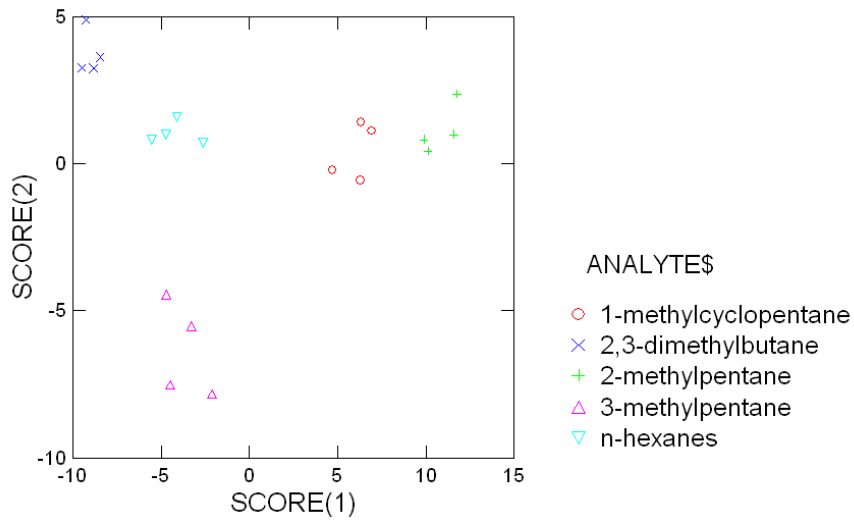
### Aromatics



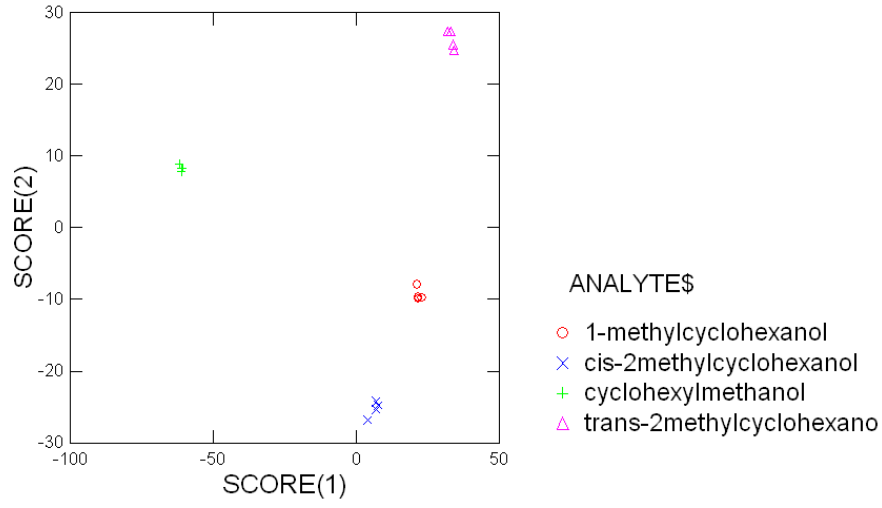
### Pesticides



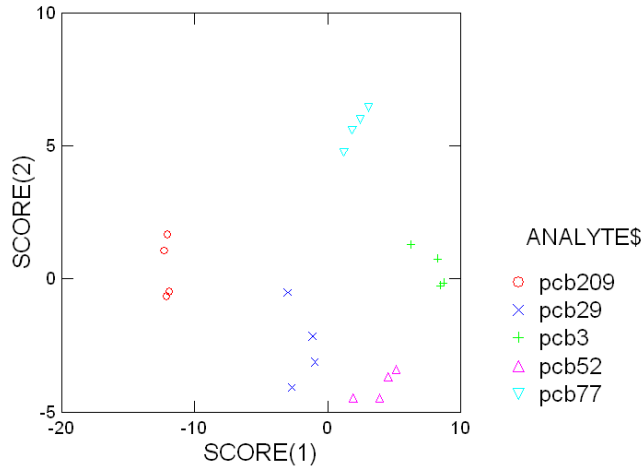
### Alkanes



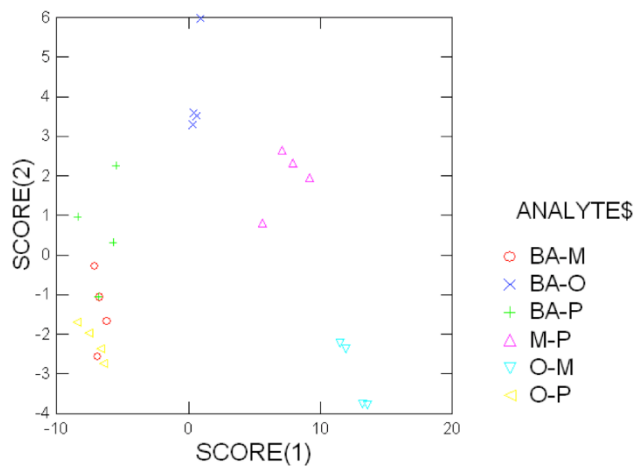
### Alcohols



### PCBs



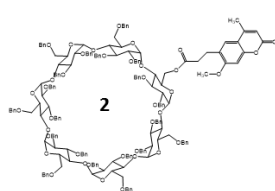
### 1:1 binary mixtures of analytes 5-8



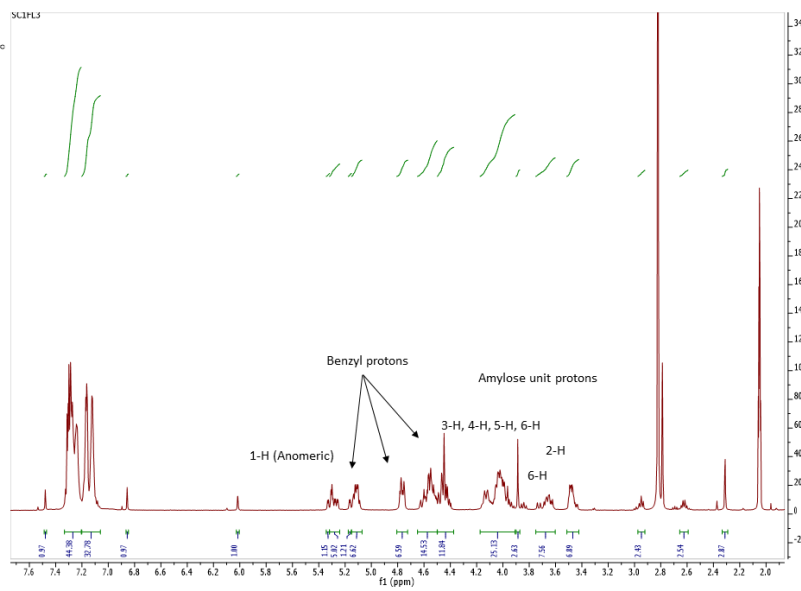
# NMR SPECTRA OF ALL NEW COMPOUNDS

## Compound 2

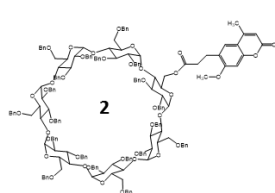
$^1\text{H-NMR}$  recorded in acetone- $d_6$



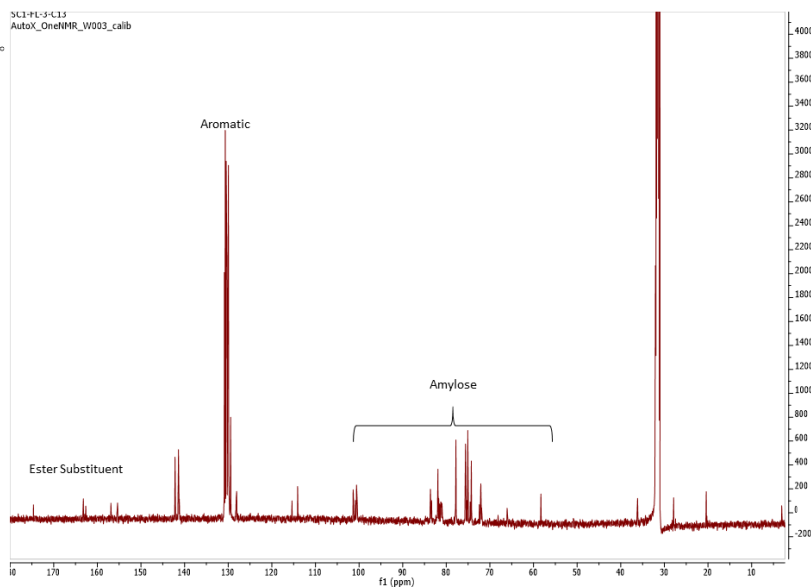
$^1\text{H-NMR}$  Spectrum  
(500MHz)



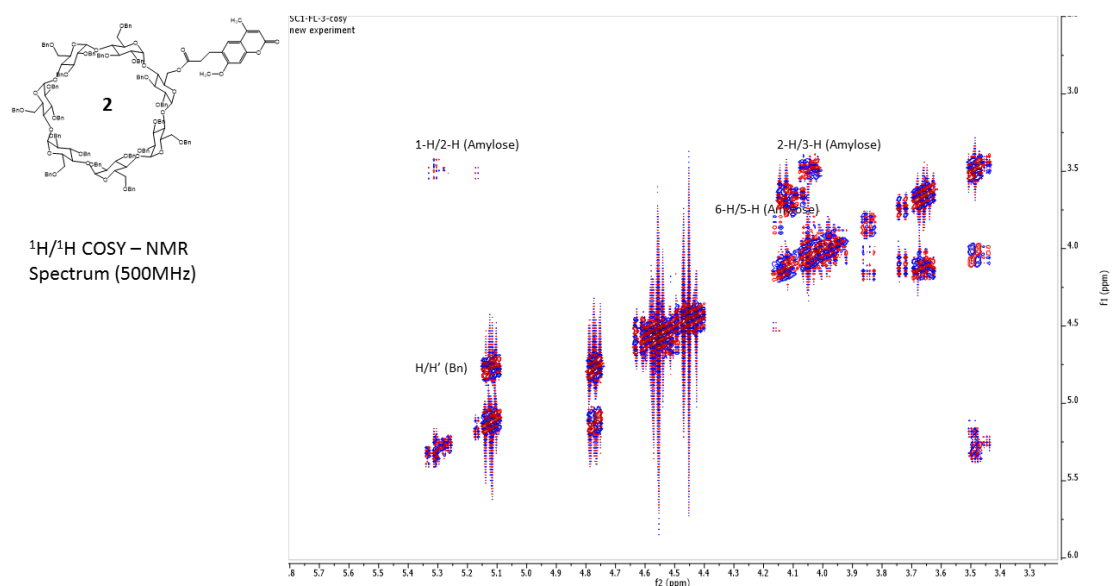
$^{13}\text{C-NMR}$  recorded in acetone- $d_6$



$^{13}\text{C-NMR}$  Spectrum  
(500MHz)

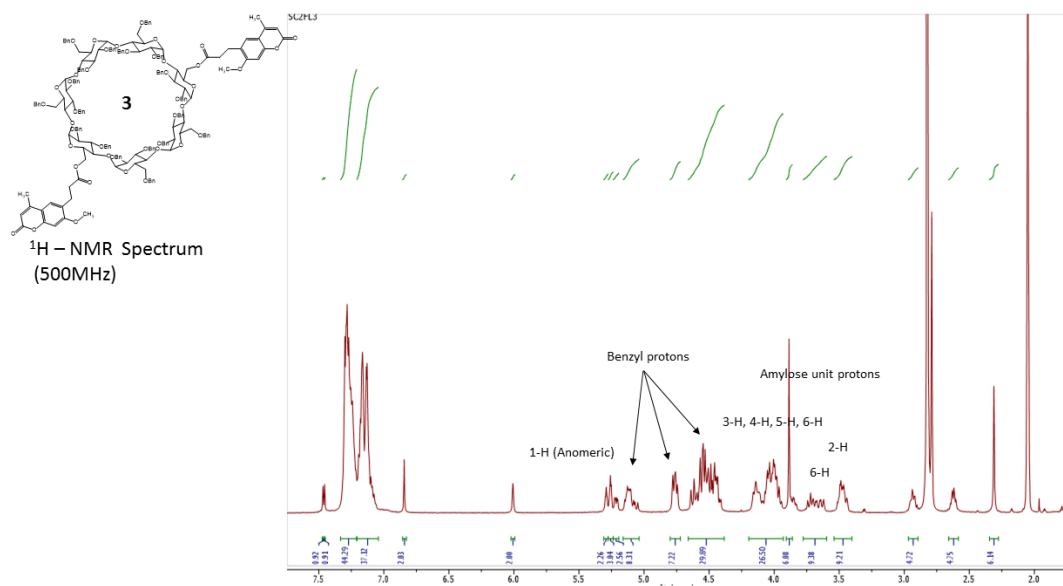


## COSY NMR recorded in acetone- $d_6$

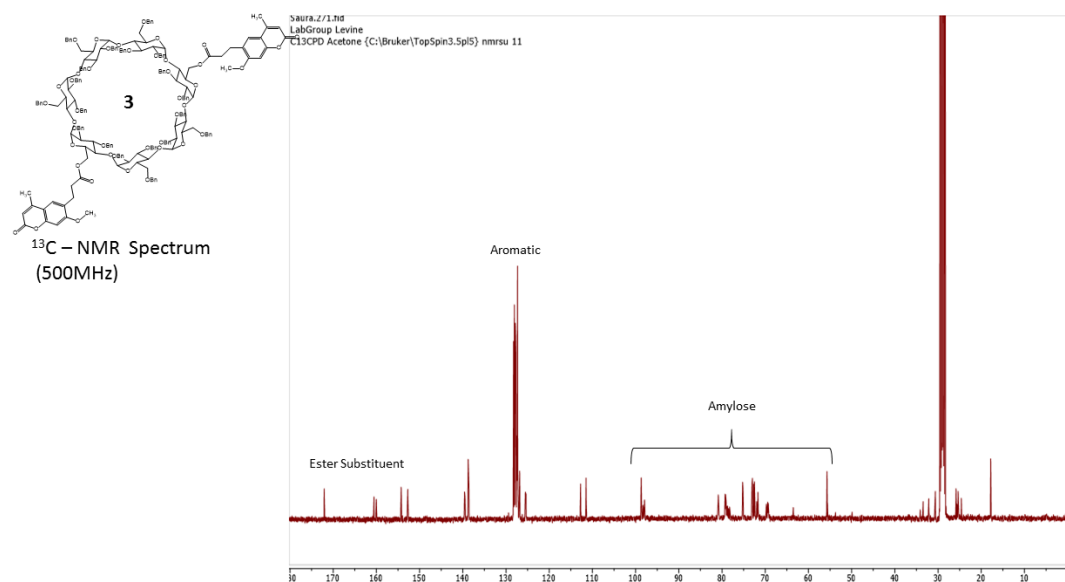


## Compound **3**

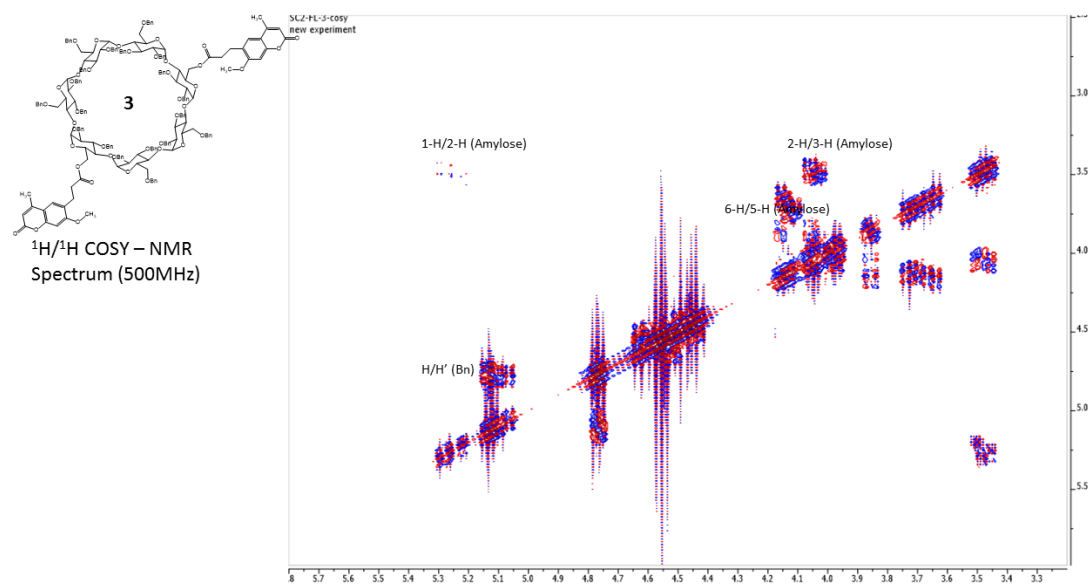
$^1\text{H}$ -NMR recorded in acetone- $d_6$



$^{13}\text{C}$ -NMR recorded in acetone- $d_6$



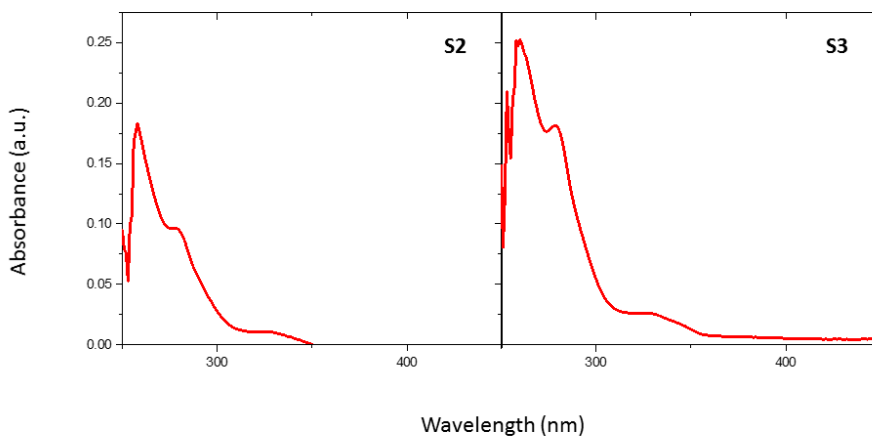
COSY NMR recorded in acetone- $d_6$



## SPECTROSCOPIC INVESTIGATIONS OF SENSORS **S1-S3**

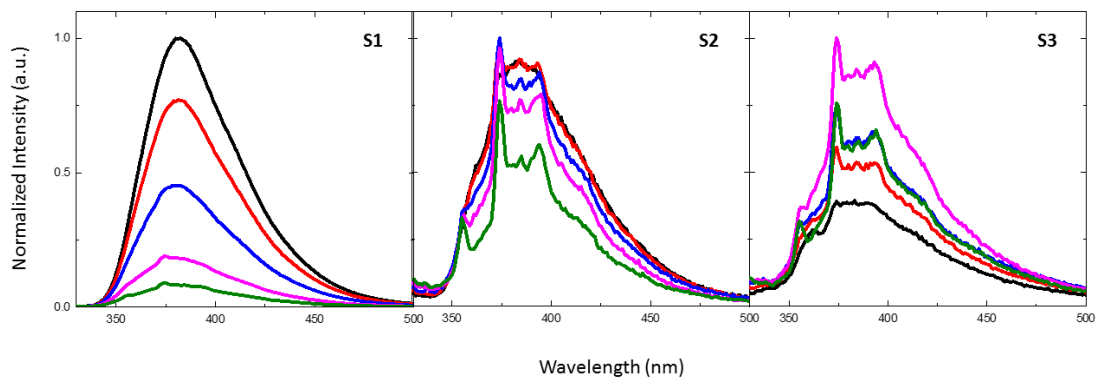
### ABSORPTION SPECTRA

UV-Visible Absorption Spectra of **S2** and **S3** (1 $\mu$ M) in DMSO measured at room temperature:



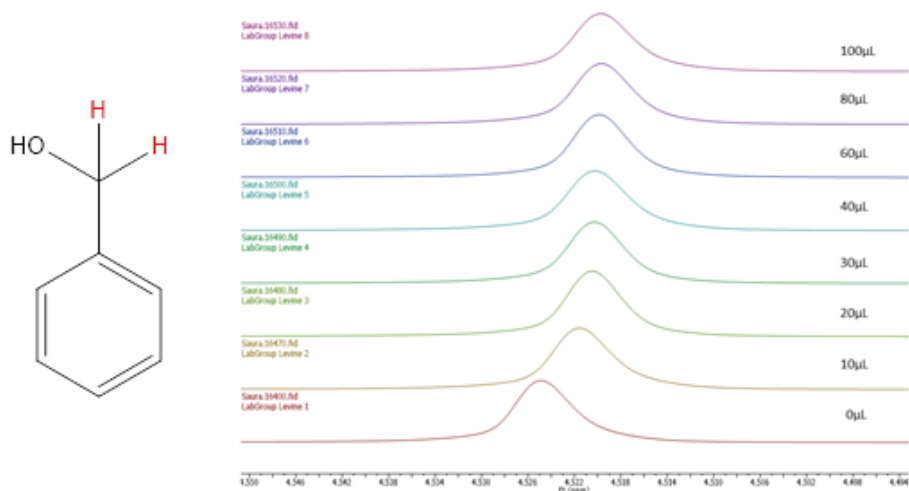
### VARIATION OF FLUORESCENCE EMISSION OF SENSORS IN H<sub>2</sub>O/DMSO MIXTURES

Fluorescence emission spectra of **S1**, **S2** and **S3** (at 1  $\mu$ M concentration) in 80:20 (H<sub>2</sub>O: DMSO) (black trace), 60:40 (H<sub>2</sub>O:DMSO) (red trace), 40:60 (H<sub>2</sub>O: DMSO) (blue trace), 20:80 (H<sub>2</sub>O: DMSO) (purple trace), 0:100 (H<sub>2</sub>O:DMSO) (green trace). ( $\lambda_{\text{ex}} = 320$  nm). All spectra were recorded at room temperature.



## BENESI-HILDEBRAND PLOTS FOR NMR TITRATION

Analyte **5** (0.2 M in 0.4 mL D<sub>2</sub>O) was titrated against 0 μL, 10 μL, 20 μL, 25 μL, 30 μL, 35 μL, 40 μL, 50 μL, 60 μL, 80 μL and 100 μL of the host (1 mg/mL dissolved in DMSO-*d*<sub>6</sub>) in a clean dry NMR tube. The volume was adjusted to 0.5 mL final volume with the addition of DMSO-*d*<sub>6</sub>. The <sup>1</sup>H-NMR spectra of the samples were recorded in 300 MHz Bruker AVANCE NMR Spectrometer at room temperature. The chemical shift of benzylic protons (highlighted in red in the figure below) were tracked, and the data was used to solve the Benesi-Hildebrand equation, below.



*Benesi-Hildebrand Equation:*

$$1/\Delta\delta = (1/ K_a \Delta\delta_{\max})1/[H] + (1/\Delta\delta_{\max}) \quad (\text{Equation S3})$$

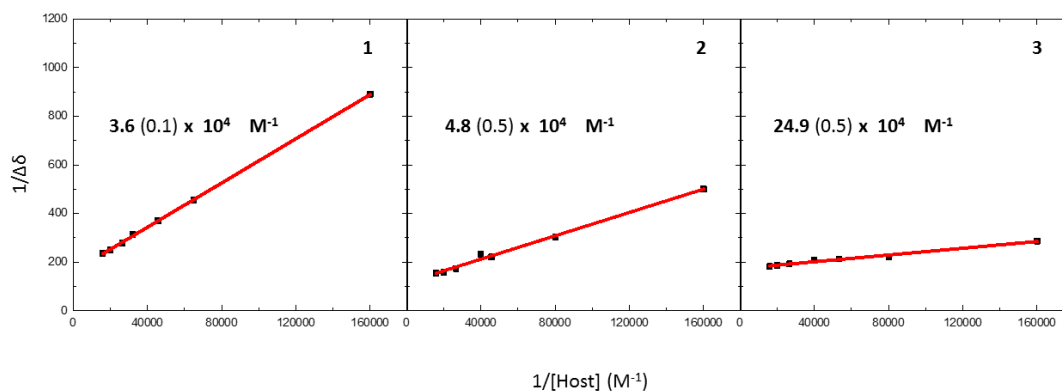


**Table S1.** Benesi-Hildebrand equations for titrations of hosts (**1-3**) with analyte **5**

Host	Equation	$K_a$ ( $M^{-1}$ )	$\Delta\delta_{\max}$ (ppm)
<b>1</b>	$y = 0.0045x + 162.97$	$3.6(0.1) \times 10^4$	0.0061
<b>2</b>	$y = 0.0024x + 116.62$	$4.8(0.5) \times 10^4$	0.0085
<b>3</b>	$y = 0.0007x + 173.27$	$24.9(0.5) \times 10^4$	0.0057

Benesi-Hildebrand plots for association constant calculations of analyte **5** with compounds **1**, **2** and **3** in 80:20 water-DMSO at room temperature. (H is the host;  $K_a$  is association constant;  $\Delta\delta_{\max}$  is maximum peak shift at infinite host concentration  $[H] = \infty$ ;  $\Delta\delta$  is the peak shift at a given host concentration. Values in parentheses indicate to the error in the  $K_a$  values from linear fit of the data points.)



## CHAPTER 4

To be Submitted to *Chemical Science*

Synthetic  $\beta$ -cyclodextrin dimers for squaraine binding: Effect of host architecture on photophysical properties, aggregate formation and chemical reactivity

Sauradip Chaudhuri, Molly Verderame, Y. M. Nuwan D. Y. Bandara, Ashvin I. Fernando, Teresa Mako, Mindy Levine

Department of Chemistry, University of Rhode Island, Kingston, RI, USA

Corresponding Author:

Mindy Levine, Ph.D.

Department of Chemistry

University of Rhode Island

Kingston, Rhode Island, 02881, USA

[mlevine@chm.uri.edu](mailto:mlevine@chm.uri.edu)

## Manuscript 4

# **Synthetic $\beta$ -cyclodextrin dimers for squaraine binding: Effect of host architecture on photophysical properties, aggregate formation and chemical reactivity**

### ABSTRACT

Reported herein is the synthesis and application of three novel  $\beta$ -cyclodextrin dimer hosts for the complexation of near-infrared (NIR) squaraine dyes in aqueous solution. A series of eight different *N*-substituted *N*-methyl anilino squaraine dyes with variable terminal groups are investigated, with an optimal *n*-hexyl substituted squaraine guest demonstrating binding constant orders of magnitude higher than the others. Moreover, hydrophobic complexation of the squaraine dyes with the  $\beta$ -cyclodextrin dimer hosts causes drastic changes in the squaraine's photophysical properties, propensity for aggregation and susceptibility to hydrolytic decay.

### INTRODUCTION

The complexation of small molecule guests inside a variety of supramolecular hosts has been extensively reported in the literature. Examples of such hosts include cyclodextrins,<sup>1</sup> which bind guests primarily via hydrophobic encapsulation inside the hydrophobic cavity;<sup>2</sup> cucurbiturils (CBs),<sup>3</sup> which bind guests via electrostatic interactions with the highly polarized carbonyl groups that line the CB rims as well as via hydrophobic association,<sup>4</sup> and synthetic macrocycles<sup>5</sup> and cavitands,<sup>6</sup> whose structures can vary widely as a result of straightforward synthetic accessibility.

Previous work by our group has focused on the use of cyclodextrin complexation to develop highly sensitive and selective fluorescence-based detection methods for multiple classes of toxicants, including polycyclic aromatic hydrocarbons (PAHs),<sup>7</sup> polychlorinated biphenyls (PCBs),<sup>8</sup> aromatic pesticides,<sup>9</sup> aliphatic alcohols,<sup>10</sup> and aromatic oil-spill components.<sup>11</sup> These detection methods operate via cyclodextrin-promoted fluorescence energy transfer,<sup>12</sup> in cases where the toxicant is photophysically active and a competent energy donor, or via cyclodextrin-promoted fluorescence modulation,<sup>13</sup> in cases where the toxicant is not photophysically active but still binds in cyclodextrin and promotes proximity-induced, analyte specific changes in the fluorophore emission. No previous work in our group has reported the use of higher order cyclodextrin architectures for detection applications, despite the fact that such architectures have been shown to have significantly enhanced binding affinities in certain cases.<sup>14</sup>

One group of guests that is known to bind well in cyclodextrins is squaraine fluorophores,<sup>15</sup> which contain a common cyclobutene-dione core.<sup>16</sup> The highly unique electronic structure of the squaraine fluorophore leads to anomalously high extinction coefficients,<sup>17</sup> narrow Stokes shifts, and high quantum yields,<sup>18</sup> with absorption and emission maxima often in the near-infrared spectral region. As a result of these properties, especially the near-infrared absorption and emission that limit interference from other analytes,<sup>19</sup> squaraine fluorophores have significant potential usage for detection. Squaraine binding in cyclodextrin hosts has been previously reported to result in changes in the absorption and emission spectra of the squaraine guest.<sup>20</sup>

Reported herein is the rational design and synthesis of dimeric cyclodextrin architectures, their ability to bind squaraine fluorophores with unprecedentedly high binding constants (orders of magnitude higher than previously reported), and the effects of such binding on the squaraines' photophysical properties, propensity for aggregate formation, and reactivity towards hydrolysis. Detailed structure-property relationships are invoked to understand the effects of the structural architectures of the dimers on squaraine guests with variable-length terminal alkyl chains.

## EXPERIMENTAL

The conversion of  $\beta$ -cyclodextrin to 6-amino-6-monodeoxy- $\beta$ -cyclodextrin was carried out following literature-reported procedures.<sup>21</sup> Naphthalene-1,4-dipropionic acid and anthracene-9,10-dipropionic acid (linkers for dimer hosts **2** and **3**) were synthesized using literature-reported procedures starting from 1,4-dimethylnaphthalene and 9,10-dimethylantracene, respectively.<sup>22</sup>  $\beta$ -cyclodextrin dimer hosts **1-3** (Figure 1) were synthesized via activated amide coupling reactions of 6-amino-6-monodeoxy- $\beta$ -cyclodextrin and bis-succinimide esters of linkers (see ESI for more details). Squaraine dyes (**4-11**) were synthesized via the condensation of *N*-substituted *N*-methyl aniline with 3,4-dihydroxycyclobut-3-ene-1,2-dione (squaric acid) in a solvent mixture of *n*-butanol/toluene (2:1) under refluxing conditions with a Dean-Stark trap (Figure 2).

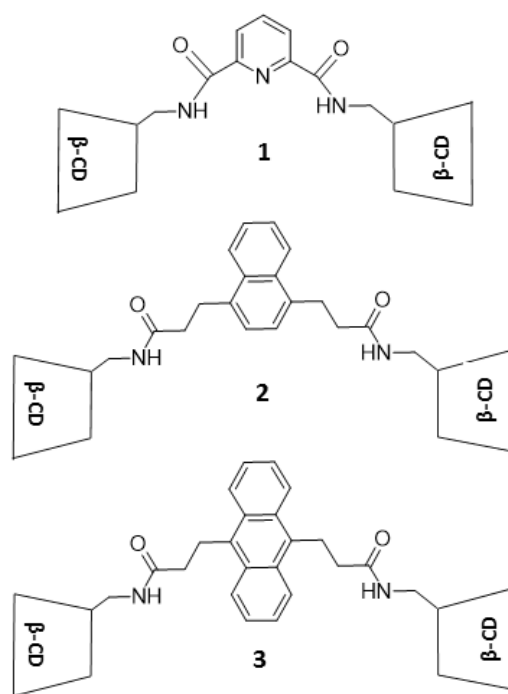


**Figure 1.** Structures of new cyclodextrin dimers hosts **1-3**.

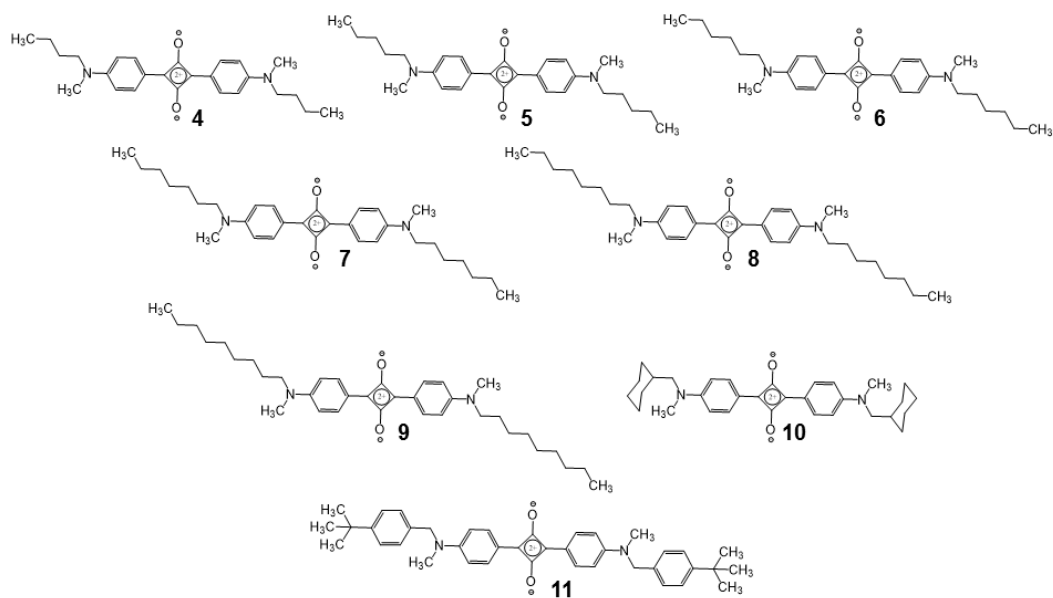


**Figure 2.** Structures of *N*-substituted *N*-methylanilino squaraine dye guests **4-11**.

The absorption spectra of a mixture of increasing concentrations of squaraine guests (**4-11**) in a solution of host dimers (8  $\mu\text{M}$  in 2.5 mL of PBS) were recorded on a Shimadzu UV-3600 Plus spectrophotometer. The UV spectra were subjected to a piecewise linear background subtraction method. The selection of spectral positions to run the background were identified by a custom threshold approach. After the background spectral subtraction, the spectral signal was fitted using “NonlinearModeFit” command in Mathematica (method set to “automatic”) with three Gaussian functions,  $A \cdot \text{Exp} \frac{(x-\mu)^2}{2\sigma^2}$ , where A,  $\mu$ ,  $\sigma$  and x have their usual meanings—amplitude, mean, standard deviation, and wavelength respectively.

For hydrolysis experiments, the absorption spectra of a mixture of a 24  $\mu\text{M}$  solution of host dimers (**1-3**) and a 24  $\mu\text{M}$  solution of guest squaraines (**4-11**) were recorded over a period of 5 hours, with the spectra acquired every 30 minutes. All linear fits were done with “NonlinearModeFit” command (method set to “automatic”) using the form  $-\log \left[ \frac{A}{A_0} - c \right] = k \cdot x$ , where c, A,  $A_0$ , k and x refer to the integrated absorption at the aggregate concentration, concentration at time t, concentration at time zero, rate constant and the independent variable, respectively. The value of c was found from the exponential fit.

Fluorescence spectra were recorded on a Shimadzu RF-6000 spectrophotometer with 3.0 nm excitation slit widths and 3.0 nm emission slit widths. For each squaraine-dimer titration, 6.25  $\mu\text{L}$  of a 0.5 mg/mL (0.2 mM) aqueous solution of the host dimer (**1-3**) was added to a cuvette containing 2.5 mL of aqueous phosphate-buffered saline solution (PBS, buffered at pH 7.4). The fluorescence spectra of this solution were measured after being titrated with solutions of the

guest dyes (0.2 mg/mL solution in THF) at the following addition volumes: 0.0, 1.5, 3.0, 4.5, 6.0, 7.5, 9.0, 10.5, 12.0, 13.5, 15.0, 20.0, 30.0, 40.0 and 50.0  $\mu\text{L}$  dye solutions. Each measurement was repeated for four trials. All fluorescence spectra were integrated vs. wavenumber on the X-axis using OriginPro Version 9.1.

All computational modelling was done using commercially available Spartan software, version 16. To obtain the molecular models, the structures were first energy-minimized using multiple runs of molecular dynamics simulations. Next, these structures were submitted to MMF94 molecular mechanics methods, and the minimized structure from this was further optimized and minimized using a PM3-level semi-empirical force field in a gaseous medium. The energy obtained from these calculations were used to calculate the stabilization energy of the complex using the equation below<sup>23</sup>:

$$\Delta E_{\text{complex}} = E_{\text{Complex}} - E_{\text{Host}} - E_{\text{Guest}} \quad (\text{Equation 1})$$

where  $\Delta E_{\text{complex}}$  is the stabilization energy of the host-guest complex,  $E_{\text{complex}}$  is the energy of formation of the host-guest complex,  $E_{\text{Host}}$  is the energy of formation of the  $\beta$ -cyclodextrin dimer hosts, and  $E_{\text{Guest}}$  is the energy of formation of the squaraine guest.

## RESULTS AND DISCUSSION

### *Synthetic routes*

Three novel, covalently linked  $\beta$ -cyclodextrin dimers (compounds **1-3**) with aromatic linkers were synthesized via coupling reactions of activated amide derivatives with

monofunctionalized  $\beta$ -cyclodextrin derivatives. While compound **1** incorporates a rigid 2,6-pyridine diamide linker, compounds **2** and **3** incorporate flexible 1,4-naphthalene and 9,10-anthracene dipropylamide linkers, respectively (Figure 1). The three linker architectures were chosen to determine the effect of a heteroaromatic moiety (compound **1**), increasing sizes of the aromatic core (compound **2** vs. compound **3**), and differences in the linker flexibility (compound **1** vs. compounds **2** and **3**) on the binding properties of  $\beta$ -cyclodextrin dimers. Such effects of flexibility can be seen in the energy-minimized structures of compounds **1-3**, obtained via PM3-level computations: whereas compound **1** exhibits an open structure as a result of its limited linker flexibility, compounds **2** and **3** are sufficiently flexible so as to fold back in on themselves and exhibit a closed, sandwich-type structure (Figure 3).

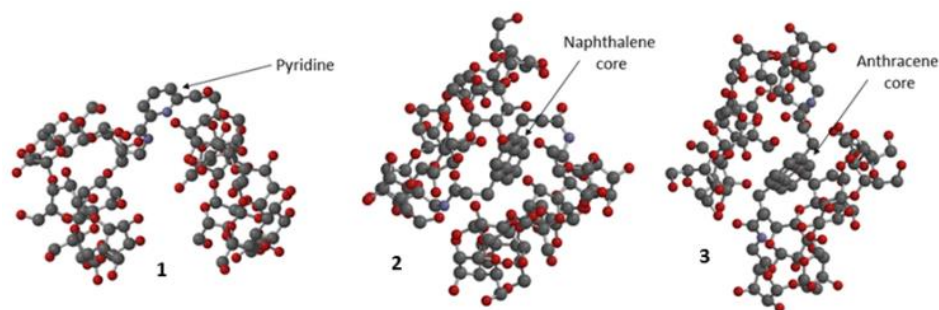


**Figure 3.** Energy minimized semi-empirical PM3-level calculations of hosts **1-3**.

Moreover, dimers **1-3** were fluorescent as a result of the incorporation of photophysically active linkers. While the integrated fluorescence intensities of compounds **2** and **3** increased linearly with increased dimer concentration, the fluorescence intensity of compound **1** displayed non-linear behaviour (see ESI). This is due to the rigid conformation of **1**, which facilitates intermolecular aggregation, especially at elevated concentrations in aqueous solutions. These



aggregated species have different fluorescence profiles and therefore complicate the observed spectroscopic trends (see ESI for more details)

Eight squaraine guests (compounds **4-11**, Figure 2) were synthesized via the condensation of squaric acid and *N*-substituted *N*-methylaniline, six of which incorporate straight chain alkyl substitutions from *n*-butyl to *n*-nonyl groups (**4-9**), with a cyclic substituent (compound **10**) and a *tert*-butyl substituted benzene (compound **11**) included in the other two structures (Figure 2). All of the cyclodextrins and squaraines were fully characterized via spectroscopic methods (see ESI for more details).

#### *Complexation-driven spectroscopic changes*

Squaraines can exist in their monomeric form under certain conditions, but are particularly prone to aggregation (as either H-aggregates or J-aggregates) due to their planar, conjugated structures (Figure 4).<sup>24</sup> Cyclodextrin complexation of the squaraines affects the equilibrium between the monomeric and aggregate states, with squaraines in  $\beta$ -cyclodextrin complexes stabilized in their monomeric states, and squaraines in  $\gamma$ -cyclodextrin complexes stabilized as dimers.<sup>25</sup> In our system, the monomeric squaraine species (shown in Figure 5 for compound **6**) shows a UV-visible absorption peak with a maximum around 650 nm (band **II**), the H-aggregate absorbs between 500 and 600 nm (band **I**), and the J-aggregate shows a strong absorption in the near-infrared spectral range (band **III**). These separate absorption profiles enable quantification of the prevalence of both H- and J-aggregates for varying squaraine concentrations in presence of dimers **1-3** (Figure 5).

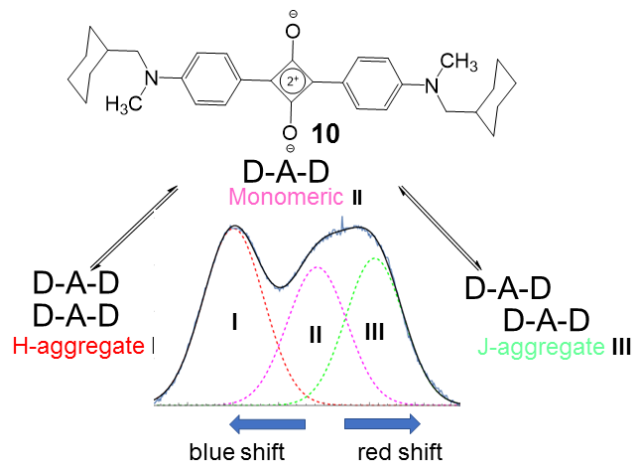


**Figure 4.** Illustration of Donor-Acceptor-Donor (D-A-D) structure of squaraine dye **10**, resulting in the formation of intense H-aggregate (red) and J-aggregate (green) bands in aqueous solution. The aggregate forms are in equilibrium with monomeric squaraine, giving rise to additional blue shifted (**I**) and red shifted (**III**) UV-vis absorption bands.

Of note, among squaraines **4-9** (with linear alkyl chains), the shorter alkyl chain-substituted squaraines **4-6** showed predominantly H-aggregate formation, whereas the longer alkyl chain-substituted squaraines **7-9** showed mostly J-aggregation. Of the two *N*-substituted squaraines with cyclic substituents (compounds **10** and **11**), H-aggregation was slightly more dominant than J-aggregation for compound **10**, whereas compound **11** favored J-aggregation. Moreover, the cyclodextrin dimers had a substantial effect in disrupting H-aggregation in the smaller squaraines, whereas lower effects were observed in the cyclodextrin-induced disruption of aggregation of the larger squaraines.

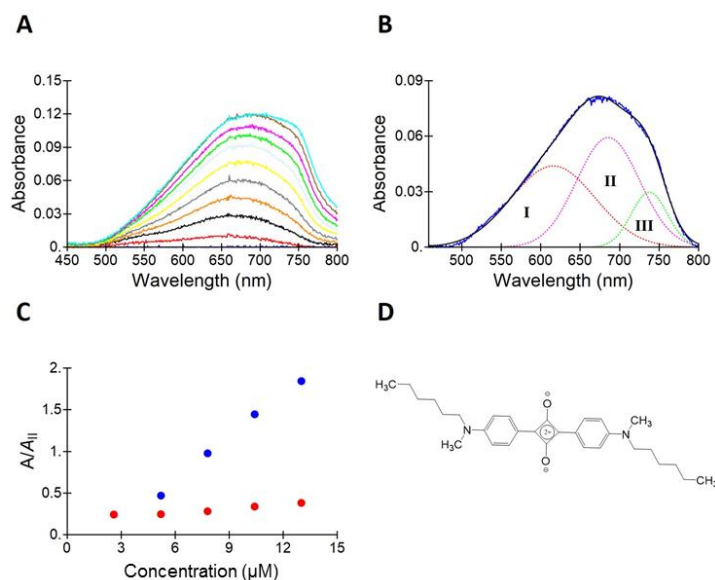


**Figure 5.** Spectral deconvolution process for investigation of H- and J- aggregate formation with increasing concentration of squaraine **6**. (A) UV-vis spectra of squaraine **6** ( $[6] = 1.3, 2.6, 3.9, 5.2, 6.5, 7.8, 9.1, 10.4, 11.7, 13.0 \mu\text{M}$ ); (B) Representative deconvoluted spectra of squaraine **6** ( $[6] = 7.8 \mu\text{M}$ , H-aggregate (I), Monomeric state (II), J-aggregate (III)); (C) Plot of H- aggregate (blue, ratio I/II) & J- aggregate (red, ratio III/II) against concentration for squaraine **6**; (D) Chemical structure of squaraine dye **6**.

While compounds **1** and **2** caused a significant decrease in the H-band of squaraine **6** (Figure 6A-C), virtually no aggregation was observed in the presence of compound **3** (Figure 6D). This effect of dimer **3** was also very pronounced for squaraine **10**, resulting in a marked decrease in both the H-aggregate and J-aggregate absorption bands (Figure 7). Squaraines with *N*-terminal substituents shorter than *n*-hexyl chains (*i.e.* compounds **4** and **5**) showed a sharp rise in the H-band with flexible dimer hosts **2** (for squaraine **4**) and **3** (for squaraines **4** and **5**) at low squaraine concentrations, which gradually diminished with increasing concentrations of the dye. This spectroscopic behavior can be explained by the ability of dimers **2** and **3** to bind two squaraines, forming a stable 1:2 host-guest complex.

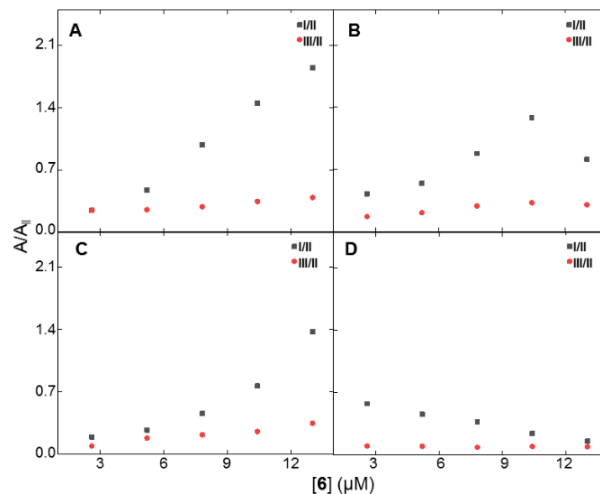


**Figure 6.** Plots of ratio of H-aggregate (I/II, grey) and J-aggregate (III/II, red) to monomeric bands against concentrations of Squaraine **6** for (A) control; (B) **1** (8 μM); (C) **2** (8 μM); (D) **3** (8 μM).

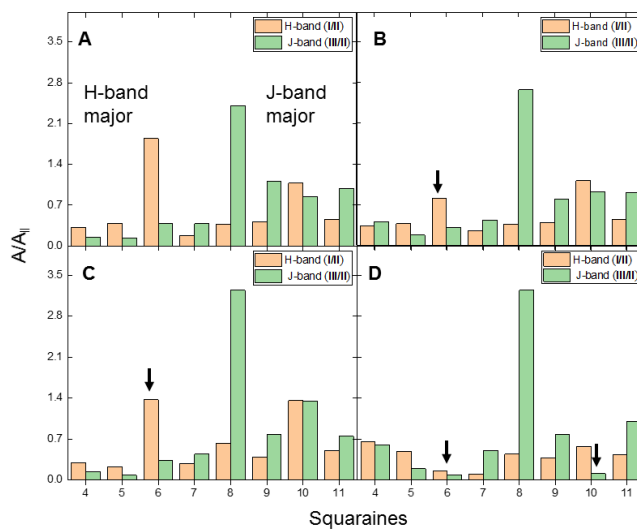


**Figure 7.** Bar graph showing the H and J-aggregate formations for various squaraines in presence of: (A) no cyclodextrin (control); (B) **1** (8 μM); (C) **2** (8 μM); and (D) **3** (8 μM). Downward arrows indicate the significant reduction of aggregate formation for squaraines **6** & **10**.

### *Complexation-induced effects on squaraine hydrolysis*

The hydrolyses of squaraine dyes **4-11** in aqueous solution at room temperature were studied in the presence of equimolar amounts of dimers **1-3** via UV-vis absorption spectroscopy. The hydrolytic decay follows an exponential first order reaction with time, which levels off at a certain concentration as per Equation 2.

$$A/A_0 = e^{-kt} + C \quad (\text{Equation 2})$$

where A is the integrated area of absorption of the dye at a given time,  $A_0$  is the initial integrated area of absorption of the dye, k is the exponential decay constant, and C is the integrated area of absorption of the dye at aggregate concentration of the decaying squaraine species (Figure 8A). The slowing down of the rate of hydrolysis is likely due to the increasingly insoluble nature of the aggregate formed in the solution.

The linear form of Equation 2 can be expressed in logarithmic form, as shown in Equation 3, below:

$$-\text{Log} (A/A_0 - C) = kt - \text{Log} (1-C) \quad (\text{Equation 3})$$

where the Y-intercept and the slope are given by  $-\text{Log} (1-C)$  and decay constant k respectively (Figure 8B).

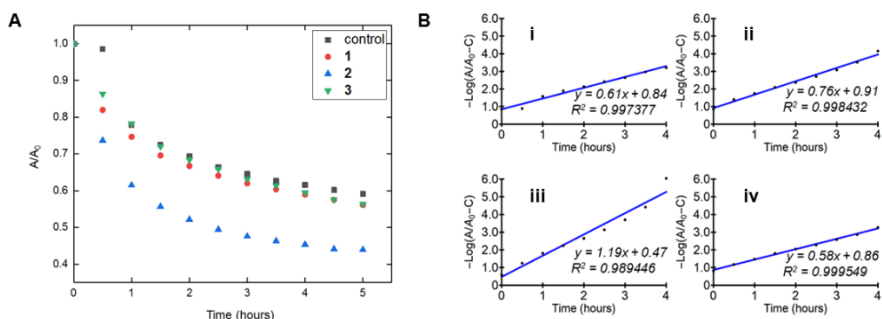


**Figure 8.** (A) Plot of  $A/A_0$  vs time for first order exponential hydrolytic decay of squaraine **6** measured at every half an hour over **5** hours. (B) Linear plot for first order exponential hydrolytic decay of squaraine **6** for (i) control; (ii) **1**; (iii) **2**; (iv) **3** (slope of the plot is a measure of the exponential decay constant  $k$ ; intercept  $c$  of the plot is a measure of the aggregate concentration  $C$ ).

In Equation 2, the two constants  $C$  and  $k$  are independent parameters that indicate the extent of hydrolysis indicating to the aggregate squaraine concentration, and the rate of hydrolysis provided by the first-order rate constant. They can be related to each other via the theoretical hydrolytic protection parameter  $T$ , defined in Equation 4, below:

$$T = -\text{Log}(1-C)/k \quad (\text{Equation 4})$$

where  $-\text{Log}(1-C)$  is the Y-intercept and  $k$  is the slope of the line. Higher  $T$  values correlate with greater degrees of hydrolytic protection, whereas lower  $T$  values indicate increased rates of hydrolytic decay.

We plotted the ratio of  $T$  in the presence of cyclodextrin hosts **1-3** ( $T_{\text{dimer}}$ ) to  $T$  in the absence of any host ( $T_{\text{control}}$ ) (Figure 9), noting that a ratio value of 1 would represent no effect of the host on rates or extents of hydrolysis. Notably, squaraines in the presence of host **1** demonstrated the lowest effects of complexation on hydrolysis behaviours (as indicated by ratios closest to 1). For

most squaraines, the presence of host **2** led to moderate protection from hydrolysis, indicated by ratio values slightly higher than 1, and host **3** conferred substantial protection to the squaraine guests from hydrolysis.

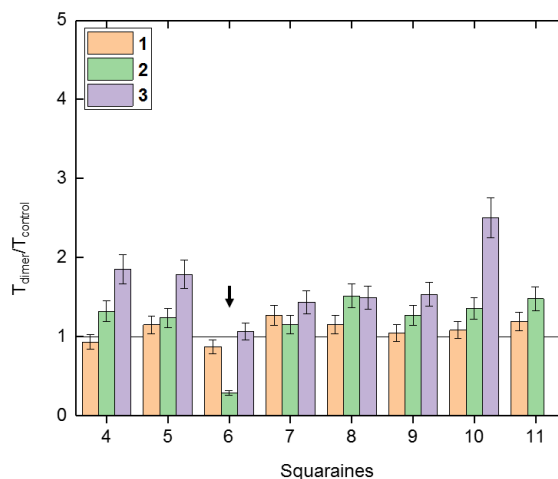


**Figure 9.** Bar graph plot of the ratio of hydrolytic protection ( $T_{\text{dimer}}/T_{\text{control}}$ ) of squaraines in presence of the dimers (**1-3**) ( $T$ , defined as the hydrolytic protection parameter is given as the ratio of the Y-intercept to the slope of the linear plot;  $T = -\text{Log}(1-C)/k$ ) (downward arrows indicate the larger extent of hydrolytic decay for the squaraine **6**; calculated  $T$  values are measured from the Y-intercept and slope  $k$  of the best fitting linear plot of average  $A/A_0$  values of four trials; errors are calculated from standard deviations of  $c$  and  $k$  from the linear plot; error bars are within 10% of the calculated  $T$  values).

Notably, squaraine **6** in the presence of host **2** demonstrated an exception to this general trend, and displayed markedly increase hydrolysis rates in the presence of the host compared to in its absence. This aberrant behaviour is a result of the optimal fit between the squaraine **6** guest and the  $\beta$ -cyclodextrin host cavities, which enables each  $\beta$ -cyclodextrin unit to activate the electrophilic squaraine for hydrolysis via hydrogen-bonding interactions with the oxoanions upon complexation (Figure 10). Host **2** was particularly effective at increasing the rates

of hydrolysis, as a result of the greater conformational flexibility of the linker in compound **2**, which enables the  $\beta$ -cyclodextrin units to access the squaraine core and promote hydrolysis. Although dimer **3** has a relatively similar architecture, the tethering of the methylene linkers to the 9,10-positions of the anthracene moiety constrains the conformational flexibility.

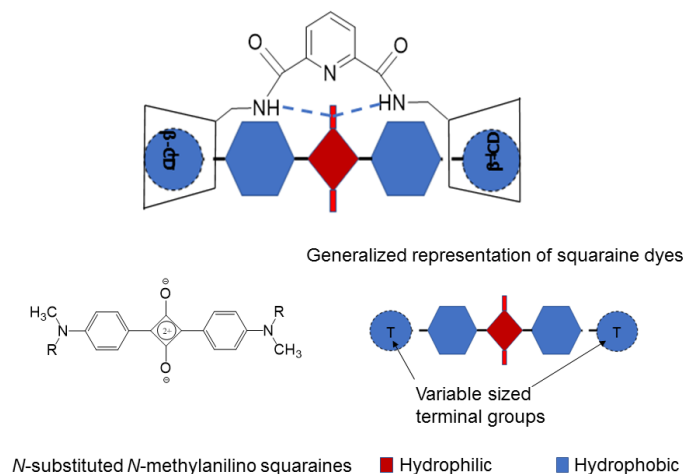


**Figure 10.** Schematic representation of the host-guest association in dimer host **1**, showing the H-bonding interactions of the two amide linkers to the oxoanion of the squaraine core.

A particularly high degree of hydrolytic protection was observed for squaraines **10** and **11** with host **3**, which is a result of the conformational changes induced by the binding of the bulky cycloalkyl and aromatic substituents in the cyclodextrin cavities. These changes further stabilize the dimer-squaraine complex, resulting in highly effective protection. Both complexes (host **3** + guest **10** and host **3** + guest **11** (ESI)) were studied computationally and shown to have different conformations than the  $n$ -alkyl substituted guest **6**.

Another combination of note was squaraine **11** with dimer **3**, in which the hydrolytic decay of the squaraine exhibited zero-order behaviour. This is likely



since the complexation-induced conformational changes minimize complex dissociation, which in turn limits the availability of free squaraine **11**. As a result, the rate of hydrolysis becomes independent of the overall squaraine concentration. In fact, all hosts **1-3** when complexed with squaraine **11** led to near zero-order behaviour as well, pointing to the likelihood of the interactions between  $\beta$ -cyclodextrin and the *tert*-butylphenyl substituent as key for inducing this behaviour.

For all squaraines except for **6** and **7**, which are particularly easily hydrolysed in the presence of dimer **2** due to optimal steric matching, the general trend in the complexation-induced hydrolytic protection follows the order **3** > **2** > **1**. This trend can be explained based on the conformation of the host-guest (dimer-squaraine) complex. While squaraines **4** and **5** form stable 1:2 host-guest complex with **3**, squaraines **6-9** thread into the  $\beta$ -cyclodextrin cavities and adapt a pseudo-rotaxane geometry. Moreover, as a result of the closed structures of  $\beta$ -cyclodextrin dimer hosts **2** and **3**, they are more able than host **1** to protect the electrophilic squaraine core against hydrolysis.

#### *Fluorescence titration on cyclodextrin dimer hosts*

The guest-induced fluorescence changes of the dimers **1-3** ([dimer] =  $5 \times 10^{-7}$  M) was studied in presence of increasing concentrations of squaraines **4-11**.<sup>26</sup> Importantly, the observed behaviours are intimately dependent on the specific interactions between each squaraine guest and cyclodextrin host, which makes general trends challenging to elucidate.

**Table 1.** Calculated association constant values for  $\beta$ -cyclodextrin dimer hosts (**1-3**) for squaraines (**4-11**). Association constant values are calculated via fluorescence titration of the dimers ( $5 \times 10^{-7}$  M) with increasing concentrations of squaraine guests (**4-11**) in aqueous PBS solution.

Squaraine guests	<b>1</b>	<b>2</b>	<b>3</b>
<b>4</b>	<sup>b</sup> 7.5 (1.3) $\times 10^{14}$	<sup>b</sup> 8.8 (2.4) $\times 10^{13}$	<sup>b</sup> 2.3 (0.4) $\times 10^{13}$
<b>5</b>	<sup>a</sup> 2.7 (0.5) $\times 10^6$	<sup>a</sup> 2.6 (0.4) $\times 10^6$	<sup>b</sup> 4.5 (1.0) $\times 10^{13}$
<b>6</b>	<sup>a</sup> 3.5 (0.5) $\times 10^6$	<sup>a</sup> 3.5 (1.2) $\times 10^5$	<sup>a</sup> 2.3 (0.1) $\times 10^8$
<b>7</b>	<sup>a</sup> 1.5 (0.7) $\times 10^6$	<sup>a</sup> 2.1 (0.8) $\times 10^5$	<sup>a</sup> 4.1 (0.5) $\times 10^6$
<b>8</b>	<sup>a</sup> 4.5 (0.8) $\times 10^6$	<sup>a</sup> 3.1 (0.1) $\times 10^5$	<sup>a</sup> 3.2 (0.4) $\times 10^7$
<b>9</b>	<sup>a</sup> 6.6 (0.8) $\times 10^6$	<sup>a</sup> 2.4 (0.7) $\times 10^5$	<sup>a</sup> 8.1 (0.5) $\times 10^5$
<b>10</b>	<sup>a</sup> 1.7 (0.4) $\times 10^5$	<sup>a</sup> 4.2 (1.0) $\times 10^5$	<sup>a</sup> 2.4 (0.6) $\times 10^6$
<b>11</b>	<sup>a</sup> 1.2 (0.2) $\times 10^7$	<sup>a</sup> 1.0 (0.1) $\times 10^6$	<sup>a</sup> 3.0 (0.2) $\times 10^6$

<sup>a</sup>Association constant ( $M^{-1}$ ) values are reported for 1:1 host-guest complex formation in aqueous (phosphate buffer) solution; <sup>b</sup>Association constant ( $M^{-2}$ ) values are reported for 1:2 host-guest complex formation in aqueous (phosphate buffer) solution. All values are calculated as an average of at least three trials. Standard deviations (errors) are included in parentheses.

While the fluorescence intensity of dimer **1** decreased with increasing concentrations of squaraine guests (for all guests except compounds **4** and **10**), the intensities of dimers **2** and **3** increased with increasing amounts of squaraine (except for guests **9-11** with dimer **3**). The smallest squaraine **4** formed stable 1:2 host-guest association complex with all three hosts, while **5** exhibited a 1:2 binding with only **3**. In contrast, the bulkier squaraines (**6-11**) formed 1:1 host-guest binding model with all the three dimers (**1-3**) in all cases (Table 1).

The association constant values for 1:2 host-guest complexes of squaraine **4** followed the trend **1**>**2**>**3**, with the  $K_1$  (association constant of first guest binding event) value several orders of magnitude lower than that of  $K_2$  (association constant value of the second guest binding event). This means that the binding of the first squaraine **4** guest renders the host cavity much more receptive to the second guest. While the association constant values for most of the cyclodextrin-

squaraine combinations were on the order of  $10^5$ - $10^7$   $M^{-1}$ , squaraine **6** exhibited extraordinary affinity for dimer host **3**, with calculated association constants of  $10^8$   $M^{-1}$ . The association constant values are comparable in magnitude to previously reported values in the literature for any other complimentary guests with cyclodextrin dimers.<sup>28</sup>

Among the straight chain alkyl-substituted squaraines, compounds **5** and **6** have optimal sizes and hydrophobicities to bind in hosts **2** and **3**, respectively. Squaraines with longer alkyl chain substituents (**7-9**) exhibited association constants that were one and two orders of magnitude lower with dimers **2** and **3**, respectively. This trend is likely due to less optimal steric matching with the host cavity for the larger squaraines.

A comparison of squaraine guests **10** and **11** revealed that compound **11** exhibited higher association constants because of the *tert*-butylphenyl substituent, which has been reported to bind strongly in  $\beta$ -cyclodextrin ( $K_a = 1.6 \times 10^4$   $M^{-1}$ ).<sup>27</sup> Despite structural similarities between hosts **2** and **3**, the association constants for compound **2** are low for most of the squaraines compared to those observed for compound **3** (Figure 11). This differential behaviour may be a result of the greater hydrophobicity of the anthracene unit in compound **3**, which in turn contributes to increased cooperativity of the  $\beta$ -cyclodextrin units in forming a stable 1:1 host-guest complex.

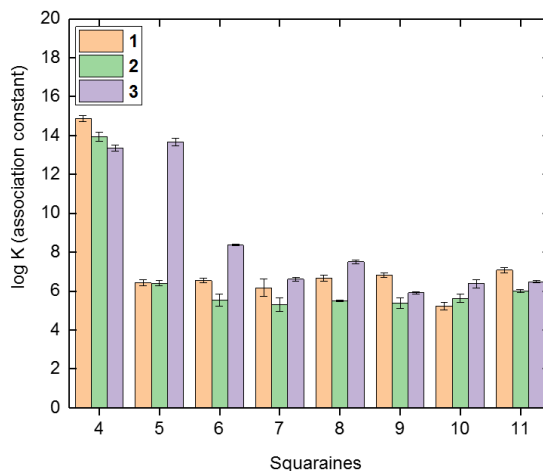


**Figure 11.** Plot of log K (association constants) versus *N*-substituted *N*-methylanilino squaraines (**4-11**) for  $\beta$ -cyclodextrin dimer hosts (**1-3**). Values for squaraine **4** (for all hosts) and squaraine **5** (for host **3**) are for 1:2 host-guest complexes (Error bars included for at least three trials).

The changes in the fluorescence of the dimer **3** upon addition of squaraine **6** and **10** were further analysed to understand the different complexation modes of the squaraine guests. While compound **6** is an example of the *n*-alkyl squaraines that caused an increase in the fluorescence of dimer **3**, compound **10** is an example of the bulky *N*-substituted squaraines that caused a decrease in the fluorescence emission of compound **3** with complex formation. These opposing trends were explained by computational energy minimized models of host-guest complexes of host **3** with guest **6** compared to host **3** with guest **10**. Unlike flexible *n*-alkyl substituents in compound **6**, the bulky substituent in compound **10** causes a significant conformational change of host **3**, resulting in the anthracene-containing linker interacting closely with the electron deficient core of guest **10** and facilitating excited state energy transfer. This host-guest conformation was also noted for **11** with bulky *tert*-butylphenyl substituents. In contrast,

complexation of guest **6** leads to a relatively open structure, where the anthracene core is displaced from the host cavity (Figure 12).

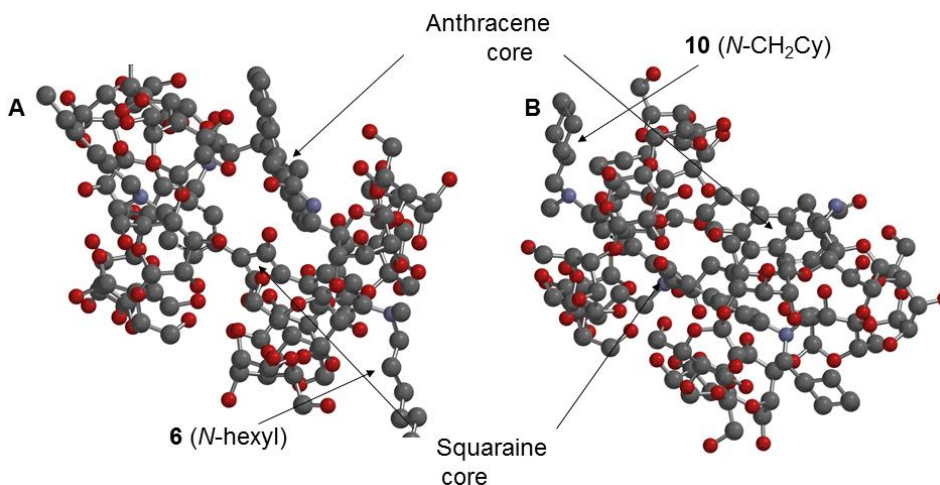


**Figure 12.** Energy minimized (semi-empirical PM3) computational models for (A) squaraine-dimer combination (**3** + **6**); (B) squaraine-dimer combination (**3** + **10**), illustrating the different location of the anthracene core w.r.t the electrophilic squaraine core in both the cases.

### *Computational Modeling*

The stabilities of the 1:1 cyclodextrin dimer-squaraine complexes were calculated using PM3 calculations (with a semi-empirical force field) for host **3** with guests **6**, **10** and **11**. Further comparisons were drawn between complexes formed by squaraine **6** with all of the hosts to determine the oxoanion-amide distances in host-guest complexes (Table 2). The calculated negative stabilization energies indicate that the squaraine guests thread inside the host cavity (**1-3**) to form a stable host-guest association complex. Complexes **3+11** and **3+10** were found to be much more stable than their *n*-hexyl counterpart **6**.

**Table 2.** Calculated stabilization energy values of  $\beta$ -cyclodextrin dimer hosts (**1-3**) with squaraine dye guest **6**, **10** (with **3**) and **11** (with **3**). Energy minimized models were carried out using PM3 level calculations with semi-empirical force field.

Energy of formation of the host, $H$ ( $E_{Host}$ , $KJ/mol$ )	Energy of formation of guest, $G$ ( $E_{Guest}$ , $KJ/mol$ )	Energy of formation of $H+G$ ( $E_{Complex}$ , $KJ/mol$ )	Stabilization energy of $H+G$ ( $\Delta E_{Complex}$ $KJ/mol$ )	Distance of the 1 <sup>st</sup> oxoanion-amide pair ( $d_1$ , Å)	Distance of the 2 <sup>nd</sup> oxoanion-amide pair ( $d_2$ , Å)	$d_2-d_1$
	<b>11</b> = 215.4040	<b>3+11</b> = -11497.6860	-52.9498	4.320	8.687	4.367
<b>3</b> = -11660.1402	<b>10</b> = -3.3860	<b>3+10</b> = -11689.1721	-25.6459	2.685	6.990	4.305
	<b>6</b> = -42.1011	<b>3+6</b> = -11719.5251	-17.2838	3.097	7.446	4.349
<b>2</b> = -11735.8080	<b>6</b> = -42.1011	<b>2+6</b> = -11841.2643	-63.3552	5.416	6.283	0.867
<b>1</b> = -11814.9656	<b>6</b> = -42.1011	<b>1+6</b> = -11890.9368	-33.8701	5.590	7.896	2.306

The distances of the two oxoanion-amide pairs ( $d_1$  and  $d_2$ ) were compared to determine the precise position of the electrophilic squaraine core. Two possible modes of interaction are possible: (a) where the two amide groups of the linker interact closely with one oxoanion of the squaraine core, resulting in a significant difference between the two measured distances ( $d_2 - d_1$ ) (*I*, Figure 13); or (b) where the two amide groups of the linkers interact equally with both oxoanions of the squaraine core, resulting in roughly equivalent distances (*II*, Figure 13). The dual hydrogen bonding interactions in the second case provide substantially more electrophilic activation compared to the first possibility. The observed trend in the difference of the measured distances ( $d_2 - d_1$ ) for squaraine **6** for all the complexes was **3**>**1**>**2**, and supports option b as the more likely mode of interaction (**2**-SQ, *II*, Figure 13) This observation explains the anomalously high rate of hydrolysis of squaraine **6** in presence of host **2**, owing to the enhanced

electron deficient nature of the squaraine core making it susceptible to hydrolytic attack.

Synthetic tetralactam macrocycles based squaraine rotaxanes have been reported in the literature with association constants 1000 times greater in aqueous solution as compared to organic solvents.<sup>28</sup> Unlike tetralactam macrocycles, where the rational design of the macrocycles is primarily targeted at hydrogen bonding-induced stabilization of the squaraine core, the complexation of squaraines in  $\beta$ -cyclodextrin dimers is entirely driven by hydrophobicity of the squaraine guests

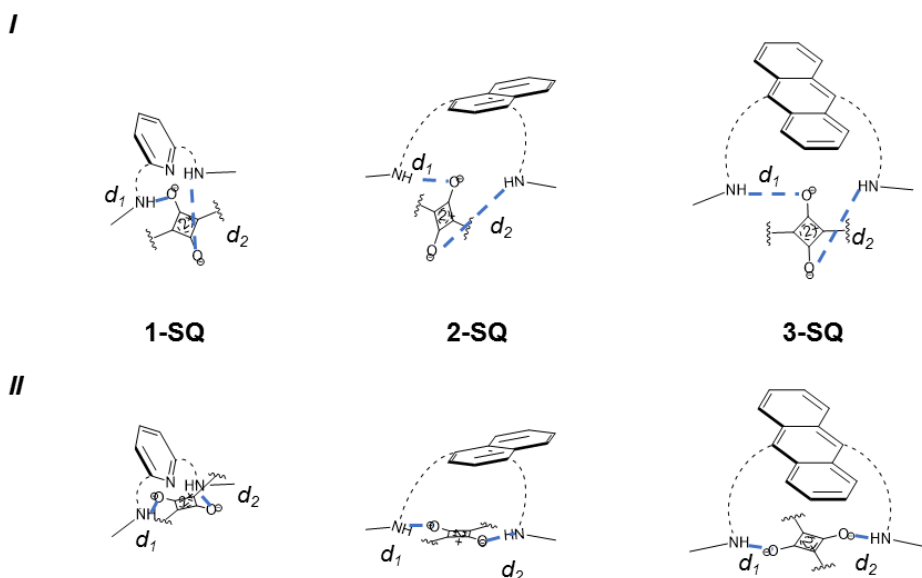


**Figure 13.** Possible modes of squaraine core - linker interactions resulting in a significantly large (case **I**) and minimum (case **II**) difference in the measured oxoanion-amide distances ( $d_2 - d_1$ ).

(**4-11**) in the aqueous medium, but results in substantial hydrogen bonding interactions. Of the three hosts investigated herein, **3** is most efficient, both in altering the aggregation properties (**6** and **10**), and in inhibiting the hydrolytic decay (**10** and **11**) of the squaraines. The hydrophobic nature of the complexation

of **3** and **6** was further evident from the two separate spots visible on the TLC plate after eluting an aqueous solution of **3** and **6** with a mixture (1:9) of methanol in chloroform (see ESI). These results mean that the squaraine guest is not bound in the host in the absence of water, because of the inability to use hydrophobic binding under such conditions. Most previous work on squaraine encapsulation, in contrast, which relies on hydrogen bonding of the oxoanions by the macrocycles, results in one spot on the TLC plate after elution in an organic solvent.

The ability of the host **3** to disrupt aggregate formation of squaraine dye **6** is manifested in the unique coloration of the complex as compared to free squaraine dye in aqueous solution (Figure 14).

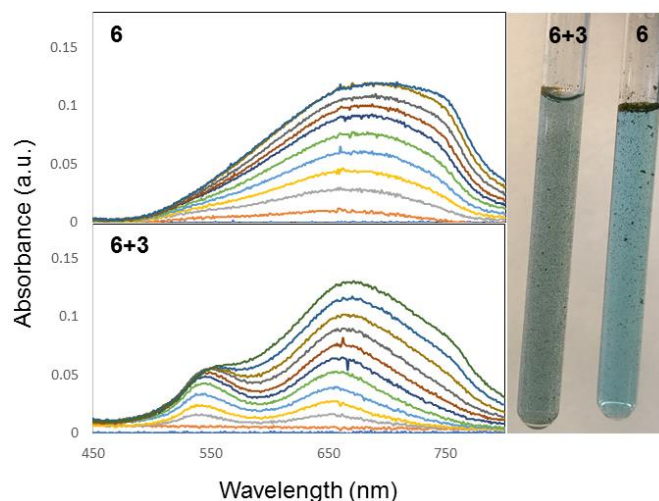


**Figure 14.** Illustration of the disruption of aggregates of squaraine **6** in the presence of host **3**, resulting in markedly reduced insoluble aggregate and unique coloration of the complexed dye in aqueous solution (Solution of **6** (1.0 mg) +**3** (1.0 mg, 0.2 eq.) compared against **6** (1.0 mg) in 10 vol. % THF in aqueous solution).



## CONCLUSION

In conclusion, we have synthesized a series of three novel  $\beta$ -cyclodextrin dimers. These three variable architectures have been synthesized through variation of the linker moieties tethering the two individual  $\beta$ -cyclodextrin units, which alters their flexibilities and associated binding properties. The incorporation of fluorescent anthracene and naphthalene units in these flexible linkers render the  $\beta$ -cyclodextrin dimer hosts both photophysically active and conformationally flexible. We also incorporated a rigid heteroaromatic (pyridyl group) linker to compare the host properties against the flexible dimer hosts, and observed that the structural adaptations exhibited by the flexible dimers directly enables unprecedentedly high association constant values for complimentary guest molecules like linear squaraine dyes. A remarkable control of photophysical properties and chemical reactivity of squaraine dyes has been shown via hydrophobic complexation with the dimer hosts in aqueous solution, which can be utilized in selective and sensitive colorimetric sensing of environmentally toxic analytes.

## ACKNOWLEDGEMENTS

In memory of a giant of biomimetic and cyclodextrin chemistry and the former Ph.D. advisor of M.L., Professor Ronald Breslow.

## NOTES AND REFERENCES

1. (a) Schmidt, B. V. K. J; Barner-Kowollik, C. *Angew. Chem. Int. Ed.* **2017**, *56*, 8350-8369. (b) Szente, L.; Szeman, J. *Anal. Chem.* **2013**, *85*, 8024-8030.

2. (a) Breslow, R.; Halfon, S. *Proc. Natl. Acad. Sci. U.S.A.* **1992**, *89*, 6916-6918. (b) Rideout, D. C.; Breslow, R. *J. Am. Chem. Soc.* **1980**, *102*, 7816-7817. (c) Schneider, H. -J. *Acc. Chem. Res.* **2015**, *48*, 1815-1822.
3. Isaacs, L. *Acc. Chem. Res.* **2014**, *47*, 2052-2062. (b) Isaacs, L. *Chem. Commun.* **2009**, 619-629.
4. Nau, W. M.; Florea, M.; Assaf, K. I. *Israel J. Chem.* **2011**, *51*, 559-577.
5. (a) Tamgho, I. -S.; Chaudhuri, S.; Verderame, M.; DiScenza, D. J.; Levine, M. *RSC Adv.* **2017**, *7*, 28489-28493. (b) Radaram, B.; Levine, M. *Eur. J. Org. Chem.* **2015**, 6194-6204. (c) B. Radaram, J. Potvin and M. Levine, *Chem. Commun.* **2013**, *49*, 8259-8261.
6. (a) Ajami, D.; Rebek, J. *Topics Curr. Chem.* **2012**, *319*, 57-78. (b) Ajami, D.; Rebek, J. *Acc. Chem. Res.* **2013**, *46*, 990. (c) Murray, J.; Kim, K.; Ogoshi, T.; Yao, W.; Gibb, B. C. *Chem. Soc. Rev.* **2017**, *46*, 2479. (d) Liu, S.; Gibb, B. C. *Chem. Commun.* **2008**, 3709-3716.
7. Mako, T.; Marks, P.; Cook, N.; Levine, M. *Supramol. Chem.* **2012**, *24*, 743-747.
8. Serio, N.; Miller, K.; Levine, M. *Chem. Commun.* **2013**, *49*, 4821-4823.
9. Serio, N.; Roque, J.; Badwal, A.; Levine, M. *Analyst* **2015**, *140*, 7503-7507.
10. DiScenza, D. J.; Levine, M. *Supramol. Chem.* **2016**, *28*, 881-891.
11. Serio, N.; Chanthalya, C.; Prignano, L.; Levine, M. *ACS Appl. Mater. Interfaces* **2013**, *5*, 11951-11957.
12. (a) Serio, N.; Moyano, D. F.; Rotello, V. M.; Levine, M. *Chem. Commun.* **2015**, *51*, 11615-11618. (b) Serio, N.; Chanthalya, C.; Prignano, L.; Levine, M. *Supramol. Chem.* **2014**, *26*, 714-721.
13. (a) DiScenza, D. J.; Verderame, M.; Levine, M. *Clean: Soil, Air, Water* **2016**, *44*, 1621-1627. (b) DiScenza, D. J.; Levine, M. *New J. Chem.* **2016**, *40*, 789-793.
14. (a) Iijima, K.; Aoki, D.; Sogawa, H.; Asai, S.; Takata, T. *Polym. Chem.* **2016**, *7*, 3492-3495. (b) Pham, D. -T.; Nguyen, H. -T.; Lincoln, S. F.; Wang, J.; Guo, X.; Easton, C. J.; Prud'homme, R. K. *J. Polym. Sci. A Polym. Chem.* **2015**, *53*, 1278-1286. (c) Aime, S.; Gianolio, E.; Arena, F.; Barge, A.; Martina, K.; Heropoulos, G.; Cravotto, G. *Org. Biomolecular Chem.* **2009**, *7*, 370-379.
15. Kauscher, U.; Ravoo, B. J. *Beilstein J. Org. Chem.* **2016**, *12*, 2535-2542.

16. (a) Beverina, L.; Sassi, M. *Synlett* **2014**, 25, 477-490. (b) Beverina, L.; Salice, P. *Eur. J. Org. Chem.* **2010**, 1207-1225. (c) Sreejith, S.; Carol, P.; Chithra, P.; Ajayaghosh, A. *J. Mater. Chem.* **2008**, 18, 264-274.
17. Ballestas-Barrientos, A. R.; Woodward, A. W.; Moreshead, W. V.; Bondar, M. V.; Belfield, K. D. *J. Phys. Chem. C* **2016**, 120, 7829-7838.
18. Wu, I. -C.; Yu, J.; Ye, F.; Rong, Y.; Gallina, M. E.; Fujimoto, B. S.; Zhang, Y.; Chan, Y. -H.; Sun, W.; Zhou, X. -H.; Wu, C.; Chiu, D. T. *J. Am. Chem. Soc.* **2015**, 137, 173-178.
19. Hemmer, E.; Acosta-Mora, P.; Mendez-Ramos, J.; Fischer, S. *J. Mater. Chem. B* **2017**, 5, 4365-4392.
20. (a) Arun, K. T.; Jayaram, D. T.; Avirah, R. R.; Ramaiah, D. *J. Phys. Chem. B* **2011**, 115, 7122-7128. (b) Das, S.; Thomas, K. G.; George, M. V.; Kamat, P. V. *J. Chem. Soc. Faraday Trans.* **1992**, 88, 3419-3422.
21. (a) Lovrinovic, M.; Niemeyer, C. M. *ChemBioChem* **2007**, 8, 61-67. (b) Tang, W.; Ng, S. *Nature Protocols* **2008**, 3, 691-697.
22. (a) Cangelosi, V. M.; Sather, A. C.; Zakharov, L. N.; Berryman, O. B.; Johnson, D. W. *Inorganic Chem.* **2007**, 46, 9278-9284. (b) Costa, D.; Fernandes, E.; Santos, J. L. M.; Pinto, D. C. G. A.; Silva, A. M. S.; Lima, J. L. F. C. *Anal. Bioanal. Chem.* **2007**, 387, 2071-2081. (c) Ryu, D.; Park, E.; Kim, D. -S.; Yan, S.; Lee, J. Y.; Chang, B. -Y.; Ahn, K. H. *J. Am. Chem. Soc.* **2008**, 130, 2394-2395. (d) Zeng, Z. -Y.; He, Y. -B.; Wu, J. -L.; Wei, L. -H.; Liu, X.; Meng, L. Z.; Yang, X. *Eur. J. Org. Chem.* **2004**, 2888-2893. (e) Fu, Y.; Li, H.; Hu, W.; Zhu, D. *Chem. Commun.* **2005**, 3189-3191. (f) Icli, S.; Demic, S.; Dindar, B.; Doroshenko, A. O.; Timur, C. *J. Photochem. Photobiol. A Chem.* **2000**, 136, 15-24.
23. Huang, M. J.; Quan, Z.; Liu, Y. *Int J Quantum Chem.* **2009**, 109(1), 81-90.
24. (a) McKerrow, A. J.; Buncel, E.; Kazmair, P. M. *Can. J. Chem.* **1995**, 73, 1605-1615. (b) Chen, G.; Sasabe, H.; Lu, W.; Wang, X.; Kido, J.; Hong, Z.; Yang, Y. *J. Mater. Chem. C* **2013**, 1, 6547-6552.
25. Chen, H.; Herkstroeter, W. G.; Perlstein, J.; Law, K. Y.; Whitten, D. G. *J. Phys. Chem.* **1994**, 98, 5138-5146.
26. Narita, M.; Itoh, J.; Kikuchi, T.; Hamada, F. *J. Inclusion Phenom. Macrocyclic Chem.* **2002**, 42, 107-114.
27. Breslow, R.; Halfon, S.; Zhang, B. *Tetrahedron* **1995**, 51, 377-388.

28. (a) Gassensmith, J. J.; Arunkumar, E.; Barr, L.; Baumes, J. M.; DiVittorio, K. M.; Johnson, J. R.; Noll, B. C.; Smith, B. D. *J. Am. Chem. Soc.* **2007**, *129*, 15054-15059.  
(b) Ke, C.; Destecroix, H.; Crump, M. P.; Davis, A. P. *Nat. Chem.* **2012**, *4*, 718-723.  
(c) Jarvis, T. S.; Collins, C. G.; Dempsey, J. M.; Oliver, A. G.; Smith, B. D. *J. Org. Chem.* **2017**, *82*, 5819-5825. (d) Liu, W.; Peck, E. M.; Hendzel, K. D.; Smith, B. D. *Org. Lett.* **2015**, *17*, 5268-5271. (e) Peck, E. M.; Liu, W.; Spence, G. T.; Shaw, S. K.; Davis, A. P.; Destecroix, H.; Smith, B. D. *J. Am. Chem. Soc.* **2015**, *137*, 8668-8671.

**Synthetic  $\beta$ -cyclodextrin dimers for squaraine binding: Effect of host architecture on photophysical properties, aggregate formation and chemical reactivity**

**MATERIALS AND METHODS**

All of the starting materials, reagents, and solvents were purchased from Sigma Aldrich, Acros Organics, TCI chemicals, Alfa Aesar, or Fisher Scientific, and were used as received. Reactions were monitored via analytical thin layer chromatography (TLC) using polyester backed TLC plates. Visualization was accomplished with UV light at 254 nm. Flash column chromatography was performed with SiliaFlash F60 (230-400 mesh) or using automated flash chromatography (Yamazen Smart Flash AI-580S & AKROS). UV-VIS spectra were recorded on a Shimadzu UV-3600 Plus spectrophotometer. Fluorescence spectra were recorded on a Shimadzu RF-6000 spectrophotometer with 3.0 nm excitation slit widths and 3.0 nm emission slit widths.

$^1\text{H}$  and  $^{13}\text{C}$ -NMR spectra were taken on a Bruker 400 MHz spectrometer and were recorded in  $\text{D}_2\text{O}$ ,  $\text{CDCl}_3$  and  $\text{DMSO-}d_6$  at room temperature. Chemical shifts ( $\delta$ ) are reported in parts per million relative to  $\text{D}_2\text{O}$  at 4.79 ppm, chloroform at 7.26 ppm, dimethyl sulfoxide at 2.59 ppm, or to tetramethylsilane (TMS) at 0.00 ppm for  $^1\text{H}$  NMR and relative to  $\text{CDCl}_3$  at 77.16 ppm or  $\text{DMSO}$  at 40.76 ppm for  $^{13}\text{C}$  NMR spectra.

Mass spectra for compounds **1**, **2** and **3** were recorded in a Bruker Omnimflex MALDI-TOF instrument (using 2,5-dihydroxybenzoic acid as a matrix) and in a Waters Q-TOF micro-mass spectrometer at the Department of Chemistry Instrumentation Facility

(DCIF) at the Massachusetts Institute of Technology (MIT), with samples run by Dr. Li Li.

#### METHODS FOR MASS SPECTROMETRY DETECTION

Compounds **4**, **6** and **10** were dissolved in a mixture of THF to make 1 mg/mL solutions, and further diluted to 5 µg/mL in methanol/water (50/50 vol/vol) to produce an analytical standard. The analytical standard was infused into a ThermoScientific LTQ Orbitrap XL™ mass spectrometer at a rate of 15 µL/min using an electrospray ionization source in positive ion mode. The rest of the ionization sources and ion optics parameters were as follows: sheath gas 25, auxiliary gas 6, spray voltage 5 kV, capillary temperature 275 °C, capillary voltage 47 V, tube lens 165 V, multipole 00 offset -5.5 V, lens 0 -6.0 V, multipole 0 offset -5.75 V, lens 1 -10.0 V, gate lens -46.0 V, multiple 1 offset -19.5 V, multipole RF amplitude 400.0 V, front lens -6.75 V. The mass spectra were collected using full scan mode with a resolution of 30000 in the range between 60 and 600 amu. The spectra were averaged over 2 microscans with 10.0 ms maximum injection time and  $2.0 \times 10^5$  ions for AGC target settings.

#### METHODS FOR SPECTRAL DECONVOLUTION AND CURVE FITTING

All spectral analysis was done using custom codes written in Mathematica 11.0.1.0 (Wolfram Research, Champaign, IL).

##### **Deconvolutions**

The UV spectra were subjected to a piecewise linear background subtraction method. The selection of spectral positions to run the background were identified by a custom

threshold approach. After the background spectral subtraction, the spectral signal was fitted using “NonlinearModeFit” command (method set to “automatic”) with three gaussian functions,  $A \cdot \text{Exp} \frac{(x-\mu)^2}{2\sigma^2}$ , where A,  $\mu$ ,  $\sigma$  and x have their usual meanings—amplitude, mean, standard deviation, and wavelength respectively.

### **Linear Fits**

All linear fits were done with “NonlinearModeFit” command (method set to “automatic”) using the form  $-\log \left[ \frac{A}{A_0} - c \right] = k \cdot x$ , where c, A,  $A_0$ , k and x refer to the integrated absorption at the aggregate concentration, concentration at time t, concentration at time zero, rate constant and the independent variable respectively. The value of c is found from the corresponding exponential fit.

### **Titration Curve Fits**

All fluorescence titration data fits were done with Solver.xlam using “GRG-Nonlinear” method in Excel 2017 using the 1:1 and 1:2 supramolecular titration equations.

## **METHODS FOR COMPUTATIONAL EXPERIMENTS**

All computational modelling was done using commercially available Spartan software, version 16. To obtain the molecular models, the structures were first energy-minimized using multiple runs of molecular dynamics simulations. Next, these structures were submitted to MMF94 molecular mechanics methods, and the minimized structure from this was further optimized and minimized using a PM3-level semi-empirical force field in a gaseous medium. The energy obtained from these calculations were used to calculate the stabilization energy of the complex using the equation below<sup>1</sup>:

$$\Delta E_{\text{complex}} = E_{\text{Complex}} - E_{\text{Host}} - E_{\text{Guest}} \quad (\text{Equation S1})$$

where  $\Delta E_{complex}$  is the stabilization energy of the host-guest complex,  $E_{complex}$  is the energy of formation of the host-guest complex,  $E_{Host}$  is the energy of formation of the  $\beta$ -cyclodextrin dimer hosts, and  $E_{Guest}$  is the energy of formation of the squaraine guest.

## METHODS FOR FLUORESCENCE TITRATION EXPERIMENTS

6.25  $\mu$ L of a 0.5 mg/mL (0.2 mM) aqueous solution of the host dimer (**1-3**) was added to a cuvette containing 2.5 mL of aqueous phosphate-buffered saline solution (PBS, buffered at pH 7.4). The fluorescence spectra of this solution were measured after being titrated with solutions of the guest dyes (0.2 mg/mL solution in THF) at the following addition volumes: 0.0, 1.5, 3.0, 4.5, 6.0, 7.5, 9.0, 10.5, 12.0, 13.5, 15.0, 20.0, 30.0, 40.0 and 50.0  $\mu$ L dye solutions. Each measurement was repeated for four trials. Both the excitation slit width and the emission slit width were 3.0 nm. All fluorescence spectra were integrated vs. wavenumber on the X-axis using OriginPro Version 9.1.

The concentration range scanned for each dye against the host concentration (approximately 0.5  $\mu$ M, depending on the host structure) was further refined based on the association constant values of the host-guest combination. In particular, for association constant values greater than  $10^6 \text{ M}^{-1}$ , the guest concentration was reduced to a sub-stoichiometric (*i.e.* 0 -0.5  $\mu$ M) range with respect to the host. This was achieved by further diluting the stock guest solution (to a final concentration of 0.04 mg/mL) and adjusting the volume additions accordingly.



**Table S1.** Concentrations of squaraine dye (**4-11**) guests added for fluorescence titration experiments.

Volumes ( $\mu\text{L}$ )	Concentrations (0.2 mg/mL)	Concentrations (0.04 mg/mL)
1.50	0.22 $\mu\text{M}$	0.04 $\mu\text{M}$
3.00	0.44 $\mu\text{M}$	0.09 $\mu\text{M}$
4.50	0.66 $\mu\text{M}$	0.13 $\mu\text{M}$
6.00	0.88 $\mu\text{M}$	0.18 $\mu\text{M}$
7.50	1.10 $\mu\text{M}$	0.22 $\mu\text{M}$
9.00	1.32 $\mu\text{M}$	0.26 $\mu\text{M}$
10.5	1.54 $\mu\text{M}$	0.31 $\mu\text{M}$
12.0	1.76 $\mu\text{M}$	0.35 $\mu\text{M}$
15.0	2.20 $\mu\text{M}$	0.44 $\mu\text{M}$
20.0	2.94 $\mu\text{M}$	0.59 $\mu\text{M}$
30.0	4.40 $\mu\text{M}$	0.88 $\mu\text{M}$
40.0	5.87 $\mu\text{M}$	1.17 $\mu\text{M}$
50.0	7.34 $\mu\text{M}$	1.47 $\mu\text{M}$

#### METHODS FOR JOB'S PLOT EXPERIMENTS

0.5 mg/mL of the dimer hosts and 0.04 mg/mL of the squaraine dye guests were prepared separately. The fluorescence spectra of the varying concentrations of the dimer host solutions were recorded (four trials each) for the following sets of mixtures (decreasing host and increasing guest). Both the excitation slit width and the emission slit width were 3.0 nm. All fluorescence spectra were integrated vs. wavenumber on the X-axis using OriginPro Version 9.1.

After diluting each mixture, with 2.5 mL of PBS solution in a cuvette, the fluorescence spectra were recorded. Normalized fluorescence intensity ( $f = (F-F_0)/F_0$ ; where  $F$  is the fluorescence intensity at a particular host concentration, and  $F_0$  is the fluorescence intensity at initial concentration) is measured for each solution. Difference in  $f$  is

calculated for solutions **A** and **B**. The product of  $\Delta f$  and mole fraction of guest ( $\gamma \cdot \Delta f$ ) is plotted against the mole fraction ( $\gamma$ ) of guests. The mole fraction corresponding to the maxima of the plot ( $\gamma_{\max}$ ) was recorded.

**Table S2.** Two sets of dimer host and squaraine guest mixtures (overall concentration of host + guest was constant) compared for Job's plot analysis.

SET A	SET B
Host (6.25 $\mu$ L) + Guest (0 $\mu$ L)	Host (6.25 $\mu$ L) + Guest (0 $\mu$ L)
Host (5.50 $\mu$ L) + Guest (0 $\mu$ L)	Host (5.50 $\mu$ L) + Guest (1.50 $\mu$ L)
Host (4.75 $\mu$ L) + Guest (0 $\mu$ L)	Host (4.75 $\mu$ L) + Guest (3.00 $\mu$ L)
Host (4.00 $\mu$ L) + Guest (0 $\mu$ L)	Host (4.00 $\mu$ L) + Guest (4.50 $\mu$ L)
Host (3.25 $\mu$ L) + Guest (0 $\mu$ L)	Host (3.25 $\mu$ L) + Guest (6.00 $\mu$ L)
Host (2.50 $\mu$ L) + Guest (0 $\mu$ L)	Host (2.50 $\mu$ L) + Guest (7.50 $\mu$ L)
Host (1.75 $\mu$ L) + Guest (0 $\mu$ L)	Host (1.75 $\mu$ L) + Guest (9.00 $\mu$ L)
Host (1.00 $\mu$ L) + Guest (0 $\mu$ L)	Host (1.00 $\mu$ L) + Guest (10.50 $\mu$ L)

## METHODS FOR UV/VIS ABSORPTION SPECTROSCOPY EXPERIMENTS

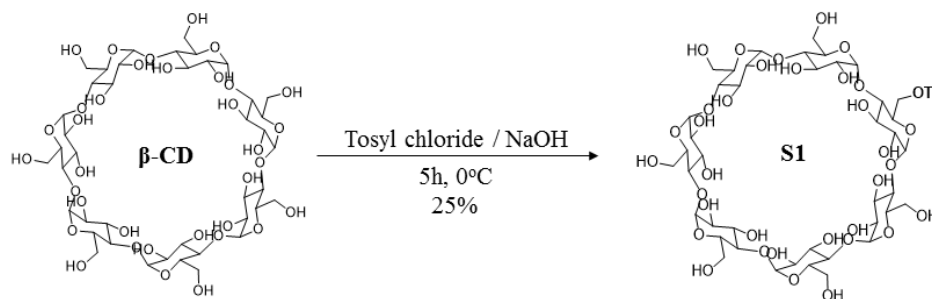
**Hydrolysis of squaraine (4-11) experiments:** The absorption spectra of a mixture of 24  $\mu$ M solution of host dimers (**1-3**) and 24  $\mu$ M solution of guest squaraines (**4-11**) were recorded over a period of 5 hours, with spectra acquired every 30 minutes. For the 1:1 absorption spectra, 30  $\mu$ L of a guest solution of squaraine (1 mg/mL in THF, 2.0 mM) and 150  $\mu$ L of host solution of dimer (1 mg/mL in DI water, 0.4 mM) was added to 2.5 mL of PBS. The solution was shaken to ensure homogeneity, and the data was collected.

**Spectroscopic studies of squaraine experiments:** In a quartz cuvette, the absorption spectra of a mixture of increasing concentration of squaraine guests (**4-11**), 8  $\mu$ M solution of host dimers (**1-3**) added to 2.5 mL of PBS were recorded. For the absorption spectra, 50  $\mu$ L of the host solution of the dimer (1 mg/mL in DI water) and increasing volumes of 1 mg/mL of squaraine guests (1.5  $\mu$ L; 3.0  $\mu$ L; 4.5  $\mu$ L; 6.0  $\mu$ L; 7.5  $\mu$ L; 9.0

$\mu\text{L}$ ; 10.5  $\mu\text{L}$ ; 12.0  $\mu\text{L}$ ; 13.5  $\mu\text{L}$ ; 15.0  $\mu\text{L}$ ) was added to 2.5 mL of PBS. The solution was shaken to ensure homogeneity and data was collected.

## SYNTHETIC PROCEDURES FOR $\beta$ -CYCLODEXTRIN PRE-FUNCTIONALIZATION

### Synthesis of 6-monotosyl-6-monodeoxy $\beta$ -cyclodextrin (S1)

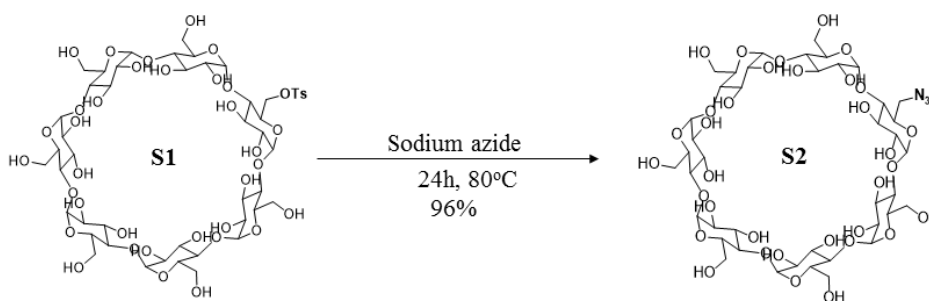


2.5 g (2.2 mmol, 1.00 eq)  $\beta$ -cyclodextrin were dissolved in a solution of 1.25 grams of sodium hydroxide in 75 mL of water and the solution was cooled to 0 °C. Subsequently, 2.5 g (13.5 mmol, 6.14 eq) *p*-toluenesulfonyl chloride were added and the reaction mixture was stirred vigorously for 2 hours at 0 °C. After the addition of additional 1.5 g (8 mmol) of *p*-toluenesulfonyl chloride, the reaction mixture was allowed to continue stirring at 0 °C for an additional 3 hours. The reaction mixture was filtered, cooled at 0 °C, and 17.5 mL of 10% aqueous HCl were carefully added to the filtrate. The resulting solution was stored overnight at 4 °C. After overnight storage, the product was filtered, dried to a constant weight and recrystallized from water to yield a white crystalline solid powder (700 mg, 25% yield).  $^1\text{H-NMR}$  (400 MHz,  $\text{DMSO-}d_6$ ):  $\delta$  (ppm) = 7.72 (d,  $J$  = 8.4 Hz, 2H), 7.41 (d,  $J$  = 8.4 Hz, 2H), 5.60–5.89 (m, 14H), 4.75–4.81 (m, 7H), 4.15–4.62 (m, 6H), 3.45–3.72 (m, 28H), 3.15–3.47 (m, overlapping with HDO, 14H), 2.41 (s,

3H).  $^{13}\text{C}$ -NMR (100 MHz,  $\text{DMSO-}d_6$ ):  $\delta$  (ppm) = 147.1, 145.1, 132.7, 131.8, 130.2, 129.6, 127.9, 125.7, 124.2, 102.2, 81.8, 81.5, 81.0, 73.3, 73.0, 72.7, 72.5, 72.3, 72.1, 70.0, 69.2, 60.2, 59.5, 21.5.

Reference: Lovrinovic, M.; Niemeyer, C. M. "Microtiter Plate-Based Screening for the Optimization of DNA-Protein Conjugate Synthesis by Means of Expressed Protein Ligation." *Chembiochem* **2007**, 8(1), 61-67.

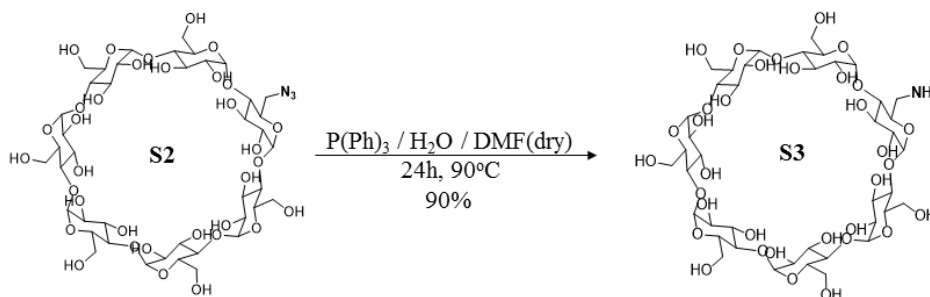
### Synthesis of 6-monoazido-6-monodeoxy $\beta$ -cyclodextrin (**S2**)



The synthesis of **S2** was performed as previously reported. In brief, 4.15 g (3.20 mmol, 1.00 eq) of compound **S1** were dissolved in 50.0 mL of water and heated to 80 °C. Subsequently, 2.90 g (48.0 mmol, 15.0 eq) of sodium azide were added and the reaction mixture was stirred overnight at 80 °C. After being cooled to room temperature, the solution was poured into acetone (250 mL), and the resulting precipitate was filtered and dried in vacuo to give the azide **S2** as a white powder (3.57 g, 96% yield), which was used without further purification.  $^1\text{H}$ -NMR (400 MHz,  $\text{DMSO-}d_6$ ):  $\delta$ (ppm) = 5.70-5.58 (m, 14 H), 4.75-4.81 (m, 7H), 4.15-4.62 (m, 6H), 3.45-3.72 (m, 28H), 3.15-3.47 (m, overlapping with HDO, 14H).  $^{13}\text{C}$ -NMR (100 MHz,  $\text{D}_2\text{O}$ ):  $\delta$  (ppm) = 104.5, 83.7, 75.7, 74.73, 74.5, 62.9, 53.7 ppm.

Reference: Lovrinovic, M.; Niemeyer, C. M. "Microtiter Plate-Based Screening for the Optimization of DNA-Protein Conjugate Synthesis by Means of Expressed Protein Ligation." *Chembiochem* **2007**, 8(1), 61-67.

### Synthesis of 6-monoamino-6-monodeoxy $\beta$ -cyclodextrin (S3)

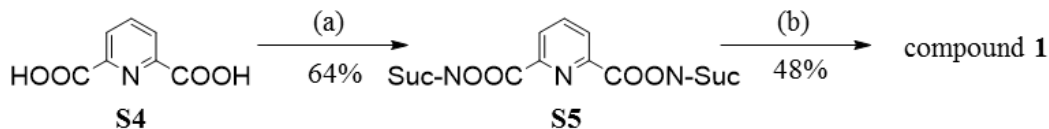


A mixture of S2 (1.16 g, 1.0 mmol, 1.0 eq) and triphenylphosphine (300 mg, 1.1 mmol, 1.1 eq) was stirred in anhydrous DMF (2.0 mL) under nitrogen atmosphere for 2 hours at room temperature. Deionized water (0.2 mL) was added, after which time the temperature of the reaction mixture was raised to 90 °C. Stirring was continued at 90 °C for 24 hours before heating was stopped and the mixture was allowed to cool to room temperature. The white precipitate was collected after adding acetone (50 mL) to the reaction mixture at room temperature. The precipitate was further washed with excess acetone and dried under high vacuum (1.02 g, 0.9 mmol, 90% yield). <sup>1</sup>H-NMR (400 MHz, DMSO-*d*<sub>6</sub>):  $\delta$  (ppm) = 5.78–5.63 (m, 14H), 4.90–4.85 (m, 7 H), 4.50–4.45 (m, 6H), 3.66–3.54 (m, 28H), 3.42–3.24 (overlap with HDO, m, 16H). <sup>13</sup>C-NMR (100 MHz, DMSO-*d*<sub>6</sub>):  $\delta$  (ppm) = 101.8, 82.9, 81.6, 81.5, 73.0, 72.3, 72.1, 59.9 .

Reference: Tang, W.; Ng, S. “Facile synthesis of mono-6-amino-6-deoxy- $\alpha$ -,  $\beta$ -,  $\gamma$ -cyclodextrin hydrochlorides for molecular recognition, chiral separation and drug delivery.” *Nature Protocols*. **2008**, 3(4), 691-697.

## SYNTHETIC PROCEDURES FOR $\beta$ -CYCLODEXTRIN DIMER HOSTS

### Synthesis of $\beta$ -cyclodextrin dimer host 1



(a) N-hydroxysuccinimide, Trifluoroacetic anhydride, Pyridine, Chlorobenzene (RT, 16h); (b) 6-monoamino-6-monodeoxy- $\beta$ -cyclodextrin, dry DMF (RT, 24h)

### Compound S5

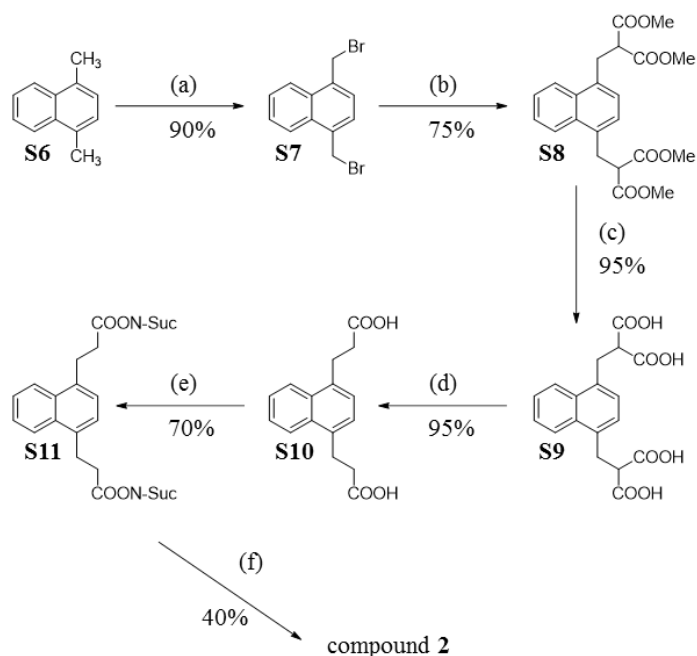
Trifluoroacetic anhydride (556  $\mu$ L, 4.0 mmol, 2.00 eq) was added dropwise to a suspension containing S4 (334 mg, 2.0 mmol, 1.00 eq) and *N*-hydroxysuccinimide (460 mg, 4.0 mmol, 2.00 eq) in pyridine (648  $\mu$ L, 8.0 mmol, 4.00 eq) and chlorobenzene (2.5 mL) at 0  $^{\circ}$ C. The mixture was stirred at 0  $^{\circ}$ C for 15 min after which stirring was continued at room temperature for an additional 16 hours. The solids were collected by filtration, thoroughly washed with ethanol, and recrystallized from acetonitrile (462 mg, 1.3 mmol, 64% yield).  $^1\text{H-NMR}$  (400 MHz; DMSO- $d_6$ ):  $\delta$  (ppm) = 8.60 (2 H, d,  $J$  = 8.0 Hz, pyridyl CH), 8.45 (1H, dd,  $J$  = 8.0, 7.5 Hz, pyridyl CH), 2.91 (8 H, s,  $\text{CH}_2\text{C}(=\text{O})$ );  $^{13}\text{C-NMR}$  (100 MHz; DMSO- $d_6$ ):  $\delta$  (ppm) = 170.9 (C(=O)N), 160.7 (RC(=O)O), 144.9 (pyridyl CC(=O)O), 141.9 (pyridyl CH), 132.0 (pyridyl CH), 26.5 ( $\text{CH}_2\text{C}(=\text{O})$ ).

Reference: Postma, T. M.; Galloway, W. R. J. D.; Cougnon, F. B. L.; Pantoú, G. D.; Stokes, J. E.; Spring, D. R. "Dynamic Combinatorial Chemistry with Novel Dithiol Building Blocks: Towards New Structurally Diverse and Adaptive Screening Collections." *Synlett* **2013**, 24, 765-769.

### Compound 1

Compound **S5** (50 mg, 0.14 mmol, 1.00 eq) and **S3** (350 mg, 0.31 mmol, 2.20 eq) were dissolved in 20 mL of anhydrous *N, N*-dimethylformamide under N<sub>2</sub> and stirred at room temperature. After 24 hrs, the reaction mixture was poured into approximately one liter of acetone to precipitate all cyclodextrin compounds. The precipitate was collected and washed with excess acetone and then dried under vacuum. Purification by recrystallization (acetone:water 20:80 (vol/vol)) afforded host **1** as an off-white powder (162 mg, yield = 48%). <sup>1</sup>H-NMR (400 MHz, DMSO-*d*<sub>6</sub>): δ (ppm) = 3.10-3.45 (m, overlap with HDO, 29H), 3.50-3.80 (m, 56H), 4.23-4.62 (m, 12H, 6-OH), 4.65-5.03 (m, 14H, 1-H), 5.60-5.85 (m, 28H, 2-OH & 3-OH), 8.06-8.26 (m, 3H, ArH), 9.23–9.36 (br s, 1H, ArNH); <sup>13</sup>C-NMR (100 MHz, DMSO-*d*<sub>6</sub>) δ (ppm) = 33.44 (s, C-6'), 59.9-60.5 (m, C-6), 71.2-73.4 (m, C-2, C-2', C-3, C-3', C-5, C-5'), 80.8-81.2 (m, C-4, C-4'), 101.6-102.0 (m, C-1, C-1'), 123.8-124.0 (s, Py), 125.3-125.6 (s, Py), 126.8-126.9 (s, Py), 177.7-177.8 (s, C=O); MS (Q-TOF): *m/z* = 2420.72 [M + Na]<sup>+</sup> (Calculated for C<sub>91</sub>H<sub>143</sub>N<sub>3</sub>O<sub>70</sub> + Na = 2420.76).

## Synthesis of $\beta$ -cyclodextrin dimer host 2



(a) NBS, Bz<sub>2</sub>O<sub>2</sub>, dry CH<sub>2</sub>Cl<sub>2</sub> (reflux, 6h); (b) Dimethylmalonate, NaH, dry THF (reflux, 2h); (c) KOH, MeOH, Water (reflux, overnight); (d) Heating at 200°C until constant weight; (e) N-hydroxysuccinimide, EDC, DMAP, dry DMF (RT, 24h); (f) 6-monoamino-6-monodeoxy- $\beta$ -cyclodextrin, dry DMF (RT, 24h)

### Compound S7

Compound **S6** (1.10 g, 7.04 mmol, 1.00 eq) was dissolved in dry dichloromethane (40.0 mL) and degassed with nitrogen. Under an active nitrogen stream, *N*-bromosuccinimide (3.75 g, 21.0 mmol, 2.98 eq) and benzoyl peroxide (172.5 mg, 0.712 mmol, 0.10 eq) were added and the suspension was degassed to give a yellow suspension. The reaction mixture was heated under nitrogen at 55 °C for 6 hours. The reaction mixture was cooled to room temperature and then washed with 2 M HCl (2 x 15 mL), 2 M NaOH (2 x 20 mL), brine, and dried with MgSO<sub>4</sub>. The solvent was evaporated to yield an off-white powder as the crude product, which was purified by column chromatography with 1:9 (vol/vol) dichloromethane/hexanes to yield the desired product in 90% yield (2.0 g, 6.34



mmol).  $^1\text{H-NMR}$  (400 MHz,  $\text{CDCl}_3$ ):  $\delta$  (ppm) = 4.94 (s, 4H,  $\text{CH}_2$ ), 7.49 (s, 2H, CH), 7.67 (m, 2H, CH), 8.22 (m, 2H, CH).

Reference: Cangelosi, V. M.; Sather, A. C.; Zakharov, L. N.; Berryman, O. B.; Johnson, D. W. "Diastereoselectivity in the Self-Assembly of  $\text{As}_2\text{L}_2\text{C}_{12}$  Macrocycles is Directed by the  $\text{As}-\pi$  Interaction." *Inorganic Chem.* **2007**, *46*, 9278-9284.

### Compound S8

A mixture of dimethylmalonate (0.38 mL, 3.28 mmol, 8.41 eq) and sodium hydride (80.0 mg, 3.33 mmol, 8.54 eq) in dry THF (30 mL) was refluxed, with stirring, for 3 hours. Through an addition funnel, a solution of compound **S7** (125 mg, 0.39 mmol, 1.0 eq) in dry THF (20.0 mL) was added to the reaction mixture over a time period of 15 minutes. The mixture was kept at reflux with stirring for an additional 2 hours. After 2 hours, the reaction was stopped via the addition of ice (50 g), water (50 mL) and hydrochloric acid (to adjust the pH to approximately pH = 3.0). The aqueous solution thus obtained was extracted with chloroform ( $3 \times 100$  mL) and dried over anhydrous sodium sulfate. The solvent and the excess diethylmalonate were evaporated to dryness, yielding the crude product as an off-white powder. Further purification was carried out by column chromatography with 1:3 (vol/vol) EtOAc/Hexane as eluant to yield a white powder (125 mg, 75 % yield):  $^1\text{H-NMR}$  (400 MHz,  $\text{CDCl}_3$ ):  $\delta$  (ppm) = 3.57 (s, 12 H), 3.87 (t, 2H,  $J = 7.7$  Hz, CH), 4.31 (d, 4H,  $\text{CH}_2$ ), 7.24 (s, 2H, H-2,3), 7.54–7.59 (m, 2H, H-6,7), 8.02–8.07 (m, 2H, H-5,8);  $^{13}\text{C-NMR}$  (100 MHz,  $\text{DMSO}-d_6$ ):  $\delta$  (ppm) = 31.5, 52.2, 61.0, 124.2, 126.1, 126.4, 131.5, 132.9, 168.4.

Reference: Costa, D.; Fernandes, E.; Santos, J. L. M.; Pinto, D. C. G. A.; Silva, A. M. S.; Lima, J. L. F. C. "New noncellular fluorescence microplate screening assay for scavenging activity against singlet oxygen." *Anal. Bioanal. Chem.* **2007**, *387*, 2071-2081.

### Compound S9

An aqueous NaOH (12.5 wt%, 1.0 mL) solution was added to the solution of **S8** (0.1 g, 0.24 mmol) in methanol (5.0 mL). The resulting mixture was heated to 90 °C with stirring for 5 hours, after which time the mixture was treated with ice, water and hydrochloric acid to adjust the pH to approximately 2. The resulting mixture is extracted with EtOAc, dried over anhydrous Na<sub>2</sub>SO<sub>4</sub> and under reduced pressure to yield a white solid **S9** (0.08 g, 0.23 mmol, 95% yield). No further purification was needed. <sup>1</sup>H-NMR (400 MHz, DMSO-*d*<sub>6</sub>): δ (ppm) = 3.49 (d, 2H, J = 7.6 Hz, CH<sub>2</sub>), 3.66 (t, 1H, J = 7.6 Hz, CH), 7.26 (s, 2H, H-2,3), 7.59–7.62 (m, 2H, H-6,7), 8.09–8.13 (m, 2H, H-5,8), 12.75 (br s, 1H, CO<sub>2</sub>H); <sup>13</sup>C-NMR (100 MHz, DMSO-*d*<sub>6</sub>): δ (ppm) = 31.3, 52.5, 124.2, 126.1, 126.2, 131.6, 133.4, 170.4.

Reference: Costa, D.; Fernandes, E.; Santos, J. L. M.; Pinto, D. C. G. A.; Silva, A. M. S.; Lima, J. L. F. C. “New noncellular fluorescence microplate screening assay for scavenging activity against singlet oxygen.” *Anal. Bioanal. Chem.* **2007**, 387, 2071-2081.

### Compound S10

Compound **S9** (82.8 mg, 0.23 mmol) in a round bottom flask was subjected to heating at 200 °C in an oven, until the weight remained constant over three successive measurements to yield **S10** (59.9 mg, 0.22 mmol, 95% yield) as a light off-white compound. <sup>1</sup>H-NMR (400 MHz, DMSO-*d*<sub>6</sub>): δ (ppm) = 2.63 (t, 4 H, J = 7.6 Hz, CH<sub>2</sub>CH<sub>2</sub>CO<sub>2</sub>H), 3.27 (t, 4 H, J = 7.6 Hz, CH<sub>2</sub>CH<sub>2</sub>CO<sub>2</sub>H), 7.30 (s, 2H, H-2,3), 7.56–7.61 (m, 2H, H-6,7), 8.07–8.11 (m, 2H, H-5,8), 12.29 (br s, 2H, CO<sub>2</sub>H); <sup>13</sup>C-NMR (100 MHz, DMSO-*d*<sub>6</sub>): δ (ppm) = 27.4, 34.6, 124.2, 125.4, 125.8, 131.5, 135.3, 173.9.

Reference: Costa, D.; Fernandes, E.; Santos, J. L. M.; Pinto, D. C. G. A.; Silva, A. M. S.; Lima, J. L. F. C. “New noncellular fluorescence microplate screening assay for

scavenging activity against singlet oxygen.” *Anal. Bioanal. Chem.* **2007**, 387, 2071-2081.

### Compound S11

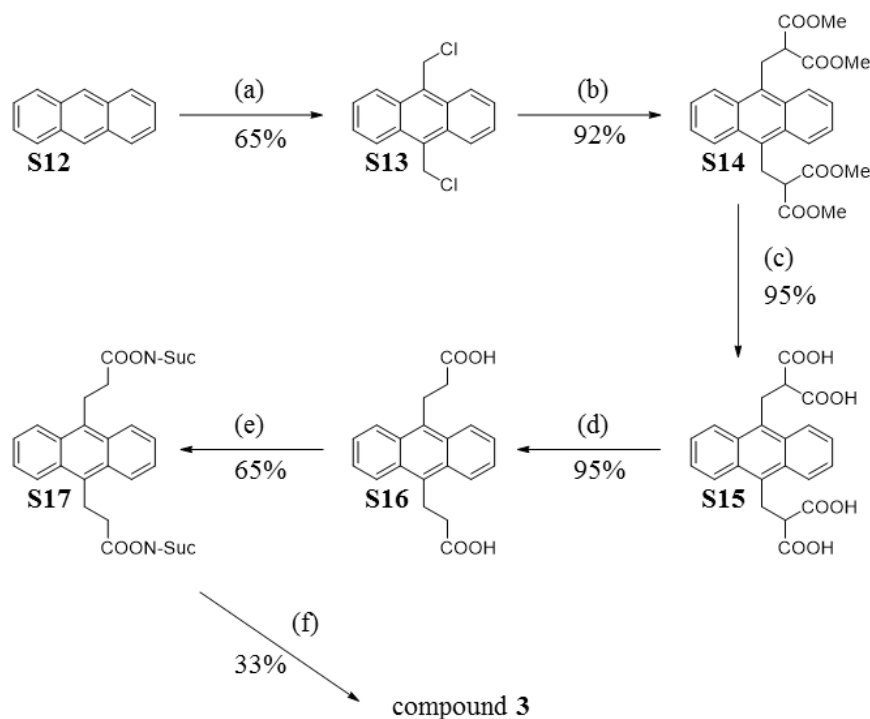
To a solution of **S10** (100 mg, 0.37 mmol, 1.00 eq) in anhydrous *N, N*-dimethylformamide (2.0 mL) under nitrogen, *N*-hydroxysuccinimide (NHS, 157 mg, 1.36 mmol, 3.67 eq), *N*-(3-dimethylaminopropyl)-*N'*-ethylcarbodiimide hydrochloride (EDC, 180 mg, 0.93 mmol, 2.51 eq) and 4-(dimethylamino) pyridine (DMAP, 7.5 mg, 0.06 mmol, 0.16 eq) were added. The reaction mixture was stirred at room temperature under nitrogen overnight. After the reaction was completed (ca. 16 hours), the solvent was removed under reduced pressure. The residue was then dissolved in dichloromethane (20 mL) and this solution was washed with water (20 mL), dried with anhydrous Na<sub>2</sub>SO<sub>4</sub> and evaporated to dryness under vacuum. The residue was dissolved in 1 mL of anhydrous *N, N*-dimethylformamide and recrystallized at 0 °C to give **S11** as a white product (120 mg, 70% yield). <sup>1</sup>H-NMR (400 MHz, DMSO-*d*<sub>6</sub>): δ (ppm) = 2.72 (t, 4 H, J = 7.6 Hz, CH<sub>2</sub>CH<sub>2</sub>CO), 2.92 (s, 8 H, Suc-H), 3.35 (t, 4 H, J = 7.6 Hz, CH<sub>2</sub>CH<sub>2</sub>CO), 7.30 (s, 2 H, H- 2,3), 7.56–7.61 (m, 2 H, H-6,7), 8.07–8.11 (m, 2 H, H- 5,8), 12.29 (br s, 2 H, CO<sub>2</sub>H); <sup>13</sup>C-NMR (100 MHz, DMSO-*d*<sub>6</sub>): δ (ppm) = 25.5, 27.4, 34.6, 124.2, 125.4, 125.8, 131.5, 135.3, 170.3, 174.5.

### Compound 2

Compound **S11** (50 mg, 0.11 mmol, 1.00 eq) and **S3** (275 mg, 0.24 mmol, 2.20 eq) were dissolved in 20 mL of anhydrous *N, N*-dimethylformamide under N<sub>2</sub> and stirred at room temperature. After 24 hrs, the reaction mixture was poured into acetone (1 L) to precipitate the cyclodextrin compounds. The precipitate was collected and washed with

excess acetone and then dried under vacuum. Purification by recrystallization (acetone/water 20:80) afforded host **2** as an off-white powder (110 mg, 40% yield).  $^1\text{H-NMR}$  (400 MHz,  $\text{DMSO-}d_6$ ):  $\delta$  (ppm) = 2.53-2.58 (s, 4 H), 3.10-3.45 (m, overlap with H<sub>2</sub>O, 34H), 3.50-3.80 (m, 56H), 4.35-4.58 (m, 12H, 6-OH), 4.75-4.90 (s, 14H, 1-H), 5.60-5.85 (m, 28H, 2-OH & 3-OH), 7.25-7.30 (s, 1H, ArH), 7.50-7.60 (m, 2H, ArH), 7.69-7.77 (br s, 1H, ArH), 8.03-8.14 (m, 2H, ArH);  $^{13}\text{C-NMR}$  (100 MHz,  $\text{DMSO-}d_6$ ):  $\delta$  (ppm) = 25.0-25.2, 30.4-30.7, 35.5-35.7, 59.5-59.9, 71.7-73.1, 80.9-81.9, 101.6-102.0, 124.6-125.5, 128.6-128.8, 162.0-162.2; MS (MALDI-TOF):  $m/z = 2525.95$  [ $\text{M} + \text{Na}$ ] $^+$  (Calculated for  $\text{C}_{100}\text{H}_{154}\text{N}_2\text{O}_{70} + \text{Na} = 2525.85$ ).

### Synthesis of $\beta$ -cyclodextrin dimer host **3**



(a) Paraformaldehyde,  $\text{ZnCl}_2$ , conc.HCl (reflux, 3h); (b) Dimethylmalonate, NaH, dry THF (reflux, 20h); (c) KOH, MeOH, Water (reflux, overnight); (d) Heating at  $260^\circ\text{C}$  (Diphenylether); (e) N-hydroxysuccinimide, EDC, DMAP, dry DMF (RT, 24h); (f) 6-monoamino-6-monodeoxy- $\beta$ -cyclodextrin, dry DMF (RT, 24h)

### Compound S13

To a stirred solution of anthracene **S12** (1.78 g, 10.0 mmol, 1.00 eq), dry ZnCl<sub>2</sub> (1.64 g, 12.0 mmol, 1.20 mmol), paraformaldehyde (1.50 g, 50 mmol, 5.00 eq) in dioxane (20.0 mL) was slowly added 37wt % fuming concentrated aqueous hydrochloric acid (40.0 mL) at room temperature. After stirring slowly at gentle reflux for 3 hours, the heating was stopped and the mixture was allowed to stand for 16 hours. The fine granular yellow solid that formed was separated by filtration, and washed with water and dioxane to give a crude product. The crude product was recrystallized from toluene to give compound **S13** as a yellowish solid (1.8 g, 65% yield): mp 256 °C; R<sub>f</sub> = 0.45 (hexane/EtOAc, 8:2); <sup>1</sup>H-NMR (400 MHz, DMSO-*d*<sub>6</sub>): δ (ppm) = 8.51 (dd, 4H, J<sub>o</sub>= 7, J<sub>m</sub>= 3 Hz), 7.71 (dd, 4H, J<sub>o</sub>= 7, J<sub>m</sub>= 3 Hz), 5.87 (s, 4H); <sup>13</sup>C-NMR (100 MHz, DMSO-*d*<sub>6</sub>): δ (ppm) = 130.7, 129.2, 126.7, 124.7.

Reference: Ryu, D.; Park, E.; Kim, D.-S.; Yan, S.; Lee, J. Y.; Chang, B.-Y.; Ahn, K. H. "A rational approach to fluorescence "turn-on" sensing of α-amino-carboxylates." *J. Am. Chem. Soc.* **2008**, *130*, 2394-2395.

### Compound S14

A mixture of excess dimethylmalonate (10.6 mL, 92.0 mmol, 97.8 eq) and sodium hydride (2.26 g, 94.3 mmol, 100 eq) in dry THF (40.0 mL) was refluxed with stirring for 3 hours. Then, a solution of compound **S13** (0.26 g, 0.94 mmol, 1.00 eq) in dry THF (20.0 mL) was added to the reaction mixture over a 15 minutes time period. The mixture was kept at reflux temperature with stirring for an additional 20 hours. The reaction was stopped by the addition of ice (50 g), water (50 mL) and hydrochloric acid (to adjust the pH ~3). The solution obtained was extracted with chloroform (3× 100 mL) and dried over anhydrous sodium sulfate. The solvent and the excess diethylmalonate were evaporated to dryness, further purification being carried out by column chromatography

with 2:8 (vol/vol) EtOAc/Hexane to yield **S14** (0.4 g, 92% yield) as a pale-yellow solid.  $R_f = 0.6$  (hexane/EtOAc, 6:4).  $^1\text{H-NMR}$  (400 MHz,  $\text{CDCl}_3$ ):  $\delta$  (ppm) = 3.57 (s, 12 H, CH<sub>3</sub>), 3.88 (t, 2H, CH,  $J = 8.2$  Hz), 4.32 (d, 4H, CH<sub>2</sub>,  $J = 8.2$  Hz), 7.53 (dd,  $J_o = 7$ ,  $J_m = 3$  Hz, 4H, ArH), 8.30 (dd,  $J_o = 7$ ,  $J_m = 3$  Hz, 4 H, ArH);  $^{13}\text{C-NMR}$  (100 MHz, DMSO- $d_6$ ):  $\delta$  (ppm) = 31.5, 52.2, 61.0, 130.7, 129.2, 126.7, 124.7, 168.4

Reference: Zeng, Z.-Y.; He, Y.-B.; Wu, J.-L.; Wei, L.-H.; Liu, X.; Meng, L.-Z.; Yang, X. "Synthesis of two branched fluorescent receptors and their binding properties for dicarboxylate anions." *Eur. J. Org. Chem.* **2004**, 2888-2893.

### Compound S15

To a solution of **S14** (0.30 g, 0.64 mmol, 1.00 eq) in  $\text{CH}_3\text{OH}$  (7.50 mL) and  $\text{H}_2\text{O}$  (10.0 mL) was added KOH (0.15 g, 2.68 mmol, 4.18 eq). The reaction mixture was refluxed overnight, after which time the solvent was removed under vacuum. The residue was washed with  $\text{CH}_2\text{Cl}_2$  (20.0 mL) and  $\text{CH}_3\text{OH}$  (3 $\times$ 5 mL) to give **S15** as light-yellow solid (0.46 g, 95% yield).  $^1\text{H-NMR}$  (400 MHz,  $\text{D}_2\text{O}$ ):  $\delta$  (ppm) = 8.31 (m, 4H), 7.47 (m, 4H), 4.00 (d, 4H, CH<sub>2</sub>,  $J = 8.2$  Hz), 3.41 (t, 2H, CH,  $J = 8.2$  Hz);  $^{13}\text{C-NMR}$  (100 MHz, DMSO- $d_6$ ):  $\delta$  (ppm) = 31.3, 52.5, 130.7, 129.2, 126.7, 124.7, 170.4.

Reference: Fu, Y.; Li, H.; Hu, W.; Zhu, D. "Fluorescence probes for thiol-containing amino acids and peptides in aqueous solution." *Chem. Commun.* **2005**, 3189-3191.

### Compound S16

Compound **S15** (0.70 g, 1.70 mmol, 1.00 eq) was dissolved in 5.0 mL of diphenyl ether and refluxed at the solution's boiling point of 259 °C for 48 hours. Carbon dioxide gas was evolved from the reaction mixture during the reflux. Precipitation was observed on cooling to room temperature. Hot sodium hydroxide (15% aqueous solution), was added into the stirred solution until all of the precipitate was dissolved. The pH was adjusted

to 5.5–6.0 with dilute HCl (10% aqueous) and the precipitate was filtered and recrystallized from an ethanol–water (1:1) mixture. A dark brown colored solid **S16** (0.50 g, 95% yield)  $^1\text{H-NMR}$  (400 MHz,  $\text{DMSO-}d_6$ ):  $\delta$  (ppm) = 2.63 (t, 4 H,  $-\text{CH}_2\text{C}=\text{O}$ ,  $J = 8.2$  Hz), 3.86 (t, 4 H,  $\text{ArCH}_2-$ ,  $J = 8.2$  Hz), 7.59 (dd, 4 H,  $\text{Ar-H}$ ,  $J_1 = 3.2$  Hz,  $J_2 = 7.0$  Hz), 8.36 (dd, 4 H,  $\text{Ar-H}$ ,  $J_1 = 3.2$  Hz,  $J_2 = 7.0$  Hz);  $^{13}\text{C-NMR}$  (100 MHz,  $\text{DMSO-}d_6$ ):  $\delta$  (ppm) = 27.4, 34.6, 130.7, 129.2, 126.7, 124.7, 173.9.

Reference: Icli, S.; Demic, S.; Dindar, B.; Doroshenko, A. O.; Timur, C. “Photophysical and photochemical properties of a water-soluble perylenediimide derivative.” *J. Photochem. Photobiol. A Chem.* **2000**, *136*, 15-24.

### Compound S17

To a solution of **S16** (100 mg, 0.31 mmol, 1.00 eq) in anhydrous *N, N*-dimethylformamide (2.0 mL) under a nitrogen atmosphere, *N*-hydroxysuccinimide (NHS, 157 mg, 1.36 mmol, 4.39 eq), *N*-(3-dimethylaminopropyl)-*N'*-ethylcarbodiimide hydrochloride (EDC, 180 mg, 0.93 mmol, 3.00 eq) and 4-(dimethylamino) pyridine (DMAP, 7.5 mg, 0.06 mmol, 0.19 eq) were added. The reaction mixture was stirred at room temperature under nitrogen overnight. After 16 hours, the solvent was removed under reduced pressure. The residue was then dissolved in dichloromethane (20 mL) and this solution was washed with water (20 mL), dried with anhydrous  $\text{Na}_2\text{SO}_4$  and evaporated to dryness under vacuum. The residue was dissolved in 1 mL of anhydrous *N, N*-dimethylformamide and recrystallized at 0 °C to give compound **S17** as a dark brown colored product (105 mg, 65% yield).  $^1\text{H-NMR}$  (400 MHz,  $\text{DMSO-}d_6$ ):  $\delta$  (ppm) = 2.82 (t, 4 H,  $J=8.2$  Hz,  $\text{CH}_2\text{CH}_2\text{CO}$ ), 2.92 (s, 8 H,  $\text{Suc-H}$ ), 3.92 (t, 4 H,  $J = 8.2$  Hz,  $\text{CH}_2\text{CH}_2\text{CO}$ ), 7.59 (dd, 4H,  $\text{Ar-H}$ ,  $J_1 = 3.2$  Hz,  $J_2 = 7.0$  Hz), 8.36 (dd, 4 H,  $\text{Ar-H}$ ,  $J_1 =$

3.2 Hz,  $J_2 = 7.0$  Hz);  $^{13}\text{C}$ -NMR (100 MHz, DMSO- $d_6$ ):  $\delta$  (ppm) = 25.5, 27.4, 34.6, 130.7, 129.2, 126.7, 124.7, 170.3, 174.5.

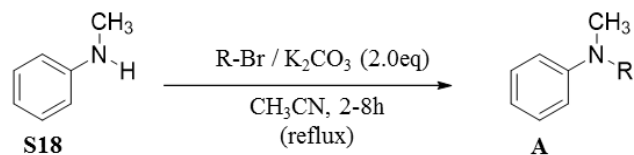
### Compound 3

Compound **S17** (50 mg, 0.10 mmol, 1.00 eq) and **S3** (250 mg, 0.22 mmol, 2.20 eq) were dissolved in 20 mL of anhydrous *N, N*-dimethylformamide under  $\text{N}_2$  and stirred at room temperature. After 24 hrs., the reaction mixture was poured into acetone (1 L) to precipitate the cyclodextrin compounds. The precipitate was collected and washed with excess acetone and then dried under vacuum. Purification by recrystallization (acetone/water 20:80) afforded host **3** as an off-white powder (84 mg, 33% yield).  $^1\text{H}$ -NMR (400 MHz, DMSO- $d_6$ ):  $\delta$  (ppm) = 2.53-2.58 (s, 4 H), 3.10-3.45 (m, overlap with HDO, 32 H), 3.50-3.80 (m, 56 H), 4.35-4.58 (m, 12H, 6-OH), 4.75-4.90 (s, 14H, 1-H), 5.60-5.85 (m, 28H, 2-OH & 3-OH), 7.25-7.65 (m, 4H, ArH), 7.65-8.40 (m, 4H, ArH);  $^{13}\text{C}$ -NMR (100 MHz, DMSO- $d_6$ ):  $\delta$  (ppm) = 25.0-25.2, 30.4-30.7, 35.5-35.7, 59.5-59.9, 71.7-72.6, 72.6-73.1, 80.9-81.9, 101.6-102.0, 124.6-125.5, 128.6-128.8, 162.0-162.2; MS (Q-TOF):  $m/z = 2575.78$   $[\text{M} + \text{Na}]^+$  (Calculated for  $\text{C}_{104}\text{H}_{156}\text{N}_2\text{O}_{70} + \text{Na} = 2575.86$ ).



## SYNTHETIC PROCEDURES FOR *N*-SUBSTITUTED *N*-METHYLANILINO SQUARAIN GUESTS

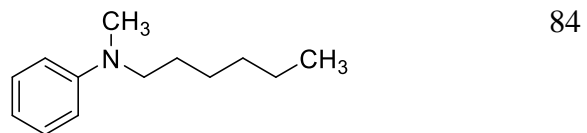
### Generalized Procedure for the Synthesis of *N*-substituted *N*-methyl Aniline **A**



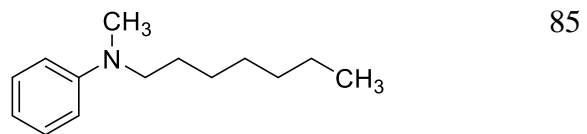
A mixture of **S18** (10-20 mmol), K<sub>2</sub>CO<sub>3</sub> (2.0-4.0 eq) and alkyl bromide (2.4 eq) in 10-20 mL acetonitrile was stirred at 120°C for 2-8 hrs in atmosphere. The reaction mixture was cooled to room temperature and dried under reduced pressure. The crude was dissolved in dichloromethane and washed with saturated sodium bicarbonate solution. The resulting organic layer was further washed with distilled water for three times, dried with anhydrous Na<sub>2</sub>SO<sub>4</sub> and dried under vacuum. The crude product was further purified by silica gel column chromatography using 2:8 (vol/vol) EtOAc/Hexane mixture as eluant. The solvent was removed under reduced pressure, and the pure product was dried under high vacuum to yield a clear yellow oil.

**Table S3.** Synthetic yields of *N*-substituted, *N*-methyl aniline precursors

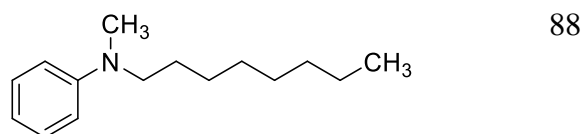
<i>N</i> -substituted <i>N</i> -methylanilines ( <b>A</b> )	Yields (%)
 <b>A4</b>	92
 <b>A5</b>	86



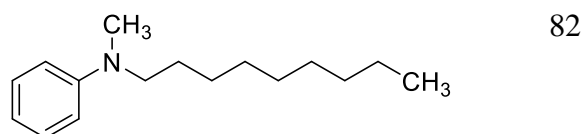
**A6**



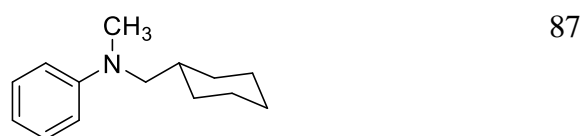
**A7**



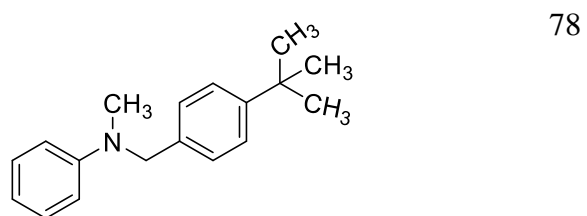
**A8**



**A9**

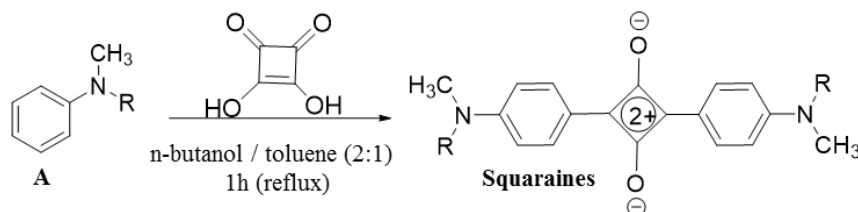


**A10**



**A11**

### Generalized Procedure for the Synthesis of *N*-substituted *N*-methylanilino Squaraines



A mixture of aniline (10-20 mmol, 1.00 eq), 3,4-dihydroxycyclobut-3-ene-1,2-dione (0.50 eq) in 10-20 mL *n*-butanol/toluene (2:1) was stirred at refluxing temperature for 1 hour in Dean-Stark apparatus. The reaction was allowed to cool to room temperature, after which the amount of solvent was reduced under reduced pressure. The remaining crude mixture was recrystallized using isopropanol to yield a shiny crystalline colored solid.

**Table S4.** Synthetic yields and UV-vis absorption details of *N*-substituted, *N*-methylanilino squaraine guests (**4-11**).

Squaraines	Yields (%)	$\lambda_{\max}$ (nm) <sup>a</sup>	Molar Absorptivity ( $\epsilon$ )( $\mu\text{M}^{-1}\text{cm}^{-1}$ ) <sup>a</sup>
<b>4</b>	60	652	85.3
<b>5</b>	51	645	101.5
<b>6</b>	52	690	44.2
<b>7</b>	42	660	152.6
<b>8</b>	45	655	175.5
<b>9</b>	50	540	153.8
<b>10</b>	44	650	79.8
<b>11</b>	53	530,750	137.7

<sup>a</sup>UV-vis absorption spectra measured in aqueous phosphate-buffered saline (PBS) solution

## UV- VIS ABSORPTION & FLUORESCENCE SPECTRA FOR $\beta$ -CYCLODEXTRIN DIMER HOSTS

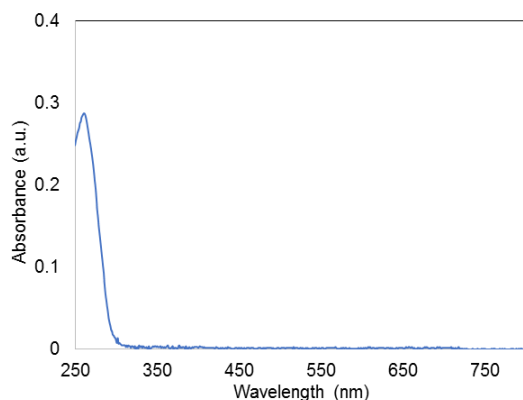


**Figure S1.** UV-vis absorption spectra of compound **1** (8  $\mu$ M) in aqueous phosphate-buffered saline (PBS) solution.

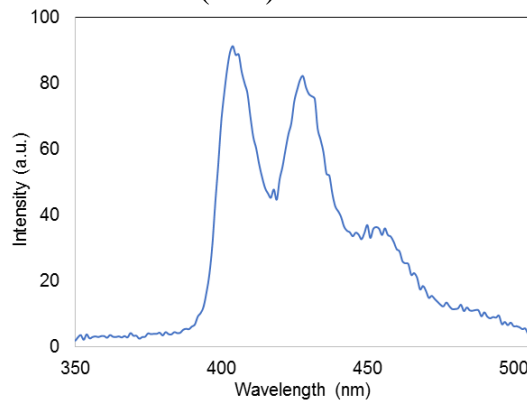


**Figure S2.** Fluorescence emission spectra of compound **1** (0.5  $\mu$ M) in aqueous phosphate-buffered saline (PBS) solution ( $\lambda_{\text{excitation}} = 260$  nm).

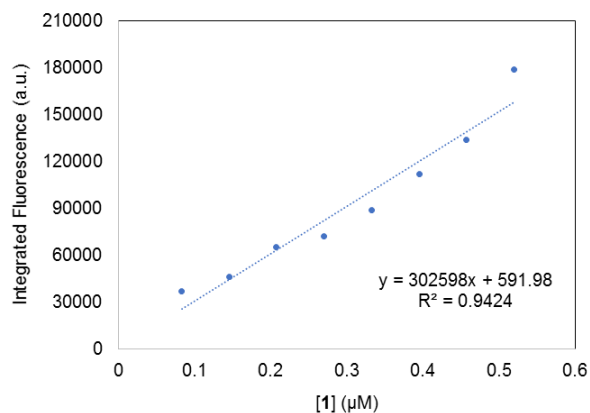


**Figure S3.** Integrated fluorescence emission vs concentration curve for compound **1** in aqueous phosphate-buffered saline (PBS) solution ( $\lambda_{\text{excitation}} = 260$  nm). The poor linear fit indicates higher-order aggregate formations.

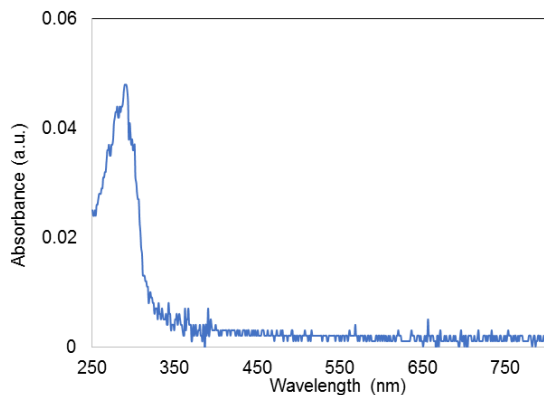


**Figure S4.** UV-vis absorption spectra of compound **2** (8  $\mu\text{M}$ ) in aqueous phosphate-buffered saline (PBS) solution.

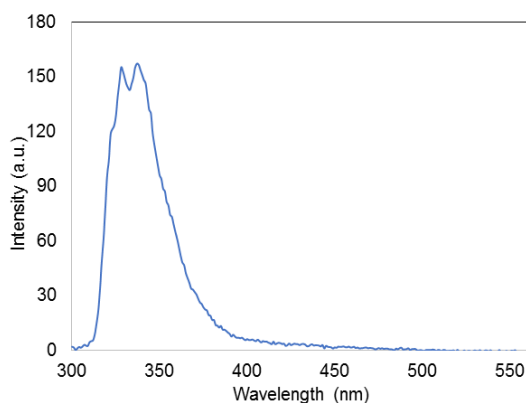


**Figure S5.** Fluorescence emission spectra of compound **2** (0.5  $\mu\text{M}$ ) in aqueous phosphate-buffered saline (PBS) solution ( $\lambda_{\text{excitation}} = 275 \text{ nm}$ ).

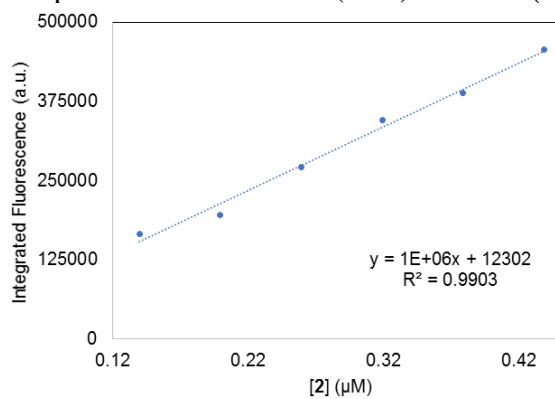


**Figure S6.** Integrated fluorescence emission vs concentration curve for compound **2** in aqueous phosphate-buffered saline (PBS) solution ( $\lambda_{\text{excitation}} = 275 \text{ nm}$ ).

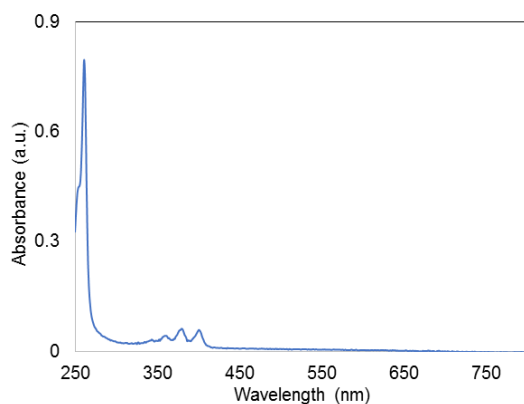


**Figure S7.** UV-vis absorption spectra of compound **3** (8  $\mu\text{M}$ ) in aqueous phosphate-buffered saline (PBS) solution.

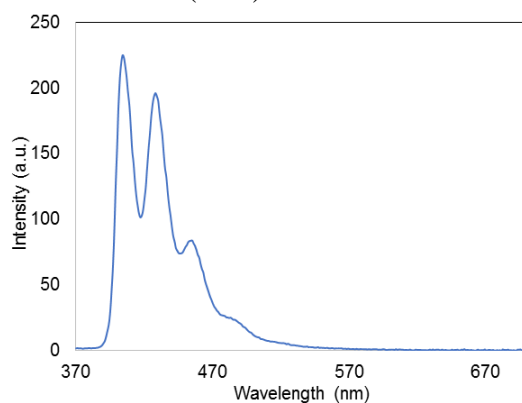


**Figure S8.** Fluorescence emission spectra of compound **3** (0.5  $\mu\text{M}$ ) in aqueous phosphate-buffered saline (PBS) solution ( $\lambda_{\text{excitation}} = 360 \text{ nm}$ ).

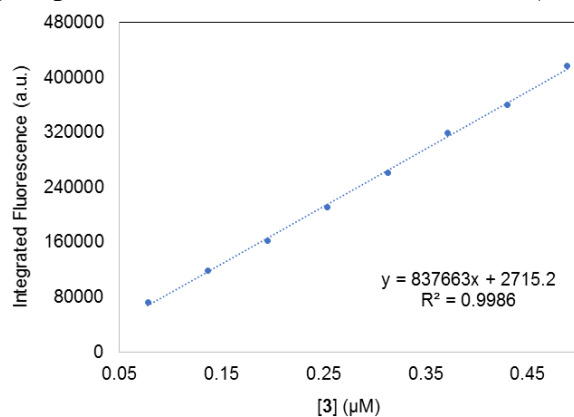


**Figure S9.** Integrated fluorescence emission vs concentration curve for compound **3** in aqueous phosphate-buffered saline (PBS) solution ( $\lambda_{\text{excitation}} = 360 \text{ nm}$ ).

DECONVOLUCTIONS OF UV- VIS ABSORPTION SPECTRA FOR SQUARAINE AGGREGATION STUDIES

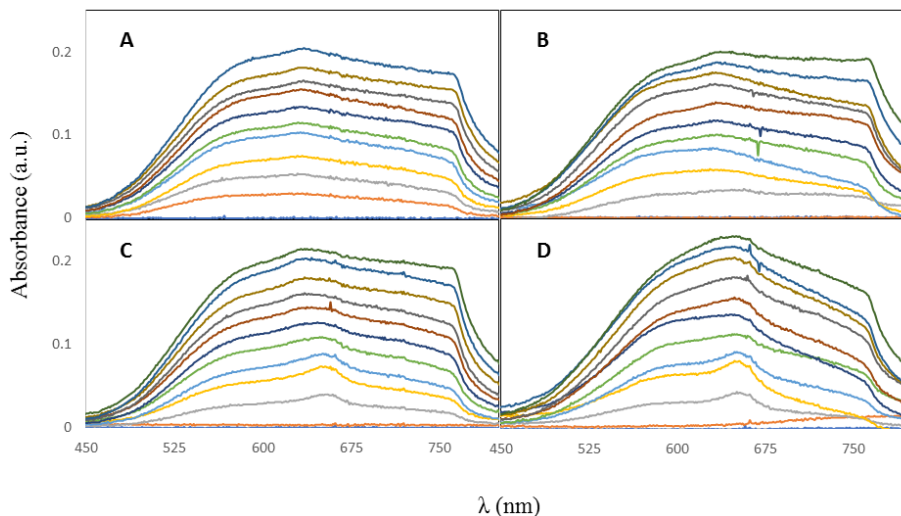


**Figure S10.** UV-vis absorption spectra of squaraine **4** for (A) control; (B) compound **1** ( $8\mu\text{M}$ ); (C) compound **2** ( $8\mu\text{M}$ ); and (D) compound **3** ( $8\mu\text{M}$ ) (squaraine **4** concentrations increase in the order as follows:  $1.5\mu\text{M}$ ;  $2.9\mu\text{M}$ ;  $4.4\mu\text{M}$ ;  $5.9\mu\text{M}$ ;  $7.4\mu\text{M}$ ;  $8.9\mu\text{M}$ ;  $10.4\mu\text{M}$ ;  $11.9\mu\text{M}$ ;  $13.3\mu\text{M}$ ;  $14.8\mu\text{M}$ ).

**Table S5.** Summary table of ratio of H-aggregate (**I/II**) and J-aggregate (**III/II**) to monomeric bands for various concentrations of squaraine **4** for control; compound **1** ( $8\mu\text{M}$ ); compound **2** ( $8\mu\text{M}$ ); and compound **3** ( $8\mu\text{M}$ ).

[ <b>4</b> ] ( $\mu\text{M}$ )	Control		<b>1</b>		<b>2</b>		<b>3</b>	
	H-band ( <b>I/II</b> )	J-band ( <b>III/II</b> )	H-band ( <b>I/II</b> )	J-band ( <b>III/II</b> )	H-band ( <b>I/II</b> )	J-band ( <b>III/II</b> )	H-band ( <b>I/II</b> )	J-band ( <b>III/II</b> )
2.966	0.2436	0.1381	0.3061	0.1557	1.792	1.180	6.138	1.836
5.932	0.2986	0.1376	0.3095	0.1232	0.1683	0.1307	10.87	10.34
8.898	0.3074	0.1174	0.8732	1.0402	0.2225	0.1459	4.133	2.396
11.86	0.3163	0.1182	0.4744	0.1884	0.2445	0.1336	2.106	1.414
14.83	0.3163	0.1529	0.3295	0.4095	0.2995	0.1390	0.6571	0.6078

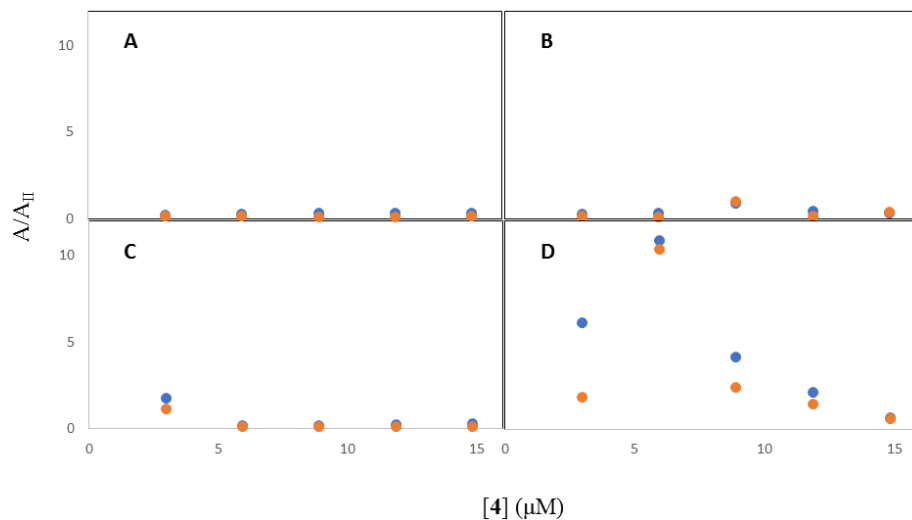


**Figure S11.** Plots of ratio of H-aggregate (**I/II**, blue) and J-aggregate (**III/II**, red) to monomeric bands against concentration of squaraine **4** for (A) control; (B) compound **1** ( $8\mu\text{M}$ ); (C) compound **2** ( $8\mu\text{M}$ ); and (D) compound **3** ( $8\mu\text{M}$ ).

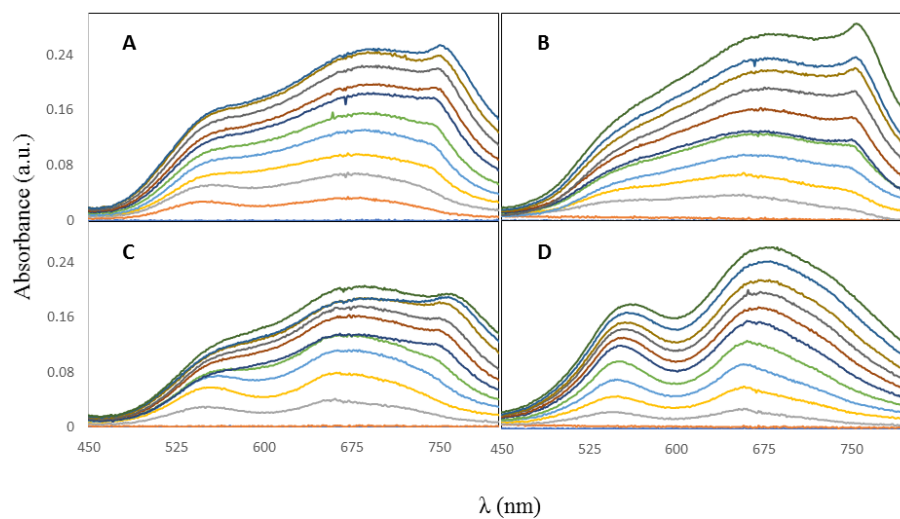


**Figure S12.** UV-vis absorption spectra of squaraine **5** for (A) control; (B) compound **1** ( $8\mu\text{M}$ ); (C) compound **2** ( $8\mu\text{M}$ ); and (D) compound **3** ( $8\mu\text{M}$ ). (squaraine **5** concentrations increase in the order as follows:  $1.4\mu\text{M}$ ;  $2.8\mu\text{M}$ ;  $4.2\mu\text{M}$ ;  $5.5\mu\text{M}$ ;  $6.9\mu\text{M}$ ;  $8.3\mu\text{M}$ ;  $9.7\mu\text{M}$ ;  $11.1\mu\text{M}$ ;  $12.5\mu\text{M}$ ;  $13.9\mu\text{M}$ ).



**Table S6.** Summary table of ratio of H-aggregate (**I/II**) and J-aggregate (**III/II**) to monomeric bands for various concentrations of squaraine **5** for control; compound **1** (8 $\mu$ M); compound **2** (8 $\mu$ M); and compound **3** (8 $\mu$ M).

[ <b>5</b> ] ( $\mu$ M)	Control		<b>1</b>		<b>2</b>		<b>3</b>	
	H-band ( <b>I/II</b> )	J-band ( <b>III/II</b> )	H-band ( <b>I/II</b> )	J-band ( <b>III/II</b> )	H-band ( <b>I/II</b> )	J-band ( <b>III/II</b> )	H-band ( <b>I/II</b> )	J-band ( <b>III/II</b> )
2.605	0.3968	0.2051	0.2405	0.1022	0.6090	0.3322	0.9683	0.6043
5.210	0.4163	0.1934	0.3477	0.1583	0.3189	0.1412	0.7429	0.3840
7.815	0.4134	0.1708	0.3832	0.1591	0.2781	0.1250	0.6369	0.3049
10.42	0.3824	0.1292	0.3842	0.1722	0.2884	0.1255	0.5740	0.2824
13.02	0.3897	0.1348	0.3694	0.1744	0.2342	0.0836	0.4928	0.1955

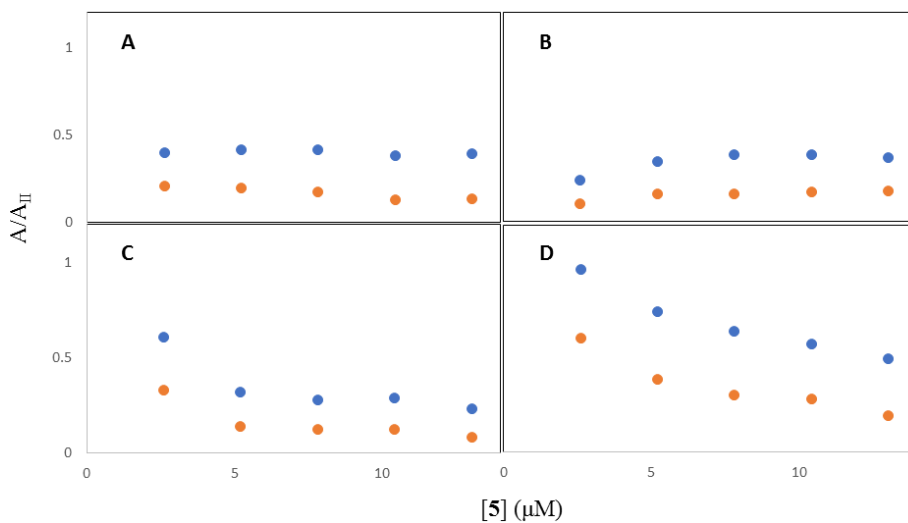


**Figure S13.** Plots of ratio of H-aggregate (**I/II**, blue) and J-aggregate (**III/II**, red) to monomeric bands against concentration of squaraine **5** for (A) control; (B) compound **1** (8 $\mu$ M); (C) compound **2** (8 $\mu$ M); and (D) compound **3** (8 $\mu$ M).

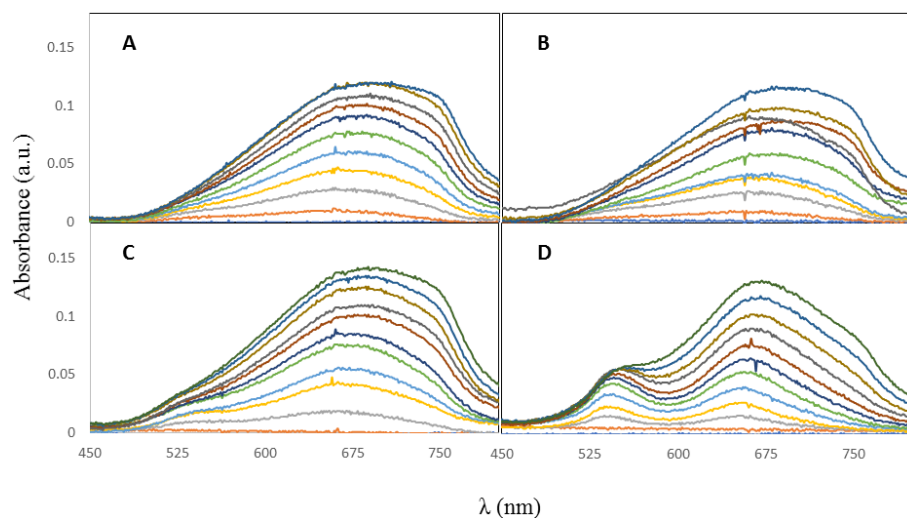


**Figure S14.** UV-vis absorption spectra of squaraine **6** for (A) control; (B) compound **1** ( $8\mu\text{M}$ ); (C) compound **2** ( $8\mu\text{M}$ ); and (D) compound **3** ( $8\mu\text{M}$ ) (squaraine **6** concentrations increase in the order as follows:  $1.3\mu\text{M}$ ;  $2.6\mu\text{M}$ ;  $3.9\mu\text{M}$ ;  $5.2\mu\text{M}$ ;  $6.5\mu\text{M}$ ;  $7.8\mu\text{M}$ ;  $9.1\mu\text{M}$ ;  $10.4\mu\text{M}$ ;  $11.7\mu\text{M}$ ;  $13.0\mu\text{M}$ ).

**Table S7.** Summary table of ratio of H-aggregate (**I/II**) and J-aggregate (**III/II**) to monomeric bands for various concentrations of squaraine **6** for control; compound **1** ( $8\mu\text{M}$ ); compound **2** ( $8\mu\text{M}$ ); and compound **3** ( $8\mu\text{M}$ ).

[ <b>6</b> ] ( $\mu\text{M}$ )	Control		<b>1</b>		<b>2</b>		<b>3</b>	
	H-band ( <b>I/II</b> )	J-band ( <b>III/II</b> )	H-band ( <b>I/II</b> )	J-band ( <b>III/II</b> )	H-band ( <b>I/II</b> )	J-band ( <b>III/II</b> )	H-band ( <b>I/II</b> )	J-band ( <b>III/II</b> )
2.605	0.2476	0.2488	0.4260	0.1698	0.1899	0.0894	0.5739	0.0977
5.210	0.4746	0.2551	0.5425	0.2135	0.2699	0.1788	0.4562	0.0958
7.815	0.9843	0.28742	0.8786	0.2876	0.45513	0.2162	0.3707	0.0831
10.42	1.449	0.3448	1.284	0.3257	0.7646	0.2509	0.2374	0.0930
13.02	1.848	0.3904	0.8149	0.3023	1.372	0.3453	0.1523	0.0896

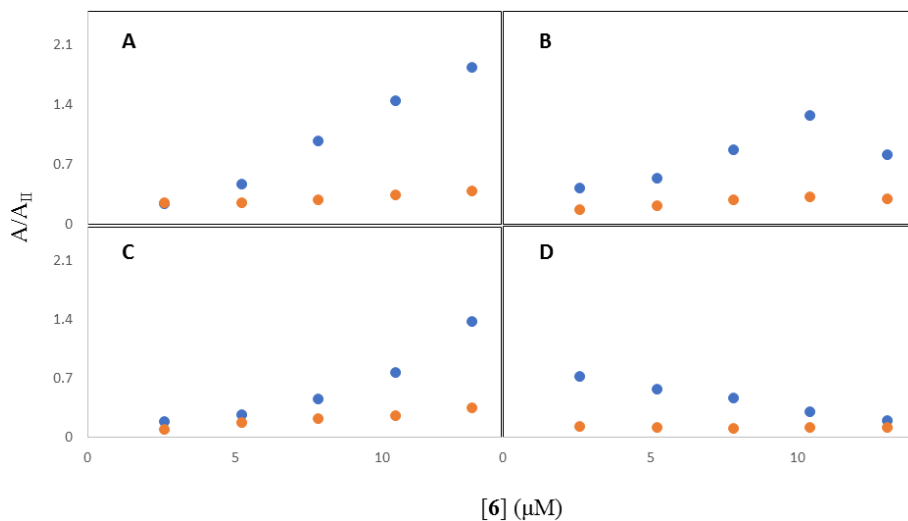


**Figure S15.** Plots of ratio of H-aggregate (I/II, blue) and J-aggregate (III/II, red) to monomeric bands against concentration of squaraine 6 for (A) control; (B) compound 1 ( $8\mu\text{M}$ ); (C) compound 2 ( $8\mu\text{M}$ ); and (D) compound 3 ( $8\mu\text{M}$ ).

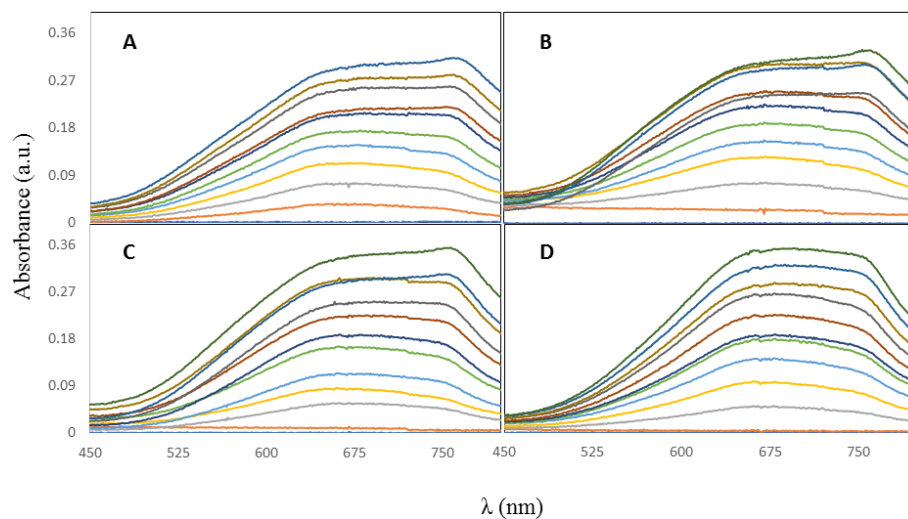


**Figure S16.** UV-vis absorption spectra of squaraine 7 for (A) control; (B) compound 1 ( $8\mu\text{M}$ ); (C) compound 2 ( $8\mu\text{M}$ ); and (D) compound 3 ( $8\mu\text{M}$ ) (squaraine 7 concentrations increase in the order as follows:  $1.2\mu\text{M}$ ;  $2.4\mu\text{M}$ ;  $3.7\mu\text{M}$ ;  $4.9\mu\text{M}$ ;  $6.1\mu\text{M}$ ;  $7.4\mu\text{M}$ ;  $8.6\mu\text{M}$ ;  $9.8\mu\text{M}$ ;  $11.0\mu\text{M}$ ;  $12.2\mu\text{M}$ ).

**Table S8.** Summary table of ratio of H-aggregate (**I/II**) and J-aggregate (**III/II**) to monomeric bands for various concentrations of squaraine **7** for control; compound **1** (8 $\mu$ M); compound **2** (8 $\mu$ M); and compound **3** (8 $\mu$ M).

[7] ( $\mu$ M)	Control		<b>1</b>		<b>2</b>		<b>3</b>	
	H-band ( <b>I/II</b> )	J-band ( <b>III/II</b> )	H-band ( <b>I/II</b> )	J-band ( <b>III/II</b> )	H-band ( <b>I/II</b> )	J-band ( <b>III/II</b> )	H-band ( <b>I/II</b> )	J-band ( <b>III/II</b> )
2.454	0.2400	0.9565	0.2592	0.6314	0.1444	0.8148	0.8754	1.884
4.908	0.0658	0.3039	0.1263	0.5882	0.1094	0.6528	0.2347	0.9859
7.362	0.0851	0.3943	0.1975	0.4353	0.1466	0.4976	0.2982	1.039
9.816	0.1204	0.3776	0.1765	0.4613	0.1970	0.4127	0.1812	0.6977
12.27	0.1834	0.3801	0.2427	0.4363	0.2845	0.4429	0.1046	0.5113

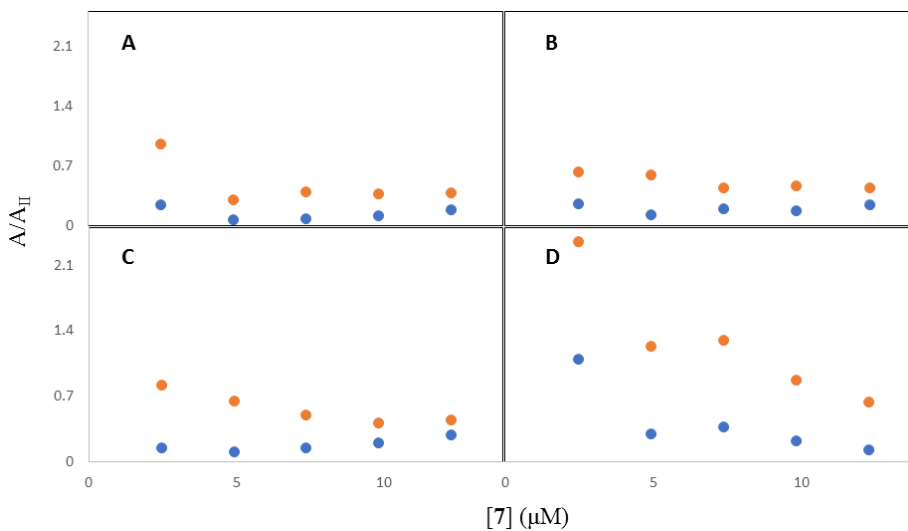


**Figure S17.** Plots of ratio of H-aggregate (**I/II**, blue) and J-aggregate (**III/II**, red) to monomeric bands against concentration of squaraine **7** for (A) control; (B) compound **1** (8 $\mu$ M); (C) compound **2** (8 $\mu$ M); and (D) compound **3** (8 $\mu$ M).

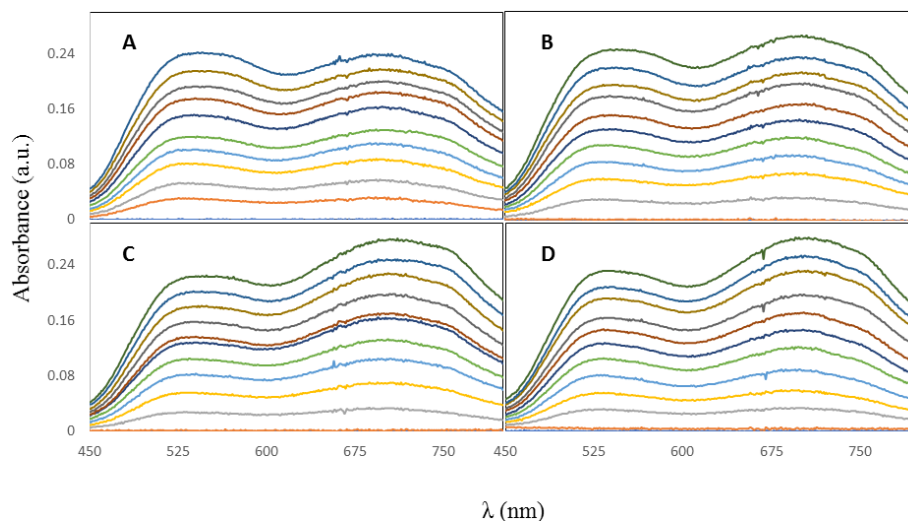


**Figure S18.** UV-vis absorption spectra of squaraine **8** for (A) control; (B) compound **1** ( $8\mu\text{M}$ ); (C) compound **2** ( $8\mu\text{M}$ ); and (D) compound **3** ( $8\mu\text{M}$ ) (squaraine **8** concentrations increase in the order as follows:  $1.2\mu\text{M}$ ;  $2.3\mu\text{M}$ ;  $3.5\mu\text{M}$ ;  $4.6\mu\text{M}$ ;  $5.8\mu\text{M}$ ;  $6.9\mu\text{M}$ ;  $8.1\mu\text{M}$ ;  $9.3\mu\text{M}$ ;  $10.4\mu\text{M}$ ;  $11.6\mu\text{M}$ ).

**Table S9.** Summary table of ratio of H-aggregate (**I/II**) and J-aggregate (**III/II**) to monomeric bands for various concentrations of squaraine **8** for control; compound **1** ( $8\mu\text{M}$ ); compound **2** ( $8\mu\text{M}$ ); and compound **3** ( $8\mu\text{M}$ ).

[ <b>8</b> ] ( $\mu\text{M}$ )	Control		<b>1</b>		<b>2</b>		<b>3</b>	
	H-band ( <b>I/II</b> )	J-band ( <b>III/II</b> )	H-band ( <b>I/II</b> )	J-band ( <b>III/II</b> )	H-band ( <b>I/II</b> )	J-band ( <b>III/II</b> )	H-band ( <b>I/II</b> )	J-band ( <b>III/II</b> )
2.322	0.4782	3.122	0.4556	3.272	0.5112	3.733	0.5001	2.991
4.644	0.4316	2.746	0.4136	3.123	0.4698	3.652	0.4489	3.304
6.966	0.4084	2.683	0.3770	2.867	0.4758	3.496	0.4603	3.379
9.288	0.3921	2.442	0.3829	2.793	0.4706	3.306	0.4471	3.239
11.61	0.3715	2.403	0.3664	2.675	0.6248	3.245	0.4460	3.245

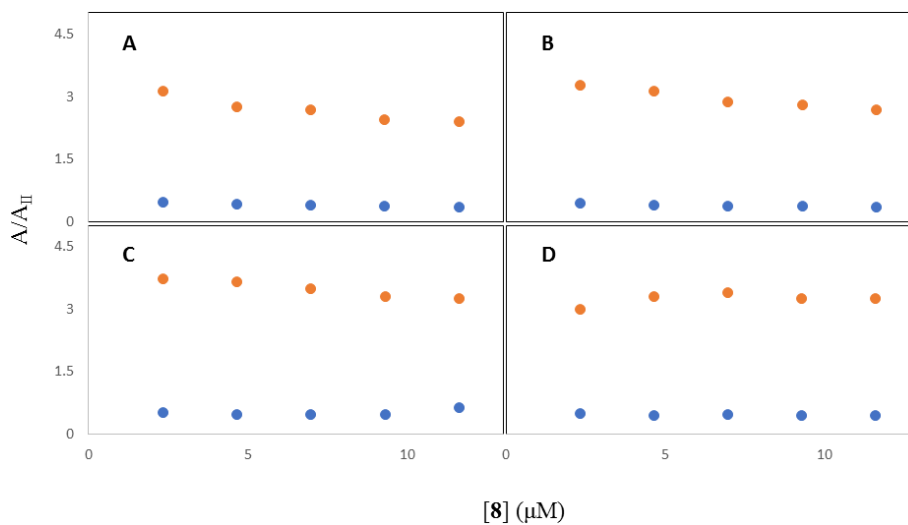


**Figure S19.** Plots of ratio of H-aggregate ( $I/II$ , blue) and J-aggregate ( $III/II$ , red) to monomeric bands against concentration of squaraine **8** for (A) control; (B) compound **1** ( $8\mu\text{M}$ ); (C) compound **2** ( $8\mu\text{M}$ ); and (D) compound **3** ( $8\mu\text{M}$ ).

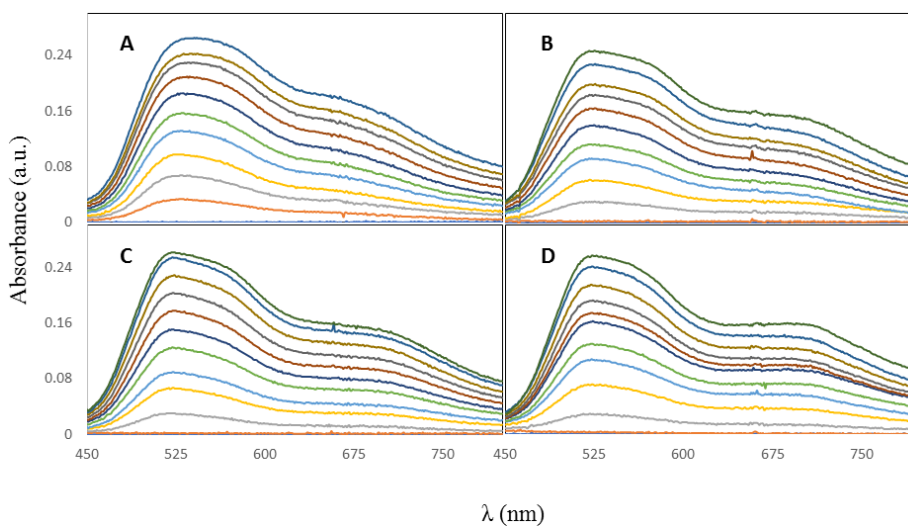


**Figure S20.** UV-vis absorption spectra of squaraine **9** for (A) control; (B) compound **1** ( $8\mu\text{M}$ ); (C) compound **2** ( $8\mu\text{M}$ ); and (D) compound **3** ( $8\mu\text{M}$ ) (squaraine **9** concentrations increase in the order as follows:  $1.1\mu\text{M}$ ;  $2.2\mu\text{M}$ ;  $3.3\mu\text{M}$ ;  $4.4\mu\text{M}$ ;  $5.5\mu\text{M}$ ;  $6.6\mu\text{M}$ ;  $7.7\mu\text{M}$ ;  $8.8\mu\text{M}$ ;  $9.9\mu\text{M}$ ;  $11.0\mu\text{M}$ ).

**Table S10.** Summary table of ratio of H-aggregate (**I/II**) and J-aggregate (**III/II**) to monomeric bands for various concentrations of squaraine **9** for control; compound **1** (8 $\mu$ M); compound **2** (8 $\mu$ M); and compound **3** (8 $\mu$ M).

[ <b>9</b> ] ( $\mu$ M)	Control		<b>1</b>		<b>2</b>		<b>3</b>	
	H-band ( <b>I/II</b> )	J-band ( <b>III/II</b> )	H-band ( <b>I/II</b> )	J-band ( <b>III/II</b> )	H-band ( <b>I/II</b> )	J-band ( <b>III/II</b> )	H-band ( <b>I/II</b> )	J-band ( <b>III/II</b> )
2.202	0.4570	1.177	0.4386	0.8601	0.3844	0.6346	0.3907	0.7606
4.405	0.4636	1.150	0.4228	0.8397	0.4111	0.7858	0.3944	0.6892
6.608	0.4508	1.140	0.4427	0.8978	0.4244	0.8014	0.3893	0.7611
8.810	0.4386	1.146	0.4007	0.8170	0.4216	0.7954	0.3639	0.7443
11.01	0.4105	1.115	0.3935	0.7971	0.3920	0.7847	0.3832	0.7749

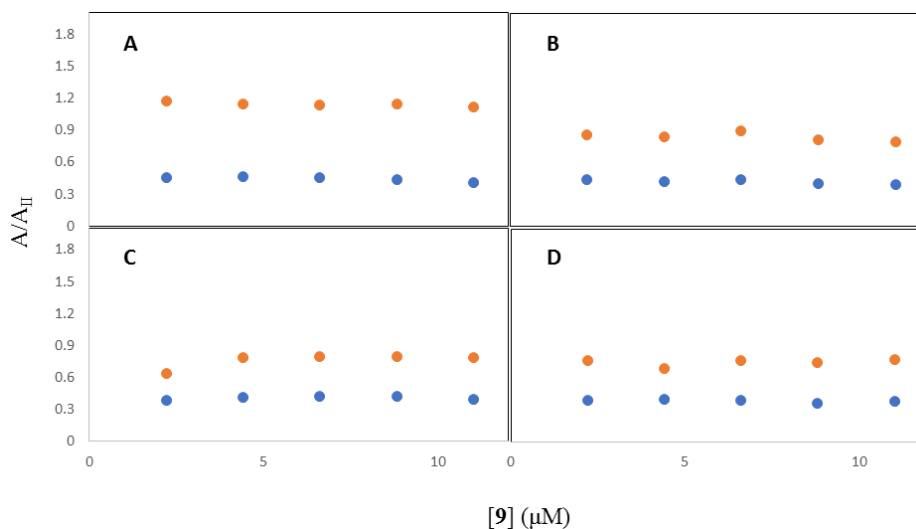


**Figure S21.** Plots of ratio of H-aggregate (**I/II**, blue) and J-aggregate (**III/II**, red) to monomeric bands against concentration of squaraine **9** for (A) control; (B) compound **1** (8 $\mu$ M); (C) compound **2** (8 $\mu$ M); and (D) compound **3** (8 $\mu$ M).

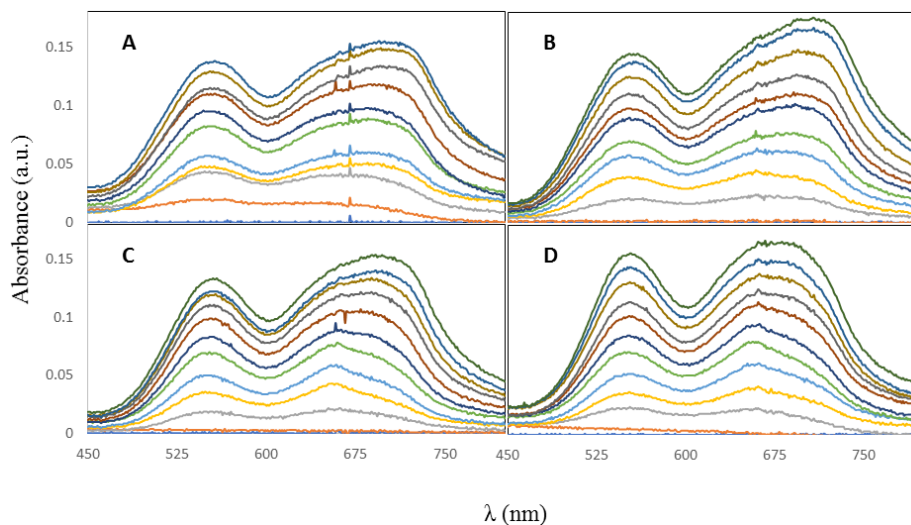


**Figure S22.** UV-vis absorption spectra of squaraine **10** for (A) control; (B) compound **1** ( $8\mu\text{M}$ ); (C) compound **2** ( $8\mu\text{M}$ ); and (D) compound **3** ( $8\mu\text{M}$ ) (squaraine **10** concentrations increase in the order as follows:  $1.2\mu\text{M}$ ;  $2.5\mu\text{M}$ ;  $3.7\mu\text{M}$ ;  $4.9\mu\text{M}$ ;  $6.2\mu\text{M}$ ;  $7.4\mu\text{M}$ ;  $8.6\mu\text{M}$ ;  $9.9\mu\text{M}$ ;  $11.1\mu\text{M}$ ;  $12.4\mu\text{M}$ ).

**Table S11.** Summary table of ratio of H-aggregate (**I/II**) and J-aggregate (**III/II**) to monomeric bands for various concentrations of squaraine **10** for control; compound **1** ( $8\mu\text{M}$ ); compound **2** ( $8\mu\text{M}$ ); and compound **3** ( $8\mu\text{M}$ ).

[ <b>10</b> ] ( $\mu\text{M}$ )	Control		<b>1</b>		<b>2</b>		<b>3</b>	
	H-band ( <b>I/II</b> )	J-band ( <b>III/II</b> )	H-band ( <b>I/II</b> )	J-band ( <b>III/II</b> )	H-band ( <b>I/II</b> )	J-band ( <b>III/II</b> )	H-band ( <b>I/II</b> )	J-band ( <b>III/II</b> )
2.476	0.6551	0.1157	0.5656	0.0497	0.7917	0.2529	0.5505	0.0275
4.952	0.9965	0.5706	0.6152	0.1205	0.5528	0.0247	0.5868	0.0456
7.428	1.301	1.029	0.8787	0.4565	0.5986	0.1051	0.5292	0.0365
9.904	1.205	1.051	1.387	1.277	0.5347	0.0929	0.5609	0.0568
12.38	1.079	0.8470	1.112	0.9198	1.359	1.351	0.5784	0.1109



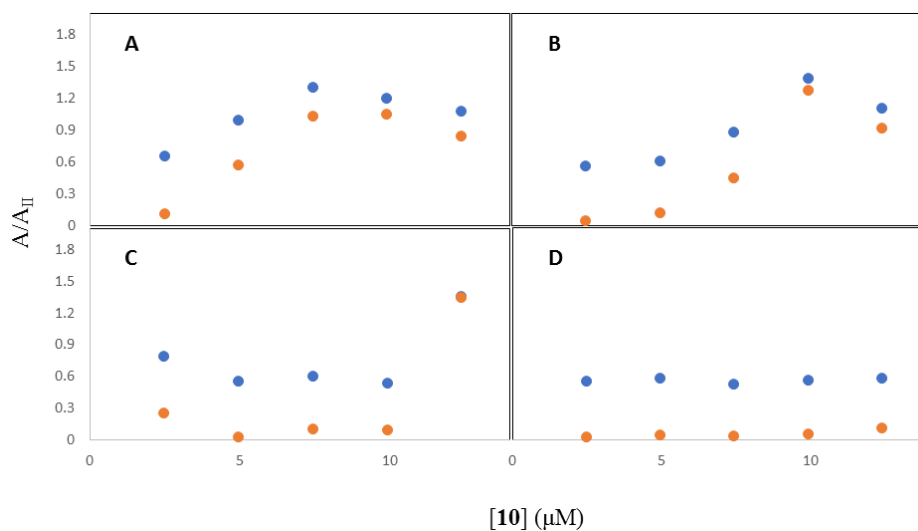


**Figure S23.** Plots of ratio of H-aggregate (I/II, blue) and J-aggregate (III/II, red) to monomeric bands against concentration of squaraine **10** for (A) control; (B) compound **1** ( $8\mu\text{M}$ ); (C) compound **2** ( $8\mu\text{M}$ ); and (D) compound **3** ( $8\mu\text{M}$ ).

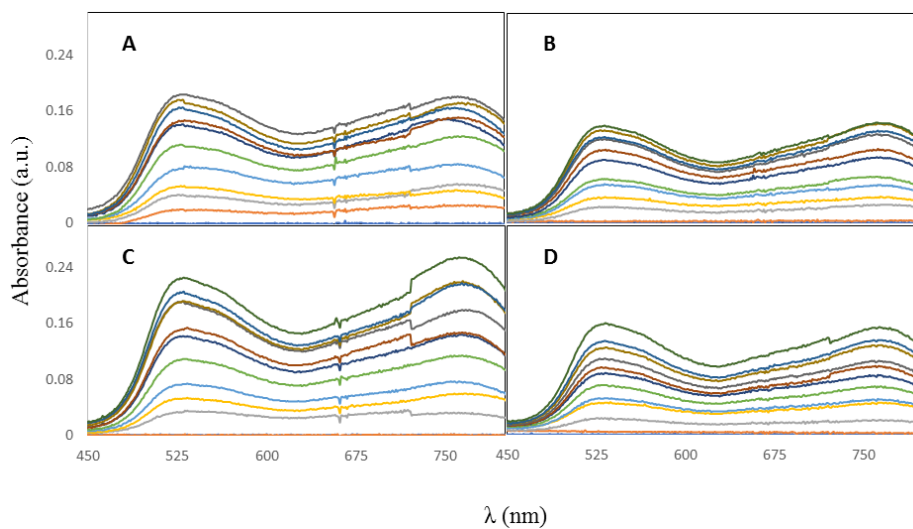


**Figure S24.** UV-vis absorption spectra of squaraine **11** for (A) control; (B) compound **1** ( $8\mu\text{M}$ ); (C) compound **2** ( $8\mu\text{M}$ ); and (D) compound **3** ( $8\mu\text{M}$ ) (squaraine **11** concentrations increase in the order as follows:  $1.0\mu\text{M}$ ;  $2.0\mu\text{M}$ ;  $3.1\mu\text{M}$ ;  $4.1\mu\text{M}$ ;  $5.1\mu\text{M}$ ;  $6.2\mu\text{M}$ ;  $7.2\mu\text{M}$ ;  $8.2\mu\text{M}$ ;  $9.2\mu\text{M}$ ;  $10.3\mu\text{M}$ ).

**Table S12.** Summary table of ratio of H-aggregate (**I/II**) and J-aggregate (**III/II**) to monomeric bands for various concentrations of squaraine **11** for control; compound **1** (8 $\mu$ M); compound **2** (8 $\mu$ M); and compound **3** (8 $\mu$ M).

[ <b>11</b> ] ( $\mu$ M)	Control		<b>1</b>		<b>2</b>		<b>3</b>	
	H-band ( <b>I/II</b> )	J-band ( <b>III/II</b> )	H-band ( <b>I/II</b> )	J-band ( <b>III/II</b> )	H-band ( <b>I/II</b> )	J-band ( <b>III/II</b> )	H-band ( <b>I/II</b> )	J-band ( <b>III/II</b> )
2.052	0.4315	1.086	0.3789	0.9145	0.4256	0.9368	0.4105	0.9499
4.104	0.4514	0.9486	0.4423	1.000	0.4331	0.9491	0.4162	1.014
6.156	0.4690	0.8268	0.3972	0.9227	0.4366	1.138	0.4306	1.065
8.208	0.4949	0.9739	0.4371	0.8035	0.5314	0.7735	0.4197	0.9391
10.26	0.4599	0.9846	0.4428	0.9110	0.5018	0.7511	0.4414	1.009

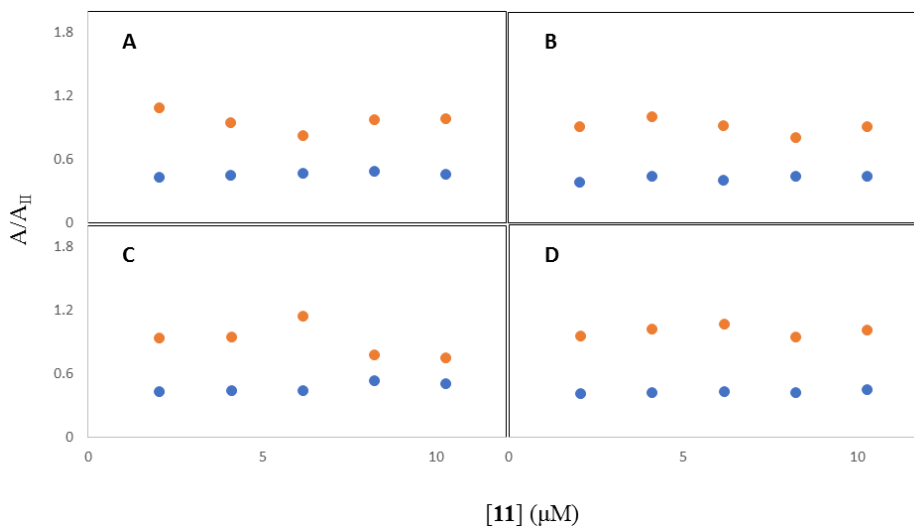


**Figure S25.** Plots of ratio of H-aggregate (**I/II**, blue) and J-aggregate (**III/II**, red) to monomeric bands against concentration of squaraine **11** for (A) control; (B) compound **1** (8 $\mu$ M); (C) compound **2** (8 $\mu$ M); and (D) compound **3** (8 $\mu$ M).

## HYDROLYTIC DECAY STUDIES OF SQUARAIN DYES

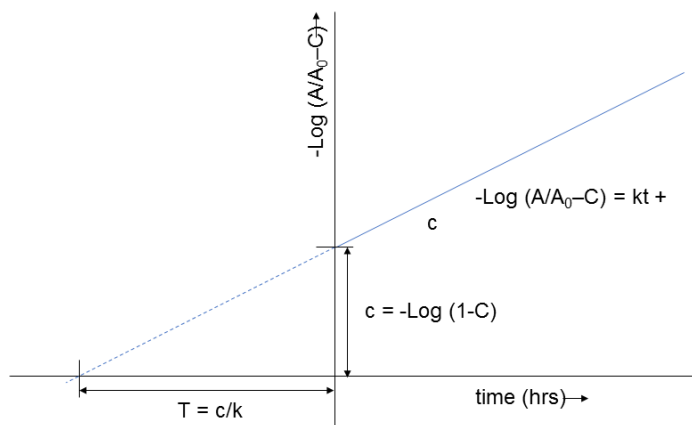
The linear form of the concentration of the squaraines in a reversible first order reaction with time is given by the following Equation S2:

$$-\text{Log}(A/A_0 - C) = kt - \text{Log}(1-C) \quad (\text{Equation S2})$$

where A is the integrated area of absorption at a given time,  $A_0$  is the initial integrated area of absorption, C denotes the aggregated concentration of the decaying species, and k represents the rate or the exponential decay constant.

T, the hydrolytic protection parameter is defined as the theoretical time taken for the decay of the aggregate concentration. It is given by the ratio of the intercept ( $c = -\text{Log}(1-C)$ ), and the slope (k) of the extrapolated linear plot of the hydrolytic decay as per the Equation S3 below:

$$T = c/k \quad (\text{Equation S3})$$



T is directly proportional to the intercept (c), and inversely proportional to the slope (k) of the linear plot of the decaying species. Hence, it is a direct measure of the hydrolytic protection of the decaying species.

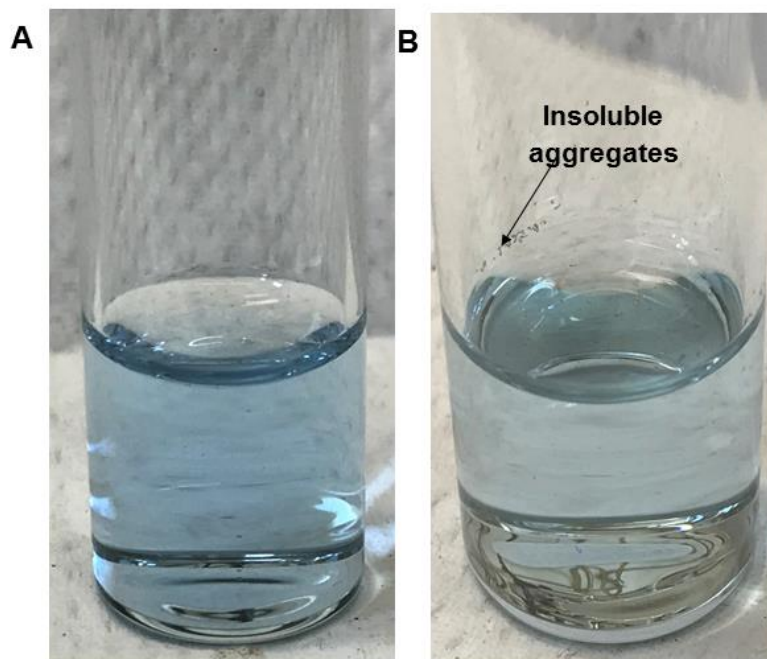


**Figure S26.** Photographs illustrating the hydrolysis of squaraine **6** ( $24\ \mu\text{M}$ ) at (A) 0 hours, showing intense coloration of the dye in the solution (B) 3 hours, showing significant loss of coloration as well as appearance of insoluble aggregates.

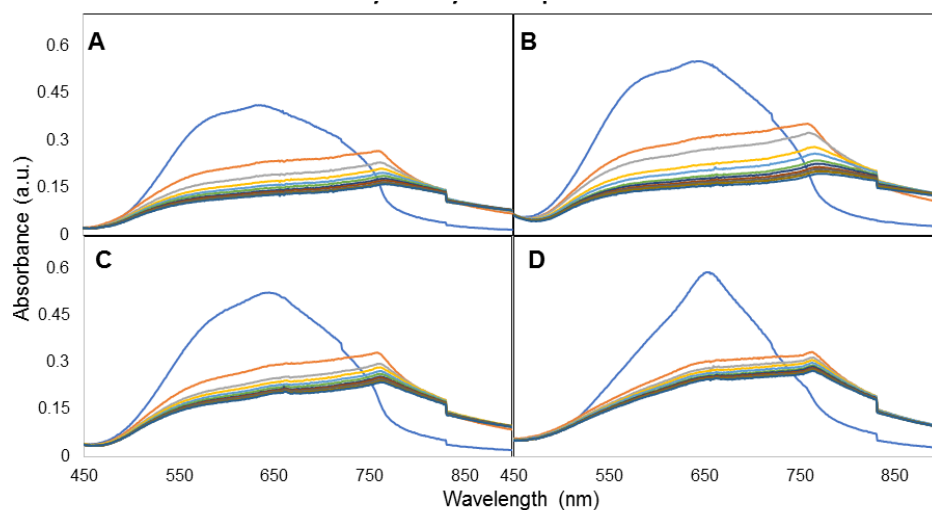


**Figure S27.** UV-vis absorption spectra of squaraine **4** ( $24\ \mu\text{M}$ ) for (A) control; (B) compound **1** ( $24\ \mu\text{M}$ ); (C) compound **2** ( $24\ \mu\text{M}$ ); and (D) compound **3** ( $24\ \mu\text{M}$ ). (Each spectrum is recorded at 30 minutes over a period of 5 hours).

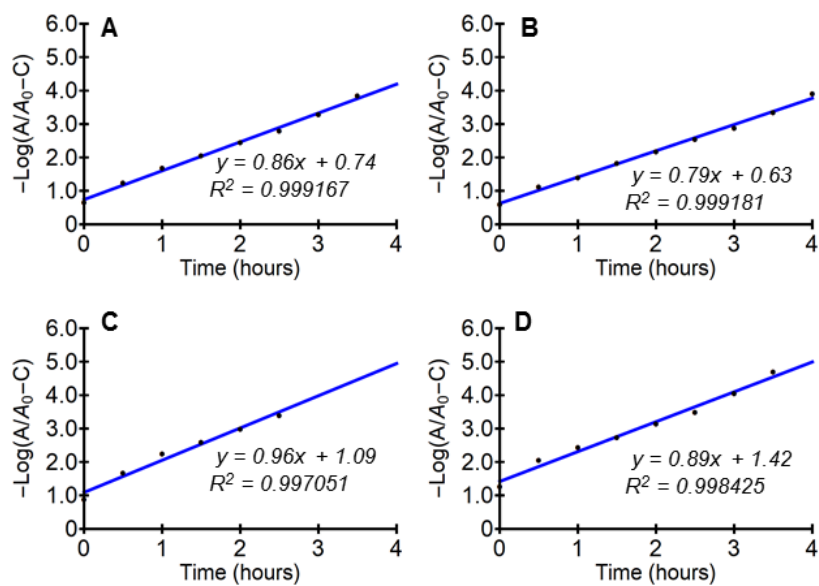


**Figure S28.** Linear plot for first order exponential hydrolytic decay of squaraine **4** (24  $\mu\text{M}$ ) for (A) control; (B) compound **1** (24  $\mu\text{M}$ ); (C) compound **2** (24  $\mu\text{M}$ ); and (D) compound **3** (24  $\mu\text{M}$ ) (slope of the plot is a measure of the exponential decay constant  $k$ ; intercept of the plot is a measure of the aggregated concentration  $C$ ).

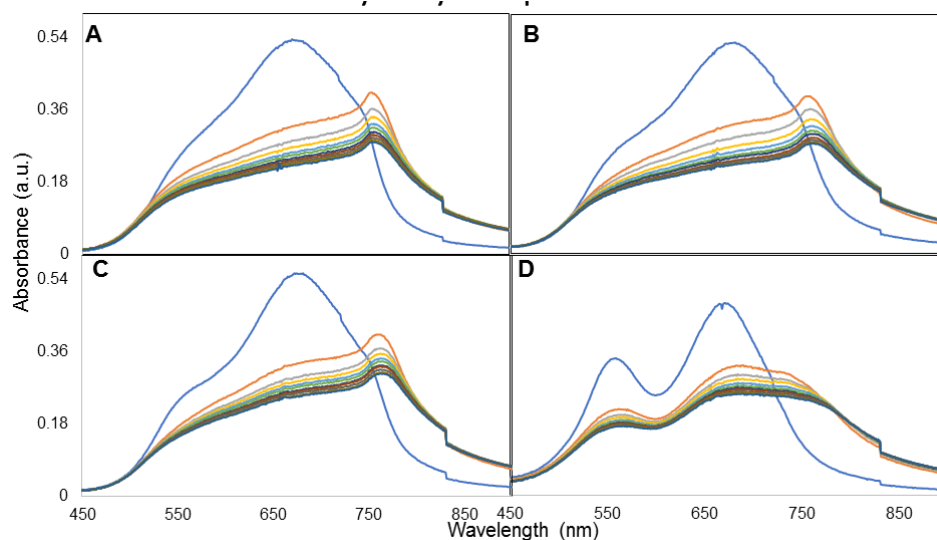


**Figure S29.** UV-vis absorption spectra of squaraine **5** (24  $\mu\text{M}$ ) for (A) control; (B) compound **1** (24  $\mu\text{M}$ ); (C) compound **2** (24  $\mu\text{M}$ ); and (D) compound **3** (24  $\mu\text{M}$ ). (Each spectrum is recorded at 30 minutes over a period of 5 hours).

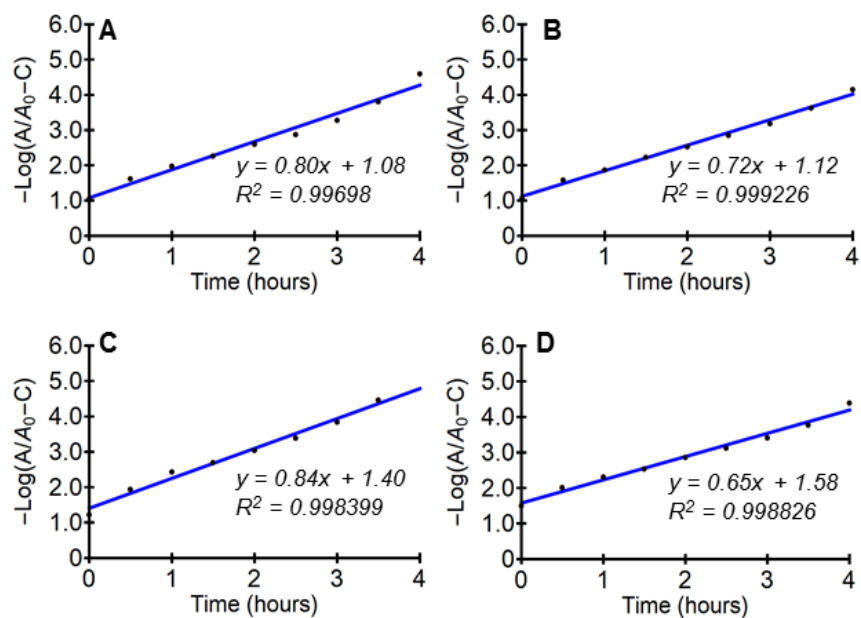


**Figure S30.** Linear plot for first order exponential hydrolytic decay of squaraine **5** (24  $\mu\text{M}$ ) for (A) control; (B) compound **1** (24  $\mu\text{M}$ ); (C) compound **2** (24  $\mu\text{M}$ ); and (D) compound **3** (24  $\mu\text{M}$ ) (slope of the plot is a measure of the exponential decay constant  $k$ ; intercept of the plot is a measure of the aggregated concentration  $C$ ).

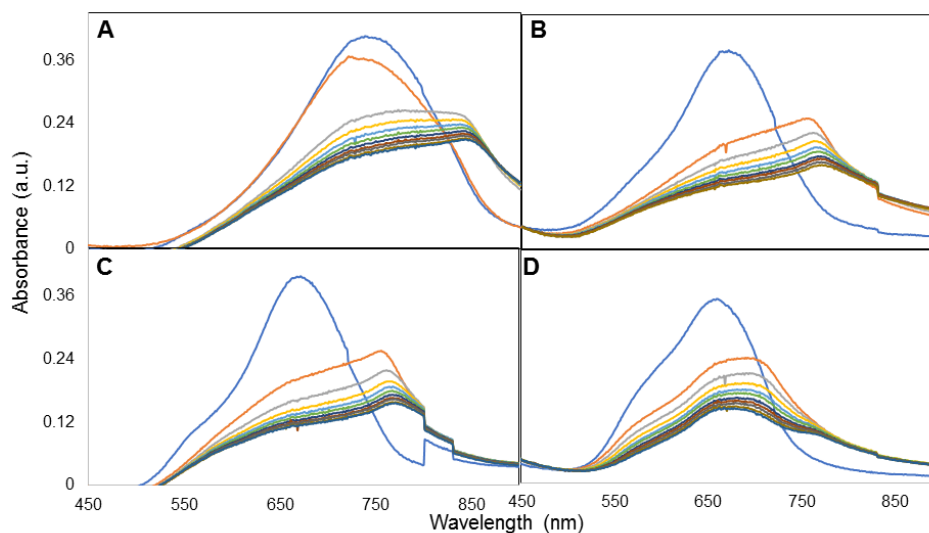


**Figure S31.** UV-vis absorption spectra of squaraine **6** (24  $\mu\text{M}$ ) for (A) control; (B) compound **1** (24  $\mu\text{M}$ ); (C) compound **2** (24  $\mu\text{M}$ ); and (D) compound **3** (24  $\mu\text{M}$ ) (Each spectrum is recorded at 30 minutes over a period of 5 hours).

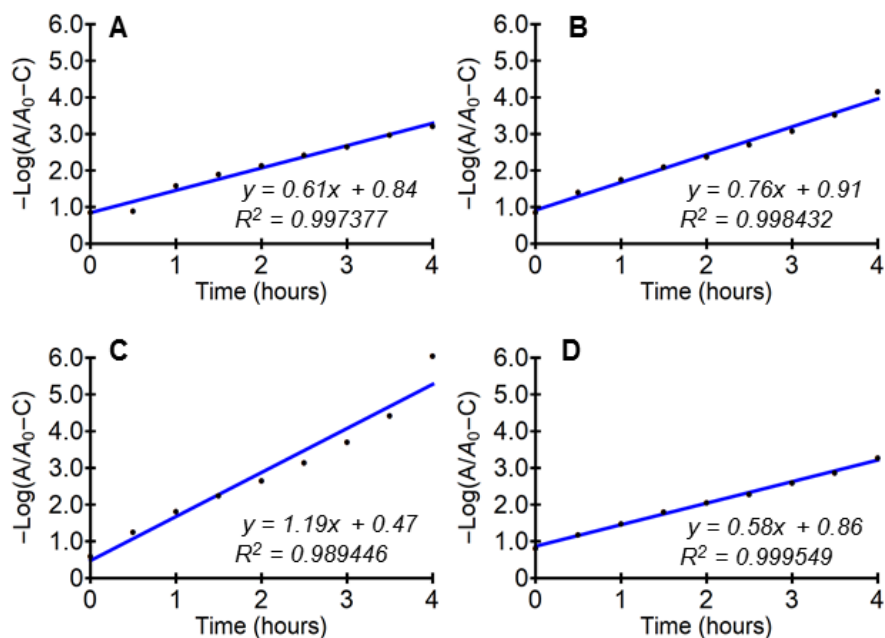


**Figure S32.** Linear plot for first order exponential hydrolytic decay of squaraine **6** (24  $\mu\text{M}$ ) for (A) control; (B) compound **1** (24  $\mu\text{M}$ ); (C) compound **2** (24  $\mu\text{M}$ ); and (D) compound **3** (24  $\mu\text{M}$ ) (slope of the plot is a measure of the exponential decay constant  $k$ ; intercept of the plot is a measure of the aggregated concentration  $C$ ).

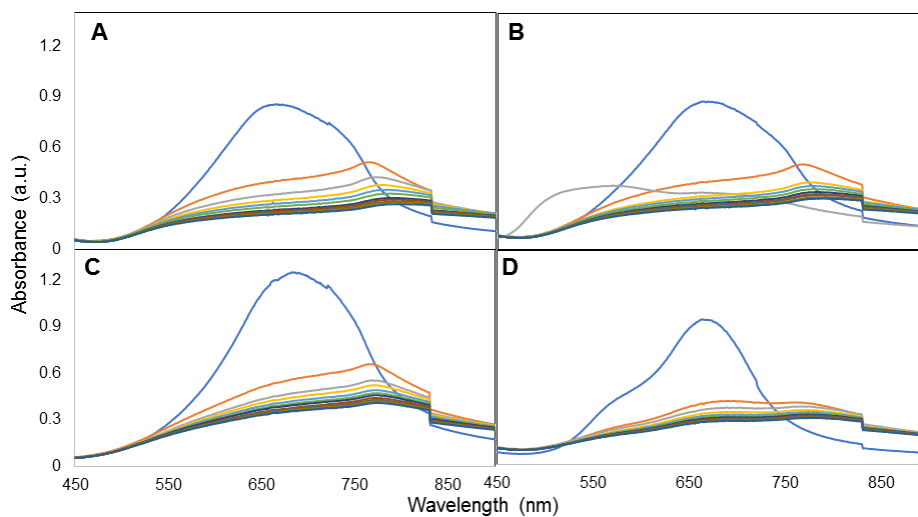


**Figure S33.** UV-vis absorption spectra of squaraine **7** (24  $\mu\text{M}$ ) for (A) control; (B) compound **1** (24 $\mu\text{M}$ ); (C) compound **2** (24 $\mu\text{M}$ ); and (D) compound **3** (24 $\mu\text{M}$ ) (Each spectrum is recorded at 30 minutes over a period of 5 hours).

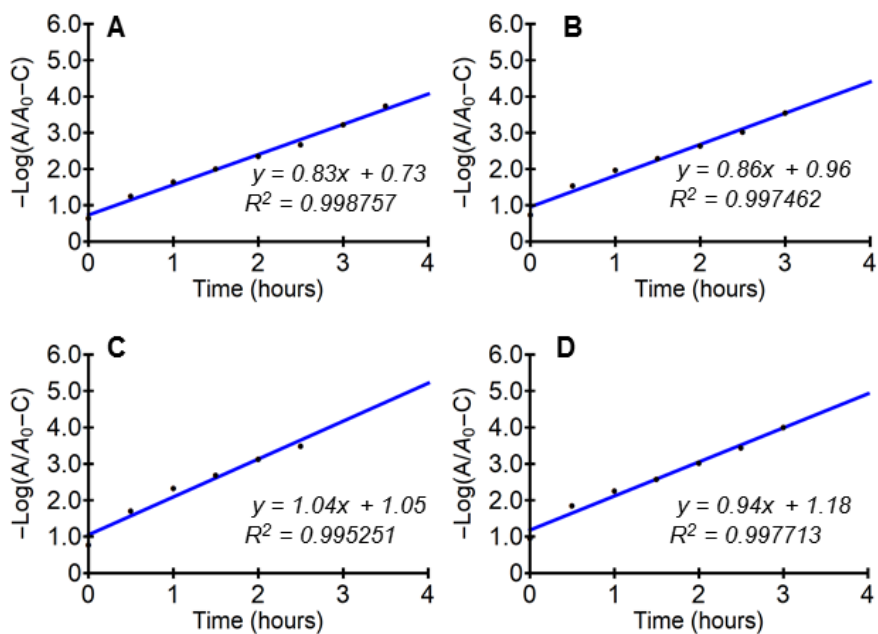


**Figure S34.** Linear plot for first order exponential hydrolytic decay of squaraine **7** (24  $\mu\text{M}$ ) for (A) control; (B) compound **1** (24  $\mu\text{M}$ ); (C) compound **2** (24  $\mu\text{M}$ ); and (D) compound **3** (24  $\mu\text{M}$ ) (slope of the plot is a measure of the exponential decay constant  $k$ ; intercept of the plot is a measure of the aggregated concentration  $C$ ).

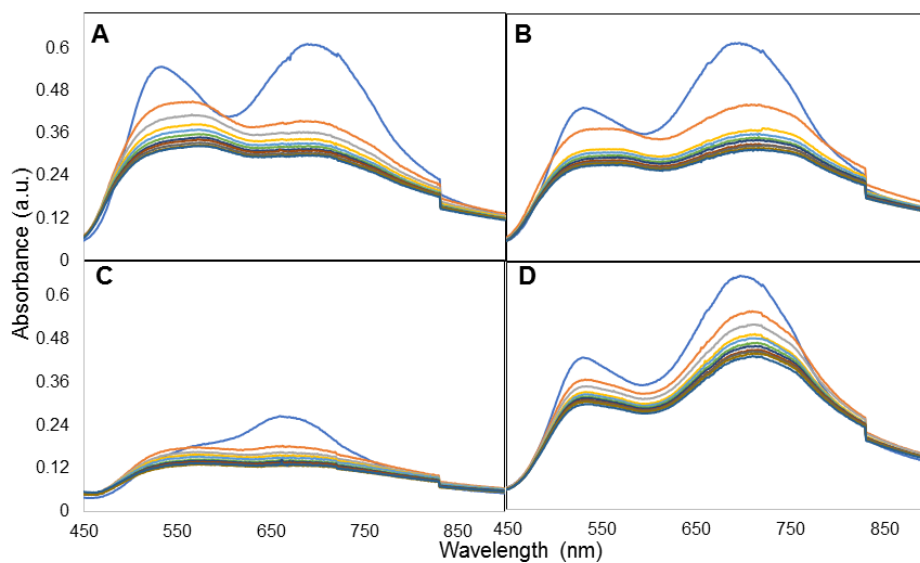


**Figure S35.** UV-vis absorption spectra of squaraine **8** (24  $\mu\text{M}$ ) for (A) control; (B) compound **1** (24 $\mu\text{M}$ ); (C) compound **2** (24 $\mu\text{M}$ ); and (D) compound **3** (24 $\mu\text{M}$ ) (Each spectrum is recorded at 30 minutes over a period of 5 hours).



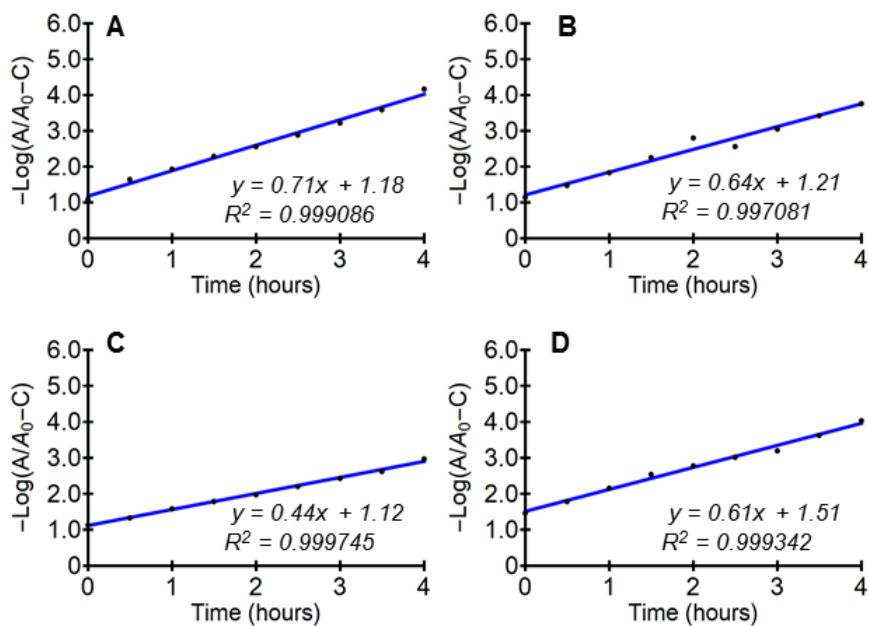


**Figure S36.** Linear plot for first order exponential hydrolytic decay of squaraine **8** (24  $\mu\text{M}$ ) for (A) control; (B) compound **1** (24  $\mu\text{M}$ ); (C) compound **2** (24  $\mu\text{M}$ ); and (D) compound **3** (24  $\mu\text{M}$ ) (slope of the plot is a measure of the exponential decay constant  $k$ ; intercept of the plot is a measure of the aggregated concentration  $C$ ).

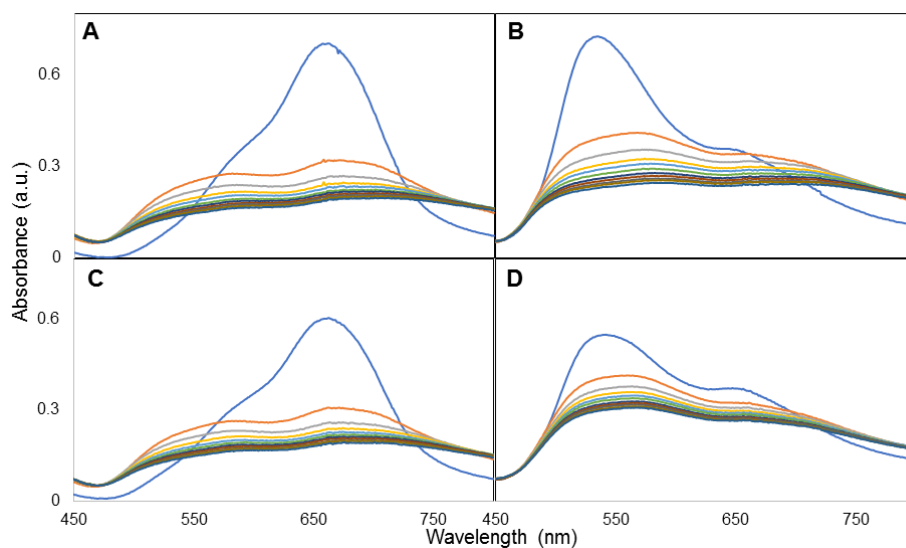


**Figure S37.** UV-vis absorption spectra of squaraine **9** (24  $\mu\text{M}$ ) for (A) control; (B) compound **1** (24 $\mu\text{M}$ ); (C) compound **2** (24 $\mu\text{M}$ ); and (D) compound **3** (24 $\mu\text{M}$ ) (Each spectrum is recorded at 30 minutes over a period of 5 hours).

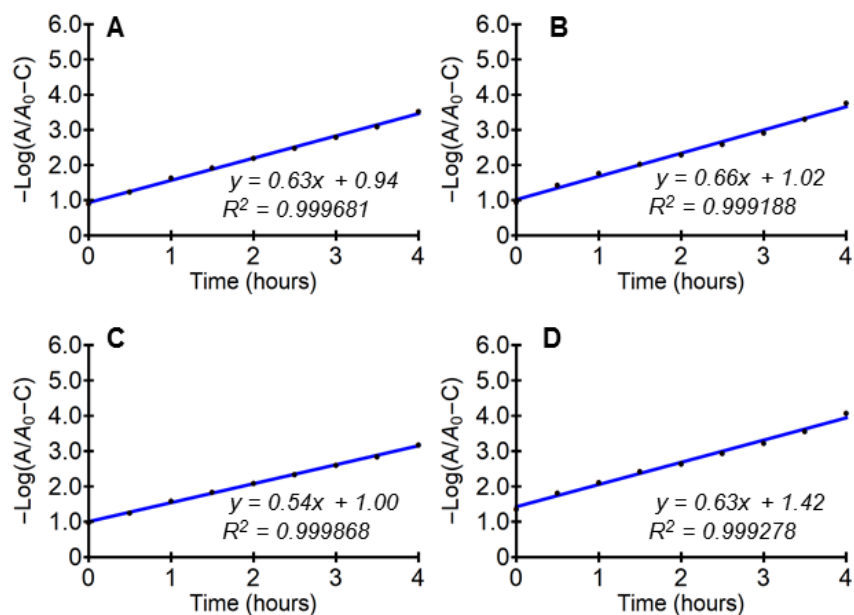


**Figure S38.** Linear plot for first order exponential hydrolytic decay of squaraine **9** (24  $\mu\text{M}$ ) for (A) control; (B) compound **1** (24  $\mu\text{M}$ ); (C) compound **2** (24  $\mu\text{M}$ ); and (D) compound **3** (24  $\mu\text{M}$ ) (slope of the plot is a measure of the exponential decay constant  $k$ ; intercept of the plot is a measure of the aggregated concentration  $C$ ).

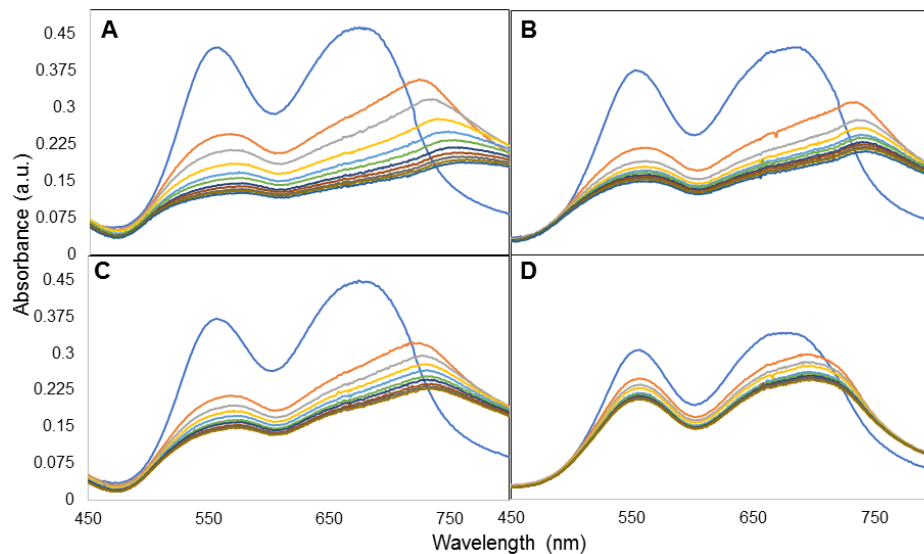


**Figure S39.** UV-vis absorption spectra of squaraine **10** (24  $\mu\text{M}$ ) for (A) control; (B) compound **1** (24  $\mu\text{M}$ ); (C) compound **2** (24  $\mu\text{M}$ ); and (D) compound **3** (24  $\mu\text{M}$ ) (Each spectrum is recorded at 30 minutes over a period of 5 hours).

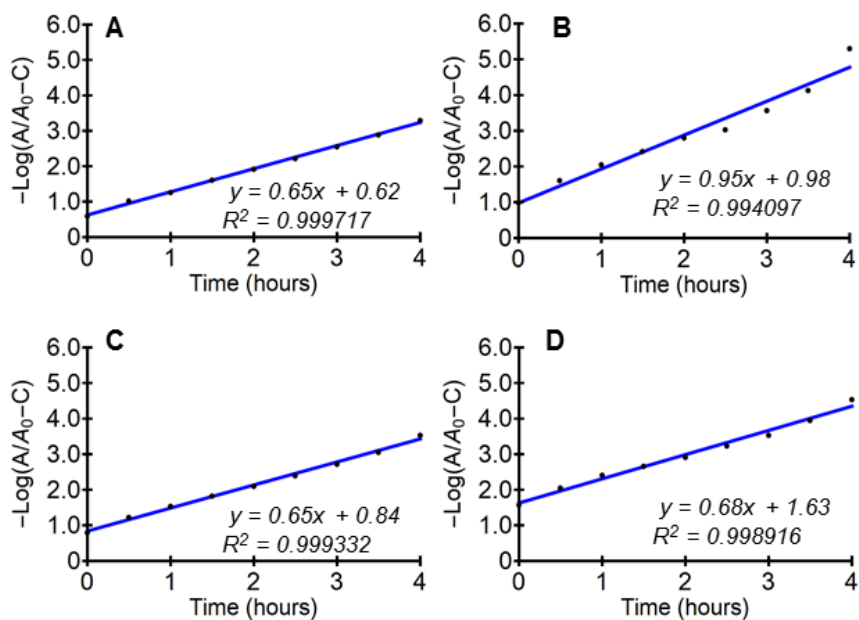


**Figure S40.** Linear plot for first order exponential hydrolytic decay of squaraine **10** (24  $\mu\text{M}$ ) for (A) control; (B) compound **1** (24  $\mu\text{M}$ ); (C) compound **2** (24  $\mu\text{M}$ ); and (D) compound **3** (24  $\mu\text{M}$ ) (slope of the plot is a measure of the exponential decay constant  $k$ ; intercept of the plot is a measure of the aggregated concentration  $C$ ).

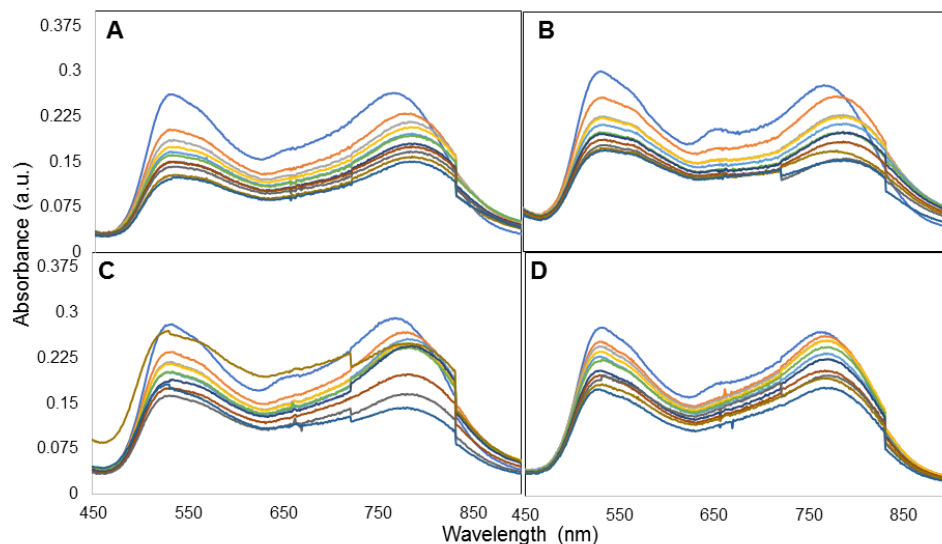


**Figure S41.** UV-vis absorption spectra of squaraine **11** (24  $\mu\text{M}$ ) for (A) control; (B) compound **1** (24  $\mu\text{M}$ ); (C) compound **2** (24  $\mu\text{M}$ ); and (D) compound **3** (24  $\mu\text{M}$ ). (Each spectrum is recorded at 30 minutes over a period of 5 hours).

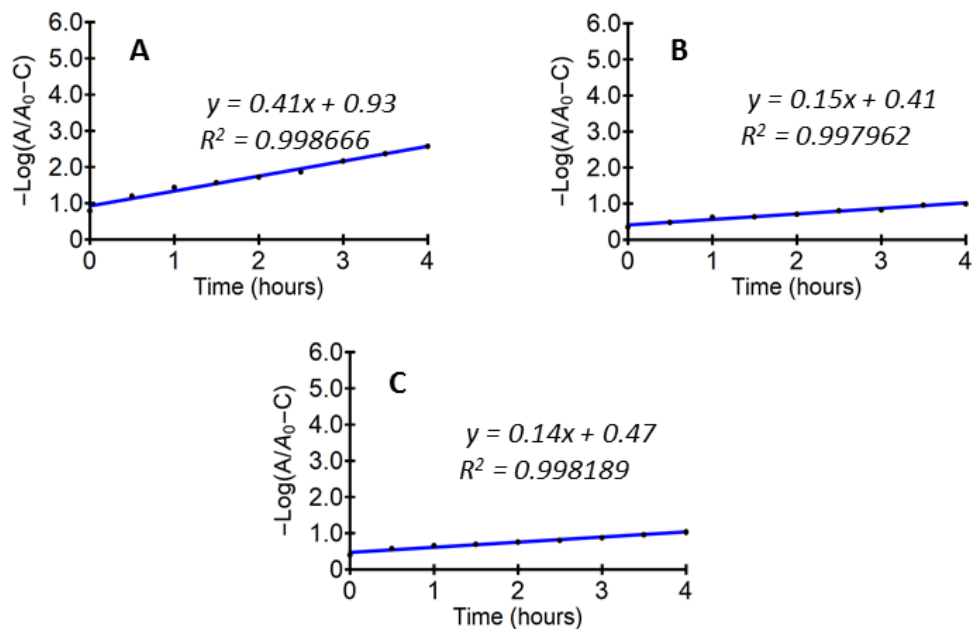


**Figure S42.** Linear plot for first order exponential hydrolytic decay of squaraine **11** (24  $\mu\text{M}$ ) for (A) control; (B) compound **1** (24  $\mu\text{M}$ ); and (C) compound **2** (24  $\mu\text{M}$ ) (slope of the plot is a measure of the exponential decay constant  $k$ ; intercept of the plot is a measure of the aggregated concentration  $C$ ).

**Table S13.** Summary table of intercept ( $c$ ), decay constant ( $k$ ), and  $T$  (hydrolytic protection parameter,  $T = c/k$ ) for hydrolytic decay of squaraines (**4-11**) under control, compound **1**, compound **2**, and compound **3**. The values are calculated from the linear plots of hydrolytic decay as per Equation S3.

Squaraine Guests	control			1			2			3		
	$c$	$k$ ( $\text{h}^{-1}$ )	$T$ ( $\text{h}$ )	$c$	$k$ ( $\text{h}^{-1}$ )	$T$ ( $\text{h}$ )	$c$	$k$ ( $\text{h}^{-1}$ )	$T$ ( $\text{h}$ )	$c$	$k$ ( $\text{h}^{-1}$ )	$T$ ( $\text{h}$ )
<b>4</b>	0.74	0.86	0.86	0.63	0.79	0.79	1.09	0.96	1.14	1.42	0.89	1.59
<b>5</b>	1.08	0.79	1.37	1.12	0.72	1.55	1.41	0.84	1.68	1.58	0.65	2.43
<b>6</b>	0.85	0.61	1.39	0.92	0.76	1.21	0.48	1.19	0.40	0.87	0.59	1.47
<b>7</b>	0.73	0.83	0.88	0.96	0.86	1.12	1.05	1.04	1.01	1.18	0.94	1.26
<b>8</b>	1.18	0.71	1.66	1.21	0.64	1.89	1.12	0.44	2.54	1.51	0.61	2.48
<b>9</b>	0.94	0.63	1.49	1.02	0.66	1.54	1.01	0.54	1.87	1.43	0.63	2.27
<b>10</b>	0.62	0.65	0.95	0.98	0.95	1.03	0.84	0.65	1.29	1.63	0.68	2.39
<b>11</b>	0.93	0.41	2.27	0.41	0.15	2.73	0.47	0.14	3.36	-	-	

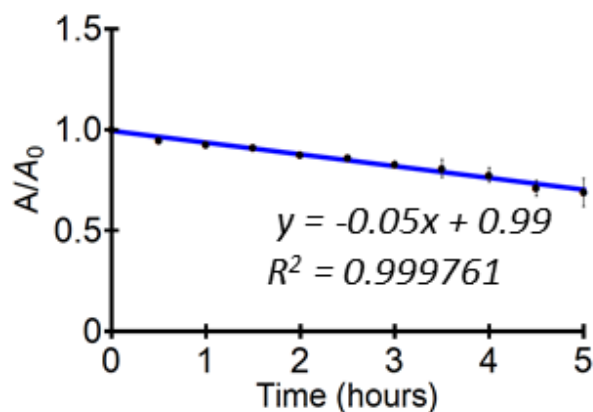


**Figure S43.** Linear plot for zero order behavior of hydrolytic decay of squaraine **11** (24  $\mu\text{M}$ ) with compound **3** (24  $\mu\text{M}$ ) (rate of decay  $k = 0.05 \text{ h}^{-1}$ ).

#### NONLINEAR CURVE FITTING OF THE FLUORESCENCE TITRATION DATA FOR ASSOCIATION CONSTANT CALCULATIONS

All fluorescence titration data fits were done with Solver.xlam using “GRG-Nonlinear” method in Excel. A nonlinear curve fitting method was employed to compare against a standard 1:1 and 1:2 host-guest interaction models, using the Equation S4 and Equation S5 respectively<sup>2</sup>:

$$\Delta f = \Delta f_{\text{HG}} (K_1[G_0] / (1 + K_1[G_0])) \quad (\text{Equation S4})$$

$$\Delta f = (\Delta f_{\text{HG}}K_1[G_0] + \Delta f_{\text{HG}2}K_1K_2[G_0]^2) / (1 + K_1[G_0] + K_1K_2[G_0]^2) \quad (\text{Equation S5})$$

where,  $\Delta f$  is the observed change in the normalized fluorescence intensity ( $\Delta f = F/F_0 - 1$ , where  $F$  is the integrated fluorescence intensity at a particular guest concentration, and  $F_0$  is the integrated fluorescence intensity in the absence of guest) of the host H;  $\Delta f_{\text{HG}}$  is the change in the normalized fluorescence intensity of host H at the first binding event;  $\Delta f_{\text{HG}2}$  is the overall change in the normalized fluorescence intensity of host H, at the second binding event;  $K_1$  is the association constant value for the first binding event to the host H;  $K_2$  is the association constant value for the second binding event to HG; and  $[G_0]$  is the concentration of guest.

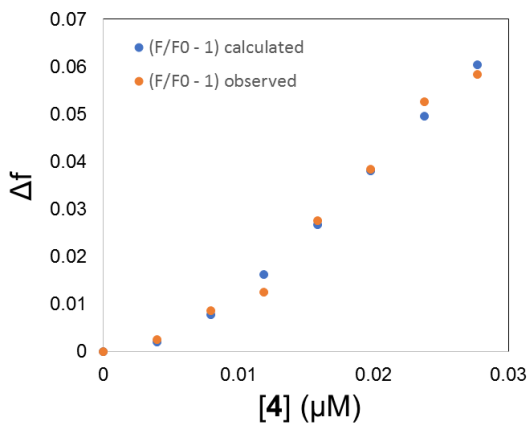


**Figure S44.** 1:2 host-guest binding isotherm for **1** and squaraine **4** ( $K_1 = 2.8 (0.3) \times 10^3 \text{ M}^{-1}$ ;  $K_2 = 2.7 (0.4) \times 10^{11} \text{ M}^{-1}$ ; Equation S5 was used for calculation).

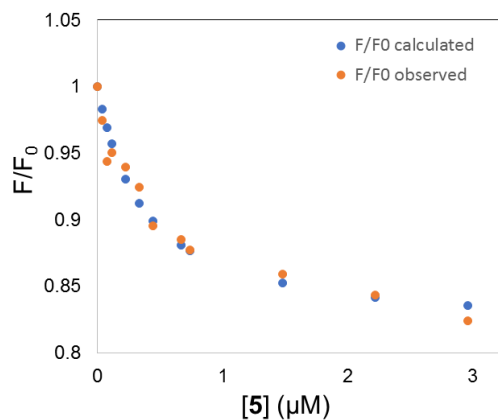


**Figure S45.** 1:1 host-guest binding isotherm for **1** and squaraine **5** ( $K_1 = 2.7 (0.5) \times 10^6 \text{ M}^{-1}$ ; Equation S4 was used for calculation).

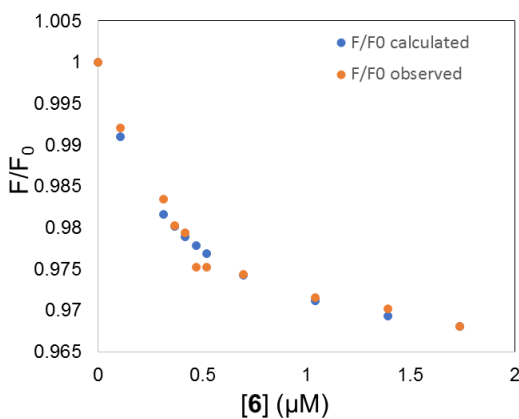


**Figure S46.** 1:1 host-guest binding isotherm for **1** and squaraine **6** ( $K_1 = 3.5 (0.5) \times 10^6 \text{ M}^{-1}$ ; Equation S4 was used for calculation).

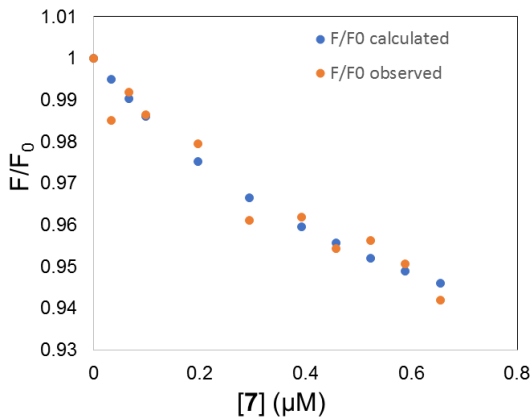


**Figure S47.** 1:1 host-guest binding isotherm for **1** and squaraine **7** ( $K_1 = 1.5 (0.7) \times 10^6 \text{ M}^{-1}$ ; Equation S4 was used for calculation).

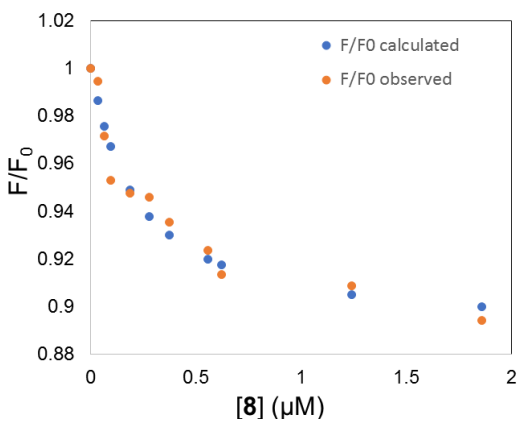


**Figure S48.** 1:1 host-guest binding isotherm for **1** and squaraine **8** ( $K_1 = 4.5 (0.8) \times 10^6 \text{ M}^{-1}$ ; Equation S4 was used for calculation).

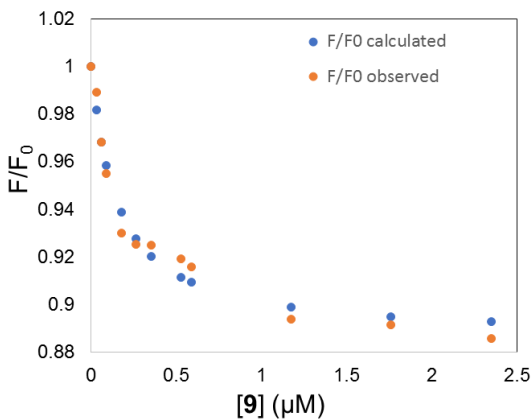


**Figure S49.** 1:1 host-guest binding isotherm for **1** and squaraine **9** ( $K_1 = 6.6 (0.8) \times 10^6 \text{ M}^{-1}$ ; Equation S4 was used for calculation).

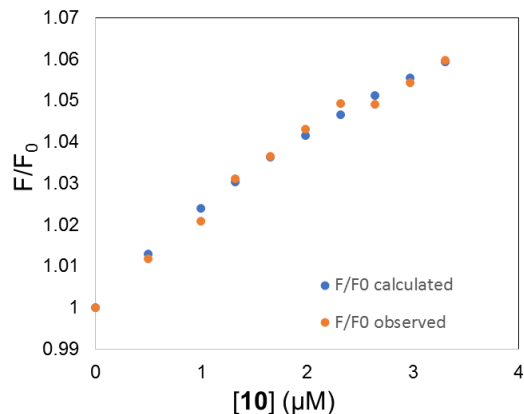


**Figure S50.** 1:1 host-guest binding isotherm for **1** and squaraine **10** ( $K_1 = 1.7 (0.4) \times 10^5 \text{ M}^{-1}$ ; Equation S4 was used for calculation).

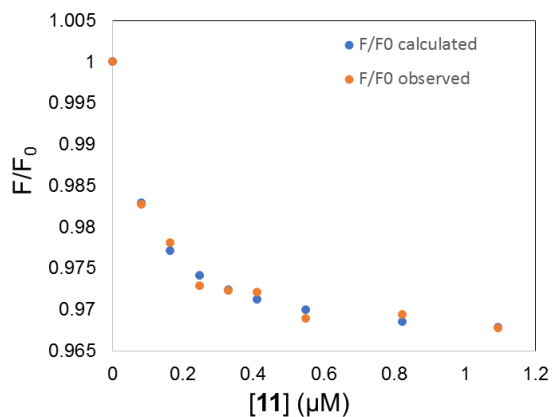


**Figure S51.** 1:1 host-guest binding isotherm for **1** and squaraine **11** ( $K_1 = 1.2 (0.2) \times 10^7 \text{ M}^{-1}$ ; Equation S4 was used for calculation).

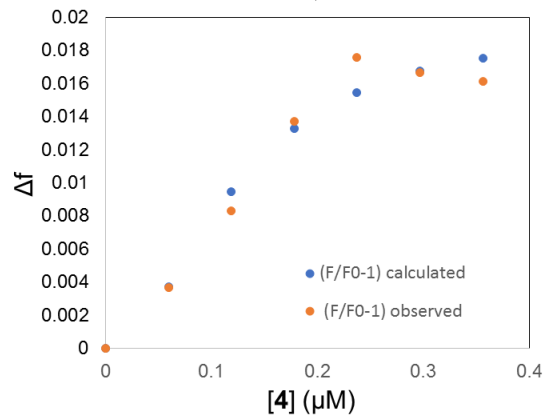


**Figure S52.** 1:2 host-guest binding isotherm for **2** and squaraine **4** ( $K_1 = 1.6 (0.4) \times 10^4 \text{ M}^{-1}$ ;  $K_2 = 5.4 (0.8) \times 10^9 \text{ M}^{-1}$ ; Equation S5 was used for calculation).



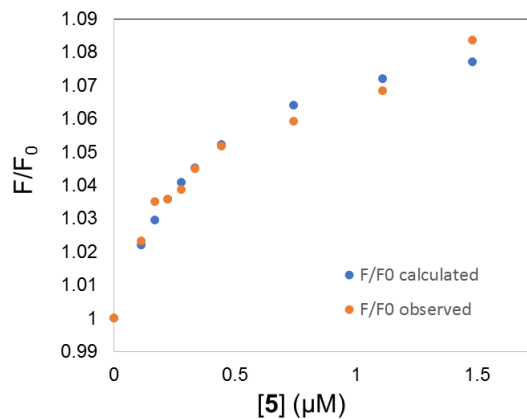


**Figure S53.** 1:1 host-guest binding isotherm for **2** and squaraine **5** ( $K_1 = 2.6 (0.4) \times 10^6 \text{ M}^{-1}$ ; Equation S4 was used for calculation).

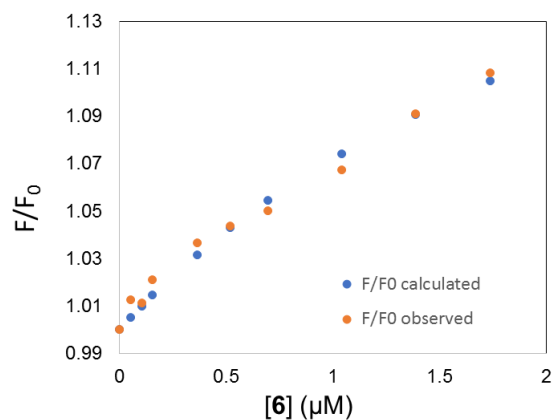


**Figure S54.** 1:1 host-guest binding isotherm for **2** and squaraine **6** ( $K_1 = 3.5 (1.2) \times 10^5 \text{ M}^{-1}$ ; Equation S4 was used for calculation).

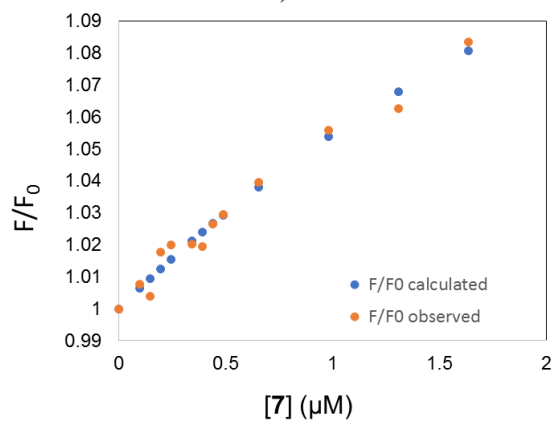


**Figure S55.** 1:1 host-guest binding isotherm for **2** and squaraine **7** ( $K_1 = 2.1 (0.8) \times 10^5 \text{ M}^{-1}$ ; Equation S4 was used for calculation).

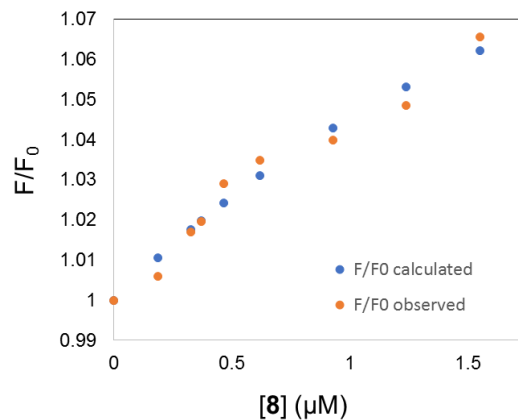


**Figure S56.** 1:1 host-guest binding isotherm for **2** and squaraine **8** ( $K_1 = 3.1 (0.1) \times 10^5 \text{ M}^{-1}$ ; Equation S4 was used for calculation).

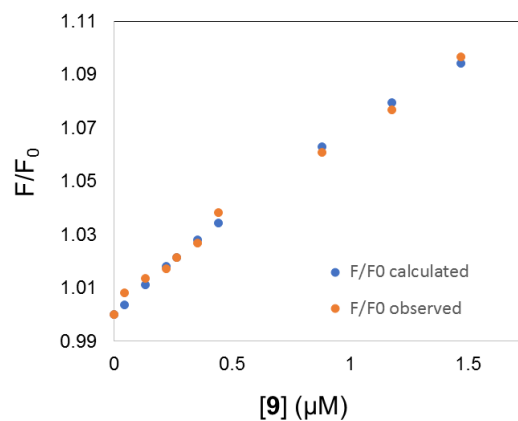


**Figure S57.** 1:1 host-guest binding isotherm for **2** and squaraine **9** ( $K_1 = 2.4 (0.7) \times 10^5 \text{ M}^{-1}$ ; Equation S4 was used for calculation).

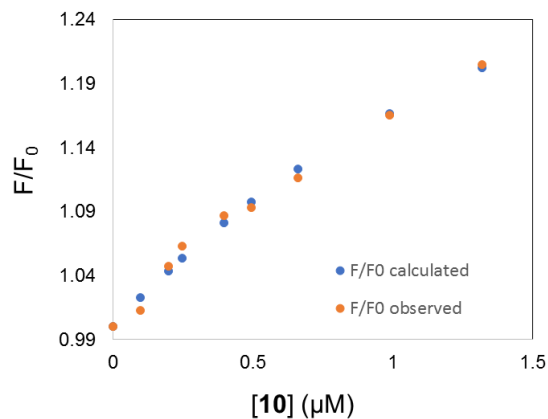


**Figure S58.** 1:1 host-guest binding isotherm for **2** and squaraine **10** ( $K_1 = 4.2 (1.0) \times 10^5 \text{ M}^{-1}$ ; Equation S4 was used for calculation).

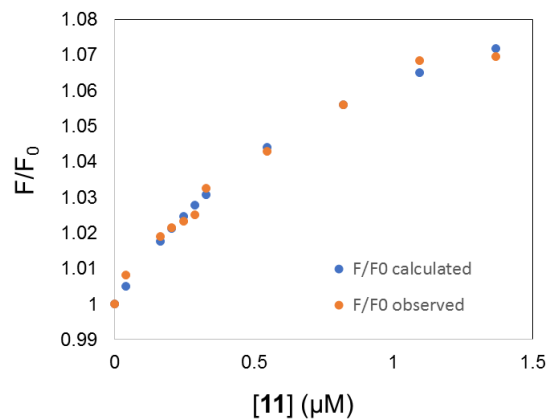


**Figure S59.** 1:1 host-guest binding isotherm for **2** and squaraine **11** ( $K_1 = 1.0 (0.1) \times 10^6 \text{ M}^{-1}$ ; Equation S4 was used for calculation).

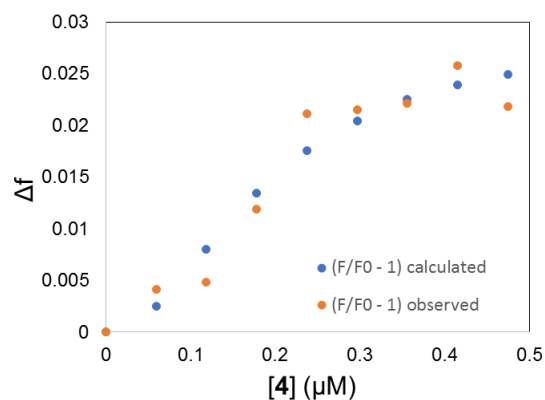


**Figure S60.** 1:2 host-guest binding isotherm for **3** and squaraine **4** ( $K_1 = 3.3 (0.4) \times 10^3 \text{ M}^{-1}$ ;  $K_2 = 7.1 (0.9) \times 10^9 \text{ M}^{-1}$ ; Equation S5 was used for calculation).

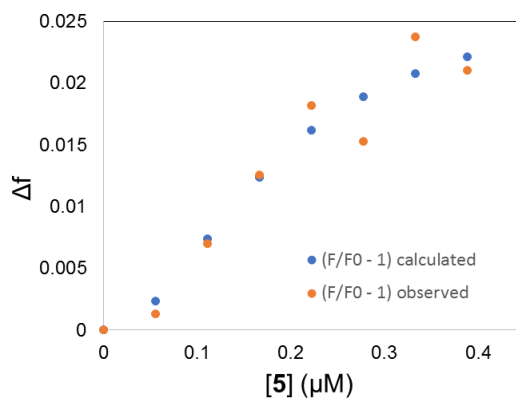


**Figure S61.** 1:2 host-guest binding isotherm for **3** and squaraine **5** ( $K_1 = 3.6 (0.6) \times 10^3 \text{ M}^{-1}$ ;  $K_2 = 1.2 (0.2) \times 10^{10} \text{ M}^{-1}$ ; Equation S5 was used for calculation).

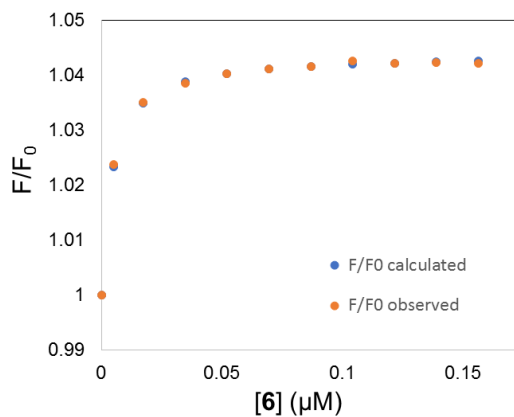


**Figure S62.** 1:1 host-guest binding isotherm for **3** and squaraine **6** ( $K_1 = 2.3 (0.1) \times 10^8 \text{ M}^{-1}$ ; Equation S4 was used for calculation).

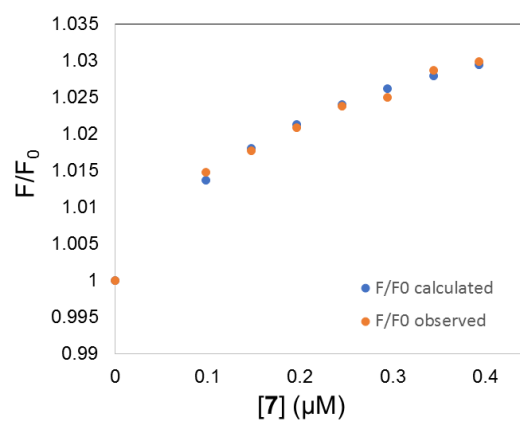


**Figure S63.** 1:1 host-guest binding isotherm for **3** and squaraine **7** ( $K_1 = 4.1 (0.5) \times 10^6 \text{ M}^{-1}$ ; Equation S4 was used for calculation).

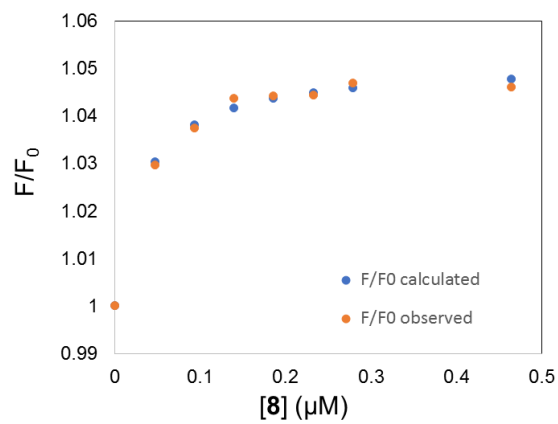


**Figure S64.** 1:1 host-guest binding isotherm for **3** and squaraine **8** ( $K_1 = 3.2 (0.4) \times 10^7 \text{ M}^{-1}$ ; Equation S4 was used for calculation).

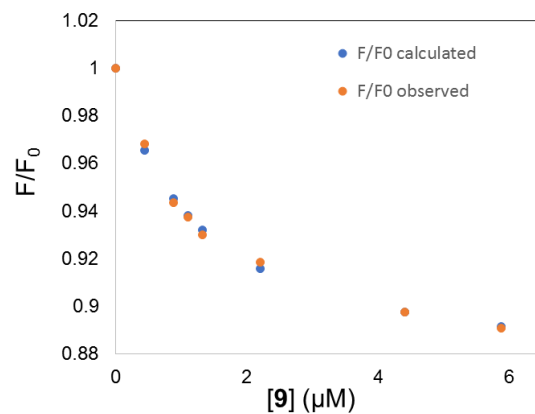


**Figure S65.** 1:1 host-guest binding isotherm for **3** and squaraine **9** ( $K_1 = 8.1 (0.5) \times 10^5 \text{ M}^{-1}$ ; Equation S4 was used for calculation).

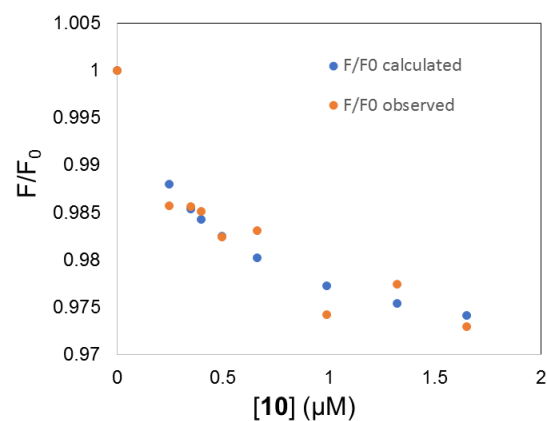


**Figure S66.** 1:1 host-guest binding isotherm for **3** and squaraine **10** ( $K_1 = 2.4 (0.6) \times 10^6 \text{ M}^{-1}$ ; Equation S4 was used for calculation).

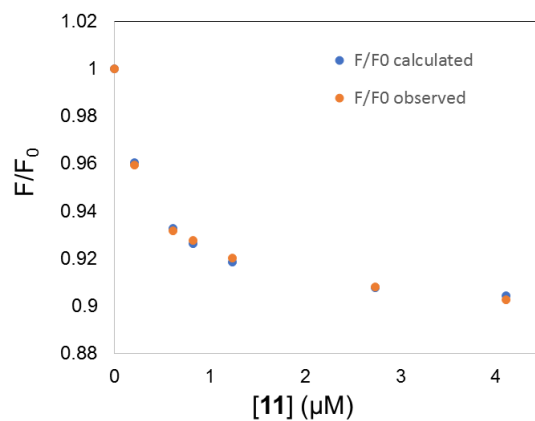


**Figure S67.** 1:1 host-guest binding isotherm for **3** and squaraine **11** ( $K_1 = 3.0 (0.2) \times 10^6 \text{ M}^{-1}$ ; Equation S4 was used for calculation).

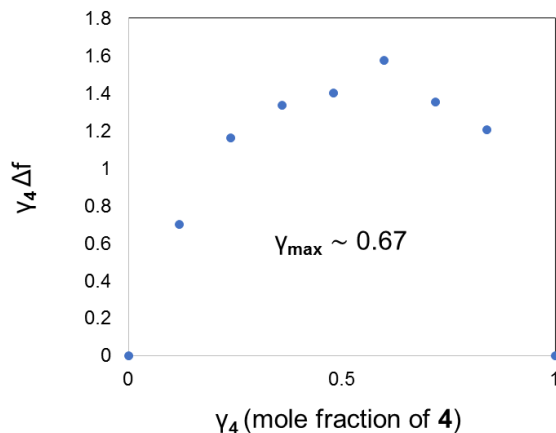


**Figure S68.** Job's plot for 1:2 host-guest binding dimer **1** and squaraine **4** ( $\gamma_{\max}$  is approximately 0.67 indicating 1:2 association).

**Table S14.** Tabulated data of Job's plot for 1:2 host-guest binding dimer **1** and squaraine **4** ( $\gamma_{\max}$  is approximately 0.67 indicating 1:2 association).

$\gamma_4$ (mole fraction of guest <b>4</b> )	$\gamma_4 * \Delta f$
1.0	0
0.84	1.2071
0.72	1.3534
0.60	1.5738
0.48	1.4023
0.36	1.3339
0.24	1.1613
0.12	0.7006
0	0

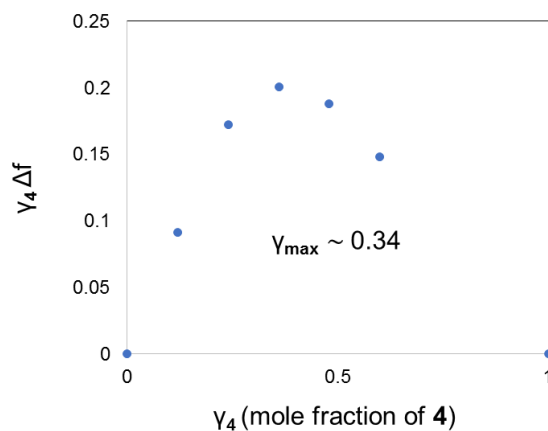


**Figure S69.** Job's plot for 1:2 host-guest binding dimer **2** and squaraine **4** ( $\gamma_{\max}$  is approximately 0.34 indicating 1:2 association).

**Table S15.** Tabulated data of Job's plot for 1:2 host-guest binding dimer **2** and squaraine **4** ( $\gamma_{\max}$  is approximately 0.34 indicating 1:2 association).

$\gamma_4$ (mole fraction of guest <b>4</b> )	$\gamma_4 \cdot \Delta f$
1.0	0
0.60	0.1480
0.48	0.1877
0.36	0.2010
0.24	0.1723
0.12	0.0912
0	0

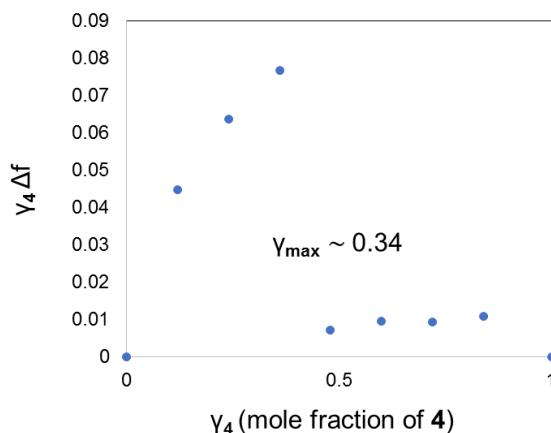


**Figure S70.** Job's plot for 1:2 host-guest binding dimer **3** and squaraine **4** ( $\gamma_{\max}$  is approximately 0.34 indicating 1:2 association).

**Table S16.** Tabulated data of Job's plot for 1:2 host-guest binding dimer **3** and squaraine **4** ( $\gamma_{\max}$  is approximately 0.34 indicating 1:2 association).

$\gamma_4$ (mole fraction of guest <b>4</b> )	$\gamma_4 \cdot \Delta f$
1.0	0
0.84	0.0108
0.72	0.0094
0.60	0.0096
0.48	0.0071
0.36	0.0768
0.24	0.0637
0.12	0.0448
0	0

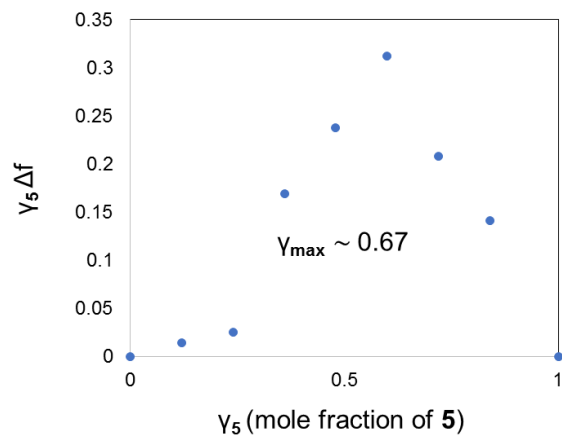


**Figure S71.** Job's plot for 1:2 host-guest binding dimer **3** and squaraine **5** ( $\gamma_{\max}$  is approximately 0.67 indicating 1:2 association).

**Table S17.** Tabulated data of Job's plot for 1:2 host-guest binding dimer **3** and squaraine **5** ( $\gamma_{\max}$  is approximately 0.67 indicating 1:2 association).

$\gamma_5$ (mole fraction of guest <b>5</b> )	$\gamma_5 \Delta f$
1.0	0
0.84	0.1413
0.72	0.2079
0.60	0.3124
0.48	0.2377
0.36	0.1695
0.24	0.0250
0.12	0.0147
0	0



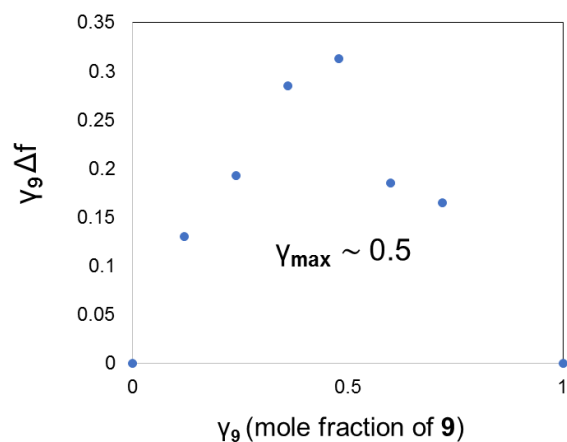


**Figure S72.** Job's plot for 1:1 host-guest binding dimer **3** and squaraine **9** ( $\gamma_{\max}$  is approximately 0.5 indicating 1:1 association).

**Table S18.** Tabulated data of Job's plot for 1:1 host-guest binding dimer **3** and squaraine **9** ( $\gamma_{\max}$  is approximately 0.5 indicating 1:1 association).

$\gamma_9$ (mole fraction of guest <b>9</b> )	$\gamma_9 * \Delta f$
1.0	0
0.72	0.1652
0.60	0.1856
0.48	0.3130
0.36	0.2847
0.24	0.1924
0.12	0.1298
0	0

ENERGY MINIMIZED COMPUTATIONAL MODELS OF HOST-GUEST COMPLEXES

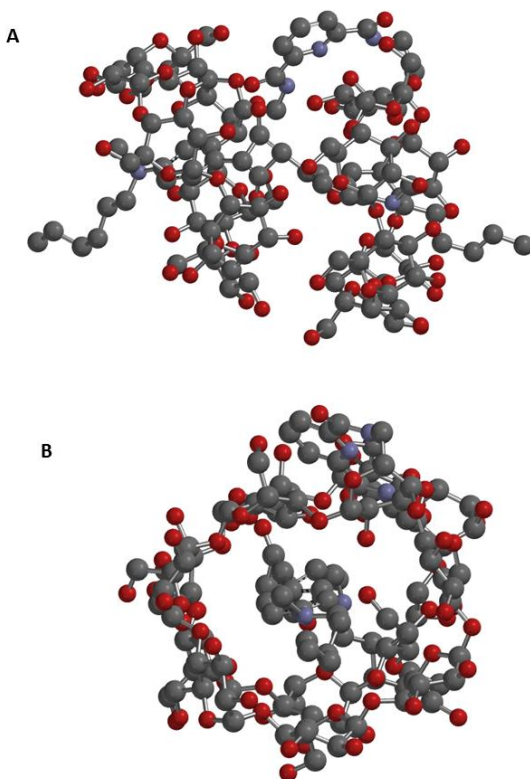


**Figure S73.** Energy minimized (semi-empirical PM3) computational models for squaraine-dimer combination (**1** + **6**), (A) transverse view; (B) cross-sectional view.

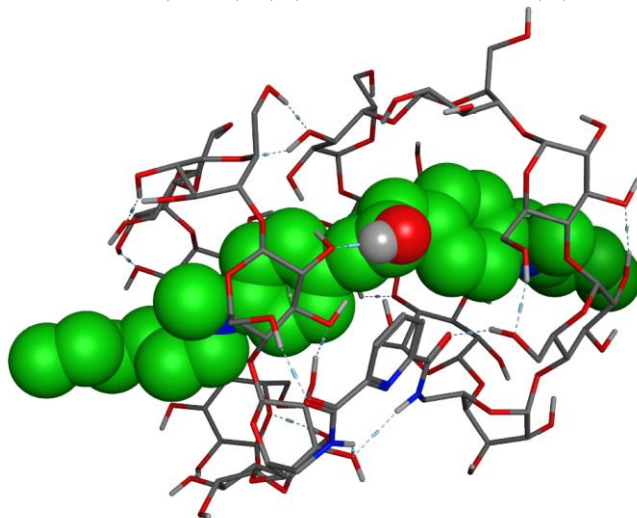


**Figure S74.** Energy minimized (semi-empirical PM3) computational models for squaraine-dimer combination (**1** + **6**) (Guest **6** is in depicted in space-filling model while host **1** is depicted in stick model generated via Molecular Operating Environment (MOE)<sup>3</sup>).

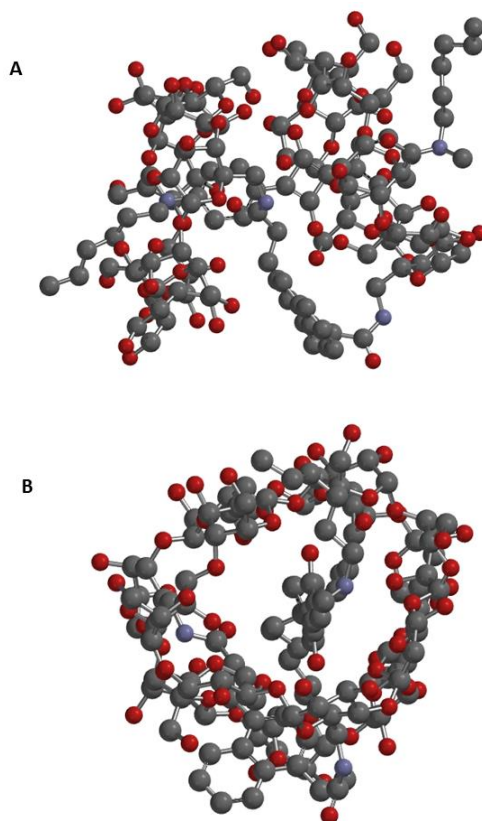


**Figure S75.** Energy minimized (semi-empirical PM3) computational models for squaraine-dimer combination (**2** + **6**), (A) transverse view; (B) cross-sectional view.

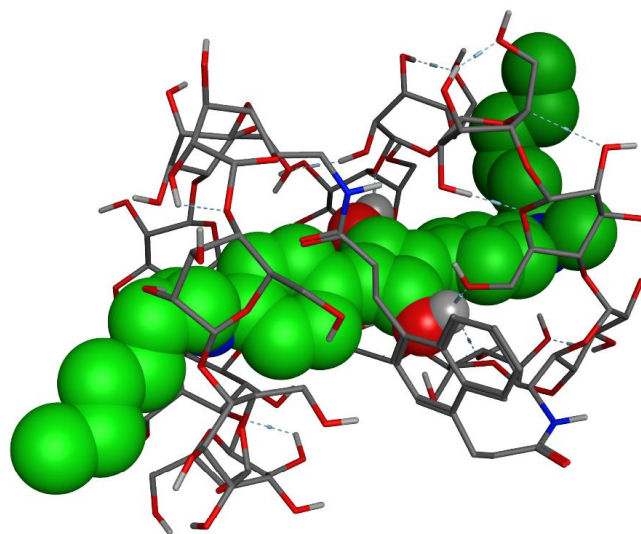


**Figure S76.** Energy minimized (semi-empirical PM3) computational models for squaraine-dimer combination (**2** + **6**) (Guest squaraine **6** is in depicted in space-filling model while host dimer **2** is depicted in stick model generated via Molecular Operating Environment (MOE)<sup>3</sup>).

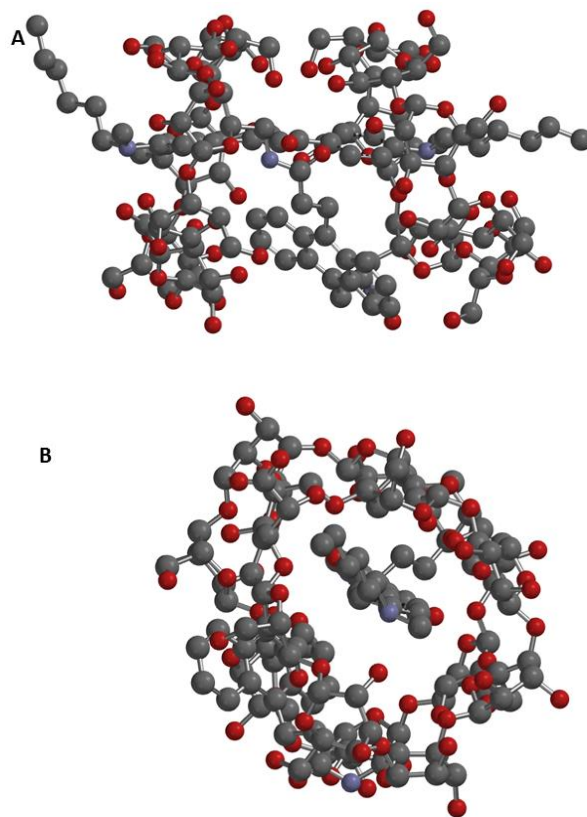


**Figure S77.** Energy minimized (semi-empirical PM3) computational models for squaraine-dimer combination (**3** + **6**), (A) transverse view; (B) cross-sectional view.

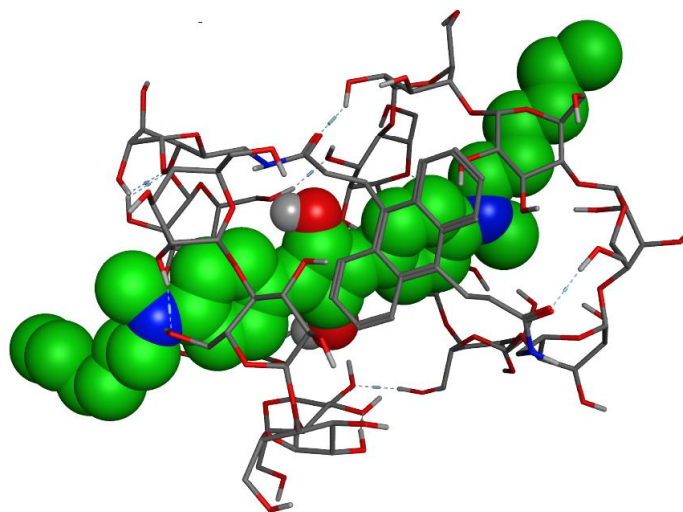


**Figure S78.** Energy minimized (semi-empirical PM3) computational models for squaraine-dimer combination (**3** + **6**) (Guest squaraine **6** is depicted in space-filling model while host dimer **3** is depicted in stick model generated via Molecular Operating Environment (MOE)<sup>3</sup>).

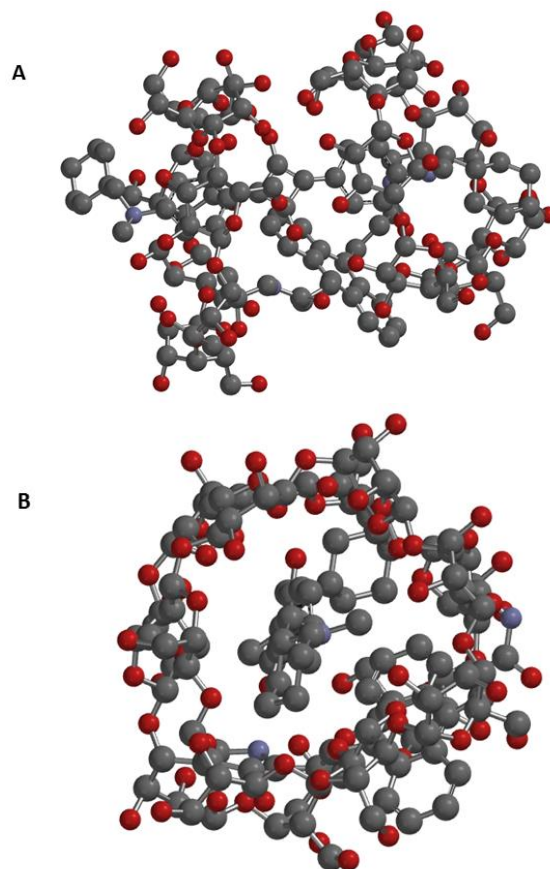


**Figure S79.** Energy minimized (semi-empirical PM3) computational models for squaraine-dimer combination (**3** + **10**), (A) transverse view; (B) cross-sectional view.

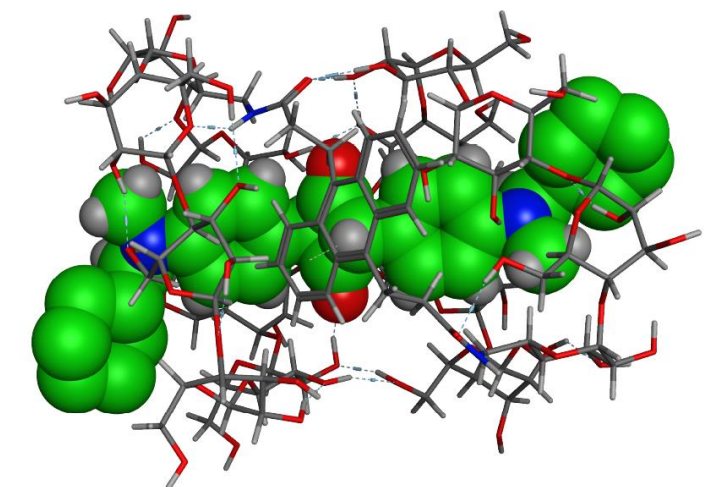


**Figure S80.** Energy minimized (semi-empirical PM3) computational models for squaraine-dimer combination (**3** + **10**) (Guest squaraine **10** is in depicted in space-filling model while host dimer **3** is depicted in stick model generated via Molecular Operating Environment (MOE)<sup>3</sup>).

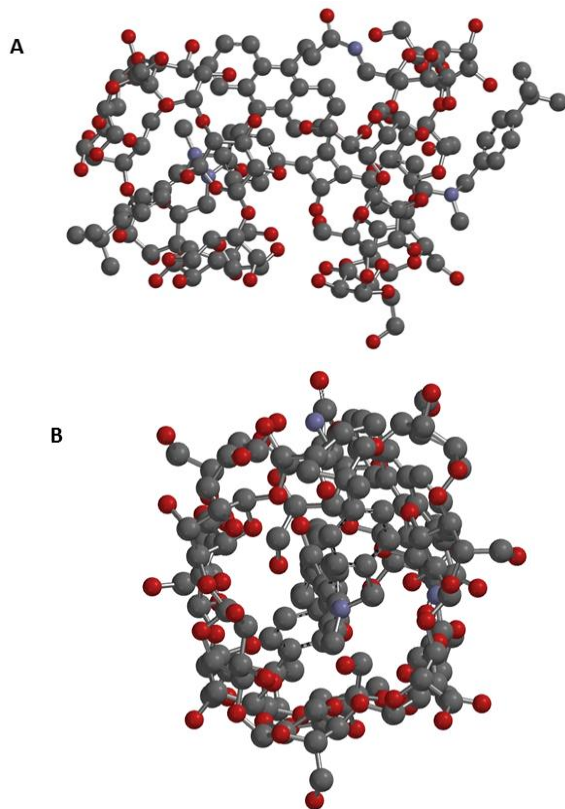


**Figure S81.** Energy minimized (semi-empirical PM3) computational models for squaraine-dimer combination (**3** + **11**), (A) transverse view; (B) cross-sectional view.

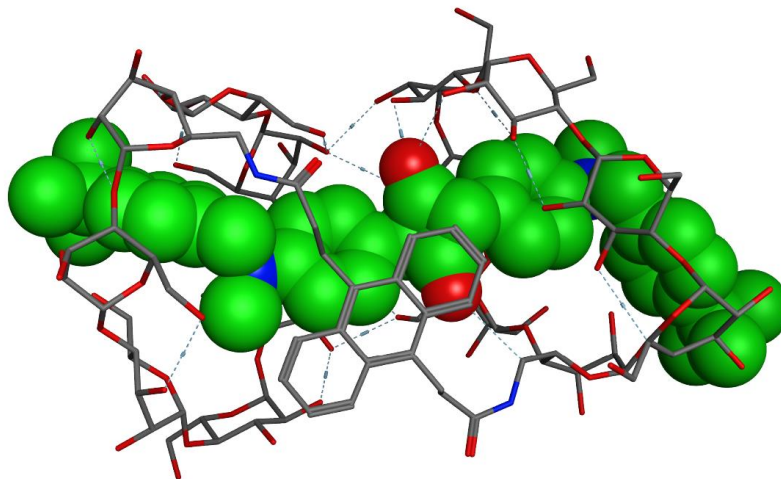


**Figure S82.** Energy minimized (semi-empirical PM3) computational models for squaraine-dimer combination (**3** + **11**) (Guest squaraine **11** is depicted in space-filling model while host dimer **3** is depicted in stick model generated via Molecular Operating Environment (MOE)<sup>3</sup>).

## TLC STUDY OF SQUARAINE 6 / DIMER 3 COMPLEXATION

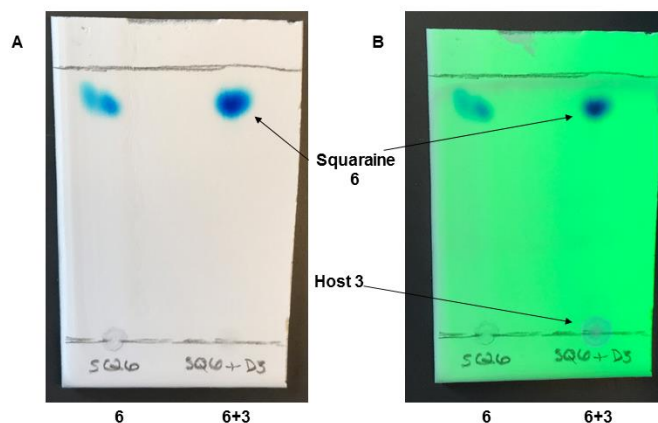
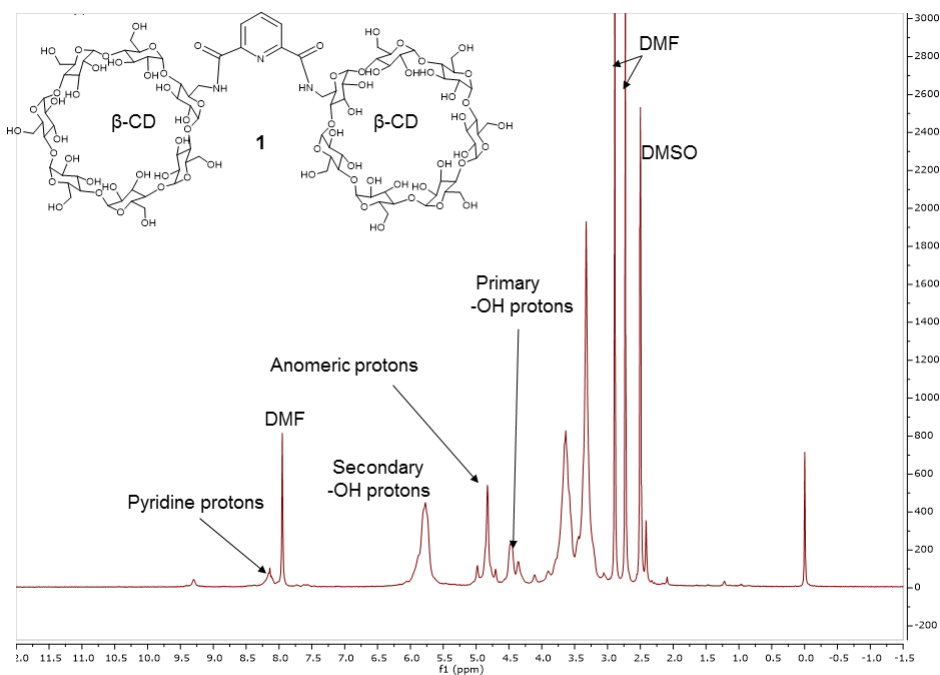


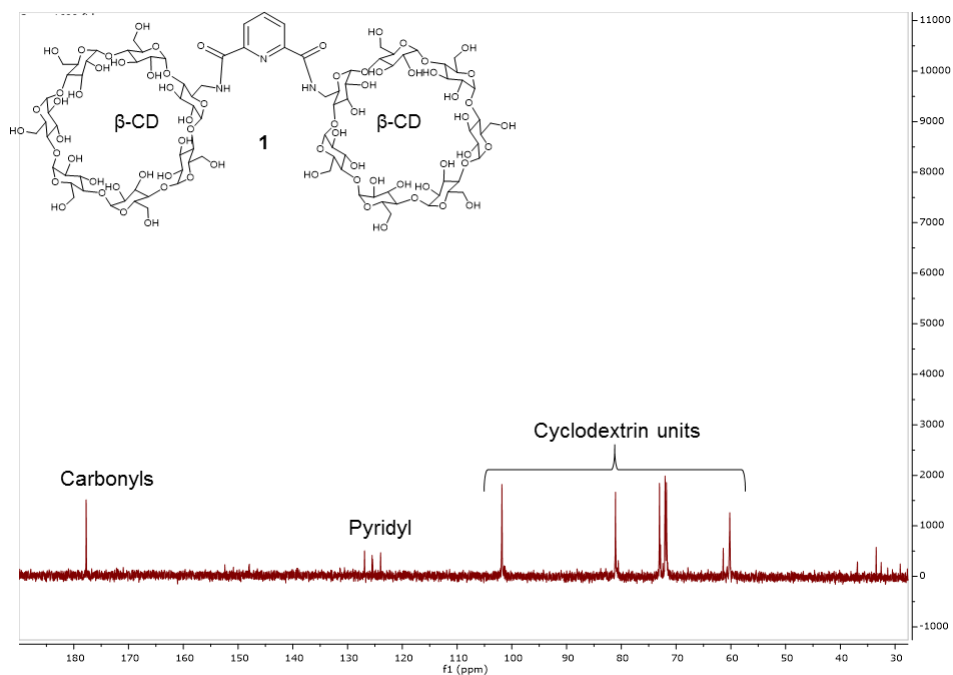
**Figure S83.** TLC plates after elution with methanol:chloroform (1:9) as the mobile phase (A) under ambient light; and (B) under a UV lamp light (short wavelength, 254 nm).

## NMR SPECTRA OF $\beta$ -CD DIMER HOSTS AND SQUARAINE GUESTS

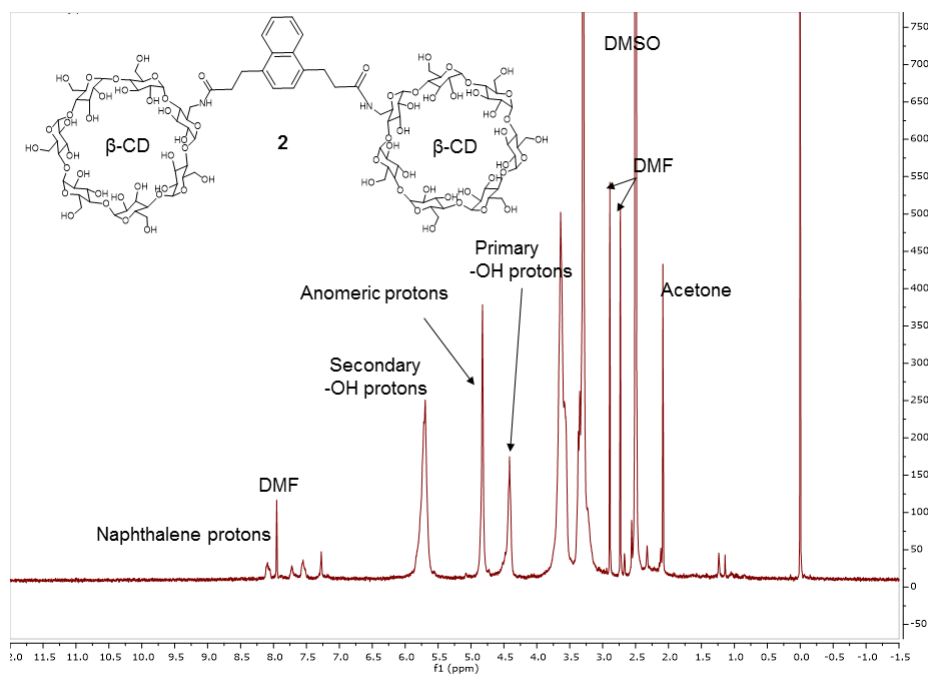
$^1\text{H}$ -NMR spectrum of compound **1** recorded in  $\text{DMSO-}d_6$  (400 MHz) at room temperature.



$^{13}\text{C}$ -NMR spectrum of compound **1** recorded in  $\text{D}_2\text{O}$  (400 MHz) at room temperature.

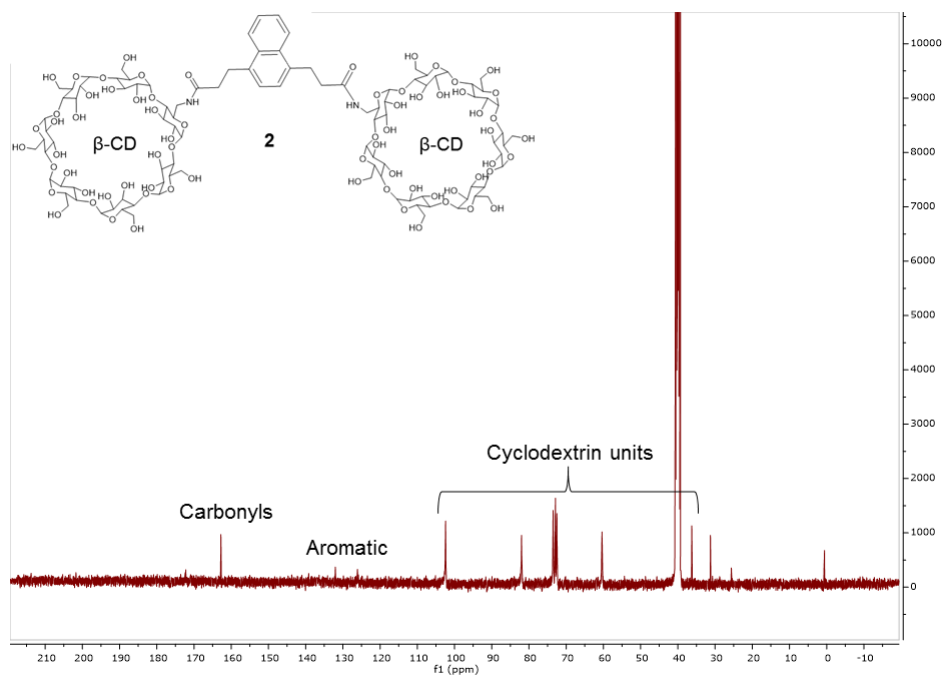


$^1\text{H}$ -NMR spectrum of compound **2** recorded in  $\text{DMSO-}d_6$  (400 MHz) at room temperature.

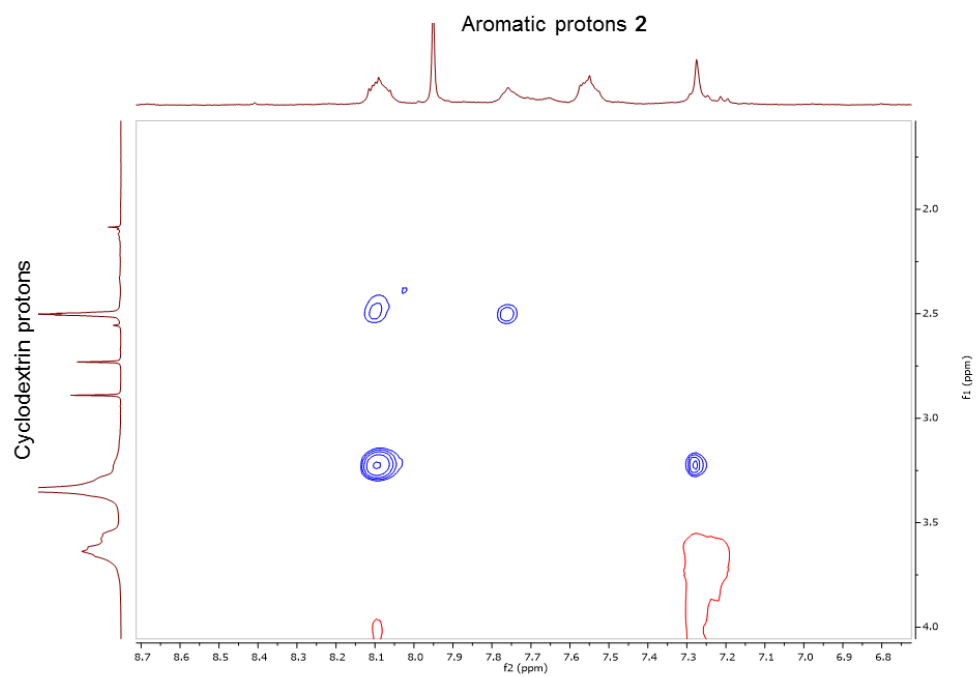




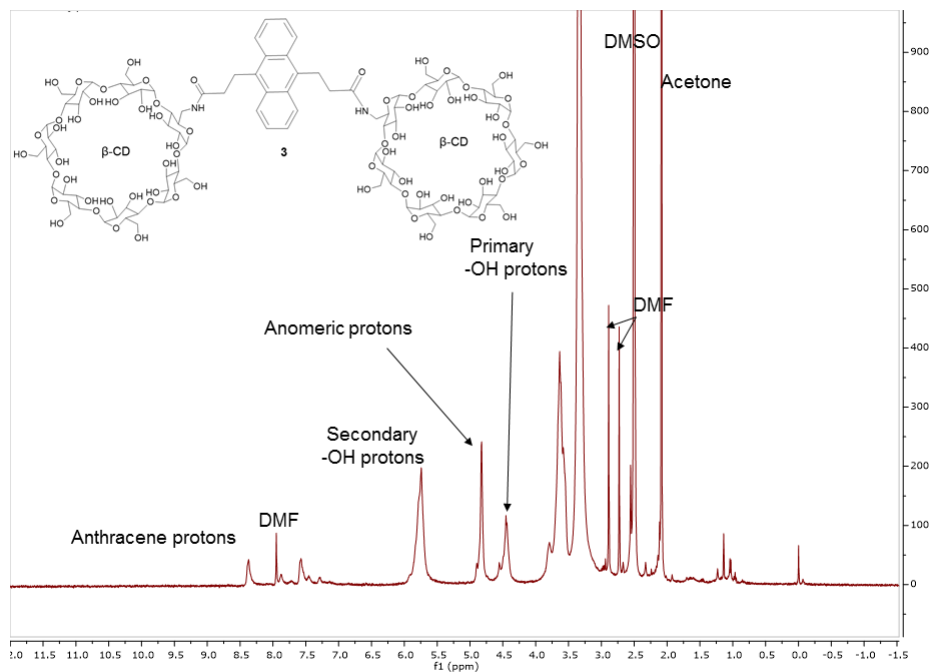
$^{13}\text{C}$ -NMR spectrum of compound **2** recorded in  $\text{DMSO-}d_6$  (400 MHz) at room temperature.



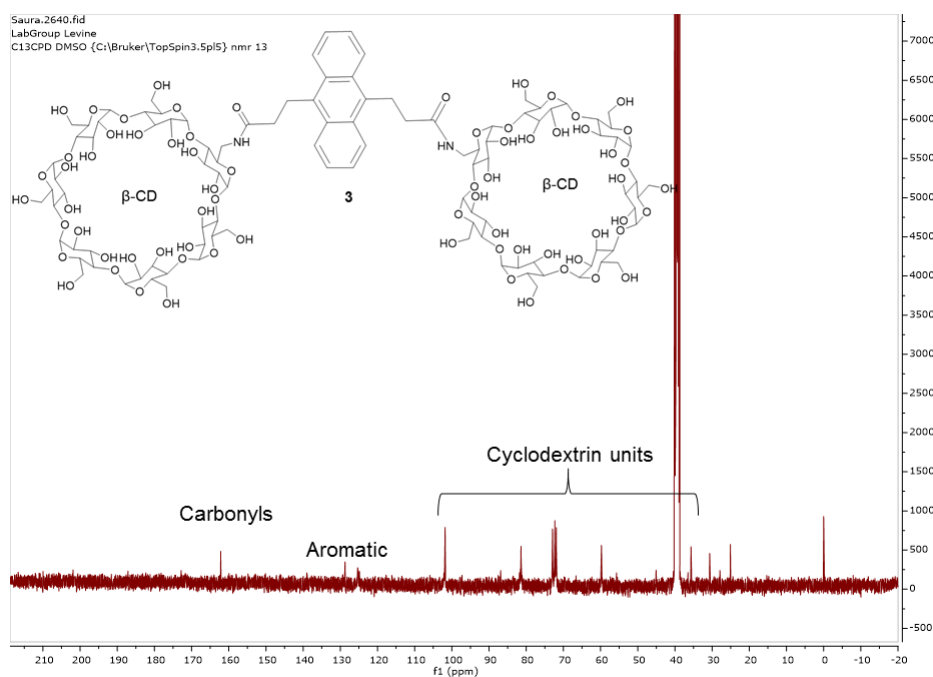
ROESY spectrum of compound **2** recorded in  $\text{DMSO-}d_6$  (400 MHz) at room temperature.



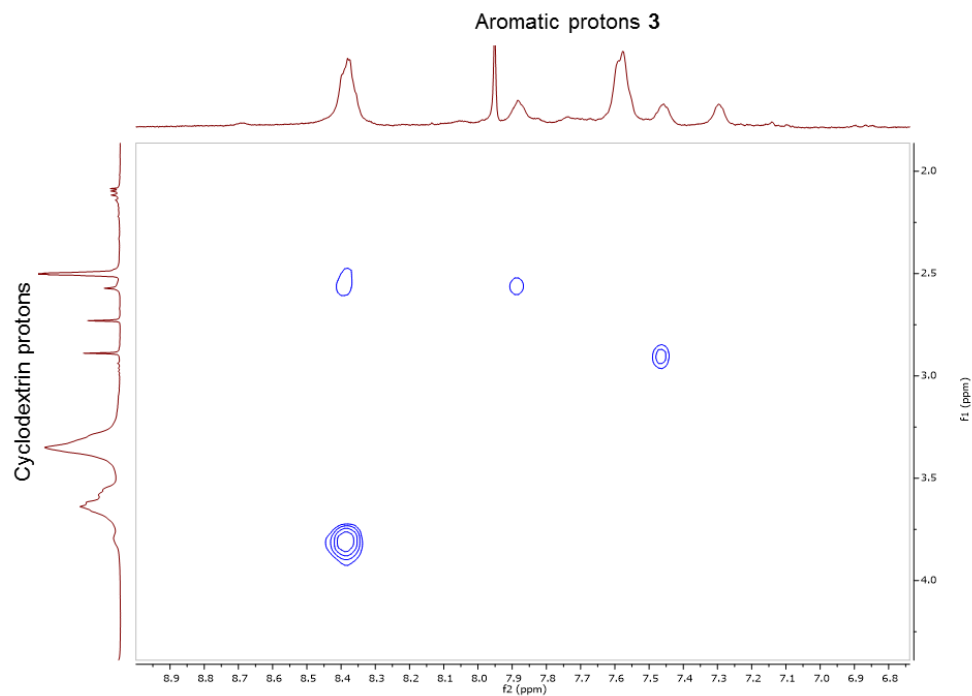
$^1\text{H}$ -NMR spectrum of compound **3** recorded in  $\text{DMSO-}d_6$  (400 MHz) at room temperature.



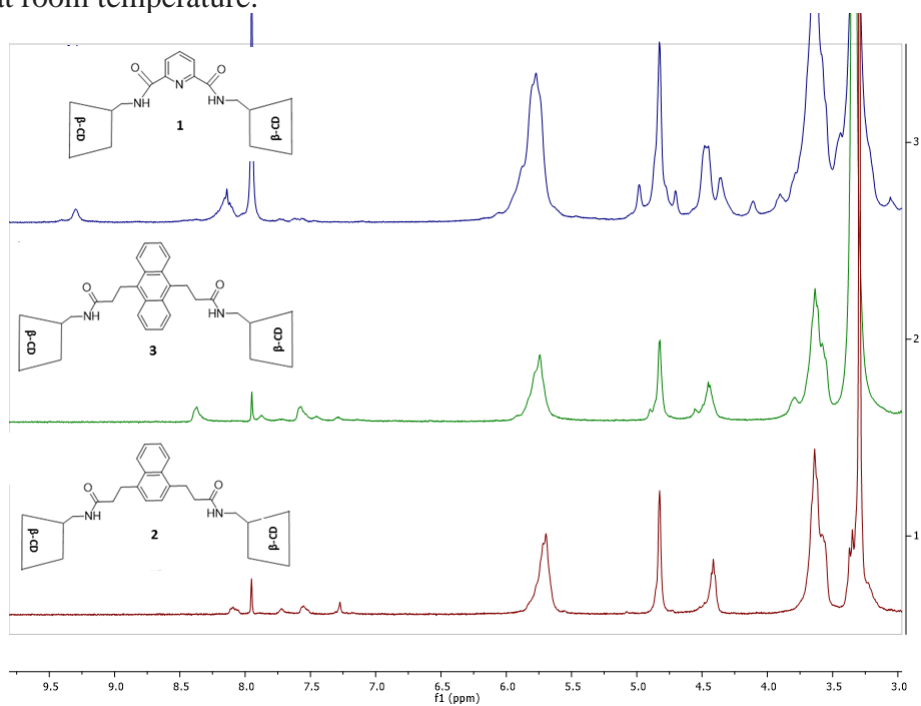
$^{13}\text{C}$ -NMR spectrum of compound **3** recorded in  $\text{DMSO-}d_6$  (400 MHz) at room temperature.



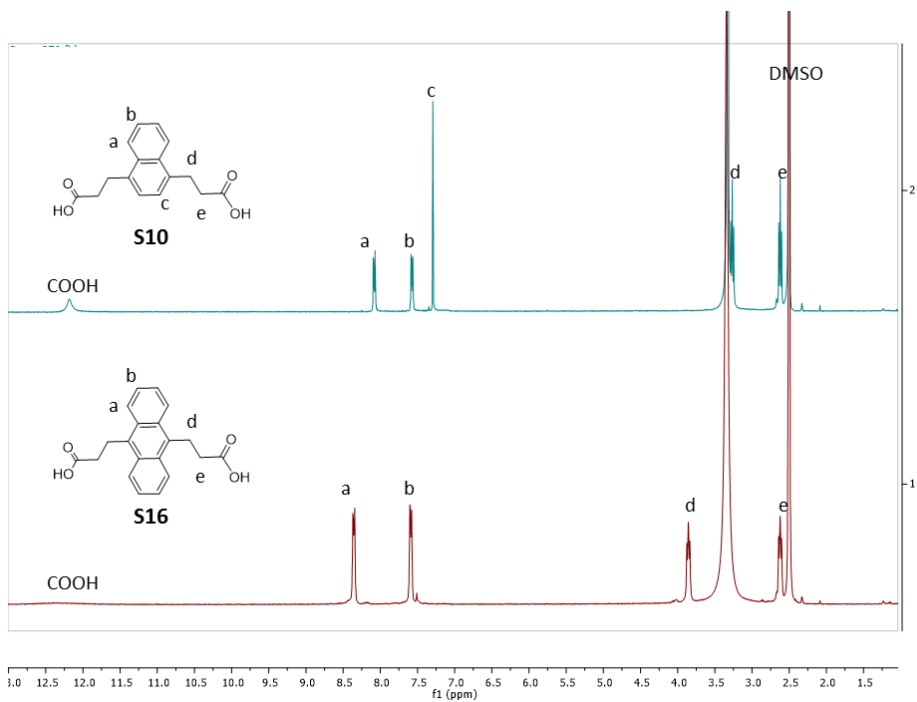
ROESY spectrum of compound **3** recorded in DMSO-*d*<sub>6</sub> (400 MHz) at room temperature.



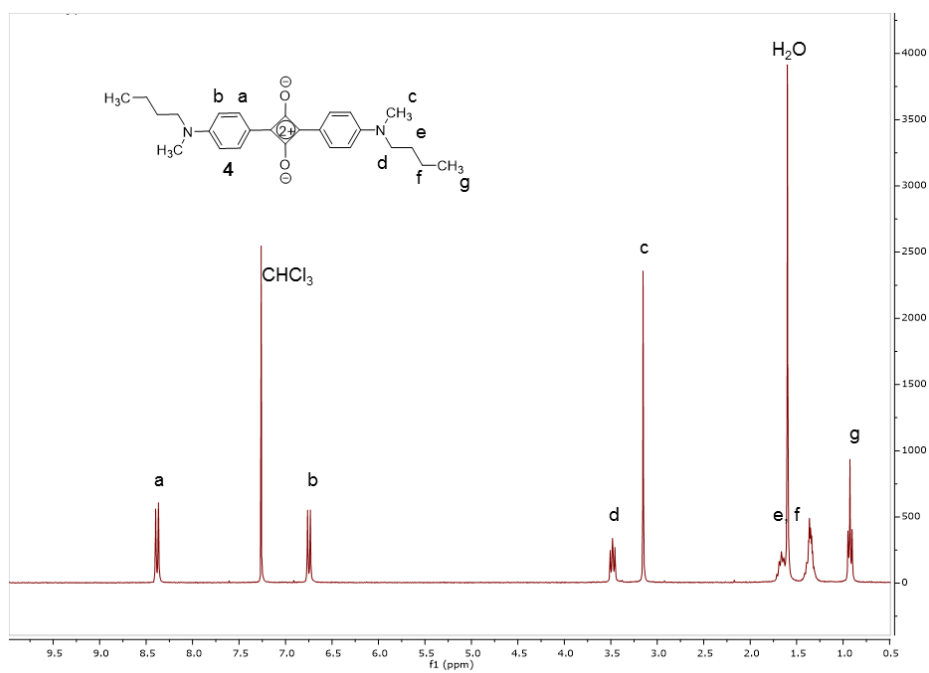
Comparison of <sup>1</sup>H-NMR spectrum of compound **1**, **2** & **3** recorded in DMSO-*d*<sub>6</sub> (400 MHz) at room temperature.



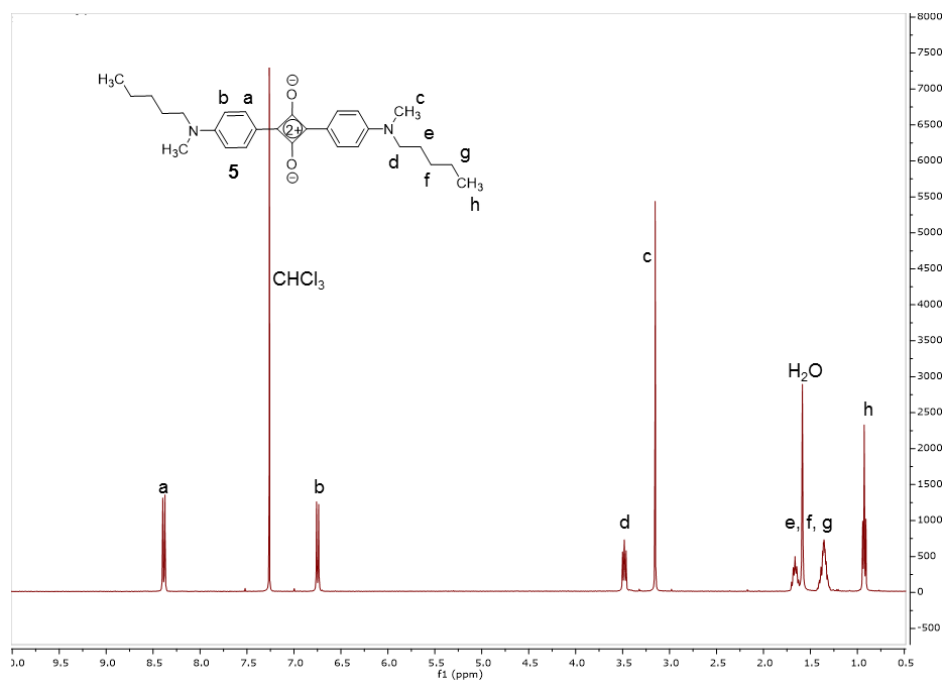
Comparison of  $^1\text{H-NMR}$  spectrum of compound **S10** & **S16** recorded in  $\text{DMSO-}d_6$  (400 MHz) at room temperature.



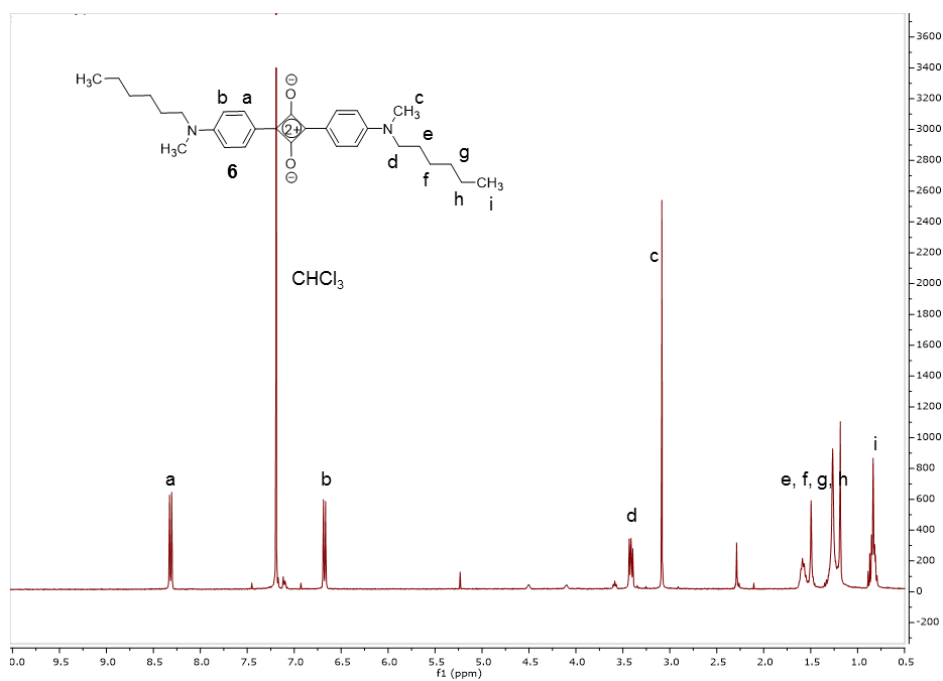
$^1\text{H-NMR}$  spectrum of compound **4** recorded in  $\text{CDCl}_3$  (400 MHz) at room temperature.



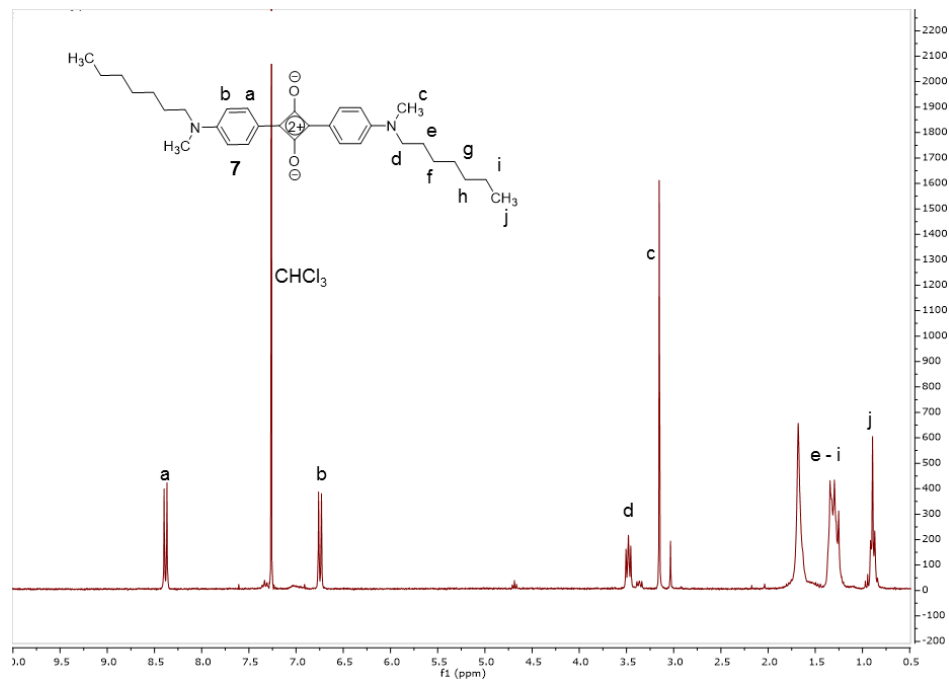
$^1\text{H-NMR}$  spectrum of compound **5** recorded in  $\text{CDCl}_3$  (400 MHz) at room temperature.



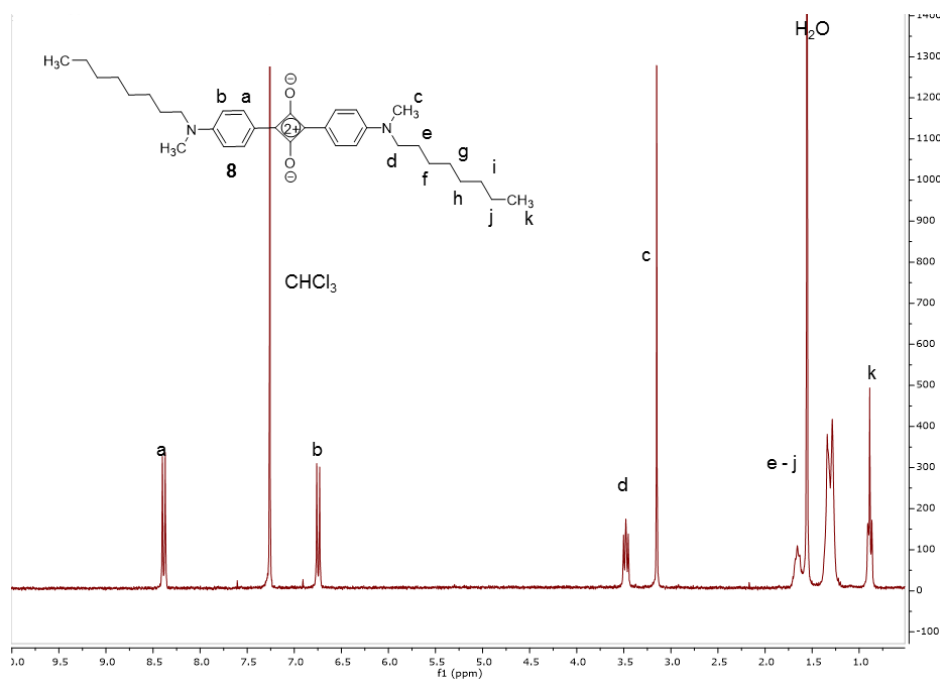
$^1\text{H-NMR}$  spectrum of compound **6** recorded in  $\text{CDCl}_3$  (400 MHz) at room temperature.



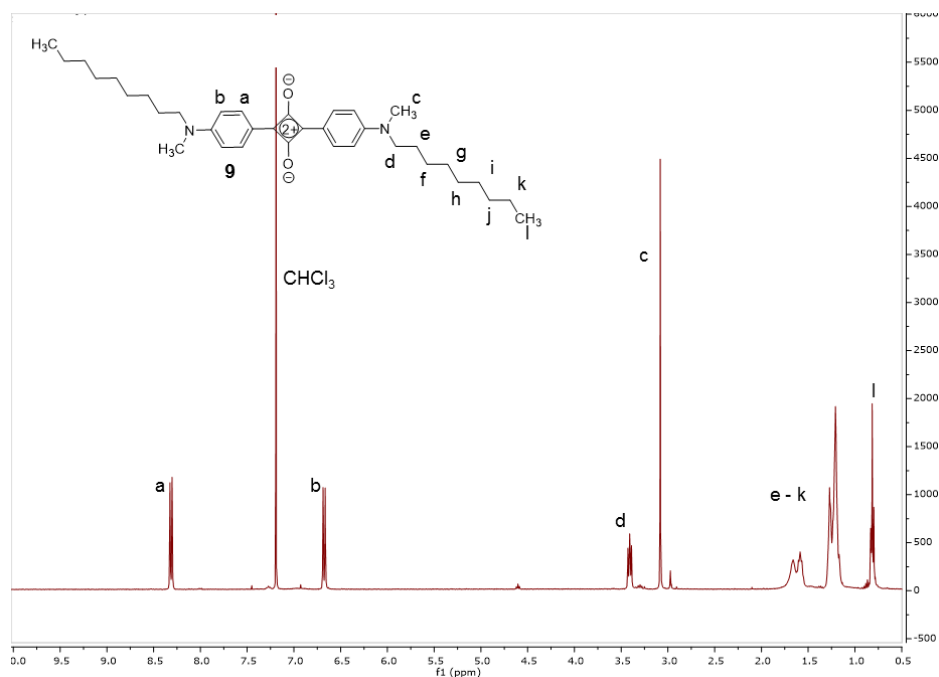
$^1\text{H-NMR}$  spectrum of compound **7** recorded in  $\text{CDCl}_3$  (400 MHz) at room temperature.



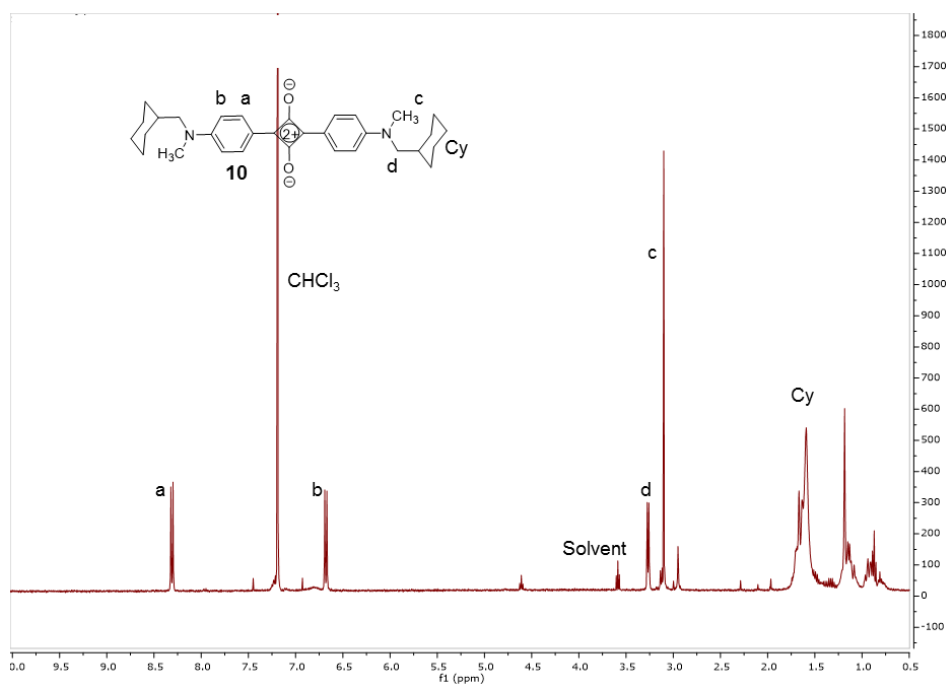
$^1\text{H-NMR}$  spectrum of compound **8** recorded in  $\text{CDCl}_3$  (400 MHz) at room temperature.



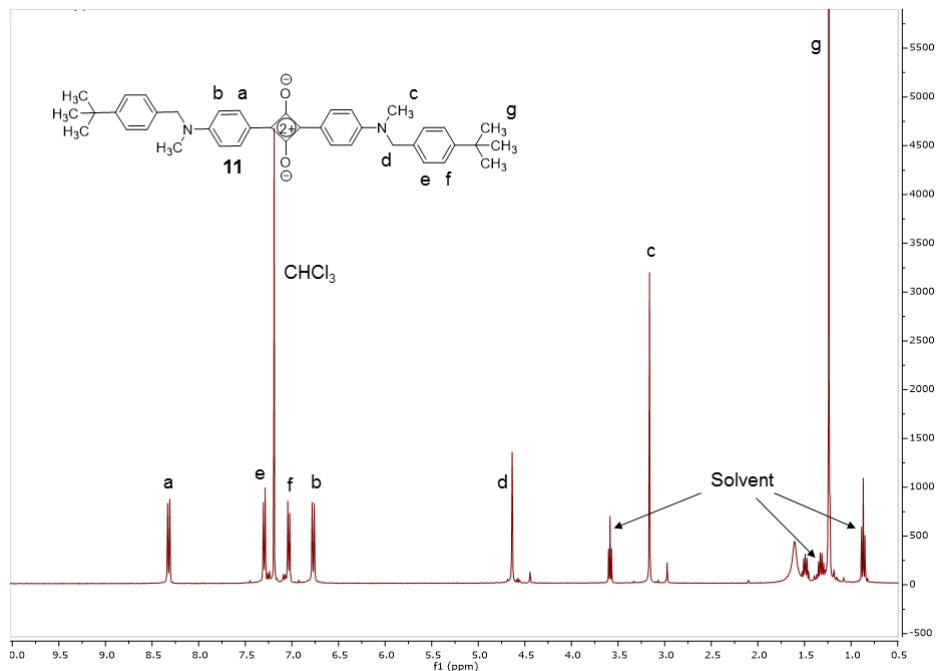
$^1\text{H-NMR}$  spectrum of compound **9** recorded in  $\text{CDCl}_3$  (400 MHz) at room temperature.



$^1\text{H-NMR}$  spectrum of compound **10** recorded in  $\text{CDCl}_3$  (400 MHz) at room temperature.

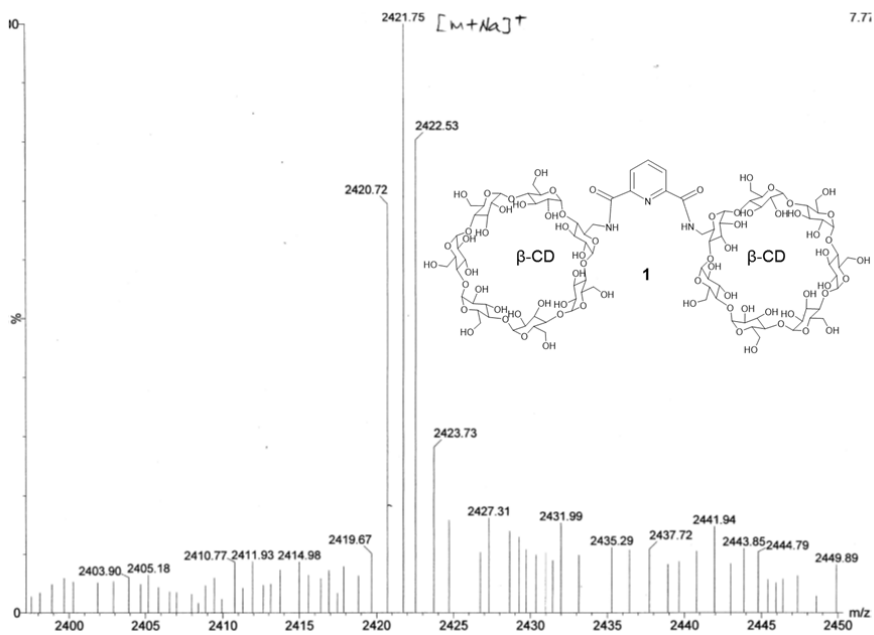


$^1\text{H-NMR}$  spectrum of compound **11** recorded in  $\text{CDCl}_3$  (400 MHz) at room temperature.



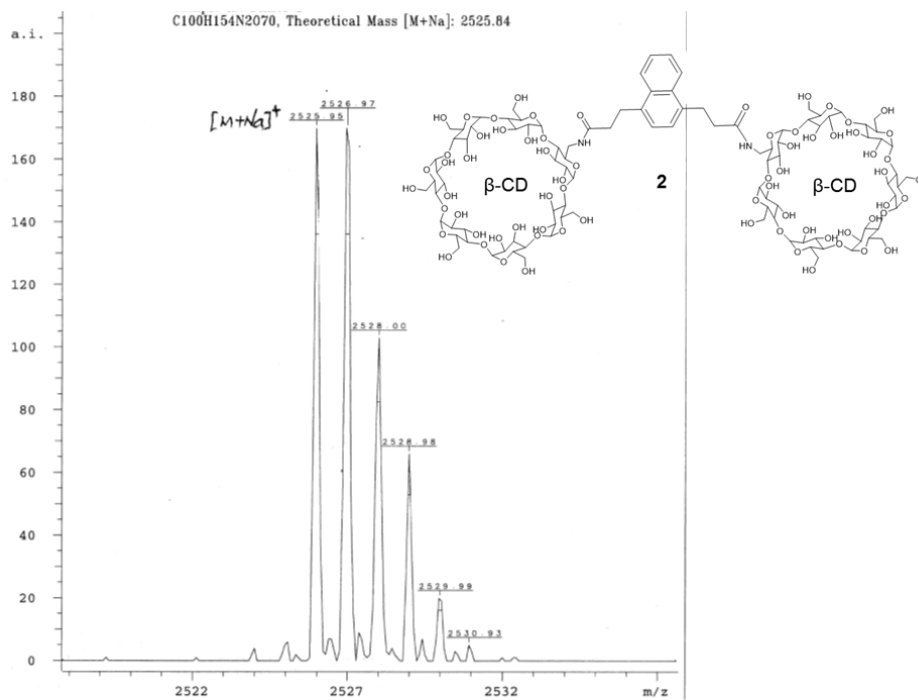
## MASS SPECTRA OF $\beta$ -CD DIMER HOSTS AND SQUARINE GUESTS

Mass spectrometry data of compound **1** recorded in Waters Q-TOF Micro Mass Spectrometer.

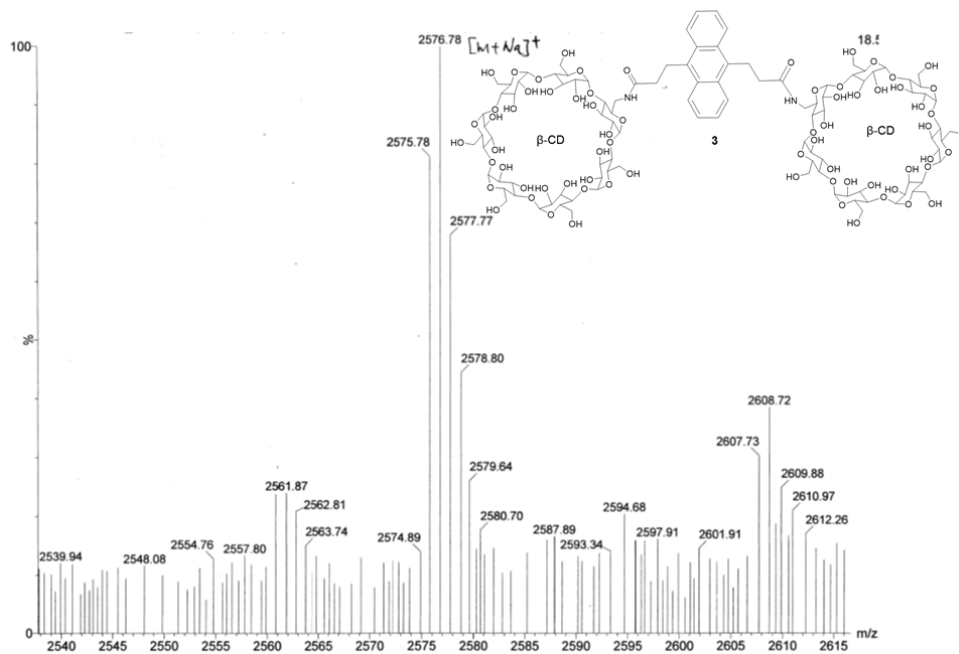




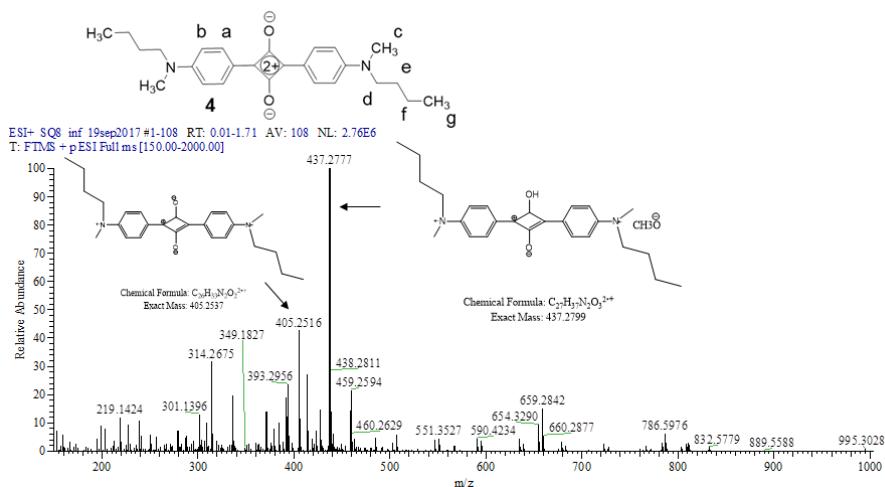
Mass spectrometry data of compound **2** recorded in Bruker Omniflex MALDI-TOF.



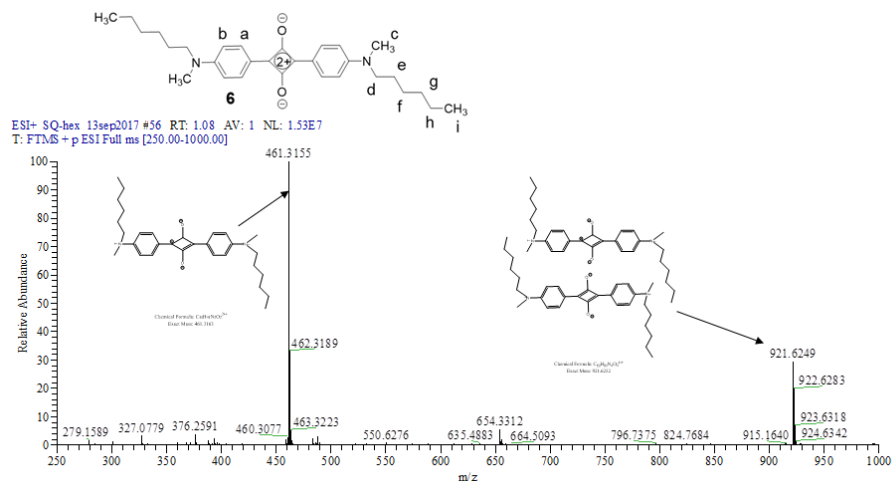
Mass spectrometry data of compound **3** recorded in Waters Q-TOF Micro Mass Spectrometer.



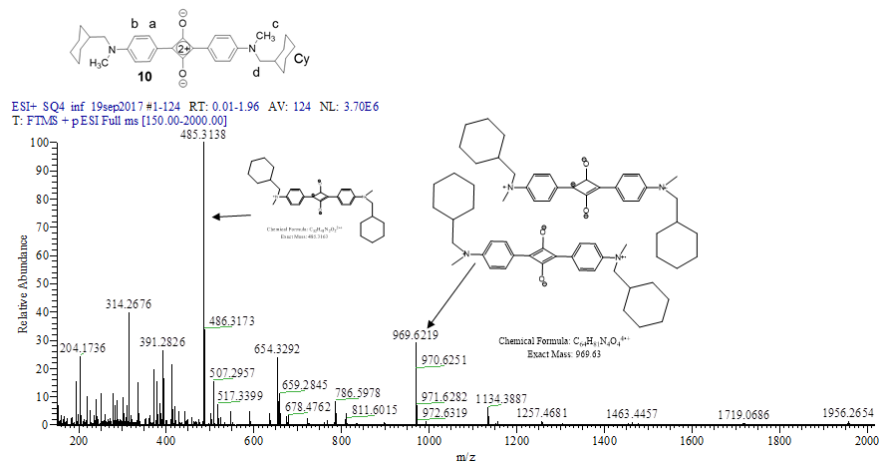
Mass spectrometry data of compound **4** recorded in Thermo Scientific LTQ Orbitrap XL™ mass spectrometer.



Mass spectrometry data of compound **6** recorded in Thermo Scientific LTQ Orbitrap XL™ mass spectrometer.



Mass spectrometry data of compound **10** recorded in Thermo Scientific LTQ Orbitrap XL™ mass spectrometer.



## REFERENCES

- Huang, M. J.; Quan, Z.; Liu, Y. “Computational Modeling of Inclusion Complexes of  $\beta$ - Cyclodextrin with enantiomers of Salsolinol, N-MethylSalsolinol, and 1-Benzyl-Tetrahydroisoquinoline” *Int J Quantum Chem.* **2009**, *109*(1), 81–90.
- Thordarson, P. “Determining association constant from titration experiments in supramolecular chemistry.” *Chem. Soc. Rev.* **2011**, *40*, 1305-1323.
- Molecular Operating Environment (MOE)*, 2013.08; Chemical Computing Group ULC, 1010 Sherbooke St. West, Suite #910, Montreal, QC, Canada, H3A 2R7, **2017**.

## CHAPTER 5

Published in *RSC Advances* **2017**, 7, 28489-28493

A highly versatile fluorenone-based macrocycle for the sensitive detection of  
polycyclic aromatic hydrocarbons and fluoride anions

Ingrid-Suzy Tamgho<sup>1</sup>, Sauradip Chaudhuri<sup>1</sup>, Molly Verderame, Dana J. DiScenza,  
Mindy Levine

Department of Chemistry, University of Rhode Island, Kingston, RI, USA

<sup>1</sup>Co-first Authors

Corresponding Author:

Mindy Levine, Ph.D.

Department of Chemistry

University of Rhode Island

Kingston, Rhode Island, 02881, USA

[mlevine@chm.uri.edu](mailto:mlevine@chm.uri.edu)

## Manuscript 5

### **A highly versatile fluorenone-based macrocycle for the sensitive detection of polycyclic aromatic hydrocarbons and fluoride anions**

#### ABSTRACT

Reported herein is the high yielding synthesis of a new fluorenone-based triazolophane and its sensing capabilities for polycyclic aromatic hydrocarbons (PAHs) and fluoride anions. Fluorescence, UV/Vis and  $^1\text{H-NMR}$  spectroscopy results showed the triazolophane has a high sensitivity for selected PAHs and binds the fluoride anion in a 1:2 stoichiometry via C–H hydrogen bonding with the triazole and fluorenone protons.

Cyclophanes, or macrocycles that contain aromatic rings linked by aliphatic chains, have been studied in the literature for a range of applications.<sup>1</sup> These macrocycles can bind a variety of guests in their interiors, including polycyclic aromatic hydrocarbons (PAHs)<sup>2</sup> as well as anions<sup>3</sup> and cations,<sup>4</sup> through multiple non-covalent interactions. Since the synthesis of the simplest cyclophane, [2.2] paracyclophane, in 1966,<sup>5</sup> the number of known cyclophanes has expanded dramatically.

Recent cyclophanes have replaced one or more of the aromatic rings with heteroaromatic moieties,<sup>6</sup> including triazole rings for the formation of triazolophane macrocycles.<sup>7</sup> Such macrocycles are attractive because of the synthetic accessibility of triazoles<sup>8</sup> as well as their ability to bind both cations (via association with the  $\text{N}_2$  and  $\text{N}_3$  of the triazole)<sup>9</sup> and anions (via hydrogen bonding with the C–H hydrogen bond donor).<sup>10</sup>

Anions are important targets for binding and detection due to their ubiquitous nature and public health relevance.<sup>11</sup> Fluoride, for example, is of interest due to the importance of fluoridated water in promoting dental health;<sup>12</sup> excessive amounts of fluoride, by contrast, can lead to fluorosis.<sup>13</sup> Other key anions include those with negative health effects including phosphate,<sup>14</sup> nitrate,<sup>15</sup> thiocyanate<sup>16</sup> and cyanide.<sup>17</sup> A third class of anions is those that are explosive such as azide.<sup>18</sup>

Polycyclic aromatic hydrocarbons (PAHs) are another class of important detection targets, with negative health and environmental effects,<sup>19</sup> and are formed from the incomplete combustion of petroleum.<sup>20</sup> Their environmental stability means that they bioaccumulate and biomagnify,<sup>21</sup> which is of concern due to their known and suspected teratogenicity,<sup>22</sup> mutagenicity<sup>23</sup> and carcinogenicity.<sup>24</sup>

Work in the Levine group has focused on the detection of toxicants using cyclodextrin-promoted energy transfer<sup>25</sup> and cyclodextrin-promoted fluorescence modulation,<sup>26</sup> as well as on the use of synthetic macrocycles for the enhanced binding and detection of PAHs.<sup>27</sup> One shortcoming is that the previously synthesized macrocycles lacked easily detectable photophysically active components, which in turn meant that an external fluorophore was required to obtain a response signal. Incorporating a UV-active moiety, such as fluorenone, directly into the backbone of the macrocycle would enable the direct use of optical detection methods, and incorporation of a triazole functionality will enable the detection of a broader variety of analytes. Reported herein is the high yielding synthesis of precisely such a macrocycle, compound **1**, containing a photophysically active fluorenone unit and two triazole moieties, and its versatility in binding and detecting both PAHs and anions with extremely high sensitivities.

Macrocycle **1** was synthesized from compounds **2** and **3** via a copper catalyzed azide–alkyne cycloaddition (Figure 1). This reaction proceeded under high dilution conditions<sup>28</sup> in toluene to obtain a 71% isolated yield. The low solubility of the macrocycle in toluene caused it to crash out of the reaction mixture, and was crucial in enabling high yields. The formation of the macrocycle was confirmed by NMR spectroscopy and mass spectrometry (see ESI).

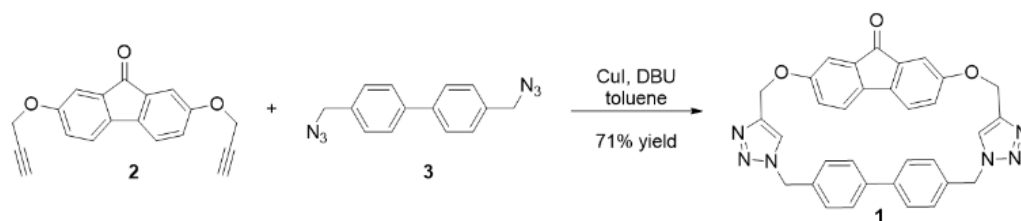


**Figure 1.** Synthesis of macrocycle **1** *via* the reaction of precursors **2** and **3**.

Photophysical characterization of the macrocycle showed a UV-visible absorption spectrum with maxima at 264, 310, and 460 nm, corresponding to the p–p\* transition of the biphenyl,<sup>29</sup> the electronic transition of the fluorenone,<sup>30</sup> and the symmetry forbidden n–p\* transition of the carbonyl moiety,<sup>31</sup> respectively.

DFT calculations of macrocycle **1** showed a well-defined cavity with dimensions of 10.6 °A x 5.043 °A, with the most stable conformation of the macrocycle having the triazole protons facing opposite sides (i.e. one pointed out of the page and one pointed into the page) (Figure 2A). Electron density mapping highlighted the strongly electron deficient nature of the macrocycle, making it well-suited for the binding of electron rich aromatic guests (Figure 2B).

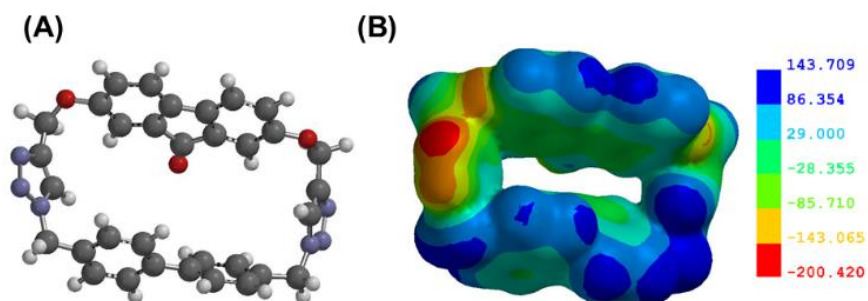


**Figure 2.** (A) Energy minimized structure of compound **1**; (B) Electron density mapping of compound **1**, with the blue regions corresponding to the electron-deficient segments and the red regions corresponding to the electron-rich segments.

The binding of polycyclic aromatic hydrocarbons **4–7** (Figure 3) in macrocycle **1** was monitored by UV-visible and fluorescence spectroscopy. In the UV-visible spectra, the absorbance spectrum of the 1:1 mixture of each analyte and macrocycle **1** was equivalent to the sum of the absorbance spectra of the individual species, indicating no significant complexation-induced absorption changes.

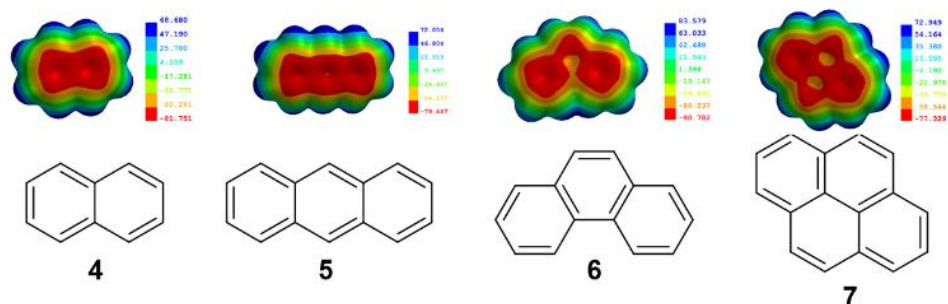


**Figure 3.** Structures of polycyclic aromatic hydrocarbons **4–7** with electron density mapping of each compound highlighting their electron rich aromatic natures.

In contrast to the limited changes in the absorbance spectra, the fluorescence emission of each of the analytes decreased with the addition of the macrocycle (Table 1), with the decrease in fluorescence quantified according to Equation 1:

$$\text{Fluorescence change} = (F_{I_m} - F_{I_a}) / F_{I_a} \times 100 \quad (\text{Equation 1})$$



where  $Fl_a$  is the integrated fluorescence emission of the analyte and  $Fl_m$  is the integrated fluorescence emission of the analyte in the presence of compound **1**.

**Table 1.** Decrease in fluorescence of analytes **4-7** in the presence of the compound **1**<sup>a</sup>

Analyte	With Macrocycle <b>1</b>	With Compounds <b>8</b> and <b>9</b>
<b>4</b>	<i>b</i>	<i>b</i>
<b>5</b>	$-8.5 \pm 0.4$	$-84.6 \pm 0.3$
<b>6</b>	$-11.9 \pm 0.3$	$63.5 \pm 1.8$
<b>7</b>	$-6.0 \pm 0.4$	$19.6 \pm 6.2$

<sup>a</sup>Fluorescence decreases were calculated according to Equation 1. All results represent an average of 3 trials. <sup>b</sup>Inner filter effects observed.

Of note, these decreases were not accompanied by significant shifts in the emission maxima, in contrast to a report of analogous system in which such a red shift is observed.<sup>32</sup> In that case, the red-shift is probably a result of excited state energy transfer between the anthracene host and guanine guest.

A direct comparison of the fluorescence changes observed in the presence of macrocycle **1** with those observed in the presence of both photophysically active components – 2,7-dihydroxy-9-fluorenone and 4,4'-dimethylbiphenyl (compounds **8** and **9**, Figure 4) indicate that the macrocycle induced fluorescence changes were markedly different from those induced by the components in a mixture (Table 1, Figure 5), thereby supporting the proposed analyte-macrocycle complexation. For analyte **5**, the presence of both **8** and **9** led to noticeable fluorescence quenching as a result of intermolecular co-facial aromatic interactions between the anthracene and fluorenone<sup>33</sup> and the anthracene and biphenyl,<sup>34</sup> in accordance with literature precedents of analogous quenching phenomena. Once these moieties are geometrically constrained in a

macrocycle (Figure 2), they are no longer completely planar and are not as available for co-facial quenching interactions. Binding of analyte **5** in macrocycle **1**, as a result, leads to a much more limited decrease in the observed fluorescence emission.

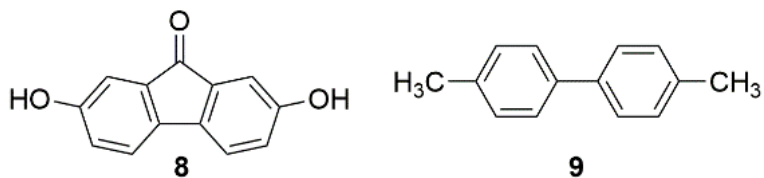


**Figure 4.** Structures of photophysically active components **8** and **9** (structurally tethered in **1**).

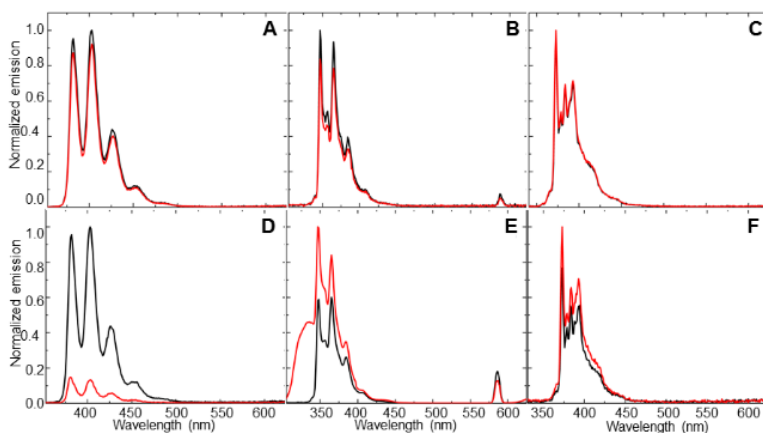


**Figure 5.** Fluorescence emission changes of analytes **5-7** in the presence of macrocycle **1** (A-C) and component moieties **8** and **9** (D-F). (A and D) analyte **5**; (B and E) analyte **6**; and (C and F) analyte **7**. The black line represents the fluorescence emission from the analyte alone, and the red line represents the fluorescence emission from the analyte in the presence of the other compounds.

In the case of analytes **6** and **7**, slight fluorescence decreases were observed in the presence of macrocycle **1**, while significant fluorescence enhancements were observed in the presence of both **8** and **9**. These results indicate different interactions of the macrocycle with analytes **6** and **7** compared to its interactions with **4** and **5**. As a result of the larger dimensions of **6** and **7**, there is likely weaker binding in the cavity; as a result, limited fluorescence quenching occurred.

In the case of naphthalene (analyte **4**), the excitation wavelength of 265 nm is a wavelength at which compounds **1**, **8**, and **9** have noticeable absorption cross-sections (see ESI). Although significant wavelength-dependent fluorescence decreases were observed, these observed changes are indicative of an inner filter mechanism, where the macrocycle absorbs energy and filters some of that energy from reaching the analyte.<sup>35</sup> The limits of detection of analytes **4–7** using this method were calculated following literature-reported procedures (Table 2).<sup>36</sup> For analyte **4**, the calculated detection limit is a result of the inner filter effect-induced fluorescence changes.<sup>35</sup> The nanomolar detection limits obtained for the analytes are close to or below the literature-reported levels of concern for three out of the four analytes (compounds **4**, **5**, and **7**),<sup>37</sup> which highlights the high sensitivity of this fluorescence method for PAH binding and concomitant detection. The limits of detection for the analytes in the absence of the macrocycle were higher, which highlights the role of the macrocycle in enhancing fluorescence sensitivities.

**Table 2.** Limit of detection for analytes **4–7** and comparisons to literature-reported values

Analyte	Limit of Detection with compound <b>1</b> <sup>a</sup> (nM)	Limit of Detection without compound <b>1</b> <sup>a</sup> (nM)	Literature-Reported Values (nM)
<b>4</b>	28.7 ± 0.1	166.5 ± 1.4	78.0(ref. 38)
<b>5</b>	2.2 ± 0.8	30.1 ± 0.9	0.8(ref. 39)
<b>6</b>	37.2 ± 0.1	59.5 ± 0.7	0.6(ref. 38)
<b>7</b>	4.2 ± 0.0	204.8 ± 1.1	0.8(ref. 39)

<sup>a</sup>Details for the limit of detection calculations can be found in the ESI. All results represent an average of at least 3 trials.

In addition to binding PAHs in the cavity interior, macrocycle **1** (10 mM in DMSO) was also investigated for its ability to bind anions. Among all anions studied (fluoride, cyanide, azide, and thiocyanate), only fluoride exhibited a noticeable spectroscopic change (Figure 6) with increases in the molar absorptivity of the macrocycle's  $\lambda_{\text{max}}$  bands at 264 and 305 nm. The response for fluoride is likely due to its ability to act as a hydrogen bond acceptor, as a result of its small size, high electronegativity, and high charge density.<sup>40</sup>

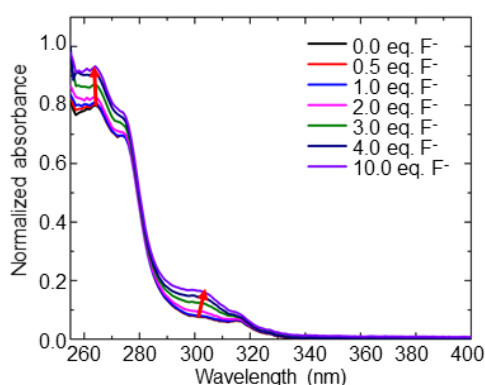


**Figure 6.** Illustration of changes in the UV-visible absorption spectrum of macrocycle **1** with the addition of up to 10 equivalents of fluoride anion.

The fluoride binding was confirmed by nonlinear curve fitting of the  $^1\text{H-NMR}$  titration data to host-guest binding models (Figure 7 and Table 3). An excellent non-linear fit was obtained for a 1:2 binding stoichiometry between macrocycle **1** and two fluoride anions, and this stoichiometry was confirmed with a Job plot analysis that showed a maximum at a mole fraction of 0.66 (see ESI for details). The calculated binding constants indicate anti-cooperativity, with the binding of the first fluoride ( $K_1 = 522 \text{ M}^{-1}$  approx.) preferred compared to binding of the second fluoride anion ( $K_2 = 333.25 \text{ M}^{-1}$  approx.). This phenomenon could be attributed to the fact that the fluorenone flexibility is constrained by the first binding, reducing the conformational flexibility for the second

fluoride binding. Each fluoride anion interacts with the triazole proton ( $H_e$ , red), and is additionally assisted by the fluorenone and biphenyl protons ( $H_b$ , blue and  $H_g$ , green) (Figure 8), as shown through the chemical shift changes of these protons with the addition of up to 10 equivalents of fluoride anion (Table 3).

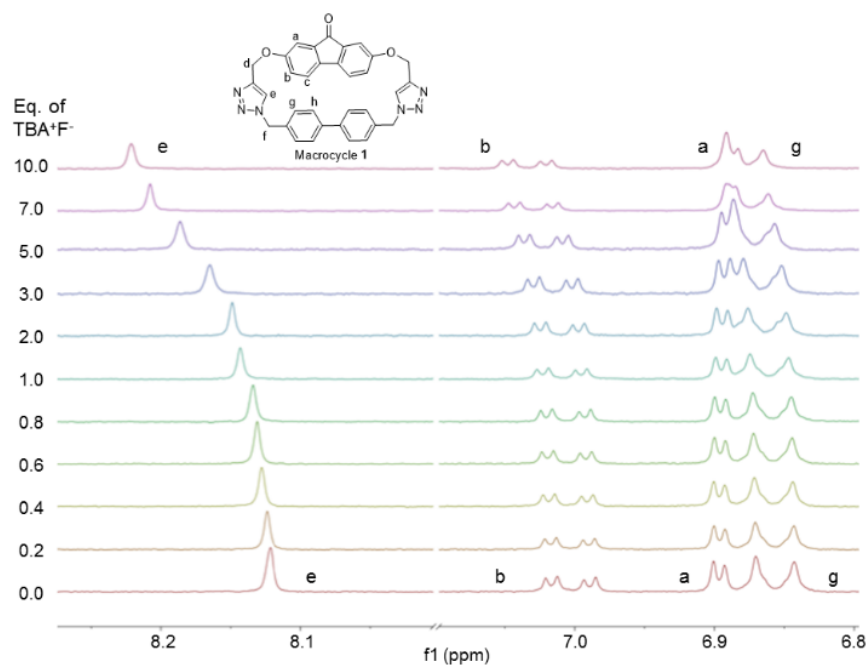


**Figure 7.** Illustration of the changes in the  $^1\text{H-NMR}$  chemical shifts of macrocycle **1** with the titration of fluoride anions.

**Table 3.** Illustration of the changes in the  $^1\text{H-NMR}$  chemical signal of macrocycle **1** with binding of fluoride anions<sup>a</sup>

Equivalents of fluoride	Change in $\delta$ (ppm)			
	$H_e$	$H_b$	$H_a$	$H_g$
1	0.014	0.004	-0.000	0.002
3	0.044	0.016	-0.003	0.009
5	0.066	0.022	-0.005	0.014
10	0.100	0.031	-0.010	0.022

<sup>a</sup>Detailed methods of the  $^1\text{H-NMR}$  titration are shown in the ESI.

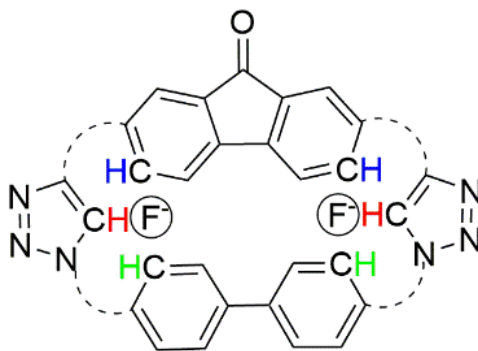


**Figure 8.** Proposed geometry of how macrocycle **1** binds two fluoride anions.

**Table 4.** Illustration of the changes in the  $^1\text{H-NMR}$  chemical signal of triazole proton with the binding of 10 equivalents of anions<sup>a</sup>

Anion	$\Delta\delta$ (ppm)
$\text{F}^-$	0.1002
$\text{CN}^-$	0.0021
$\text{SCN}^-$	0.0025
$\text{N}_3^-$	0.0024

<sup>a</sup>Detailed methods of the  $^1\text{H-NMR}$  titration are shown in the ESI.

The small size of fluoride makes it compatible with the binding pockets in each arm of the macrocycle. This compatibility results in selective binding of fluoride, with significantly higher chemical shift changes compared to the other anions (Table 4).

Moreover, the solvent used in these NMR titration experiments has a significant effect on the magnitude of the shifts observed. Chemical shift changes of higher magnitude have been reported in the literature with  $[\text{HF}_2]^-$  and triazolophane hosts in deuterated dichloromethane.<sup>41</sup> Because of solubility constraints, binding analyses were carried out in  $\text{DMSO-}d_6$ . Even though hydrogen fluoride and  $[\text{HF}_2]^-$  anions are present to a minor extent, their relatively small amounts (see ESI) means that they are unlikely to have a significant effect on fluoride binding. Moreover, chemical shift changes of the

tetrabutylammonium indicated no significant association between the counterion and the macrocycle–fluoride complex.

In conclusion, we have successfully synthesized a new macrocycle composed of biphenyl and fluorenone moieties linked by two triazoles. We demonstrated that macrocycle **1** is sensitive towards small amounts of PAHs with limits of detections in the nanomolar range. Additionally, compound **1** is able to bind selectively to fluoride in 1:2 stoichiometry through the use of triazole, fluorenone and biphenyl-facilitated C–H binding. This macrocycle can be used as a scaffold for additional detection applications as well as a crucial tool in our efforts to understand fundamental intermolecular interactions. Results of these and other investigations are currently underway in our laboratory, and results will be reported in due course.

#### ACKNOWLEDGEMENTS

The authors acknowledge Dr Li Li (MIT) and the Smith-Oxley research group (University of Rhode Island) for their help with mass spectrometry. This research was supported by the University of Rhode Island Department of Chemistry.

#### NOTES AND REFERENCES

1. Dale, E. J.; Vermeulen, N. A.; Juricek, M.; Barnes, J. C.; Young, R. M.; Wasielewski, M. R.; Stoddart, J. F. *Acc.Chem. Res.* **2016**, *49*, 262-273.
2. Barnes, J. C.; Juricek, M.; Strutt, N. L.; Frasconi, M.; Sampath, S.; Giesener, M. A.; McGrier, P. L.; Bruns, C. J.; Stern, C. L.; Sarjeant, A. A.; Stoddart, J. F. *J. Am. Chem. Soc.* **2013**, *135*, 183-192.
3. Kim, A.; Ali, R.; Park, S. H.; Kim, Y. -H.; Park, J. S. *Chem. Commun.* **2016**, *52*, 11139-11142.

4. Makrlik, E.; Bohm, S.; Sykora, D.; Klepetarova, B.; Petr, V.; Polasek, M. *Chem. Phys. Lett.* **2015**, *642*, 39-42.
5. Cram, D. J.; Montgomery, C. S.; Knox, G. R. *J. Am. Chem. Soc.* **1966**, *88*, 515-525.
6. Kato, S.-i.; Yamazaki, N.; Tajima, T.; Nakamura, Y. *Chem. Lett.* **2013**, *42*, 401-403.
7. Busch, M.; Cayir, M.; Nieger, M.; Thiel, W. R.; Brase, S. *Eur. J. Org. Chem.* **2013**, 6108-6123.
8. Wei, F.; Wang, W.; Ma, Y.; Tung, C.-H.; Xu, Z. *Chem. Commun.* **2016**, *52*, 14188-14199.
9. Lau, Y. H.; Rutledge, P. J.; Watkinson, M.; Todd, M. H. *Chem. Soc. Rev.* **2011**, *40*, 2848-2866.
10. Cai, J.; Sessler, J. L. *Chem. Soc. Rev.*, **2014**, *43*, 6198-6213.
11. Thakur, L. S.; Semil, P. *Int. J. ChemTech Res.*, **2013**, *5*, 1299-1308.
12. Palmer, C. A.; Gilbert, J. A. *J. Acad. Nutr. Diet.*, **2012**, *112*, 1443-1453.
13. Borysewicz-Lewicka, M.; Opydo-Szymaczek, J. *Pol. J. Environ. Stud.* **2016**, *25*, 9-15.
14. Komaba, H.; Fukagawa, M. *Kidney Int.* **2016**, *90*, 753-763.
15. Gorenjak, A. H.; Cencic, A. *Acta Aliment.* **2013**, *42*, 158-172.
16. Barrett, T. J.; Hawkins, C. L. *Chem. Res. Toxicol.* **2012**, *25*, 263-273.
17. Jackson, R.; Logue, B. A. *Anal. Chim. Acta* **2017**, *960*, 18-39.
18. Badgajar, D. M.; Talawar, M. B.; Asthana, S. N.; Mahulikar, P. P. *J. Hazard. Mater.* **2008**, *151*, 289-305.
19. Marzooghi, S.; Di Toro, D. M. *Environ. Toxicol. Chem.* **2017**, *36*, 1138-1148.
20. Claxton, L. D. *Mutat. Res., Rev. Mutat. Res.* **2014**, *762*, 108-122.
21. Mearns, A. J.; Reish, D. J.; Oshida, P. S.; Ginn, T.; Rempel-Hester, M. A.; Arthur, C.; Rutherford, N.; Pryor, R. *Water Environ. Res.* **2015**, *87*, 1718-1816.
22. Verma, N.; Pink, M.; Rettenmeier, A. W.; Schmitz-Spanke, S. *Proteomics* **2012**, *12*, 1731-1755.



23. Balcioglu, E. B. *Toxin Rev.* **2016**, *35*, 98-105.
24. Ceccaroli, C.; Pulliero, A.; Geretto, M.; Izzotti, A. *J. Environ. Sci. Health, Part C: Environ. Carcinog. Ecotoxicol. Rev.* **2015**, *33*, 188-228.
25. Serio, N.; Moyano, D. F.; Rotello, V. M.; Levine, M. *Chem. Commun.* **2015**, *51*, 11615-11618.
26. (a) DiScenza, D. J.; Levine, M. *Supramol. Chem.* **2016**, *28*, 881-891. (b) DiScenza, D. J.; Levine, M. *New J. Chem.* **2016**, *40*, 789-793.
27. (a) Radaram, B.; Levine, M. *Eur. J. Org. Chem.* **2015**, 6194-6204. (b) Radaram, B.; Potvin, J.; Levine, M. *Chem. Commun.* **2013**, *49*, 8259-8261.
28. Knops, P.; Sendhoff, N.; Mekelburger, H. B.; Voegtle, F. *Top. Curr. Chem.* **1992**, *161*, 1-36.
29. Ohana, T.; Kaise, M.; Nimura, S.; Kikuchi, O.; Yabe, A. *Chem. Lett.* **1993**, 765-768.
30. Yu, W. -L.; Pei, J.; Huang, W.; Heeger, A. J. *Adv. Mater.* **2000**, *12*, 828-831.
31. Uckert, F.; Setayesh, S.; Mullen, K. *Macromolecules* **1999**, *32*, 4519-4524.
32. Kwon, J. Y.; Singh, N. J.; Kim, H. N.; Kim, S. K.; Kim, K. S.; Yoon, J. *J. Am. Chem. Soc.* **2004**, *126*, 8892-8893.
33. Becker, H. -D.; Burgdorff, C.; Loehmannsroeben, H. -G. *J. Photochem. Photobiol. A* **1995**, *86*, 133-139.
34. Chen, Y. -H.; Tang, K. -C.; Chen, Y. -T.; Shen, J. -Y.; Wu, Y. -S.; Liu, S. -H.; Lee, C. -H.; Chen, C. -H.; Lai, T. -Y.; Tung, S. -H.; Jeng, R. -J.; Hung, W. -Y.; Jiao, M.; Wu, C. -C.; Chou, P. -T. *Chem. Sci.* **2016**, *7*, 3556-3563.
35. (a) Akhgari, F.; Samadi, N.; Farhadi, K. *J. Fluoresc.* **2017**, *27*, 921-927 (b) Marks, P.; Radaram, B.; Levine, M.; Levitsky, I. A. *Chem. Commun.* **2015**, *51*, 7061-7064.
36. Saute, B.; Narayanan, R. *J. Raman Spectrosc.* **2013**, *44*, 1518-1522.
37. Blasch, K.; Kolivosky, J.; Hill, B. *Inhalation Toxicol.* **2016**, *28*, 216-225.
38. Center for Disease Control and Prevention, The National Institute for Occupational Safety and Health (NIOSH): Naphthalene, <https://www.cdc.gov/niosh/npg/npgd0439.html>, accessed, Mar 27, 2017.

39. Center for Disease Control and Prevention, The National Institute for Occupational Safety and Health (NIOSH): Coal tar pitch volatiles, <https://www.cdc.gov/niosh/npg/npgd0145.html>, accessed, Mar 27, 2017.
40. Cametti, M.; Rissanen, K. *Chem. Commun.* **2009**, 2809-2829.
41. Ramabhadran, R. O.; Liu, Y.; Hua, Y.; Ciardi, M.; Flood, A. H.; Raghavachari, K. *J. Am. Chem. Soc.* **2014**, *136*, 5078-5089.

## *Supporting Information*

### **A highly versatile fluorenone-based macrocycle for the sensitive detection of polycyclic aromatic hydrocarbons and fluoride anions**

#### MATERIALS AND METHODS

All the starting materials, reagents, and solvents were purchased from Sigma Aldrich, Acros Organics, TCI chemicals, Alfa Aesar, or Fisher Scientific and were used as received. Reactions were all monitored via analytical thin layer chromatography (TLC) using polyester backed TLC plates. Visualization was accomplished with UV light at 254 nm. Flash column chromatography was performed with SiliaFlash F60 (230-400 mesh) or using automated flash chromatography (Yamazen Smart Flash AI-580S & AKROS). UV-VIS spectra were recorded on a Shimadzu UV-3600 Plus spectrophotometer. Fluorescence spectra were recorded on a Shimadzu RF-6000 fluorophotometer with 3.0 nm excitation and 3.0 nm emission slit widths.

$^1\text{H}$  and  $^{13}\text{C}$ -NMR spectra were taken on a Bruker 300 MHz spectrometer and were recorded in  $\text{CDCl}_3$  and  $\text{DMSO-}d_6$  at room temperature. Chemical shifts ( $\delta$ ) are reported in parts per million relative to chloroform at 7.26 ppm, dimethyl sulfoxide at 2.59 ppm, or to tetramethylsilane (TMS) at 0.00 ppm for  $^1\text{H}$ -NMR and relative to  $\text{CDCl}_3$  at 77.16 ppm or  $\text{DMSO-}d_6$  at 40.76 ppm for  $^{13}\text{C}$ -NMR spectra.

#### METHODS FOR MASS SPECTROMETRY DETECTION

Compounds **1** and **2** were dissolved in a mixture of water/acetonitrile (50/50) or chloroform to make 1 mg/mL or 0.285 mg/mL solutions respectively, and further diluted

to 5  $\mu\text{g/mL}$  in methanol/water (50/50) to produce an analytical standard. The latter was infused into a ThermoScientific LTQ Orbitrap XL<sup>TM</sup> mass spectrometer at a rate of 15  $\mu\text{L/min}$  using an electrospray ionization source in a positive mode. The rest of the ionization source and ion optics parameters were as follows: sheath gas 25, auxiliary gas 6, spray voltage 5 kV, capillary temperature 275  $^{\circ}\text{C}$ , capillary voltage 47 V, tube lens 165 V, multipole 00 offset -5.5 V, lens 0 -6.0 V, multipole 0 offset -5.75 V, lens 1 -10.0 V, gate lens -46.0 V, multiple 1 offset -19.5 V, multipole RF amplitude 400.0 V, front lens -6.75 V. The mass spectra were collected using full scan mode with a resolution of 30000 in the range between 60 and 600 amu. The spectra were averaged over 2 microscans with 10.0 ms maximum injection time and  $2.0 \times 10^5$  ions for AGC target settings.

#### METHODS FOR COMPUTATIONAL EXPERIMENTS

Computational work was performed with Spartan software (Spartan 10, version 1.1.0), obtained from Wavefunction, Inc. CA. All calculations were performed using equilibrium geometry at the ground state, HF-DFT (B3LYP, 6-31G\*) level. All the conformations shown were energy minimized.

#### METHODS FOR FLUORESCENCE EXPERIMENTS

12  $\mu\text{L}$  of a 5 mM solution of the analyte was added to a cuvette containing 2 mL of chloroform. In a separate cuvette, 12  $\mu\text{L}$  of a 5 mM of the analyte was added to 2 mL (30  $\mu\text{M}$ ) of **1** in chloroform. Both samples were excited at the analyte's excitation wavelength and the fluorescence emission spectra were recorded. Both the excitation

slit width and the emission slit width were 3.0 nm. All fluorescence spectra were integrated vs. wavenumber on the X-axis using OriginPro Version 9.1. The fluorescence change was determined using the following equation:

$$\text{Fluorescence change (\%)} = \frac{Fl_m - Fl_a}{Fl_a}$$

Where  $Fl_a$  is the integrated fluorescence emission of the analyte and  $Fl_m$  is the integrated fluorescence emission of the analyte in the presence of macrocycle **1**.

Analyte	Excitation Wavelength (nm)
<b>4</b>	275
<b>5</b>	343
<b>6</b>	295
<b>7</b>	321

#### METHODS FOR LIMIT OF DETECTION EXPERIMENTS

Reference: Cheng, D.; Zhao, W.; Yang, H.; Huang, Z.; Liu, X.; Han, A. "Detection of  $Hg^{2+}$  by a FRET Ratiometric Fluorescent Probe Based on a Novel BODIPY-RhB System." *Tetrahedron Lett.* **2016**, *57*, 2655-2659.

The limit of detection (LOD) is defined as the lowest concentration of analyte at which a signal can be detected. To determine this value, the following steps were performed for each macrocycle-analyte combination. In a quartz cuvette, 2.5 mL of a 3  $\mu$ M solution of **1** in chloroform was added. The fluorescence emission spectra were recorded. Six repeat measurements were taken.

Next, 3  $\mu\text{L}$  of analyte (0.5 mM) was added, and again the solution was excited at the analyte's excitation wavelength, and the fluorescence emission spectra were recorded. Six repeat measurements were taken. This step was repeated for 6  $\mu\text{L}$  of analyte, 12  $\mu\text{L}$  of analyte, 18  $\mu\text{L}$  of analyte, 24  $\mu\text{L}$  of analyte, 30  $\mu\text{L}$  of analyte, 36  $\mu\text{L}$  of analyte, and 42  $\mu\text{L}$  of analyte. All of the fluorescence emission spectra were integrated vs. wavenumber on the X-axis, and calibration curves were generated. The curves plotted the analyte concentration in  $\mu\text{M}$  on the X-axis, and the fluorescence change on the Y-axis. The curve was fitted to a straight line and the equation of the line was determined. The limit of detection is defined according to the following equation:

$$\text{LOD} = (3 \text{SD}_{\text{blank}})/m$$

Where  $\text{SD}_{\text{blank}}$  is the standard deviation of the blank sample and  $m$  is the slope of the calibration curve.

#### METHODS FOR UV/VIS ABSORPTION SPECTROSCOPY EXPERIMENTS

For polycyclic aromatic hydrocarbons (PAHs): The absorption spectra of a 30  $\mu\text{M}$  solution of both **1** and each guest (PAH) were collected separately. For the 1:1 absorption spectra, 12  $\mu\text{L}$  of a guest solution of 5 mM was added to 2 mL of a 30  $\mu\text{M}$  solution of **1**, the solution was shaken and data was collected.

For anion binding experiments: In a quartz cuvette, 2.5 mL of a 10  $\mu\text{M}$  solution of **1** was added. During titration, aliquots of a 4 mM solution of the anion (as its tetrabutylammonium salt) were added to the cuvette. The solution was shaken, and data was collected following each addition.

Titration experiments: Solutions of receptor **1** (1 mM, DMSO-*d*<sub>6</sub>) were titrated by adding known quantities of a stock 20 mM solution of tetrabutylammonium fluoride. The chemical shifts of the triazole protons were monitored and plotted. Nonlinear curve fitting method was employed to compare against a standard 1:2 host-guest interaction model.

Calculation of other complexed species: Interferences from the *in situ* generation of HF and [HF<sub>2</sub>]<sup>-</sup> were quantified based on stoichiometric analyses of their integrated peak ratios against that of the predominant complexed species. With the overall concentration of the receptor **1** held constant throughout the titration, the percentage of each complexed species is calculated according to the equation shown below:

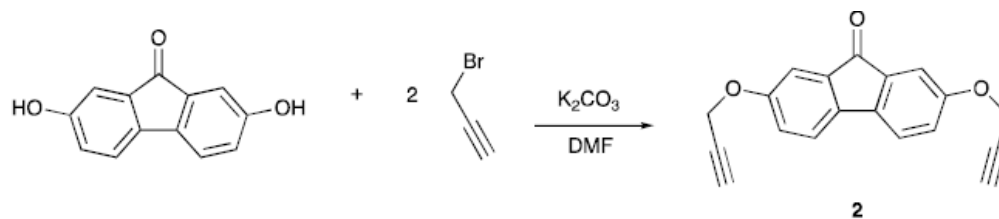
% complexed species *n* = (Integrated area of peak for species *n*) / (Sum of the integrated peak areas of all the complexed species)

#### METHODS FOR JOB'S PLOT ANALYSIS

Job's plot experiment: Stock solutions of the macrocycle **1** and TBAF (3.2 mM each) were prepared separately in DMSO-*d*<sub>6</sub>. The <sup>1</sup>H-NMR spectra was taken for each of 11 different solutions (total volume 0.5 mL) containing the macrocycle **1** and the tetrabutylammonium salt in the following molar fraction ratio (of the macrocycle): 1, 0.9, 0.8, 0.7, 0.6, 0.5, 0.4, 0.3, 0.2, 0.1 and 0.0. δ is measured with respect of the triazole proton of **1**.

## SYNTHETIC PROCEDURES

### Synthesis of fluorenone-propargyl ether (**2**)



In a 25 mL round-bottomed flask containing 15 mL of *N,N*-dimethylformamide (DMF), 2,7-dihydroxy-9-fluorenone (compound **8**) (212 mg, 1.0 mmol, 1.0 eq.) and potassium carbonate (414 mg, 3.0 mmol, 3.0 eq.) were added. The reaction mixture was stirred at room temperature for 30 min, then propargyl bromide (0.379 mL, 5.0 mmol, 5 eq.) was added and the reaction mixture was stirred for 24 hours at room temperature. After 24 hours, distilled water (100 mL) was added and the product was extracted with ethyl acetate (3x10 mL). The organic layer was washed with water (3 x 10 mL) and dried over  $Na_2SO_4$ . The pure compound was isolated as an orange solid after recrystallization from chloroform (244 mg, 85% yield).  $^1H$ -NMR (300 MHz, DMSO- $d_6$ ):  $\delta$  (ppm) = 7.61 (d, 2 H,  $J = 8.1$  Hz), 7.19 (d, 2 H,  $J = 2.4$  Hz), 7.13 (dd, 2 H,  $J = 8.1, 2.5$  Hz), 4.90 (d, 4 H,  $J = 2.4$  Hz), 3.64 (t, 2 H,  $J = 2.3$  Hz).  $^{13}C$ -NMR (100 MHz, DMSO- $d_6$ ):  $\delta$  (ppm) = 193.2, 158.0, 138.1, 136.0, 121.3, 120.7, 110.9, 78.0, 76.1, 56.2. ESI-TOF-MS: ESI-MS calcd for  $C_{19}H_{12}O_3$   $m/z = 288.0786$ , found  $[M+Na]^+$   $m/z = 311.0679$ .



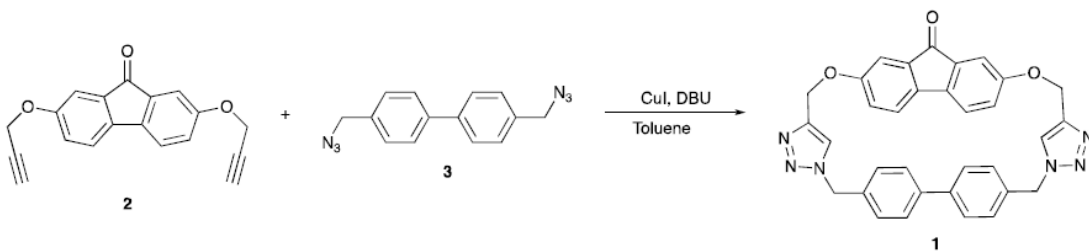
### Synthesis of 4,4'-bis(azidomethyl)-1,1'-biphenyl (**3**)



In a 50 mL round-bottom flask containing 25 mL of DMF, 4,4'-bis(chloromethyl)-1,1'-biphenyl (251 mg, 2.0 mmol, 1.0 eq.) and sodium azide (390 mg, 6.0 mmol, 6.0 eq) were added. The reaction mixture was stirred at 60 °C for 16 hours, at which point water (100 mL) was added and the product was extracted with  $\text{Et}_2\text{O}$  (3x10 mL). The combined organic phases were washed with water and brine, and then dried over  $\text{Mg}_2\text{SO}_4$ . The pure compound was isolated as a white solid after evaporation of  $\text{Et}_2\text{O}$  in 90% yield (475 mg).  $^1\text{H-NMR}$  (300 MHz,  $\text{DMSO-}d_6$ ):  $\delta$  (ppm) = 7.72 (d, 4 H,  $J = 7.6$  Hz), 7.47 (d, 4 H,  $J = 7.6$  Hz), 4.50 (s, 4 H).

The spectroscopic characteristics were in good agreement with those found in the literature (J. Polym. Sci., Part A: Polym. Chem. 2014, 52, 223–231).

### Synthesis of the macrocycle **1**



Under nitrogen, 1,8-diaza[5.4.0] bicycloundec-7-ene (DBU) (0.4 mL, 2.25 mmol) and  $\text{CuI}$  (5 mg, 0.026 mmol) were added to dry toluene (200 mL), degassed for 30 min and heated to 70 °C. Then **2** (58 mg, 0.20 mmol) and **3** (54 mg, 0.20 mmol) in dry toluene (100 mL) were added to the solution dropwise over 10 h and stirred for another 12 hrs.

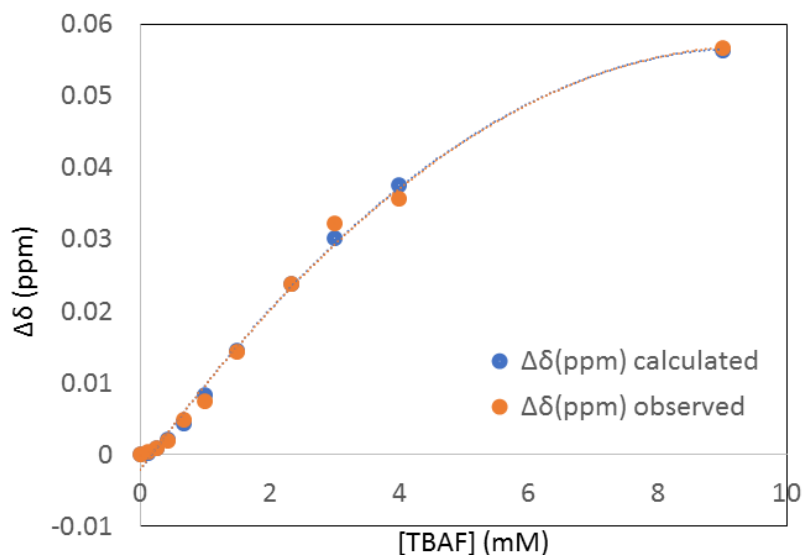
The mixture was then cooled to room temperature. The filtrate was concentrated in vacuum, and the product was purified by column chromatography (SiO<sub>2</sub>, CHCl<sub>3</sub>/MeOH 99:1) to afford **1** (79 mg, 0.14 mmol, 71% yield) as a light orange solid. <sup>1</sup>H-NMR (300 MHz, DMSO-d<sub>6</sub>): δ (ppm) = 8.15 (s, 2 H), 7.52 (d, 2 H, J = 8.1 Hz), 7.23 (d, 4 H, J = 8.1 Hz), 7.00 (dd, 2 H, J = 8.3, 2.5 Hz) 6.90 (d, 2 H, J = 2.4 Hz) 6.86 (d, 4 H, J = 8.1 Hz) 5.62 (s, 4 H), 5.40 (s, 4 H). <sup>13</sup>C-NMR (100 MHz, DMSO-d<sub>6</sub>): δ (ppm) = 192.7, 157.4, 143.9, 139.5, 137.2, 136.7, 135.4, 127.6, 127.1, 125.8, 121.5, 113.1, 79.7, 61.8, 52.8. ESI-TOF-MS: MS calcd for C<sub>19</sub>H<sub>12</sub>O<sub>3</sub> m/z 552.1909, found [M+H]<sup>+</sup> m/z 553.1958.

#### SUMMARY TABLE FOR <sup>1</sup>H-NMR EXPERIMENTS

Chemical shift changes of the triazole proton of macrocycle **1** in the presence of 10 equivalents of each anion (as its tetrabutylammonium salt). The changes are calculated relative to the peak position for free macrocycle **1**.

Anion	Δδ (ppm)
F <sup>-</sup>	0.1002
CN <sup>-</sup>	0.0021
SCN <sup>-</sup>	0.0025
N <sub>3</sub> <sup>-</sup>	0.0024

<sup>1</sup>H-NMR SUMMARY DATA FOR FITTING OF THE NMR TITRATION DATA TO A NONLINEAR BINDING ISOTHERM



A nonlinear curve fitting method was employed to compare against a standard 1:2 host-guest interaction model, using the following equation<sup>1</sup>:

$$\Delta\delta = (\Delta\delta_{HG}K_1[G_0] + \Delta\delta_{HG2}K_1K_2[G_0]^2) / (1 + K_1[G_0] + K_1K_2[G_0]^2)$$

where,  $\Delta\delta$  is the observed change in the chemical shift of the host H;  $\Delta\delta_{HG}$  is the change in the chemical shift of host H at the first binding event;  $\Delta\delta_{HG2}$  is the overall change in the chemical shift of host H, at the second binding event;  $K_1$  is the association constant value for the first binding event to the host H;  $K_2$  is the association constant value for the second binding event to HG; and  $[G_0]$  is the concentration of guest.

## SUMMARY TABLES FOR LIMIT OF DETECTION EXPERIMENTS

### With macrocycle 1:

Analyte	Equation	R <sup>2</sup>	LOD (nM)
<b>4</b>	$y = 0.6473x + 2.7969$	0.995	$28.8 \pm 0.1$
<b>5</b>	$y = 15.766x + 113.52$	0.964	$2.2 \pm 0.8$
<b>6</b>	$y = 1.1217x + 9.5484$	0.973	$37.2 \pm 0.1$
<b>7</b>	$y = 11.148x + 152.42$	0.952	$4.2 \pm 0.0$

### Without macrocycle:

Analyte	Equation	R <sup>2</sup>	LOD (nM)
<b>4</b>	$y = 0.3163x + 1.0405$	0.997	$166.5 \pm 1.4$
<b>5</b>	$y = 1612.9x + 16780$	0.9836	$30.1 \pm 0.9$
<b>6</b>	$y = 0.7606x + 2.577$	0.992	$59.5 \pm 0.7$
<b>7</b>	$y = 0.3848x + 2.2844$	0.9898	$204.8 \pm 1.1$

## SUMMARY TABLES FOR JOB'S PLOT ANALYSIS

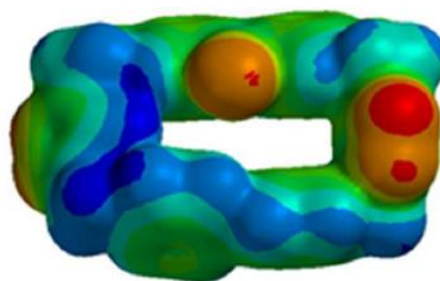
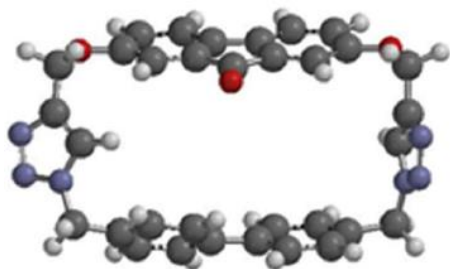
[1] (mM)	[F <sup>-</sup> ](mM)	$\gamma_1$	$\delta$ (ppm)	$\Delta\delta$ (ppm)	$\gamma_1 * \Delta\delta$
3.2	0	1	8.128	0	0
2.88	0.32	0.9	8.1295	0.0015	0.00135
2.56	0.64	0.8	8.1304	0.0024	0.00192
2.24	0.96	0.7	8.1315	0.0035	0.00245
1.92	1.28	0.6	8.132	0.004	0.0024
1.6	1.6	0.5	8.1321	0.0041	0.00205
1.28	1.92	0.4	8.1325	0.0045	0.0018
0.96	2.24	0.3	8.133	0.005	0.0015
0.64	2.56	0.2	8.1329	0.0049	0.00098
0.32	2.88	0.1	8.133	0.005	0.0005
0	3.2	0			

## SUMMARY FIGURES FOR COMPUTATIONAL EXPERIMENTS

Representative energy-minimized conformations and potentials of macrocycle 1 as deduced by ab initio HF-DFT (B3LYP, 6-31G\*) level measurements. The energy of the conformation is shown beneath each structure. The structure shown in the paper is structure **1** with  $E = 727.6230$  KJ/mol.

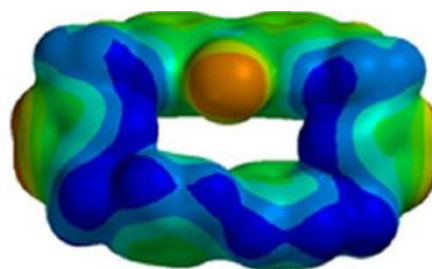
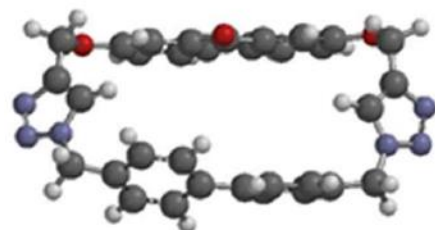
Cavity dimensions of structure 1: 10.6 Å x 5.043 Å.

**Structure 1:**



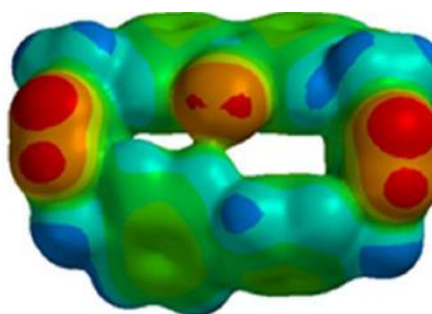
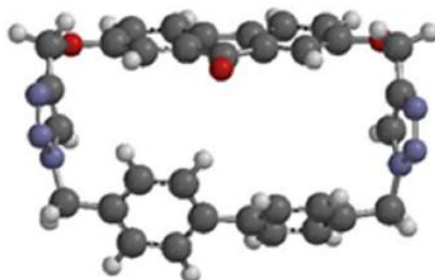
E = 727.6230 KJ/mol

**Structure 2:**



E = 736.5206 KJ/mol

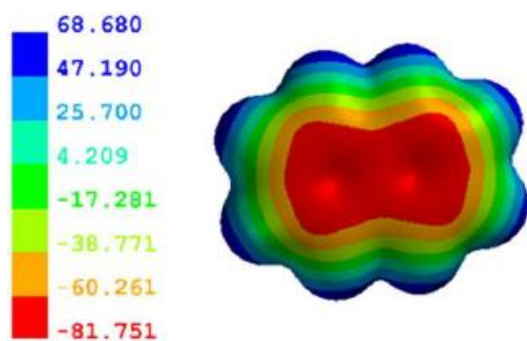
**Structure 3:**



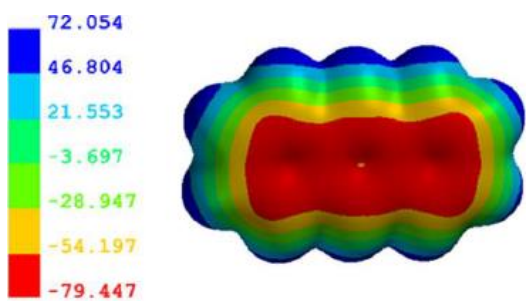
E = 741.7002 KJ/mol

Electrostatic potential maps of analytes 4-7:

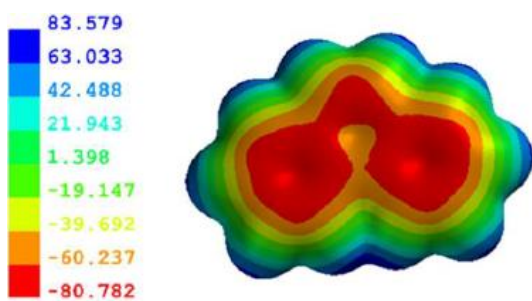
Analyte 4:



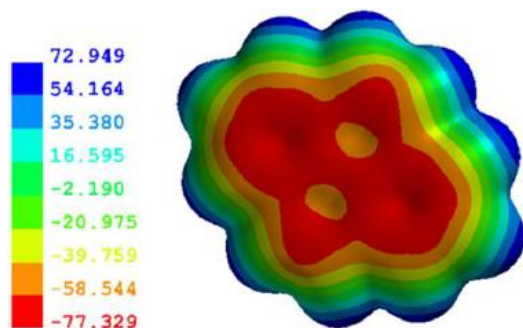
Analyte 5:



Analyte 6:



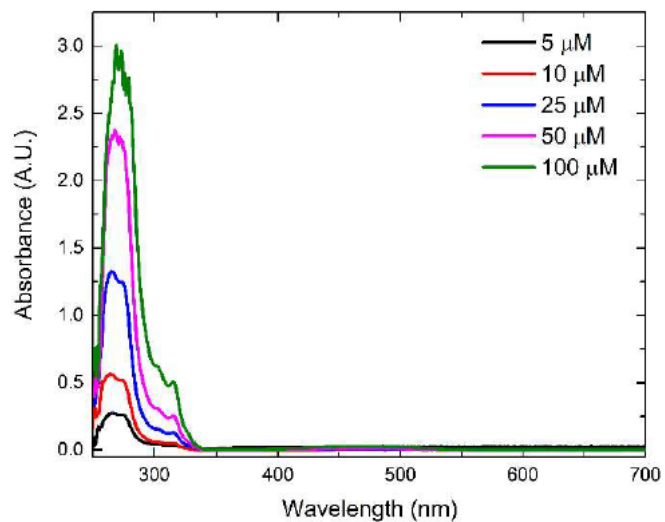
Analyte **7**:



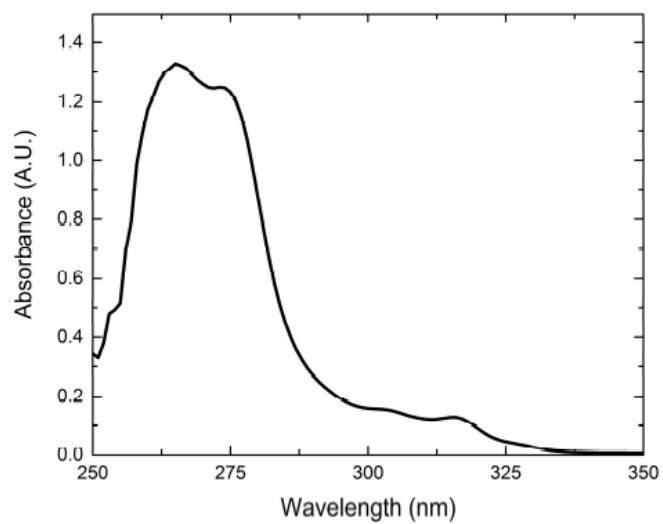
#### SUMMARY FIGURES FOR ABSORBANCE EXPERIMENTS

The concentration of the analyte and **1** taken separately was 30  $\mu\text{M}$ . The final concentrations of the analyte and **1** in the 1:1 mixture was 30  $\mu\text{M}$ .

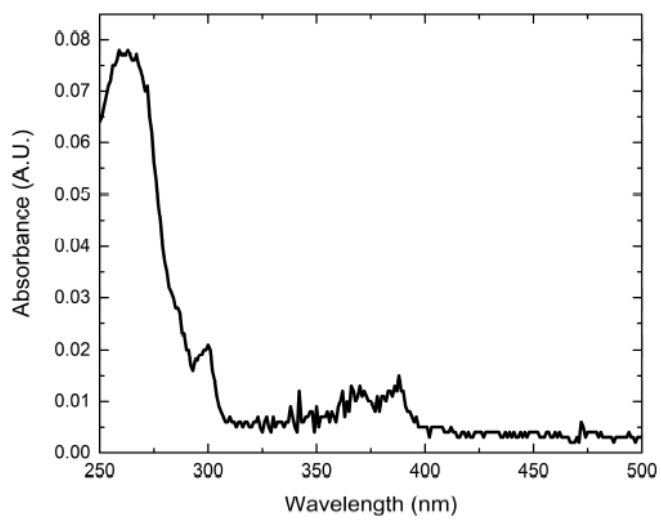
Absorbance Spectra of the Macrocycle without Analyte



Zoomed in on the shorter wavelength spectral region:

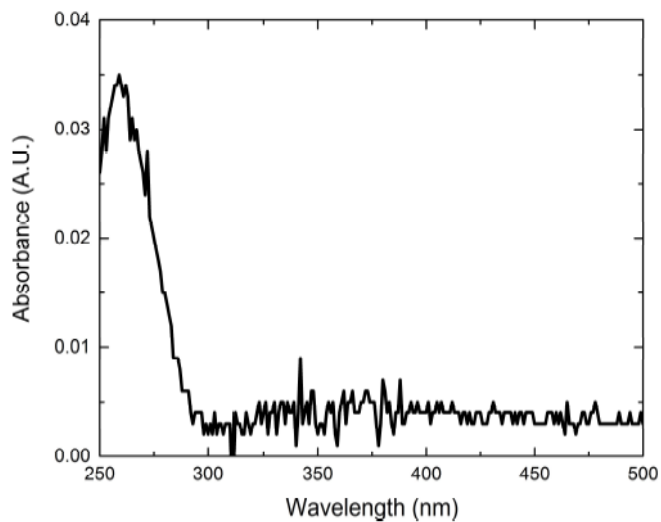


Absorbance spectrum of compound **8**:



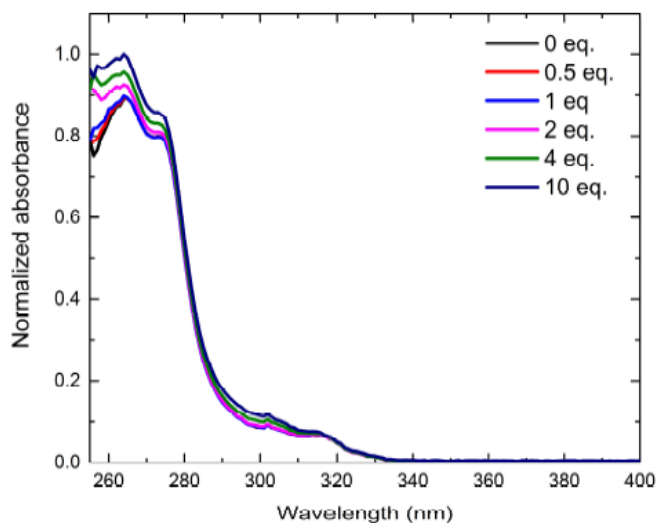


Absorbance spectrum of compound **9**:

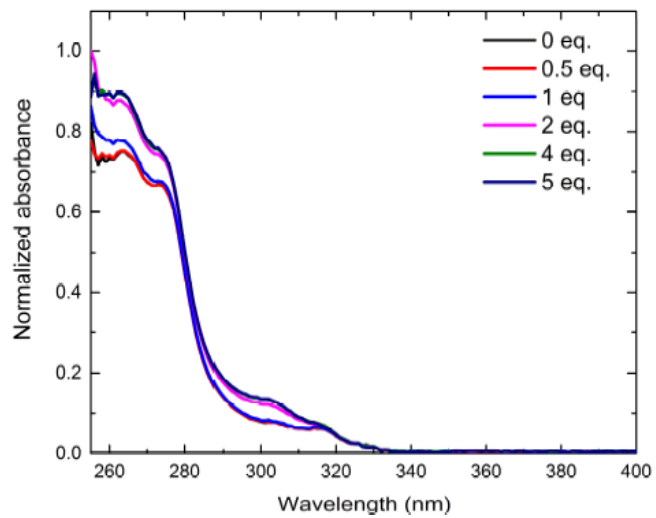


**Anion experiments:** The concentration of **1** was kept constant throughout the titration at 10  $\mu\text{M}$ .

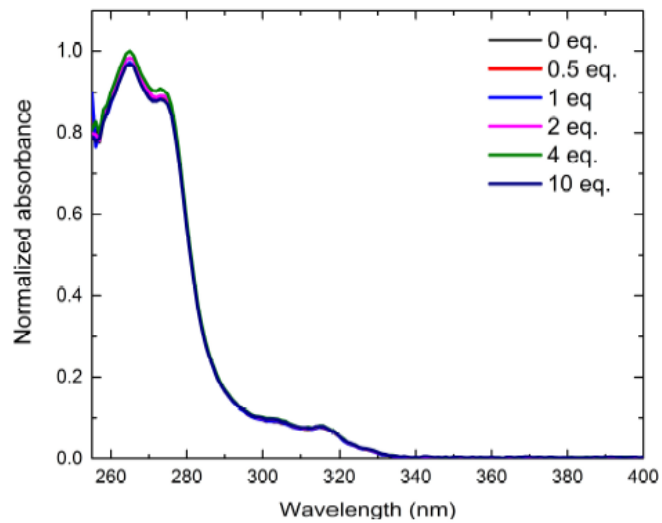
Thiocyanate:



Azide:

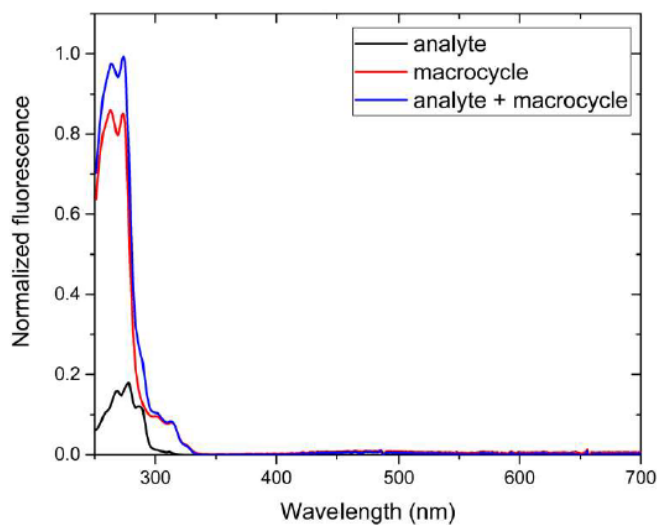


Cyanide:

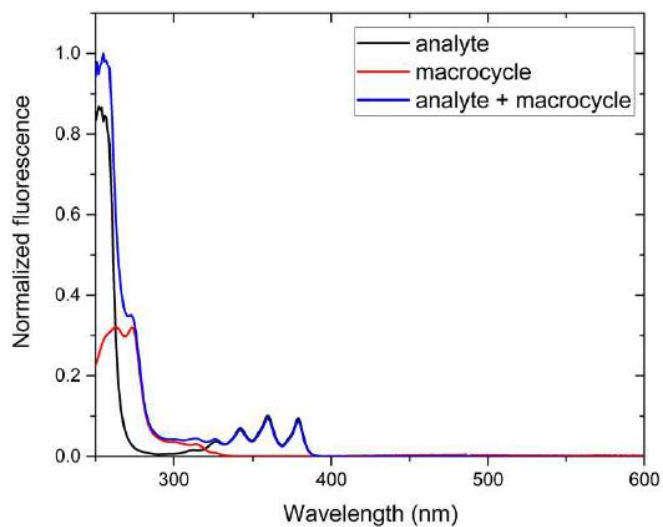


## SUMMARY FIGURES FOR FLUORESCENCE EXPERIMENTS

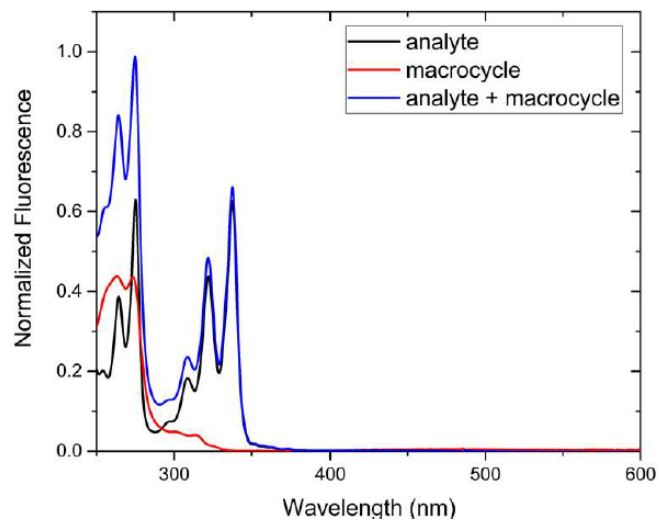
### Fluorescence Spectra of the Macrocycle with Naphthalene



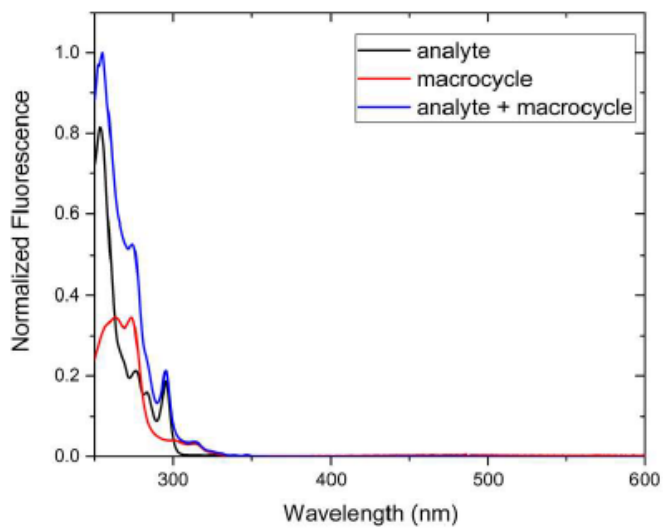
### Fluorescence Spectra of the Macrocycle with Anthracene



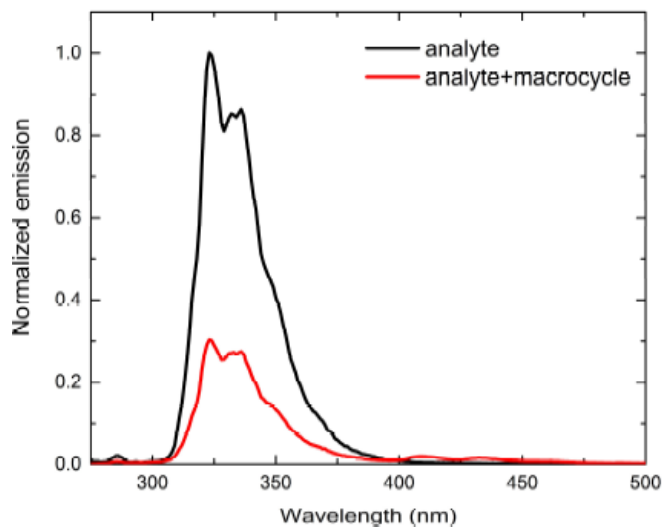
### Fluorescence Spectra of the Macrocycle with Pyrene



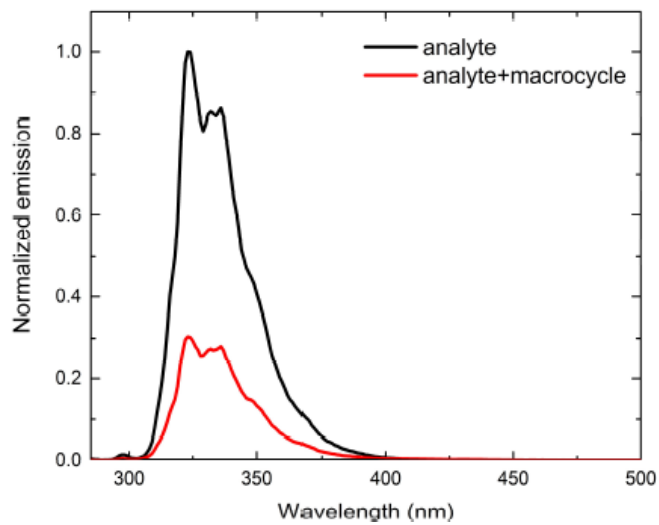
### Fluorescence Spectra of the Macrocycle with Phenanthrene



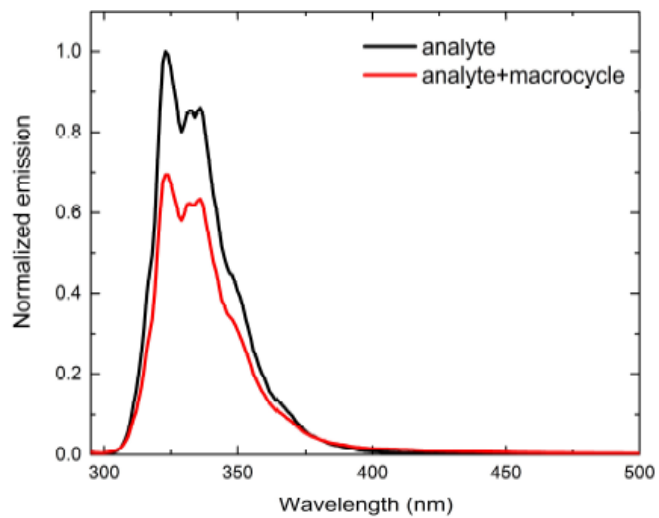
Macrocycle with naphthalene  
265 nm excitation:



275 nm excitation:



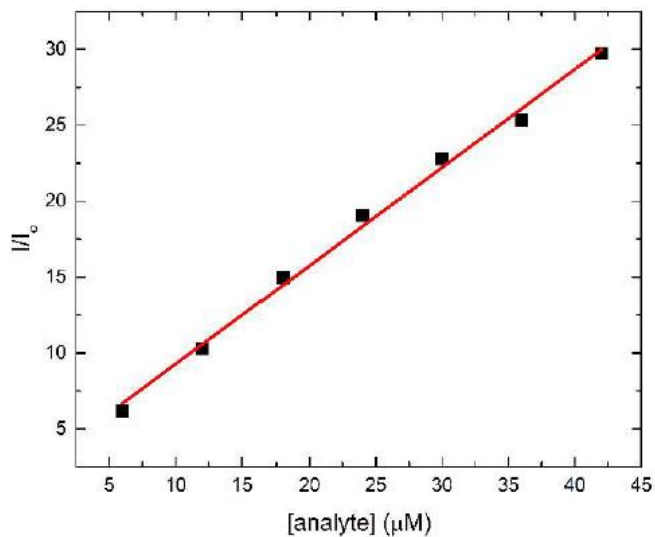
285 nm excitation:



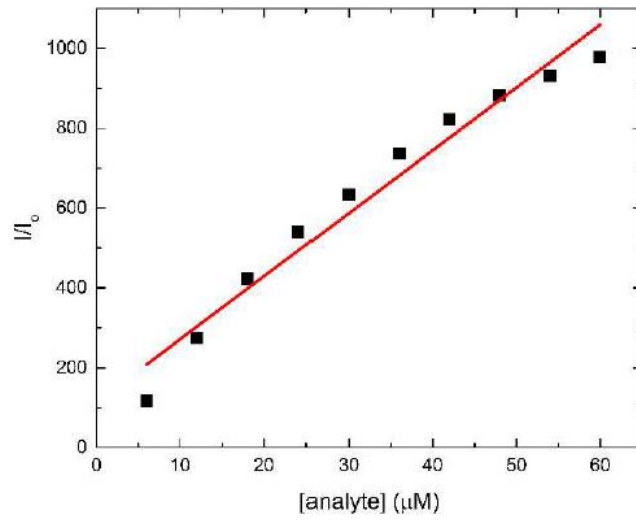
## SUMMARY FIGURES FOR LIMIT OF DETECTION EXPERIMENTS

### With macrocycle 1:

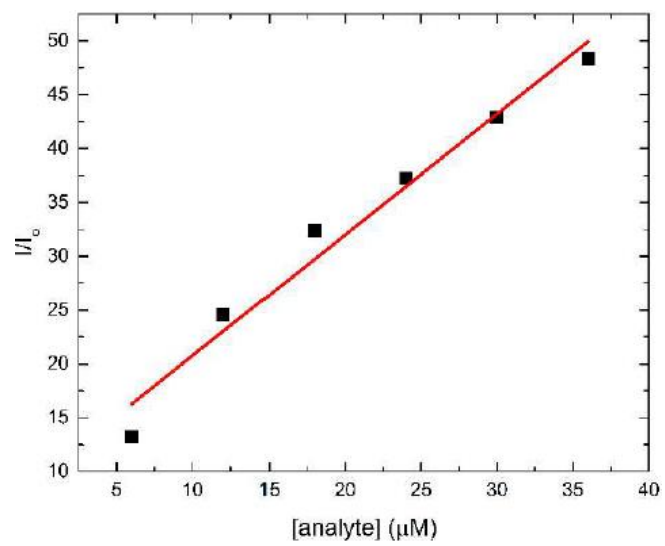
Naphthalene



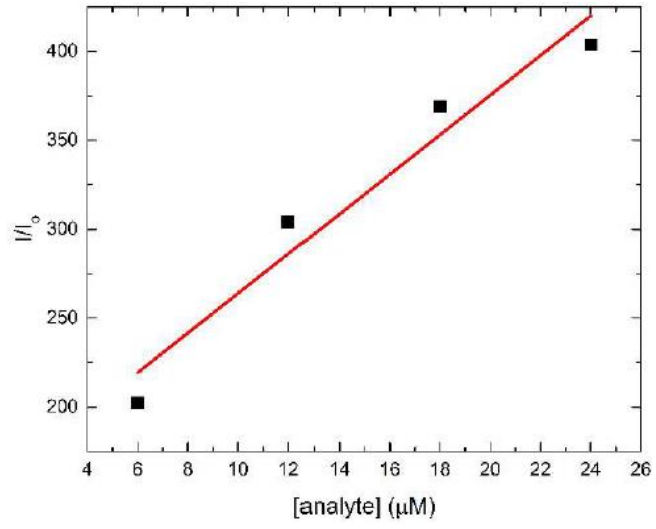
## Anthracene



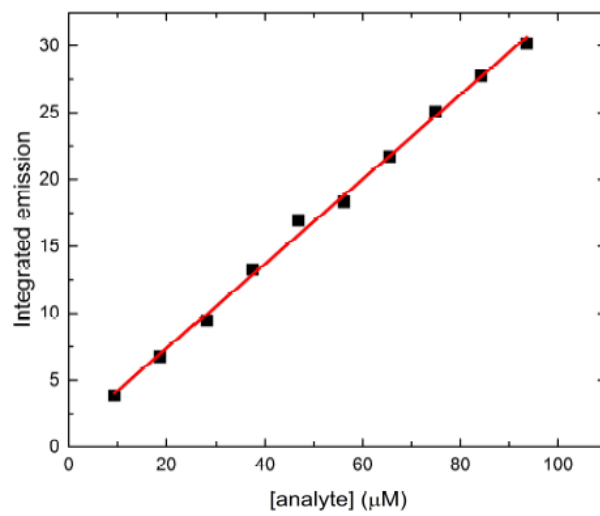
## Phenanthrene



## Pyrene

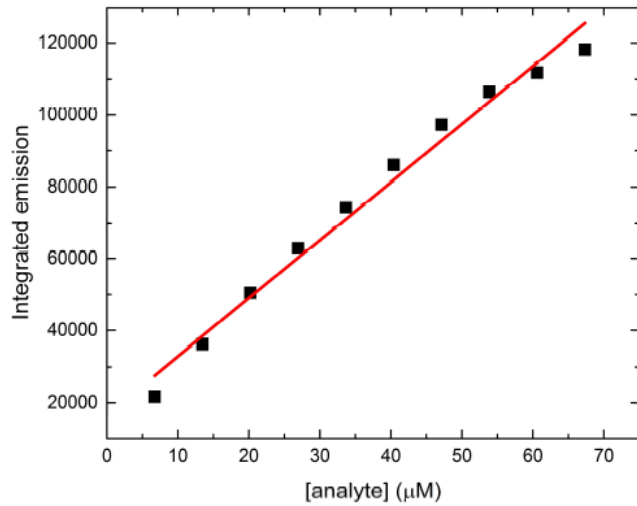


## LOD experiments without macrocycle 1: Naphthalene

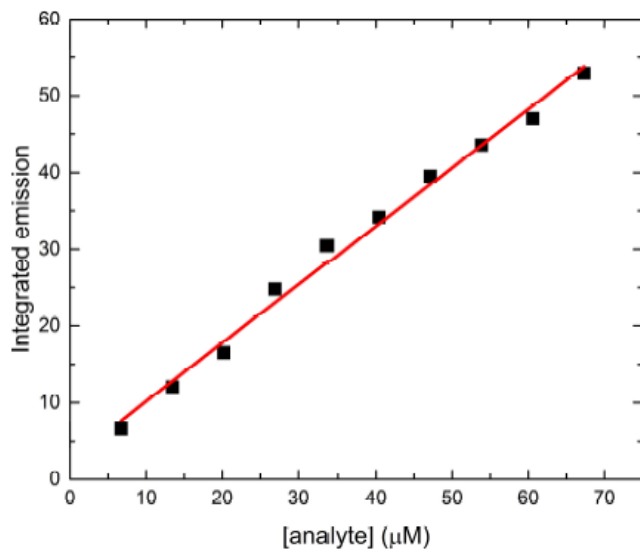




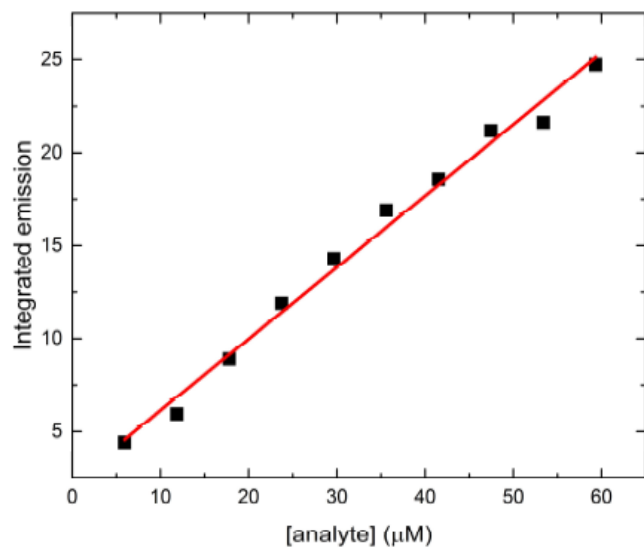
### Anthracene



### Phenanthrene

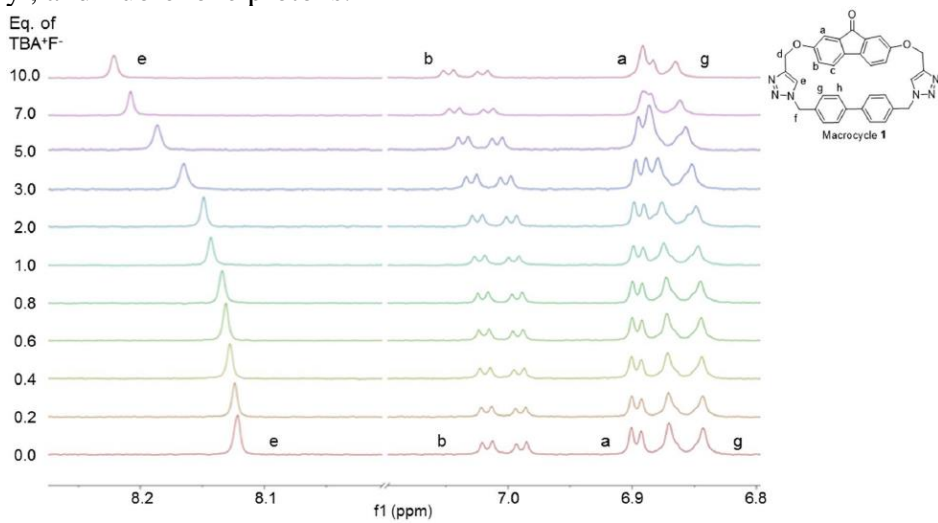


## Pyrene

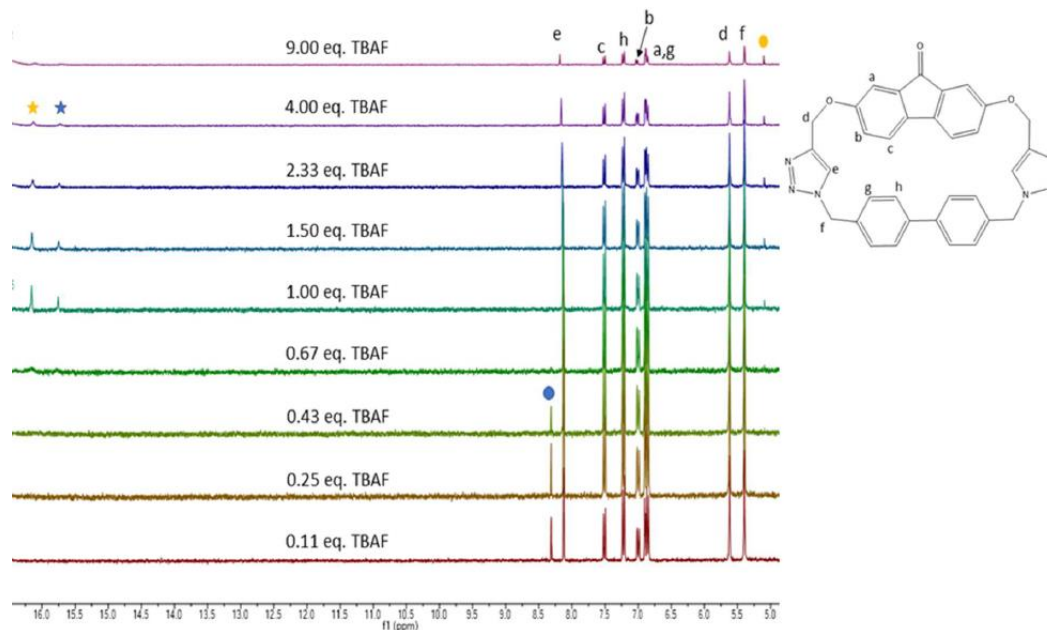


## SUMMARY FIGURES FOR NMR TITRATION EXPERIMENTS

a)  $^1\text{H}$ -NMR titration of **1** with TBAF indicating chemical shifts in the triazole, biphenyl, and fluorenone protons.



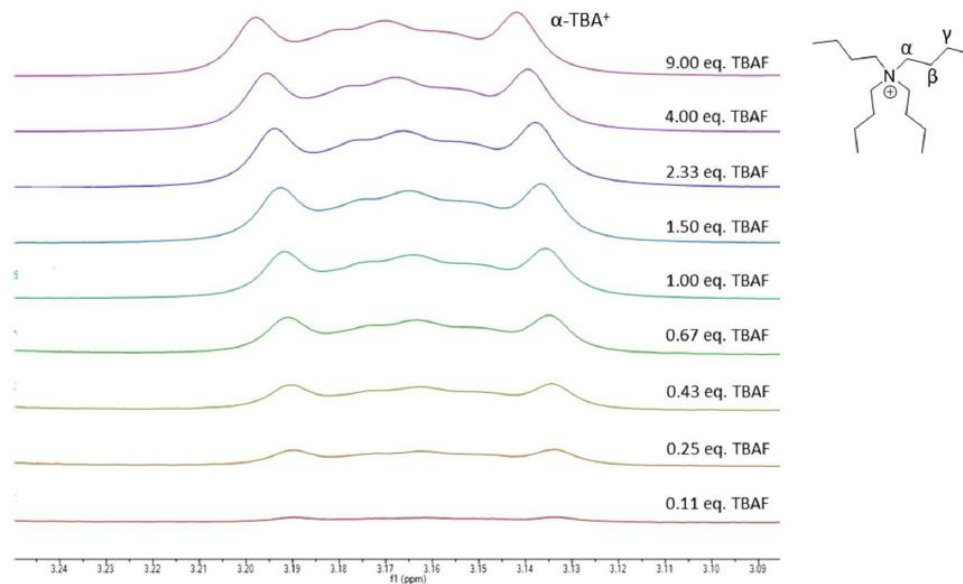
b)  $^1\text{H-NMR}$  titration of **1** with TBAF indicating the formation of other complexes from interfering fluorine species



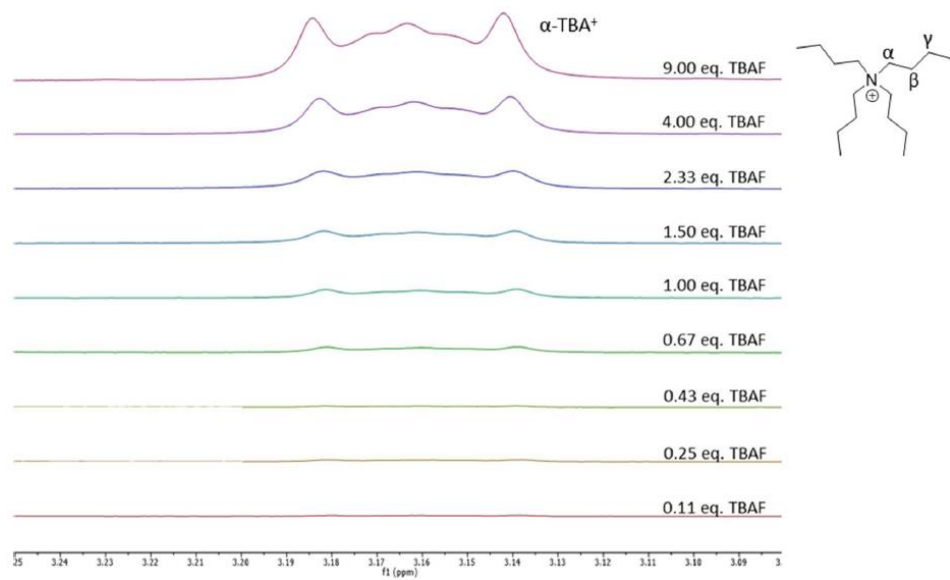
c) Calculated relative percentages of interfering fluorine species in the complexation

<i>Eq. of TBAF</i>	NH-bonded <b>1</b> [F $^-$ ] $_2$ (blue circle) (%)	<b>1</b> [F $^-$ ] $_2$ (%)	<b>1</b> [HF $_2$ ] $^-$ (yellow circle) (%)
0.11	21.26	78.74	0.00
0.25	16.66	83.34	0.00
0.43	10.71	89.29	0.00
0.67	0.00	100.0	0.00
1.00	0.00	95.24	4.76
1.50	0.00	94.34	5.66
2.33	0.00	94.34	5.66
4.00	0.00	92.60	7.40
9.00	0.00	90.91	9.09

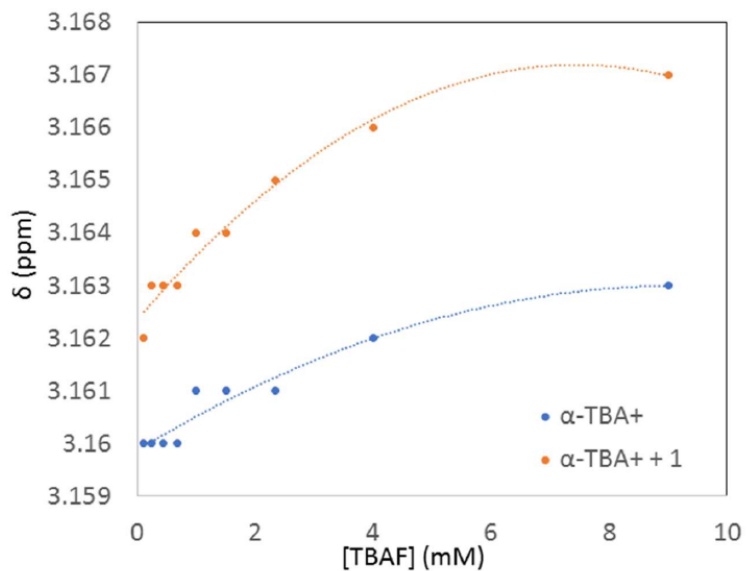
d) Chemical shift changes of  $\alpha$ -TBA<sup>+</sup> protons at 1 mM concentration of **1**



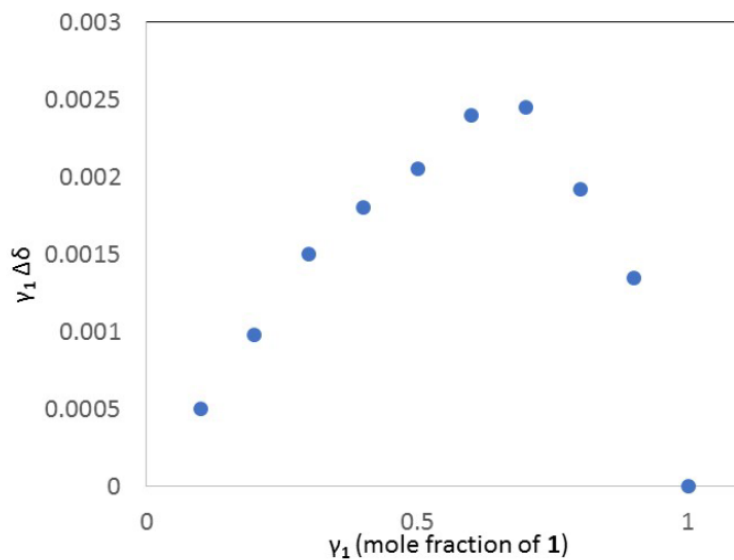
e) Chemical shift changes of  $\alpha$ -TBA<sup>+</sup> protons at 0 mM concentration of **1**



f) Plot of chemical shift changes of  $\alpha$ -TBA<sup>+</sup> protons (d) vs. (e)

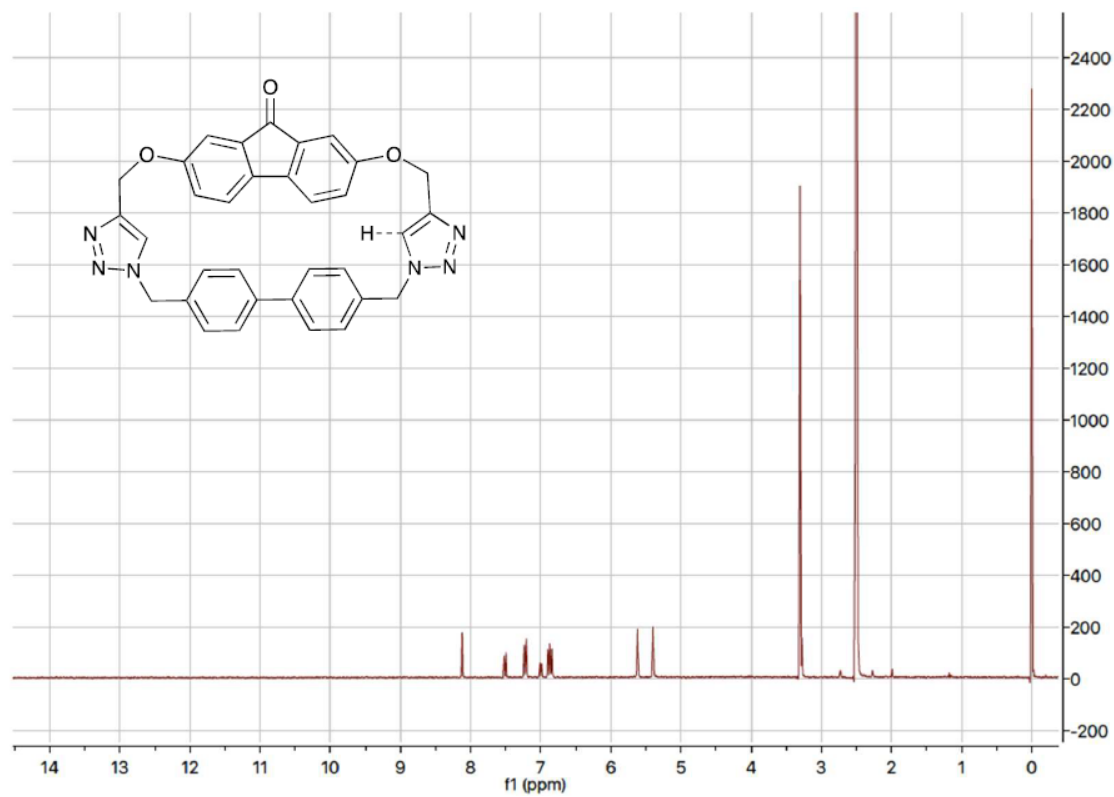


SUMMARY FIGURE FOR JOB'S PLOT ANALYSIS

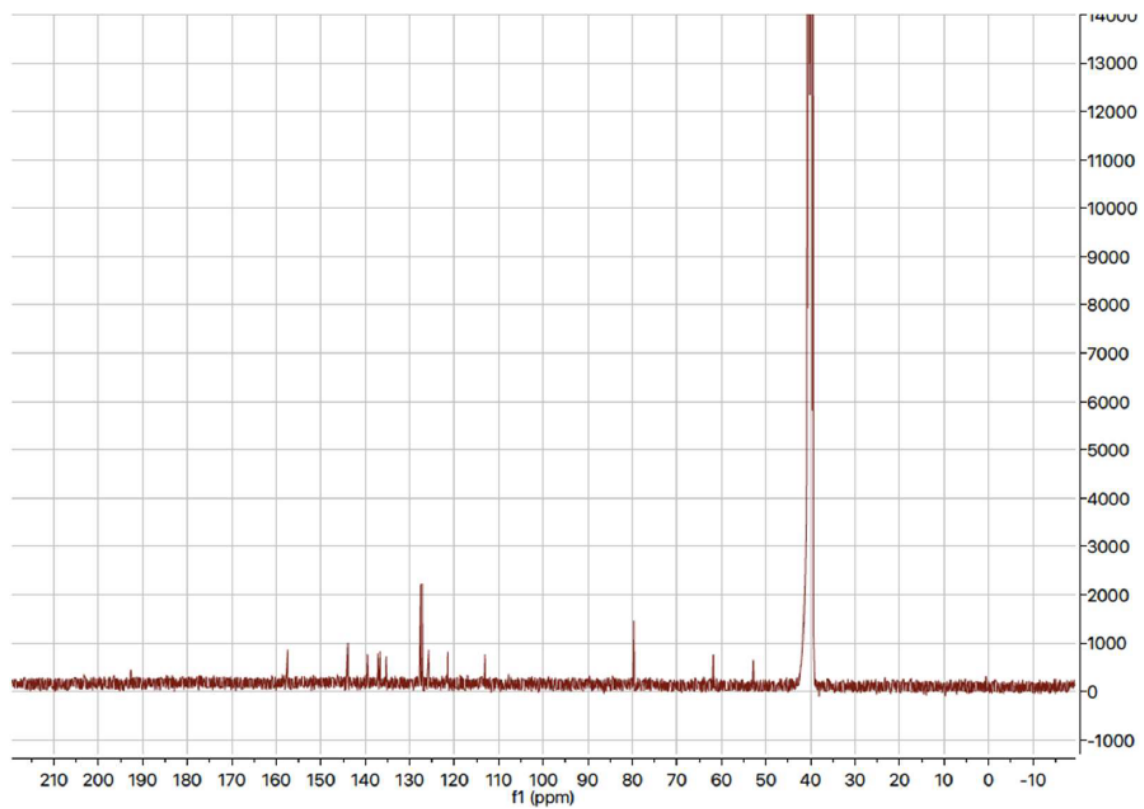


COPIES OF ALL SPECTRA

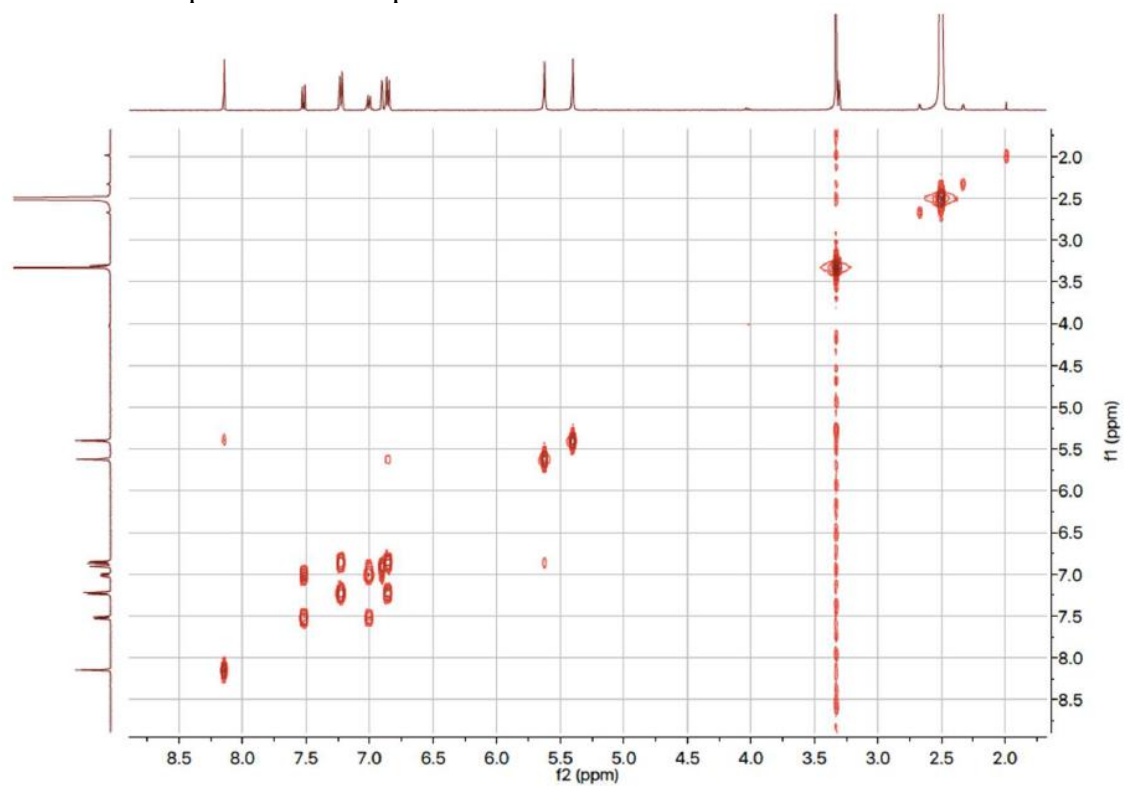
<sup>1</sup>H-NMR spectrum of compound **1** in DMSO-*d*<sub>6</sub>



$^{13}\text{C}$ -NMR of **1** in  $\text{DMSO-}d_6$

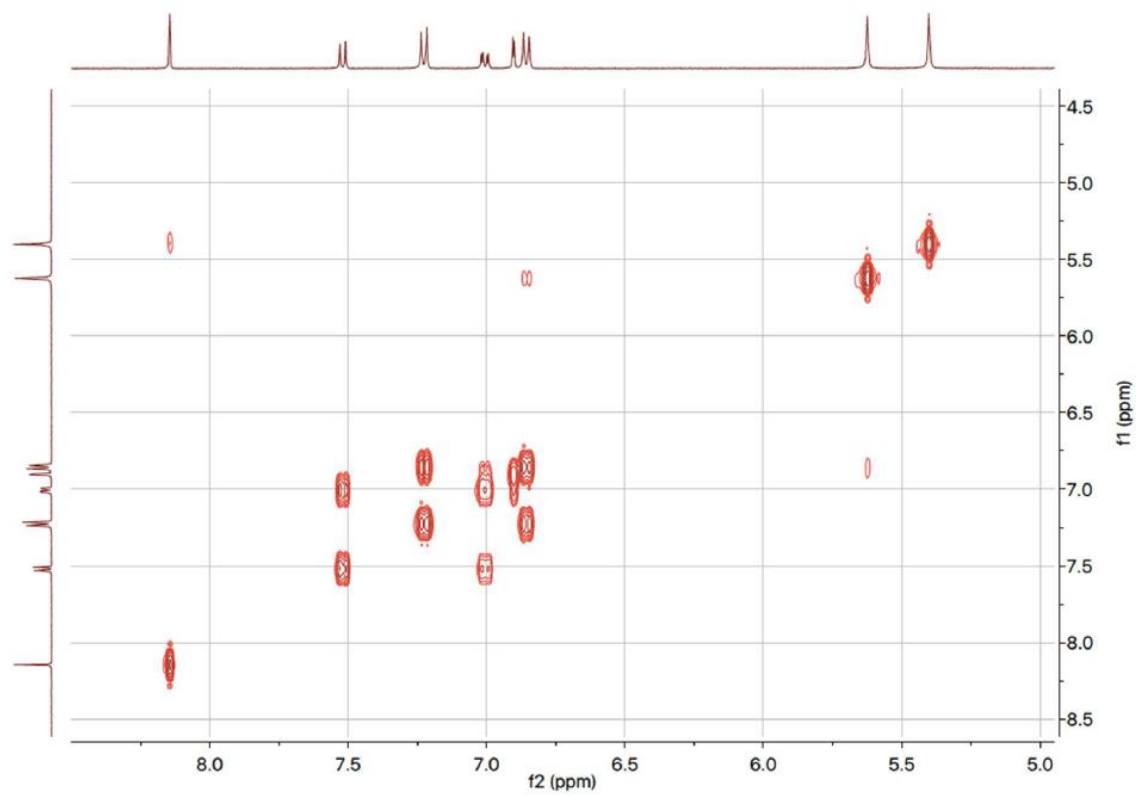


COSY NMR spectrum of compound **1**

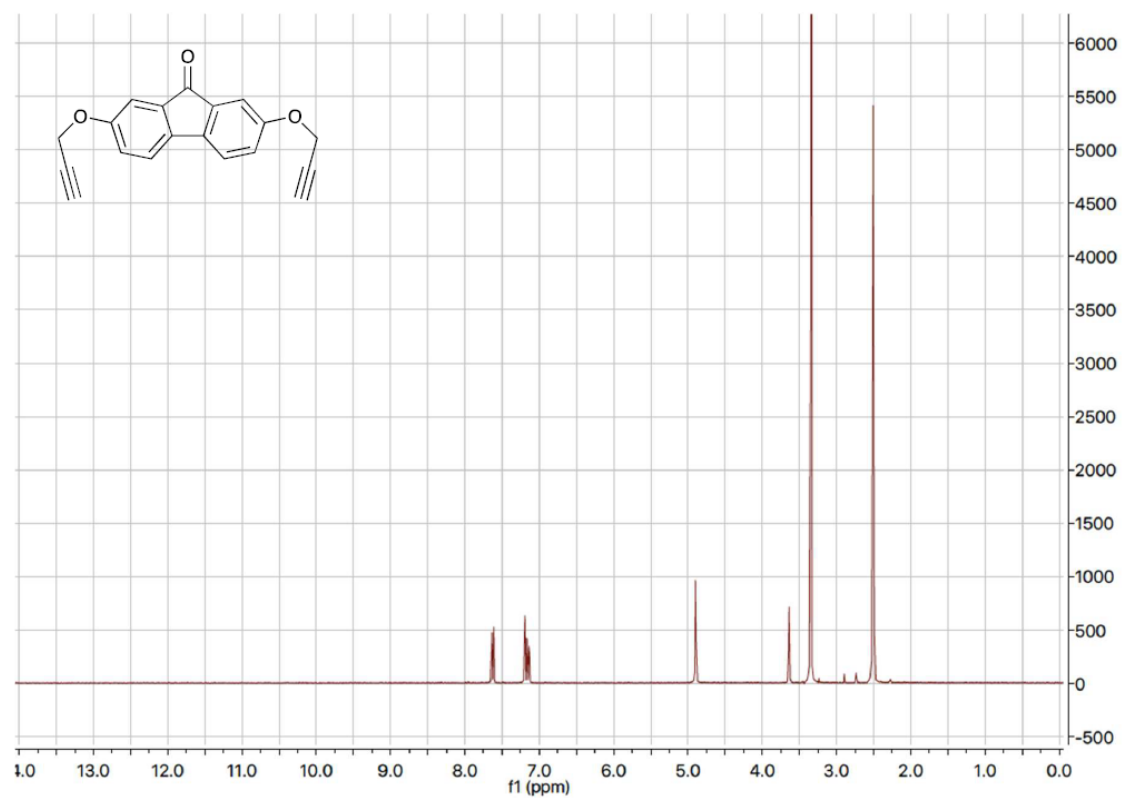




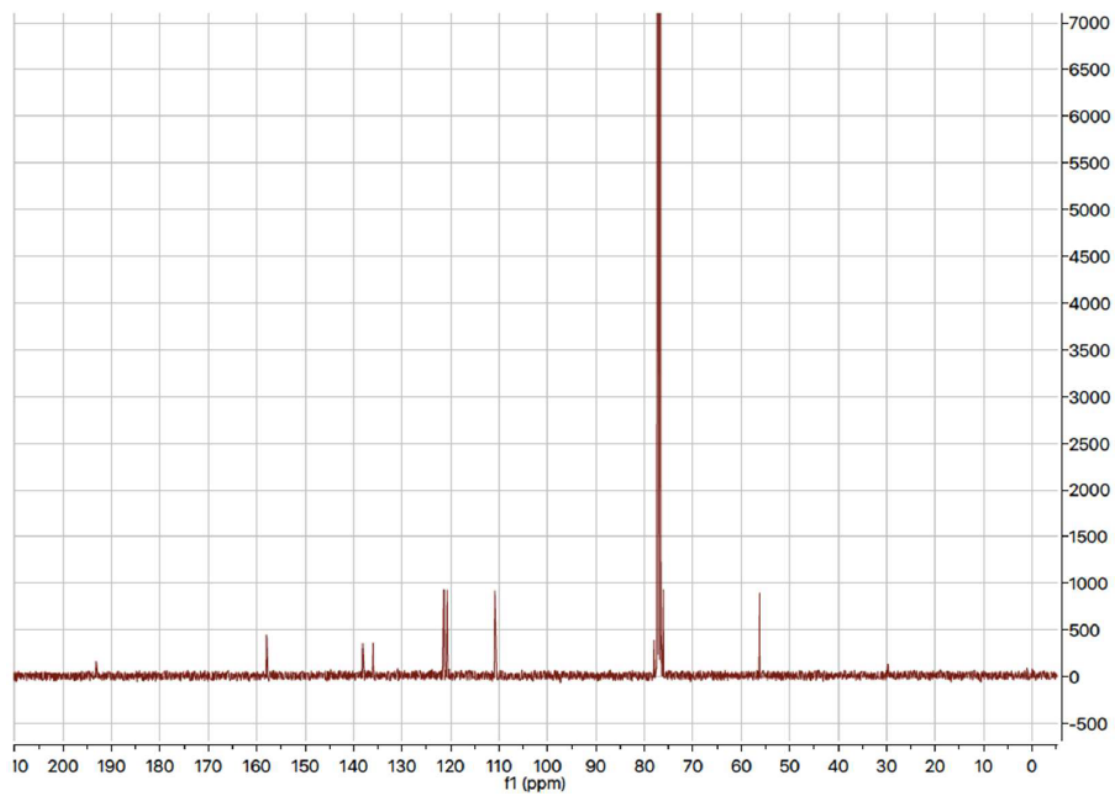
Zoomed-in close-up on the COSY NMR



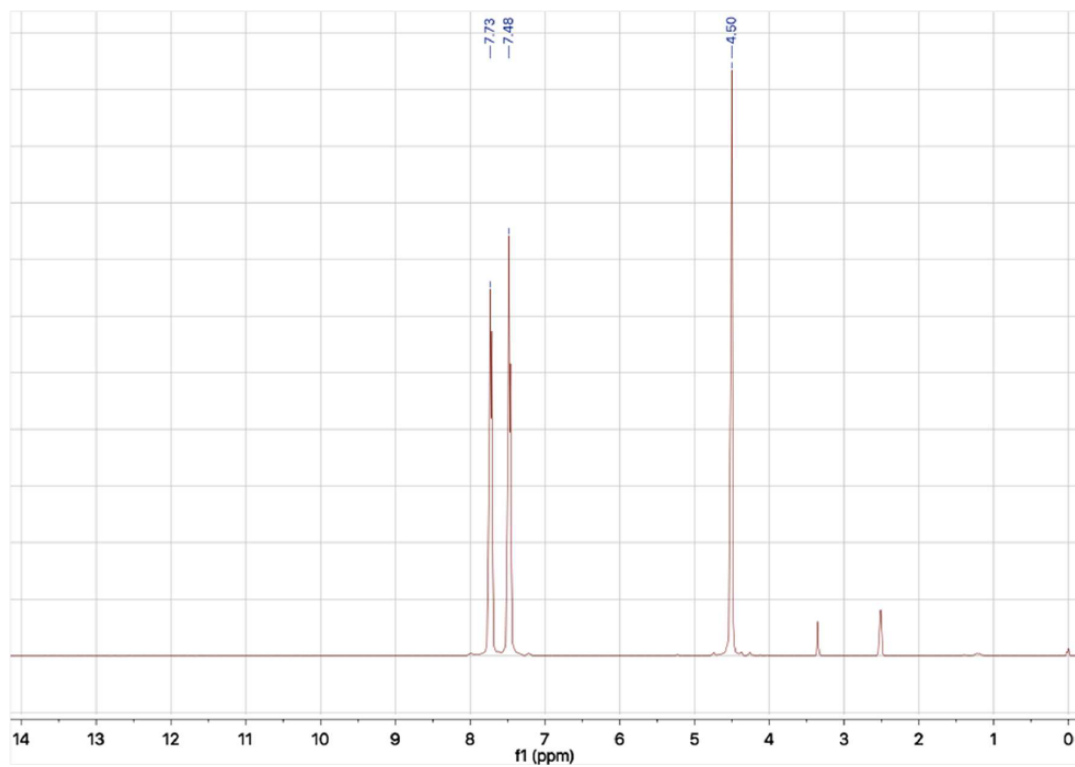
$^1\text{H-NMR}$  of **2** in  $\text{DMSO-}d_6$



$^{13}\text{C}$ -NMR of **2** in  $\text{CDCl}_3$

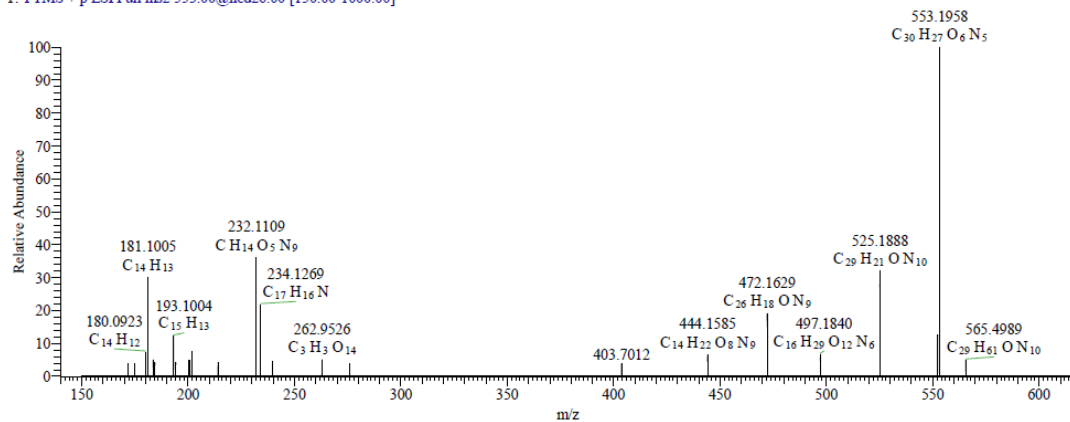


$^1\text{H-NMR}$  of **3** in  $\text{DMSO-}d_6$



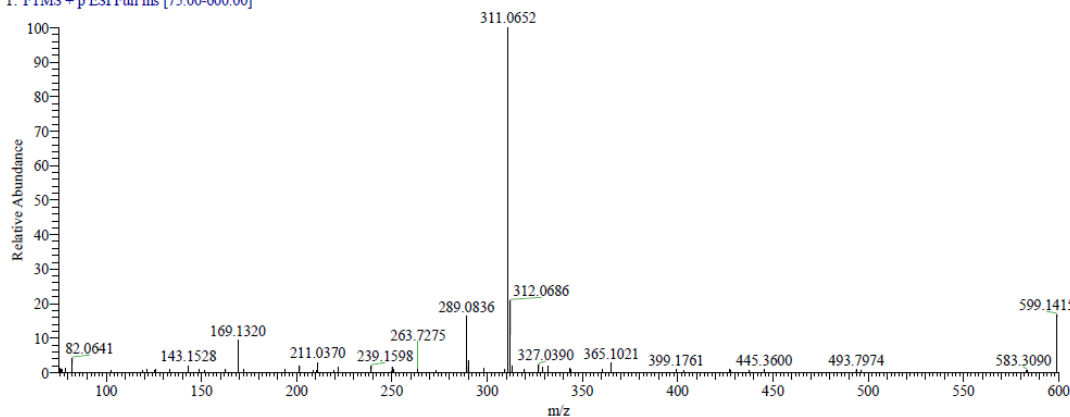
## High resolution mass spectrometry of compound 1

ESI+ IST02\_23mar2017 #193 RT: 2.74 AV: 1 NL: 4.39E4  
T: FTMS + p ESI Full ms2 553.00@hcd26.00 [150.00-1000.00]



## High resolution mass spectrometry of compound 2

ESI+ IST01\_23mar2017 #9 RT: 0.08 AV: 1 NL: 3.35E6  
T: FTMS + p ESI Full ms [75.00-600.00]



## REFERENCE

1. Thordarson, P. "Determining association constant from titration experiments in supramolecular chemistry." *Chem. Soc. Rev.* **2011**, *40*, 1305-1323.

## CHAPTER 6

Published in *Industrial & Engineering Chemistry Research* **2017**, *56*, 899-906

### Impact of Nearly Water-Insoluble Additives on the Properties of Vesicular Suspensions

Amitesh Saha,<sup>†,‡</sup> Sauradip Chaudhuri,<sup>‡,‡</sup> Michael P. Godfrin,<sup>§</sup> Marc Mamak,<sup>||</sup> Bob Reeder,<sup>||</sup> Travis Hodgdon,<sup>||</sup> Pieter Saveyn,<sup>||</sup> Anubhav Tripathi,<sup>§</sup> and Arijit Bose<sup>\*,†</sup>

<sup>†</sup>Department of Chemical Engineering, University of Rhode Island, Kingston, RI, USA

<sup>‡</sup>Department of Chemistry, University of Rhode Island, Kingston, RI, USA

<sup>§</sup>School of Engineering, Brown University, Providence, Rhode Island 02906, United States

<sup>||</sup> Research and Development, Procter & Gamble, Cincinnati, Ohio 45202, United States

<sup>‡</sup>Co-first Authors

Corresponding Author:

Prof. Arijit Bose

Department of Chemical Engineering

University of Rhode Island

Kingston, Rhode Island, 02881, USA

[bosea@uri.edu](mailto:bosea@uri.edu)

## Manuscript 6

### Impact of Nearly Water-Insoluble Additives on the Properties of Vesicular Suspensions

#### ABSTRACT

Nearly water-insoluble additives are commonly used in surfactant-based consumer products to enhance their appeal or performance. We used viscosity measurements, time-resolved cryogenic transmission electron microscopy, and NMR spectroscopy to investigate the effect of several additives, linalyl acetate (LA), cyclohexanol, phenol, catechol, guaiacol, and eugenol, that have extremely low water solubility, on the evolution of microstructures in an aqueous multilamellar vesicle suspension of diethylester dimethylammonium chloride (DEEDMAC), a major ingredient in fabric softeners. LA and eugenol are used as fragrances in some detergent-related consumer products. The other additives were chosen to have degrees of aromaticity that are intermediate between LA and eugenol. The viscosity of the DEEDMAC suspension increased only marginally upon addition of LA, while it rose significantly upon addition of eugenol. Cryo-TEM revealed no observable changes to the multilamellar structures in the DEEDMAC suspension when LA was added. The addition of eugenol triggers a transition from multilamellar vesicles to predominantly unilamellar vesicles and bilayer fragments through exfoliation and breakage. By examining NMR results from all the additives, we propose that  $\pi$  electrons in aromatic rings interact strongly with the cationic DEEDMAC head groups. Such interactions are strong in eugenol but not present in LA.

## INTRODUCTION

Vesicles are made up of single or multiple bilayers consisting of surfactants or lipids<sup>1,2</sup> and are promising delivery vehicles for drugs, enzymes, and other active ingredients.<sup>3-6</sup> In cosmetics, vesicles not only deliver encapsulated ingredients like perfume but also counter skin dryness as the surfactants are hydrated.<sup>7,8</sup>

Esterquats such as diethylester dimethylammonium chloride (DEEDMAC) are double-chained cationic surfactants that are used as the major ingredients in fabric softeners.<sup>9-11</sup> During the latter stage of a laundry cycle, DEEDMAC adsorbs onto negatively charged fabrics, producing a thin lubricating layer that reduces friction between fabric filaments. The inability to form hydrogen bonds also aids in the reduction of static charge. Because of ester linkages, DEEDMAC is readily degradable by hydrolysis in a post-washing cycle.<sup>12</sup> The phase behavior of double-tailed cationic surfactants such as didodecyl dimethylammonium bromide<sup>13,14</sup> (DDAB), dioctadecyl dimethylammonium bromide (DODAB), and dioctadecyl dimethylammonium chloride (DODAC) in water has been studied extensively.<sup>15,16,17,18</sup> These surfactants self-assemble to form unilamellar and multilamellar vesicles in the concentration range of 0.15–30 wt % and above the main phase transition temperature of the bilayer. These vesicles often exist in a kinetically stabilized state.<sup>19-21</sup>

Fragrance is an integral part of many consumer products.<sup>22</sup> Perfume raw materials (PRMs) are added to these products to generate a pleasant odor over extended periods of time. PRM molecules, typically oils, usually have extremely low water solubility. They are therefore distinct from cosurfactants and hydrotopes. However, PRMs even in small concentrations can interact with vesicles in a suspension and perturb vesicular



structures. For example, addition of a PRM can trigger a change from multilamellar to unilamellar vesicles. Excluded volume interactions because of the much larger volume occupied by unilamellar vesicles can cause the viscosity of the suspension to increase substantially.<sup>8</sup> This change is undesirable from shelf life and product end use perspectives. The effect of aromatic ring bearing additives on surfactant and lipid membranes has been studied previously.<sup>23-25</sup> Here, we focus on how the presence of some specific additives cause changes to suspension viscosity that are connected to microstructure evolution.

We have identified linalyl acetate (LA) and eugenol as PRMs of interest because they are used in softener formulations, and the former has a small effect, while the latter has a large effect on the DEEDMAC suspension viscosity. We employ time resolved cryogenic transmission electron microscopy to observe microstructural changes that can be linked to viscosity variations. In addition, we use <sup>1</sup>H-NMR spectroscopy to examine interactions between the additives and DEEDMAC and use this data to explain the underlying mechanisms behind the structural transformations. To provide additional insights, we evaluate changes induced upon addition of nonallyl-substituted structural analogs of eugenol with increasing aromaticity, cyclohexanol, phenol, catechol, and guaiacol, to DEEDMAC suspensions. These molecules are therefore “intermediate” between LA and eugenol, transitioning from the nonaromatic character of LA to the highly aromatic character of eugenol.

## MATERIALS

An aqueous 10 wt % DEEDMAC suspension containing 1200 ppm calcium chloride ( $\text{CaCl}_2$ ) was obtained from Procter & Gamble (P&G). Linalyl acetate (LA;  $\text{C}_{12}\text{H}_{20}\text{O}_2$ , 97%), acetone (99%), cyclohexanol ( $\text{C}_6\text{H}_{12}\text{O}$ , 99%), phenol ( $\text{C}_6\text{H}_6\text{O}$ , 99%), and eugenol ( $\text{C}_{10}\text{H}_{12}\text{O}_2$ , 99%) were obtained from Sigma-Aldrich. Guaiacol ( $\text{C}_7\text{H}_8\text{O}_2$ , 99%) and anhydrous calcium chloride were obtained from Alfa Aesar. Catechol ( $\text{C}_6\text{H}_6\text{O}_2$ , 99+ %) and deuterium oxide (99.9 atom % D) were obtained from Acros Organics. All materials were used as received.

## METHODS

### *Viscosity*

LA and eugenol were added to the DEEDMAC suspension to a final concentration of 2 wt % PRM. The samples were vigorously hand shaken in a vial and left undisturbed at room temperature before being examined at various time points. A TA Instruments AR2000 EX stress-controlled rheometer with a 40 mm diameter and  $0.5^\circ$  steel cone was used for measuring the steady shear viscosity as a function of shear rate.

### *Cryogenic Transmission Electron Microscopy (cryo-TEM)*

The DEEDMAC suspension by itself as well as a suspension diluted by a factor of 10 using a 1200 ppm of a  $\text{CaCl}_2$  solution in water were prepared. This salt concentration ensured that the dilution of the DEEDMAC was isotonic. All additives were mixed with the diluted DEEDMAC suspension, and the samples were hand shaken in a vial. A few microliters of the undiluted or diluted DEEDMAC or the mixed DEEDMAC/additive

suspensions, equilibrated in a controlled environment vitrification system (CEVS) at 25 °C and 95%–100% humidity, were deposited on a holey carbon grid. The high humidity suppresses water evaporation from the sample prior to vitrification. The grid was blotted and then plunged into a liquid ethane reservoir cooled by liquid nitrogen. Rapid heat transfer away from the grid leads to sample vitrification. The samples were vitrified at designated time points after mixing was ceased. The grid containing the sample was transferred to a cooled tip of a Gatan 626DH cryo-transfer stage. The stage was then inserted into a JEOL JEM 2100 transmission electron microscope. The sample was maintained at  $-175$  °C; a low electron dosage ( $\sim 20$  e $^{-}/\text{\AA}^2$ ) and a slight underfocus (1–6  $\mu\text{m}$ ) were used for imaging.

#### *Nuclear Magnetic Resonance (NMR)*

$^1\text{H}$ -NMR spectra were recorded at room temperature on a Bruker-Avance 300 MHz spectrometer with the singlet peak of HDO at 4.79 ppm as reference. All the  $\text{D}_2\text{O}$  used in the NMR samples contain 1200 ppm of  $\text{CaCl}_2$ . Also, 2 wt % eugenol in the  $\text{CaCl}_2$ -containing  $\text{D}_2\text{O}$ , as well as the DEEDMAC suspension added to this mixture, were probed. Despite the low solubility of cyclohexanol, guaiacol, and eugenol in water, these compounds disperse homogeneously after vigorous shaking and provide a clean  $^1\text{H}$ -NMR signal. It was not possible to get a homogeneous dispersion of LA in  $\text{D}_2\text{O}$ , and thus a good NMR signal, as the sample phase separated within several minutes. For probing the LA-containing samples, an 80 vol % solution in acetone was first prepared. This solution was diluted with the  $\text{CaCl}_2$ -containing  $\text{D}_2\text{O}$  to a 2 wt % concentration of

LA. The DEEDMAC suspension was then added, and peak intensities as well as the broadening of specific peaks relevant to LA were monitored.

## RESULTS AND DISCUSSION

Figure 1(a) shows the shear rate dependence of the steady shear viscosity for DEEDMAC suspensions and DEEDMAC suspensions upon mixing with LA and with eugenol. The error bars on the DEEDMAC data represent the spread from three repeats and are indicative of the heterogeneity of the sample. The steady shear viscosities of suspensions with LA increased very moderately from that of DEEDMAC suspensions alone (the error bars for the sample mixed with LA are the same size as those for DEEDMAC alone, so they are not shown). The steady shear viscosities of the DEEDMAC samples mixed with eugenol were almost 2 orders of magnitude higher than that of the DEEDMAC suspension by itself. All the samples were shear thinning for shear rates  $\dot{\gamma} \sim 0.1 \text{ sec}^{-1} - 10 \text{ sec}^{-1}$ . The shear thinning behavior of the DEEDMAC suspension and the ones with additives were very similar. Figure 1(b) shows the viscosity at a shear rate  $\dot{\gamma} = 0.1 \text{ sec}^{-1}$  of DEEDMAC suspensions, measured at various times after mixing. Addition of LA triggers a 1.5–3-fold increase in the suspension viscosity; however, addition of eugenol shows an  $\sim 100$ –200-fold increase in viscosity (the error bars for the eugenol-containing samples are within the size of the symbols). This large increase in viscosity suggests that the addition of eugenol leads to greater changes in the microstructures of DEEDMAC in the suspension, which we explore with cryo-TEM and discuss in the following sections. We note here that the viscosities of both LA and eugenol by themselves are of the order of  $10^{-3} \text{ Pa s}$ . The increase in

viscosities reported here cannot be explained entirely by an increase in volume fraction of material in the suspension. Rather, it is indicative of the interaction of additives with the DEEDMAC causing microstructure changes, negligible in the case of LA and strong in the case of eugenol.

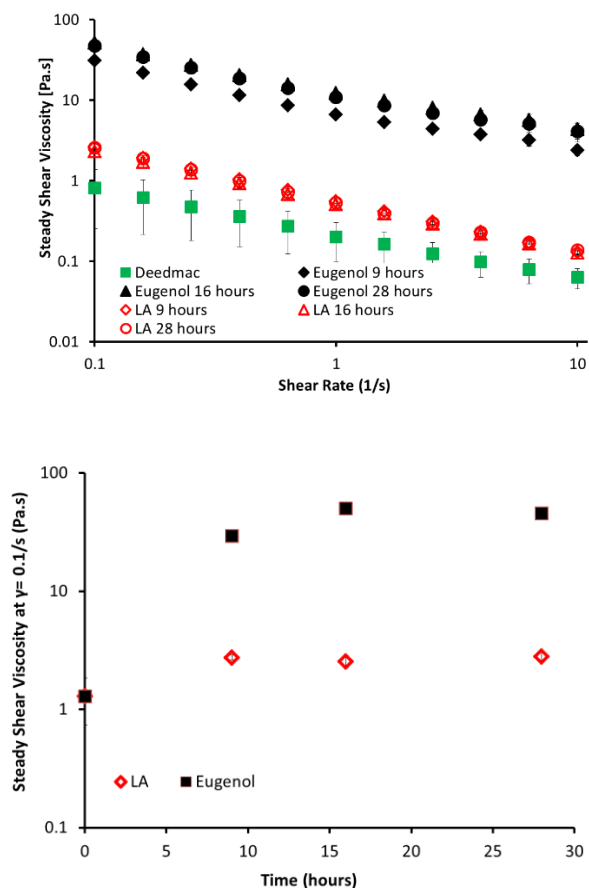


**Figure 1.** Suspension rheometric data. After mixing, the samples were aged to the reported times and then characterized. **(a)** Steady shear viscosity versus shear rate for DEEDMAC suspensions, as well as LA and eugenol added to DEEDMAC suspensions. Given the error bars which correspond to the spread in the data from 3 runs, the increase in viscosity of the LA + DEEDMAC suspension compared to DEEDMAC by itself is small. The increase in viscosity for the eugenol + DEEDMAC suspension is about an order of magnitude higher. The error bars for the eugenol + DEEDMAC suspension are within the size of the plotting symbols **(b)** Viscosity, measured at a shear rate of  $0.1 \text{ sec}^{-1}$ , versus time. Addition of 2 wt% LA to the DEEDMAC vesicle suspension results in a small increase of the viscosity. Addition of 2 wt% eugenol results in a 100-200-fold increase in viscosity.

Figure 2(a) is a cryo-TEM image of an ~10 wt % DEEDMAC suspension as supplied by P&G, showing multilamellar vesicles. The formulation process for the DEEDMAC suspension consists of hydrating dried layers of the surfactant by an aqueous medium. The layers peel off and form multilamellar vesicles when the suspension is agitated. From an application perspective, this is important, as multilamellar structures are able to “store” surfactant in the inner leaflets and thus provide greater supply of DEEDMAC surfactant/volume of suspension than their unilamellar counterparts. In this work, we did not undertake a detailed study of the phase behavior of DEEDMAC in a salt-containing aqueous medium but focused only on the role of additives on this suspension. The DEEDMAC suspension supplied by P&G contains  $\text{CaCl}_2$ . When this suspension was diluted by a 1200 ppm calcium chloride solution in a 1:1 volume ratio, the multilamellar structures, shown in Figure 2(b), were preserved, and the samples look identical to those in Figure 2(a). Osmotic pressure changes caused by an increase in salt concentration outside dioctadecyldimethylammonium bromide (DODAB) vesicles has been known to deflate them into cup-like shapes where the poles of the vesicles approached each other, until they fuse into bilamellar twinned vesicles.<sup>26</sup> Figure 2(c) shows that dilution with water without salt changes the microstructure to unilamellar vesicles because osmotic stresses drive water into multilamellar vesicles and cause them to rupture. This phenomenon has also been observed by others.<sup>8</sup> The absence of this structural change upon addition of a 1200 ppm of  $\text{CaCl}_2$  solution indicated isotonic conditions matching this salt concentration for our sample. Thus, all additives were formulated in water containing 1200 ppm of  $\text{CaCl}_2$ . Any observed changes could then

be directly attributed to the presence of additives. This issue is also important for our NMR experiments.

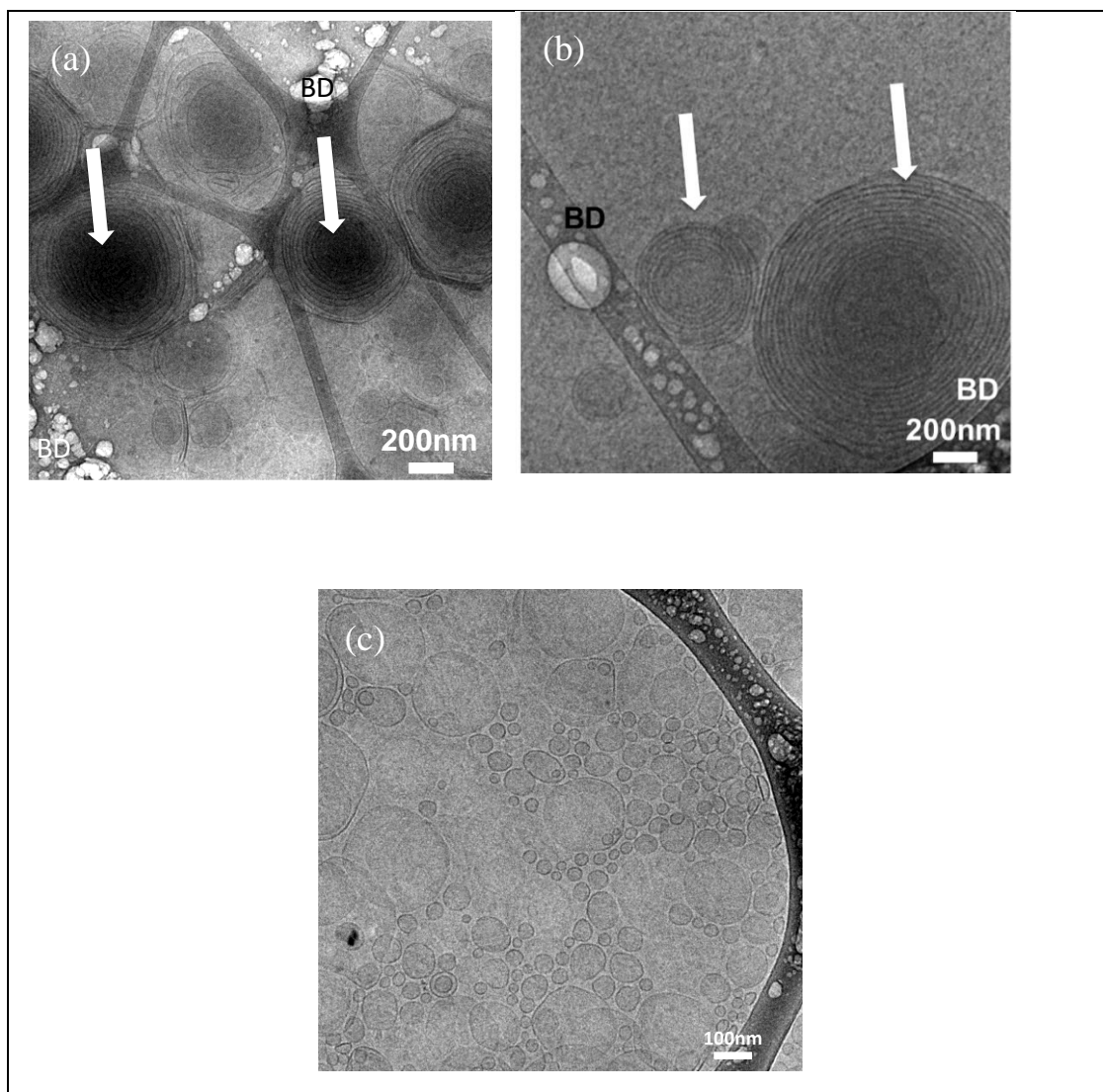


**Figure 2.** Cryo-TEM image of (a) multilamellar vesicles in a DEEDMAC vesicle suspension, indicated by white arrows. BD indicates beam damage. (b) DEEDMAC suspension diluted 1:1 by volume with 1200 ppm CaCl<sub>2</sub>. The structures remain the same as in (a) because of the isotonic dilution. (c) DEEDMAC suspension after 1:1 dilution by volume with deionized water, showing unilamellar vesicles.

Figures 3(a) and 3(b) show no changes to the multilamellar structures after addition of LA to the DEEDMAC vesicle suspension. The vesicles remain fairly polydispersed with diameters around 300–350 nm, close to the sizes of the multilamellar structures without

additives. However, when eugenol was added to the DEEDMAC vesicle suspension, the microstructures changed over time. A few seconds after mixing, multilamellar vesicles were observed, as shown in Figure 4(a). After 6 hrs, we observe undulating bilayers, indicated by the arrows in Figure 4(b) and (c). We speculate that the insertion of the eugenol into the bilayer lowers the phase transition temperature,<sup>27</sup> and thus the bending modulus, and promotes these undulations. Some of the external lamellae got exfoliated and broke off from the vesicles 12 h after mixing, resulting in a reduction in vesicle size. Bilayer fragments were also observed. The newly uncovered lamellae get exposed to eugenol and follow a similar path, ultimately resulting in predominantly unilamellar vesicles in the suspension 24 hrs after mixing. Some tubules were also formed in this process. These are shown in Figure 4(d).

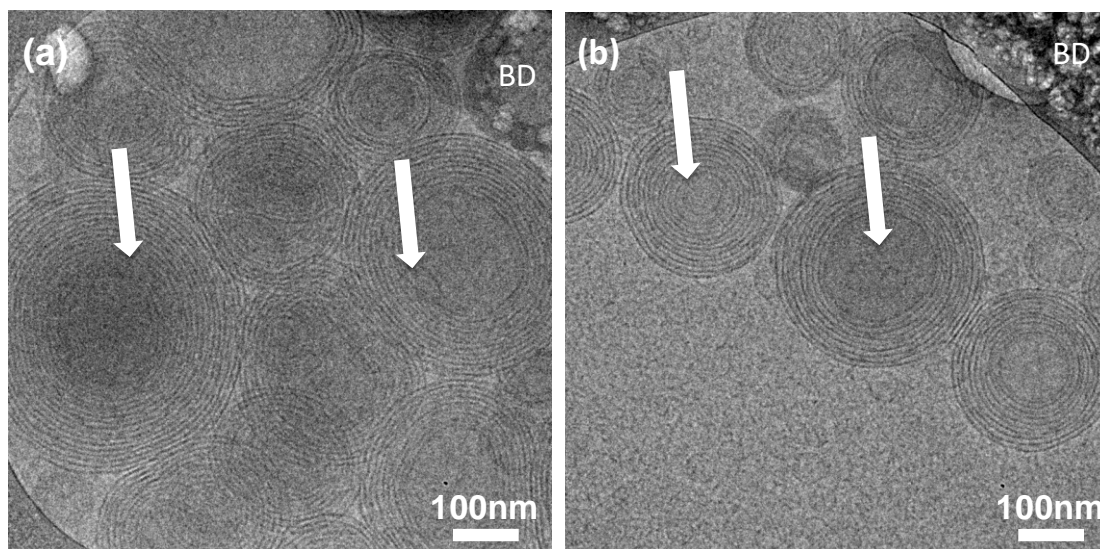


**Figure 3.** Cryo-TEM images showing no changes after addition of 2wt% LA to a DEEDMAC vesicle suspension (a) 10 secs after mixing and (b) 24 hrs after mixing. BD indicates beam damage. White arrows indicate vesicles. Multilamellar vesicles remain as the predominant structure after addition of LA.



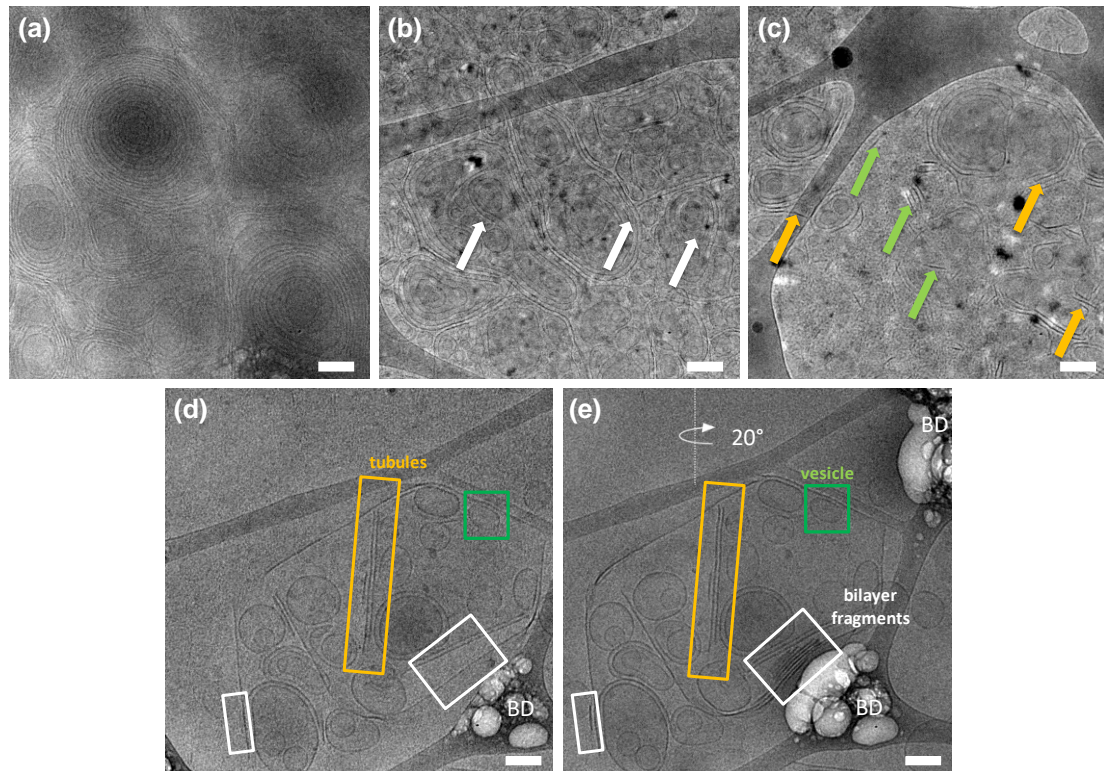


**Figure 4.** Cryo-TEM images of a DEEDMAC vesicle suspension with 2wt% eugenol (a) 10 secs after mixing, showing multiple lamellae; (b) 6 hrs after mixing, showing undulations, marked by arrows and (c) 12 hrs after mixing, showing exfoliation and breakup of bilayers marked by yellow arrows, and free bilayer fragments indicated by green arrows. (d) 24 hrs after mixing, showing unilamellar vesicles, tubules and bilayer fragments (e) morphologies from (d) after tilting the TEM stage by 20°. Vesicle projections do not change shape, but their distance from each other can change. Bilayer fragments are not always visible in 4(d) but become visible as lines in 4(e). The distance between tubule edges does not change upon tilting. Scale bars = 100 nm. BD indicates beam damage.

Cryo-TEM images are two-dimensional projections of three dimensional objects. Tilting of the cryo-stage and reimaging the same region provides an additional set of projections that can be used to identify morphologies of objects vitrified in the sample. Figure 4(e) are images of the samples from Figure 4(d), after the stage has been tilted by 20° around the axis shown by the dashed line. Vesicles are like hollow spheres filled with salt solution, and their morphologies remain the same in both projections. The

distance between neighboring vesicles can change in the projected images after tilting. Bilayer fragments are not very visible when seen normal to their surfaces because of insufficient contrast with the background, in Figure 4(d), but they become edge on and provide enough contrast to become visible in Figure 4(e). Tubules appear as lines, and their relative distance does not change upon tilting.<sup>28</sup> The exfoliation of the multilamellar vesicles over time into predominantly unilamellar vesicles, bilayer fragments, and tubules results in a more volume filling arrangement that causes a rise in the low shear viscosity.

We probed the interaction of LA and eugenol with the DEEDMAC vesicles using <sup>1</sup>H-NMR. Addition of 2 or 4 wt % DEEDMAC vesicle suspension to a 2 wt % eugenol suspension in D<sub>2</sub>O containing 1200 ppm of CaCl<sub>2</sub> showed peak broadening at chemical shifts of 3.75 ppm (methoxide protons), 5.90 ppm (vinyl proton), and 6.75 ppm (aromatic protons), marked by the arrows in Figure 5. This intense peak broadening for eugenol indicates strong association with the DEEDMAC vesicle bilayer, which can be ascribed to cation- $\pi$  electron interaction<sup>29</sup> of the electron-rich aromatic group of eugenol with the positively charged headgroup of DEEDMAC. The linear alkene portion of eugenol also promotes its insertion into the vesicles, positioning the eugenol for reduced mobility in the bilayer. Figure 6 shows an increase in the intensity of the peak associated with the protons in the methyl groups of DEEDMAC over 24 hrs,<sup>30</sup> because of the increased mobility of DEEDMAC caused by bilayer exfoliation and breakage.

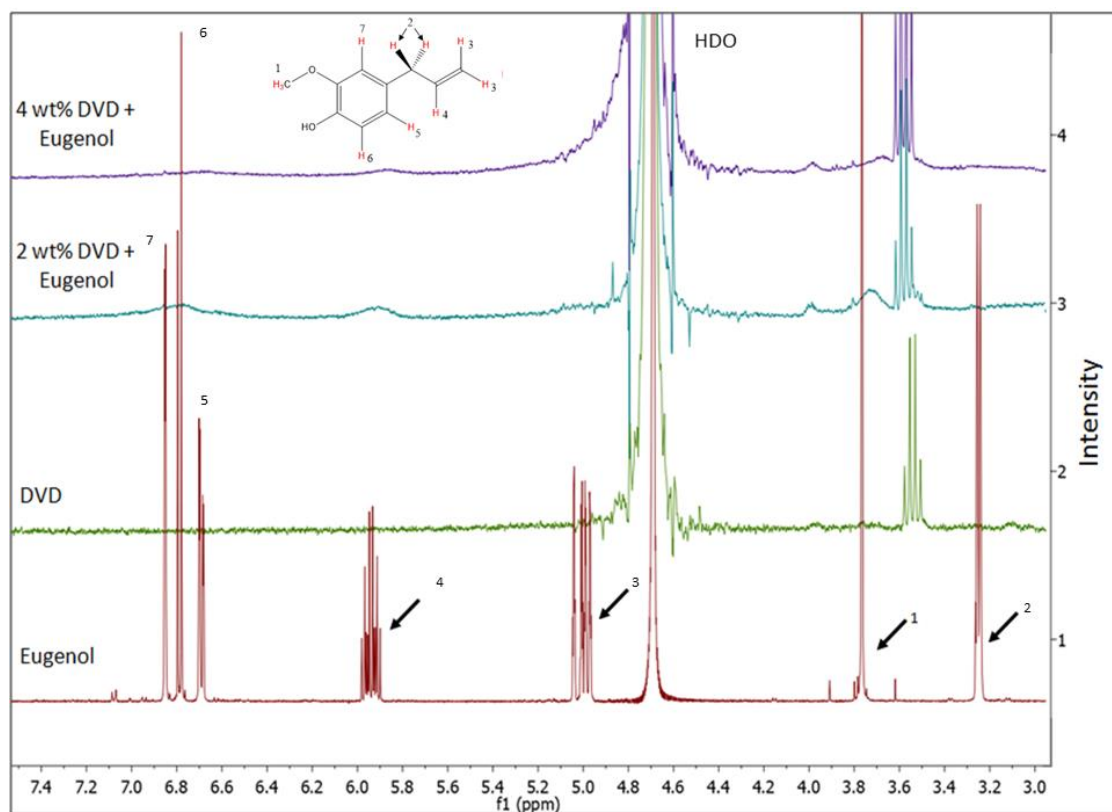


**Figure 5.**  $^1\text{H-NMR}$  spectra showing the impact of adding a DEEDMAC vesicle suspension (DVD) to 2wt% and 4wt% eugenol dissolved in a 1200 ppm  $\text{CaCl}_2$  solution in  $\text{D}_2\text{O}$  24 hrs after mixing. The broadening of several proton peaks from eugenol, marked by the arrows, indicates that the eugenol interacts with the DEEDMAC.

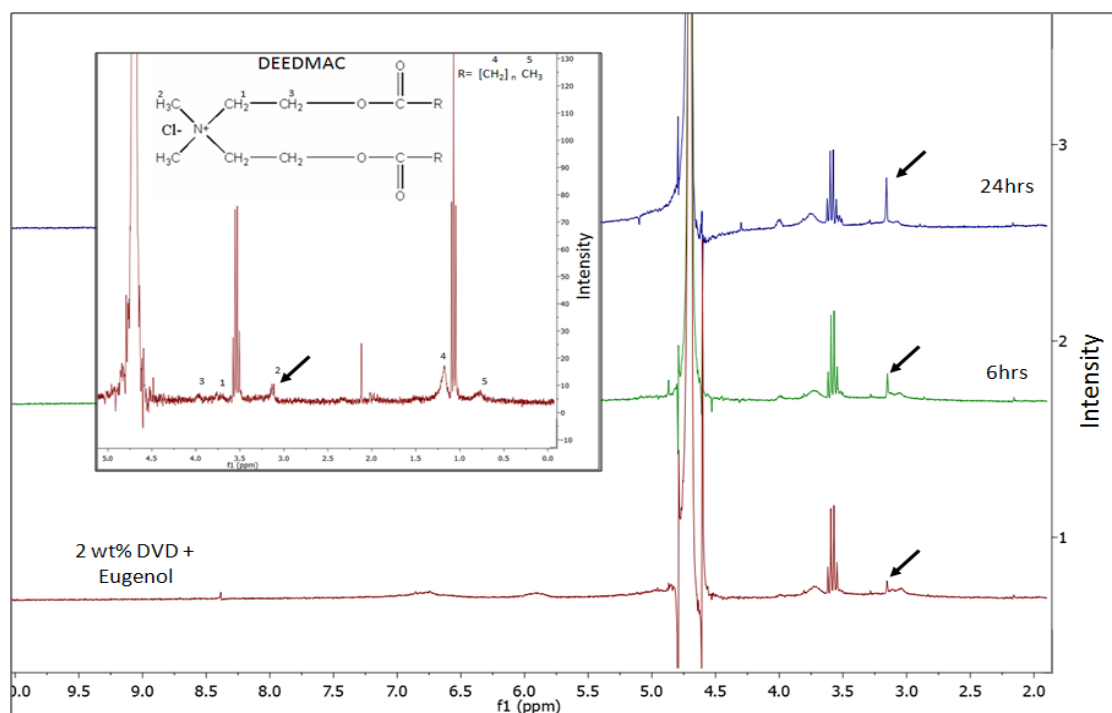


**Figure 6.** Time evolution of  $^1\text{H-NMR}$  spectra after the addition of a 2wt% DEEDMAC vesicle suspension (DVD) to a 2wt% eugenol dissolved in a 1200ppm  $\text{CaCl}_2$  solution in  $\text{D}_2\text{O}$ . The peak intensity corresponding to methyl protons from the DEEDMAC head group, marked by the arrows, increases up to 24 hrs after mixing.

Figure 7 shows  $^1\text{H-NMR}$  spectra of 2 wt % LA in  $\text{D}_2\text{O}$  containing 1200 ppm of  $\text{CaCl}_2$  24 h after exposure to a 4 wt % DEEDMAC vesicle suspension. Peaks at chemical shifts of 1.38, 1.45, 1.54, and 1.79 ppm that represent methyl protons, remain unchanged, indicating no association with DEEDMAC vesicles. No changes were observed for the multiplets of alkene protons at chemical shifts of 5.1 and 5.8 ppm. These observations confirm that LA does not interact with DEEDMAC.

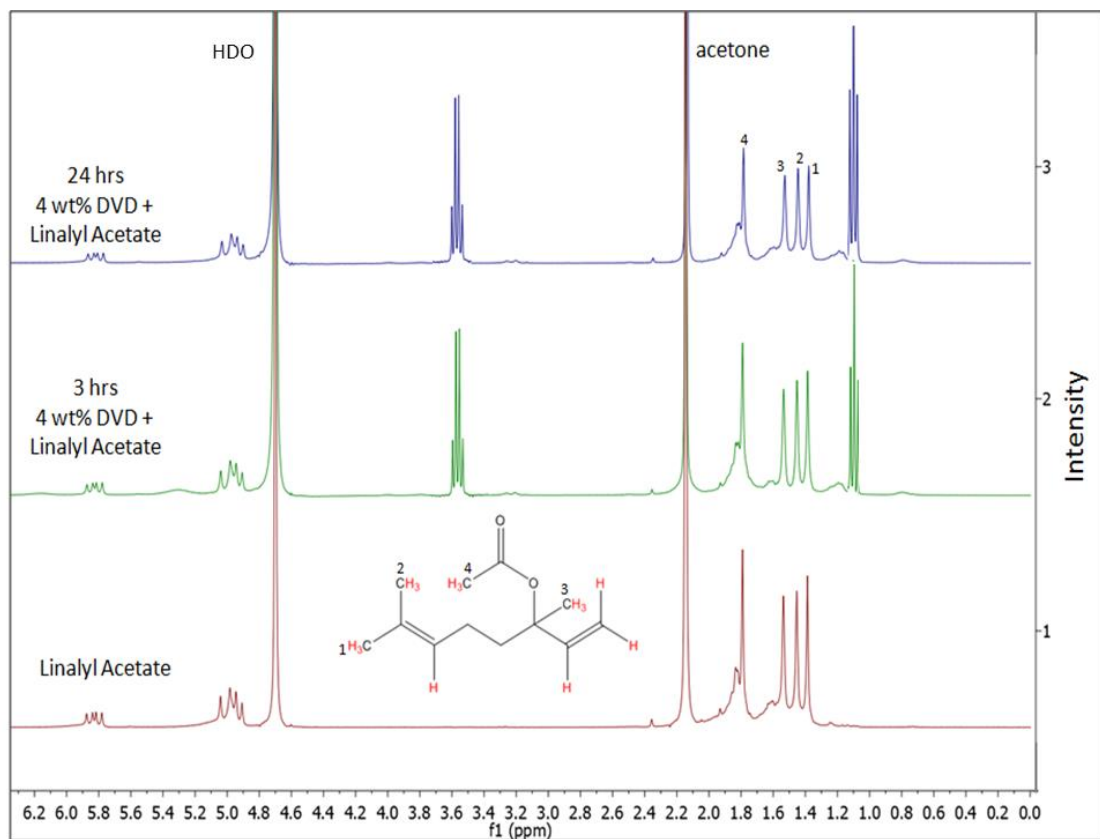


**Figure 7.**  $^1\text{H-NMR}$  spectra showing the impact of adding 2 wt % DEEDMAC vesicle suspension (DVD) to LA, showing no peak broadening. The intensity of the peaks also remains stable over time.

To further understand why the aromatic core and hydrophobic allyl substituent in eugenol caused microstructural changes to DEEDMAC vesicles, we investigated a series of additives - cyclohexanol, phenol, catechol, and guaiacol. These are chosen as structural analogs of eugenol without the hydrophobic allyl substituent and with increasing aromatic strength.  $^1\text{H-NMR}$  results of DEEDMAC interactions with each of these probes in comparison to LA and eugenol are shown in Figure 8. While the aromatic protons exhibit increasing peak broadening as we go from phenol to eugenol, the aliphatic protons of cyclohexanol and LA remain unchanged upon addition of 2 wt %

DEEDMAC solution. This increasing peak broadening indicates strong cation- $\pi$  electron interaction, which is shown in the schematic as an aromatic core interacting with the cationic surfactant headgroup of DEEDMAC.

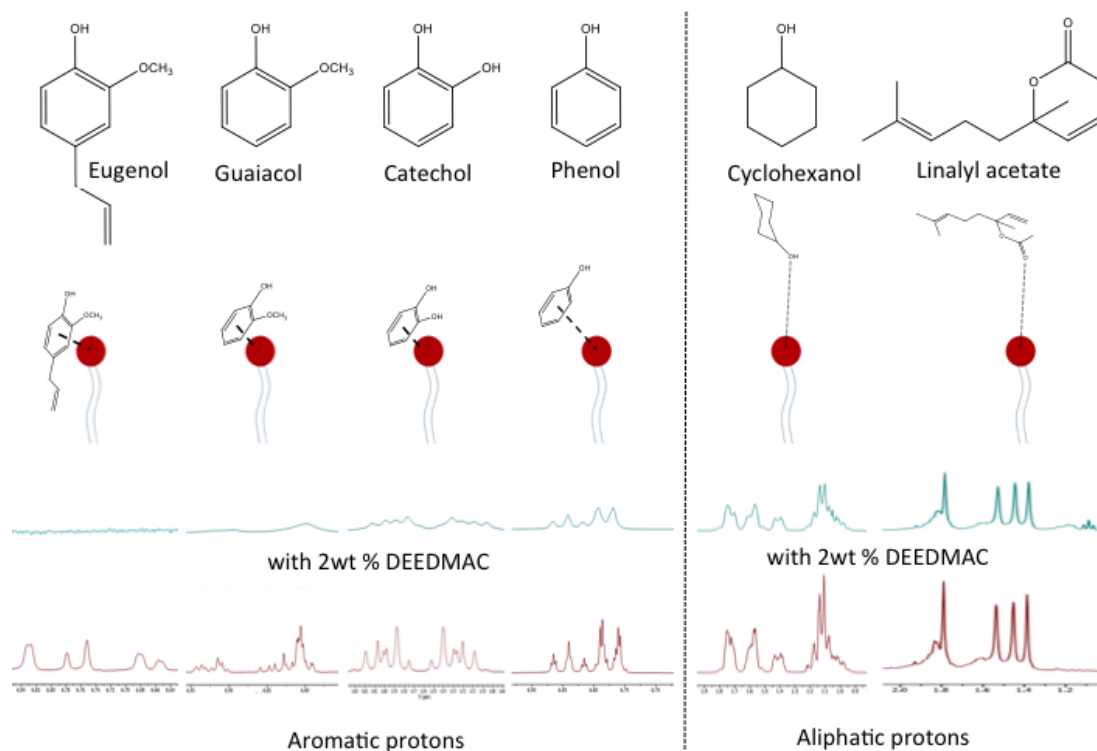


**Figure 8.**  $^1\text{H-NMR}$  spectra showing the impact of adding 2 wt % DEEDMAC vesicle suspension (DVD) to various additives. While  $^1\text{H-NMR}$  peaks of cyclohexanol and LA exhibit no change, the aromatic proton peaks of phenol, catechol, guaiacol and eugenol show strong broadening due to cation- $\pi$  electrons interaction with the cationic DEEDMAC head group. The thickness of the dashed lines is meant to indicate the strength of the interactions.

A comparison of cryo-TEM images of DEEDMAC vesicles 24 hrs after the addition of 2 wt % eugenol, guaiacol, catechol, phenol, cyclohexanol, and LA, along with the corresponding  $^1\text{H-NMR}$  results (Figures S1–S4 in the Supporting Information) confirm that the stronger association of aromatic additives as well as their possible intrusion into the DEEDMAC vesicle bilayer is indicative of their contribution to bilayer exfoliation.

The additives chosen for our experiments had varying amounts of aromaticity and different substituents.  $^1\text{H-NMR}$  results indicate that cation- $\pi$  electron interactions play a dominant role. Both cryo-TEM images show morphology variations, and viscosity measurements show changes that are consistent with cation- $\pi$  electron interactions between the DEEDMAC and the additives. The microstructures did not change when the substituents on the aromatic rings were modified, but they did respond to a change from an aliphatic to an aromatic additive. Thus, any other contributions, such as hydrophobic interactions and steric effects, which can dominate interactions between some surfactants and additives, appear to be less important for the additives used in our experiments. We note that association of a PRM with a bilayer has consequences on the olfactory effects of these materials through its impact on release kinetics. This latter issue has not been studied in this paper.

## CONCLUSIONS

Vesicles in these commercial surfactant-based systems are excellent sources of surfactant, as well as good carriers of hydrophobic, water-insoluble additives that are commonly used to enhance product attributes. Using steady shear and time-resolved viscosity, cryo-TEM and NMR measurements, we have probed the interaction of two model additives, LA and eugenol to a vesicular suspension of DEEDMAC. These are complemented by cryo-TEM and  $^1\text{H-NMR}$  results from four additional probes, cyclohexanol, phenol, catechol, and guaiacol. Our results indicate that the aromatic character of eugenol is responsible for strong association with DEEDMAC vesicle bilayers, predominantly via cation- $\pi$  electron interactions, thereby resulting in

microstructural changes. This change was accompanied by a large increase in the low shear viscosity compared to the DEEDMAC suspension by itself. Specific interactions of LA with DEEDMAC were not observed by  $^1\text{H-NMR}$ , consistent with a negligible increase in the viscosity and no noticeable structural changes in the multilamellar vesicular dispersion. The intermediate compounds show behavior that is consistent with their aromaticity. Thus,  $\pi$  electron–cation interactions trigger the transformations from multilamellar to unilamellar vesicles through an exfoliation process. Understanding additive molecule-specific interactions with vesicles is key to developing stable vesicular formulations with multifunctional properties.

#### ACKNOWLEDGEMENT

We gratefully acknowledge the financial support provided by Procter & Gamble, Cincinnati, Ohio, and a URI Graduate Fellowship to A.S. We thank Dr. Al Bach for help with the NMR measurements.

#### NOTES AND REFERENCES

1. Seifert, U. *Adv. Phys.* **1997**, *46*(1), 13–137.
2. Israelachvili, J. N. *Intermolecular and Surface Forces*, Second ed.; Academic Press, 2005.
3. Schreier, H.; Bouwstra, J. *J. Controlled Release* **1994**, *30*(1), 1–15.
4. Walde, P.; Ichikawa, S. *Biomol. Eng.* **2001**, *18*(4), 143–177.
5. Sakai, H.; Tsuchida, E. *J. Liposome Res.* **2007**, *17* (3–4), 227–235.
6. Pohorille, A.; Deamer, D. *Trends Biotechnol.* **2002**, *20* (3), 123–128.



7. Heynderickx, P. M.; De Clercq, S.; Saveyn, P.; Dewulf, J.; Van Langenhove, H. *Chem. Eng. J. (Amsterdam, Neth.)* **2013**, *217*, 281–288.
8. Seth, M.; Ramachandran, A.; Murch, B. P.; Leal, L. G. *Langmuir* **2014**, *30*(34), 10176–10187.
9. Obendorf, S. K. *J. Ind. Text.* **1983**, *13*(1), 24–34.
10. Obendorf, S. K.; Dixit, V.; Woo, D. J. *J. Surfactants Deterg.* **2009**, *12*(3), 225–230.
11. Obendorf, S. K.; Solbrig, C. M. *In Performance of Protective Clothing*; ASTM International **1986**, 187–204.
12. Giolando, S. T.; Rapaport, R. A.; Larson, R. J.; Federle, T. W.; Stalmans, M.; Masscheleyn, P. *Chemosphere* **1995**, *30*(6), 1067–1083.
13. Dubois, M.; Zemb, T. *Langmuir* **1991**, *7*(7), 1352–1360.
14. Marques, E. F.; Regev, O.; Khan, A.; da Graca Miguel, M.; Lindman, B. *J. Phys. Chem. B* **1999**, *103*(39), 8353–8363.
15. Svitova, T. F.; Smirnova, Y. P.; Pisarev, S. A.; Berezina, N. A. *Colloids Surf., A* **1995**, *98*(1-2), 107–115.
16. Haas, S.; Hoffmann, H.; Thunig, C.; Hoinkis, E. *Colloid Polym. Sci.* **1999**, *277*(9), 856–867.
17. Feitosa, E.; Karlsson, G.; Edwards, K. *Chem. Phys. Lipids* **2006**, *140*(1–2), 66–74.
18. Laughlin, R. G.; Munyon, R. L.; Fu, Y. C.; Fehl, A. J. *J. Phys. Chem.* **1990**, *94*(6), 2546–2552.
19. Laughlin, R. G. *Colloids Surf., A* **1997**, *128*(1–3), 27–38.
20. Luisi, P. L. *J. Chem. Educ.* **2001**, *78*(3), 380–384.
21. Pansu, R. B.; Arrio, B.; Roncin, J.; Faure, J. *J. Phys. Chem.* **1990**, *94*(2), 796–801.
22. Jellinek, J. S. *The Use of Fragrance in Consumer Products*; Wiley: New York, 1975.
23. Xu, L.; Yokoyama, E.; Satoh, M. *Langmuir* **2005**, *21*, 7153–7160.
24. El Maghraby, G. M. M.; Williams, A. C.; Barry, B. W. *Int. J. Pharm.* **2005**, *292*(1-2), 179–185.

25. El Maghraby, G. M. M.; Campbell, M.; Finnin, B. C. *Int. J. Pharm.* **2005**, *305*, 90–104.
26. Hubert, D. H. W.; Jung, M.; Frederik, P. M.; Bomans, P. H. H.; Meuldijk, J.; German, A. L. *Langmuir* **2000**, *16* (23), 8973–8979.
27. van Gorkom, L. C.; Nie, S. Q.; Epand, R. M. *Biochemistry* **1992**, *31*, 671–677.
28. Hiemenz, P. C. *Principles of Colloid and Surface Chemistry*, Second ed.; CRC Press, **1986**.
29. Ma, J. C.; Dougherty, D. A. *Chem. Rev. (Washington, DC, U. S.)* **1997**, *97*(5), 1303–1324.
30. Saveyn, P.; Van der Meeren, P.; Cocquyt, J.; Drakenberg, T.; Olofsson, G.; Olsson, U. *Langmuir* **2007**, *23* (21), 10455–10462.

**Impact of Nearly Water-Insoluble Additives on the Properties of Vesicular Suspensions**



**Figure S1 (A)** Cryo-TEM image showing effect of addition of 2wt% cyclohexanol to a DEEDMAC vesicle suspension after 24 hrs. Multilamellar vesicles (white arrows). Scale bar = 100nm.

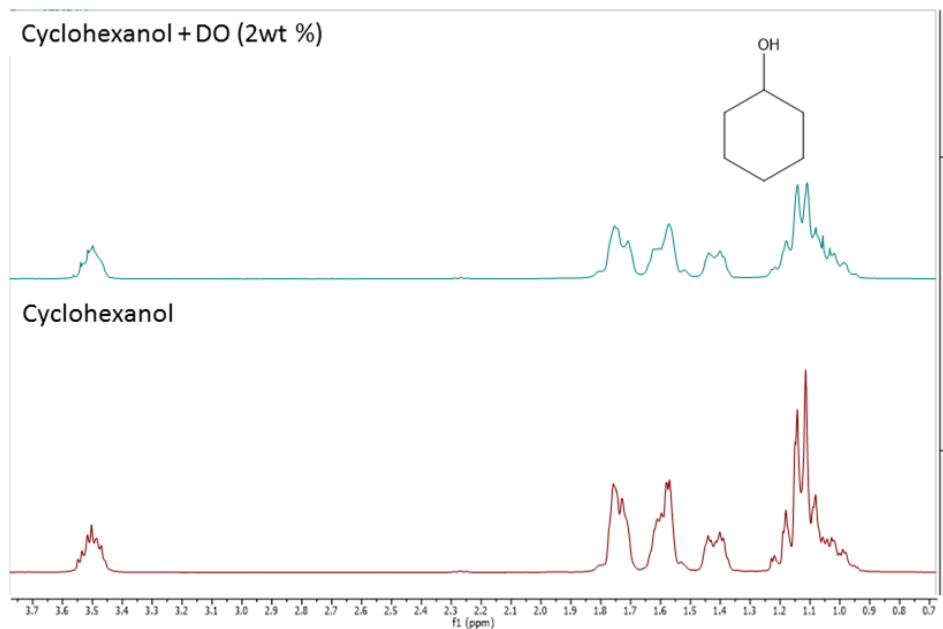


**Figure S1 (B)** <sup>1</sup>H-NMR spectra of addition of 2wt% DEEDMAC suspension to cyclohexanol after 24 hrs showing no peak broadening.

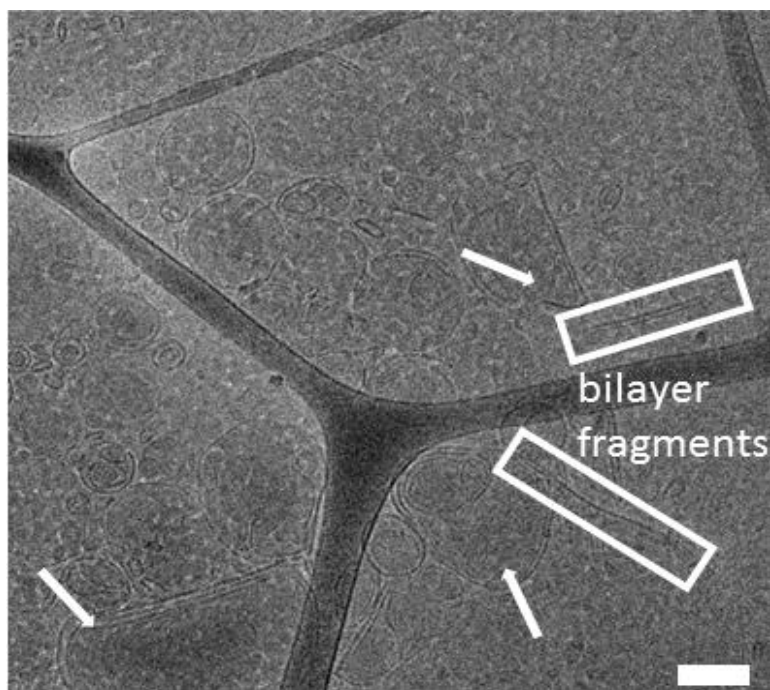


**Figure S2 (A)** Cryo-TEM image showing effect of addition of 2wt% phenol to a DEEDMAC vesicle suspension after 24 hrs. Undulated vesicles (white arrows) and bilayer fragments (white box) Scale bar = 100nm.

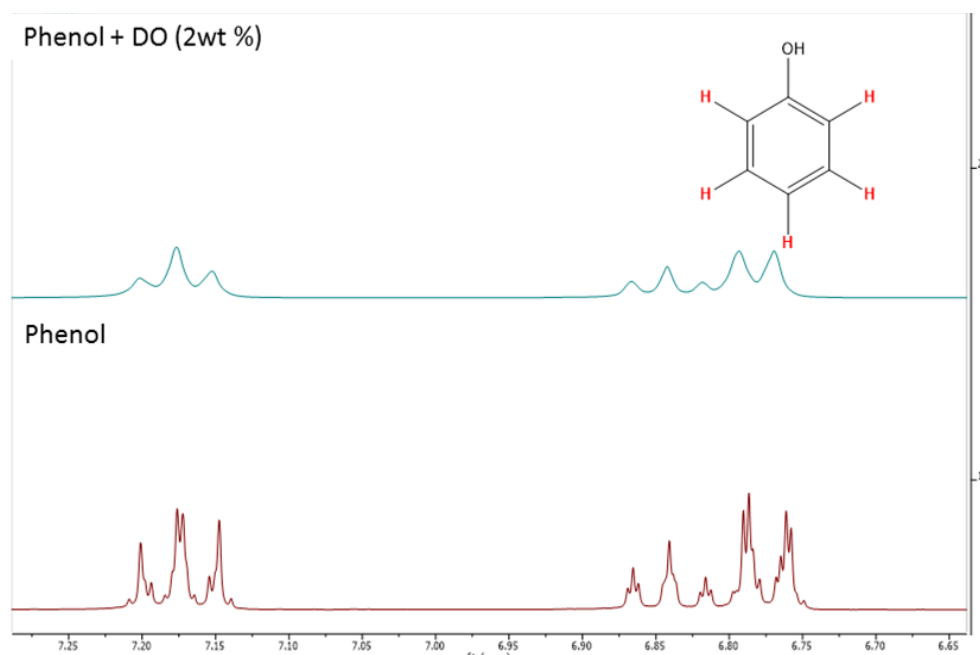


**Figure S2 (B)** <sup>1</sup>H-NMR spectra of addition of 2wt% DEEDMAC suspension to phenol after 24 hrs showing modest peak broadening.

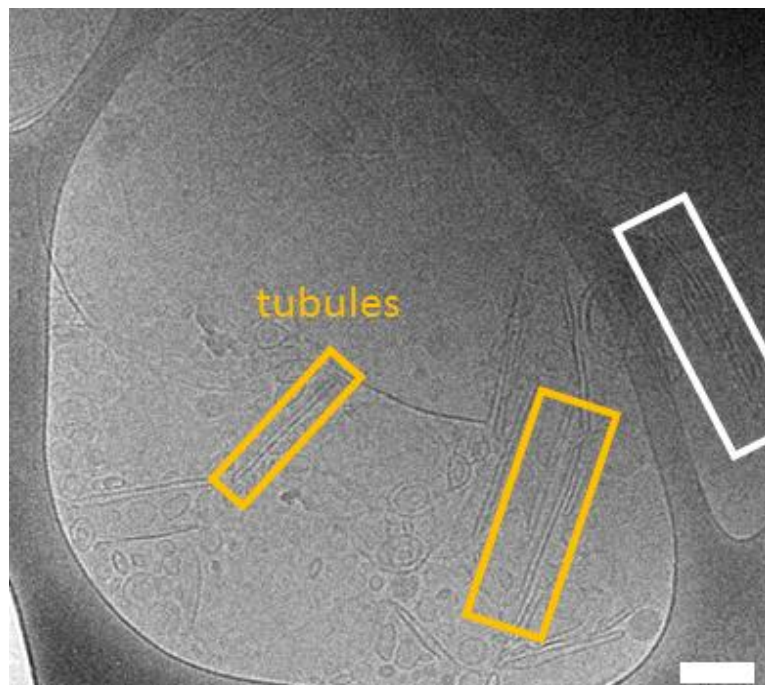


**Figure S3 (A)** Cryo-TEM image showing effect of addition of 2wt% catechol to a DEEDMAC vesicle suspension after 24 hrs. Tubules (yellow boxes) and bilayer fragments (white box). Scale bar = 100nm.

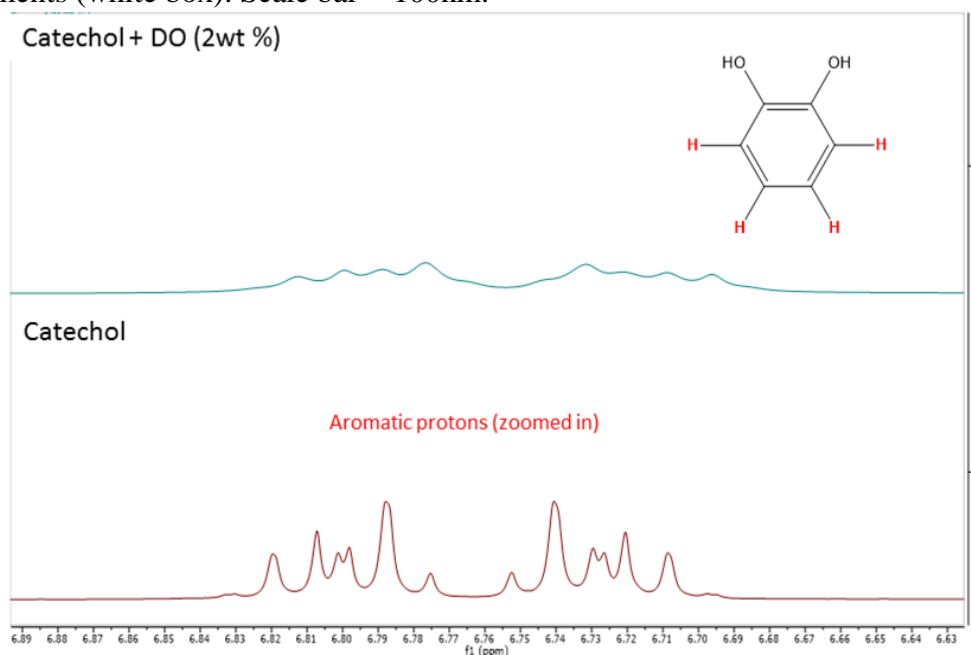


**Figure S3 (B)**  $^1\text{H-NMR}$  spectra of addition of 2wt% DEEDMAC suspension to catechol after 24 hrs showing strong peak broadening.

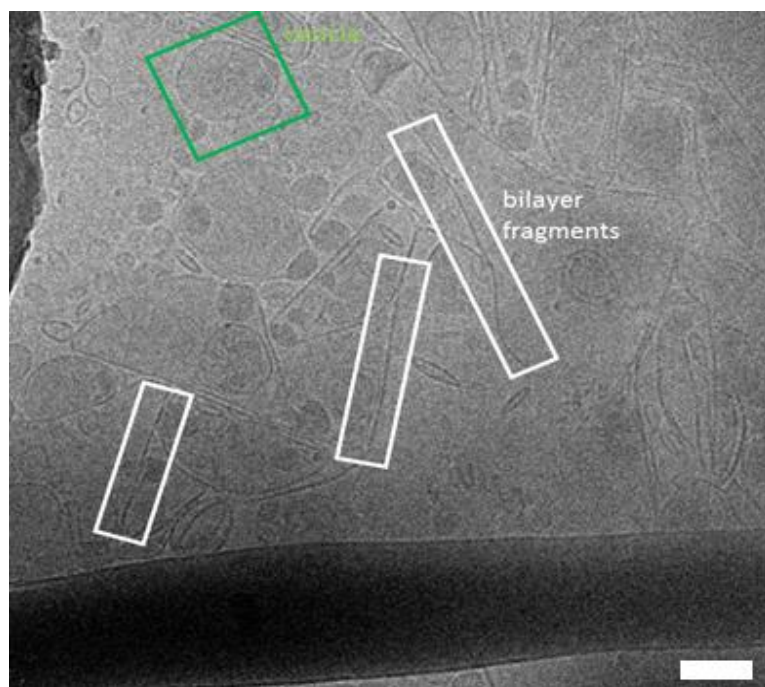


**Figure S4 (A)** Cryo-TEM image showing effect of addition of 2wt% guaiacol to a DEEDMAC vesicle suspension after 24 hrs. Unilamellar vesicles (green box) and bilayer fragments (white boxes). Scale bar = 100nm.

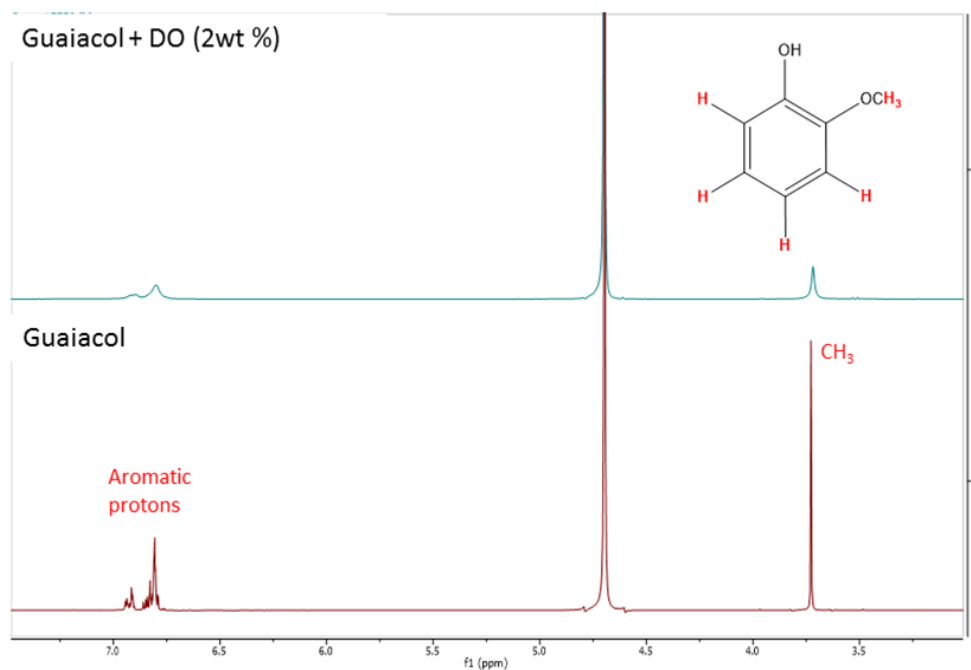


**Figure S4 (B)** <sup>1</sup>H-NMR spectra of addition of 2wt% DEEDMAC suspension to guaiacol after 24 hrs showing strong peak broadening.